

**Regulating Activity and Expression  
of Cell Signaling Molecules  
in Nervous System Development  
and Disease**

**Susan van Erp**

*"Can a biologist fix a radio?"*  
Yuri Lazebnik, Cancer Cell, 2002

## **Colofon**

The research described in this thesis was performed at the Department of Translational Neuroscience, Brain Center Rudolf Magnus, University Medical Center Utrecht, The Netherlands.

Publication of this thesis was financially supported by Carl Zeiss Microscopy and the Brain Center Rudolf Magnus.

**About the cover:** Microscopy image displaying a fluorescently labelled *in vitro* network of migrating cerebellar neurons. In green:  $\beta$ III-Tubulin (neuronal marker), red: Neogenin (guidance receptor) and blue: DNA (nucleus).

**Lay-out:** Proefschrift-AIO.nl

**Printing:** DPP

**ISBN:** 978-90-393-6294-5

Copyright © 2015, Susan van Erp

All rights reserved. No part of this thesis may be reproduced, stored, or transmitted in any form by any means, without prior permission of the author.



# **Regulating Activity and Expression of Cell Signaling Molecules in Nervous System Development and Disease**

## **Regulatie van Activiteit en Expressie van Cel Signaal Moleculen in Zenuwstelsel Ontwikkeling en Ziekte**

(met een samenvatting in het Nederlands)

### **Proefschrift**

ter verkrijging van de graad van doctor aan de Universiteit Utrecht  
op gezag van de rector magnificus, prof.dr. G.J. van der Zwaan,  
ingevolge het besluit van het college voor promoties  
in het openbaar te verdedigen

op donderdag 12 maart 2015 des middags te 4.15 uur

door

**Susan van Erp**

geboren op 13 november 1984 te Veghel

**Promotoren:** Prof.dr. R.J. Pasterkamp  
Prof.dr. J.P.H. Burbach

# Contents

---

## **Chapter 1**

General Introduction

**p. 7**

---

## **Chapter 2**

Semaphorin signaling: molecular switches at the midline

**p. 29**

---

## **Chapter 3**

Structure of the RGMb-Neogenin signaling hub

**p. 41**

Supplemental Information

**p. 52**

---

## **Chapter 4**

The leucine-rich repeat protein Lrig2 regulates the ectodomain shedding of axon guidance receptors at the neuronal growth cone

**p. 71**

Supplemental Information

**p. 110**

---

## **Chapter 5**

Neogenin and its novel binding partner Dock7 are required for RGMa-regulated radial cerebellar granule neuron migration

**p. 127**

---

## **Chapter 6**

A role for BicD2 in radial cerebellar granule neuron migration

**p. 155**

Supplemental Information

**p. 168**

---

## **Chapter 7**

Genome-wide microRNA profiling of human temporal lobe epilepsy identifies modulators of the immune response

**p. 177**

---

## **Chapter 8**

General Discussion

**p. 199**

---

## **Addendum**

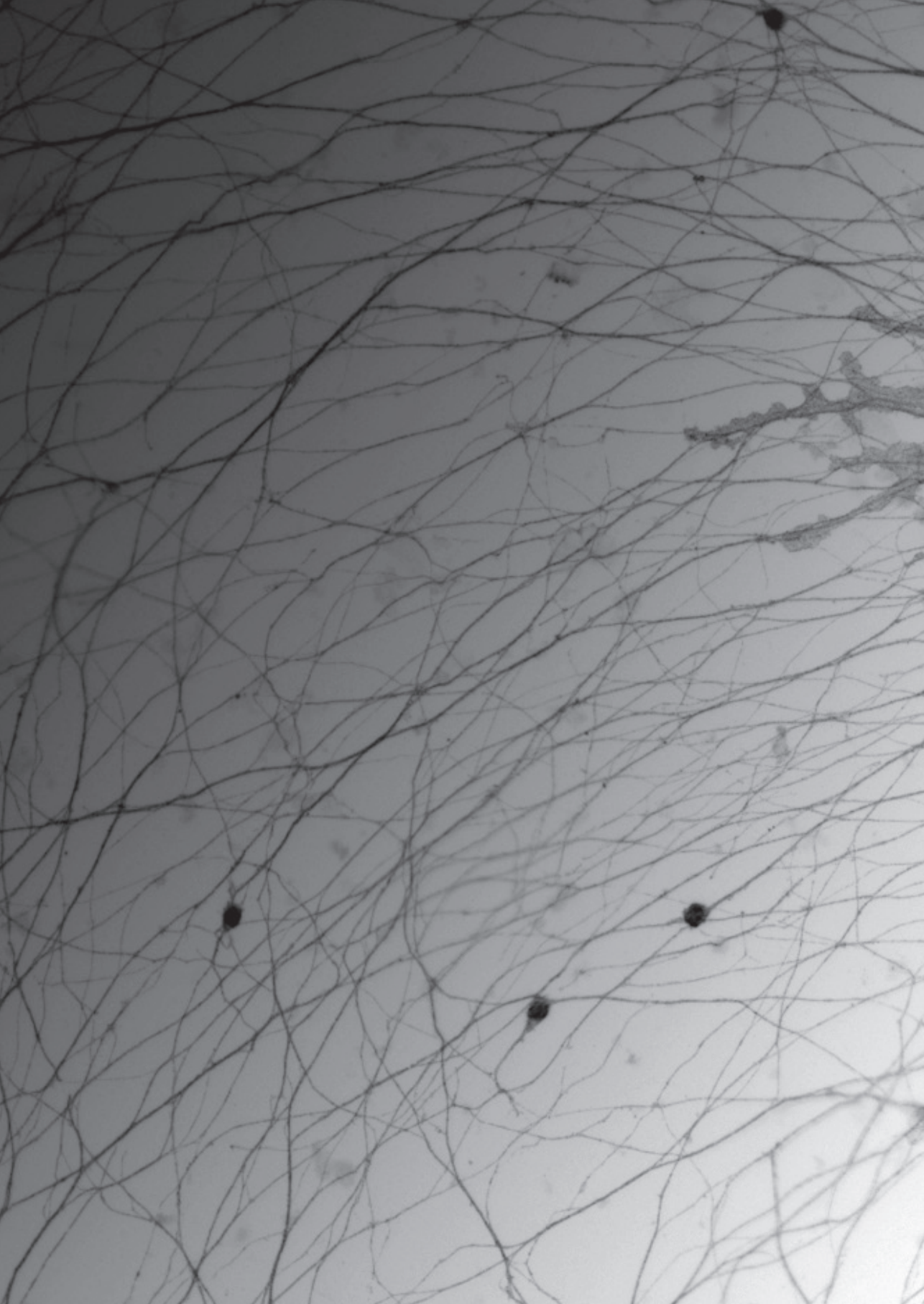
Nederlandse Samenvatting

Curriculum Vitae

List of Publications

Dankwoord

**p. 217**





A grayscale microscopic image of a neural network, showing a dense web of thin, branching processes (dendrites and axons) with several larger, darker cell bodies (soma) scattered throughout. A semi-transparent white rectangular box is overlaid on the top left portion of the image, containing the chapter title. A dotted line is positioned above the text within the box.

# Chapter 1

## General Introduction

---

## Preface

The construction of our most complex organ, the brain, takes place in an astonishingly rapid and efficient manner. The complexity of the brain is underlined by the sheer number of cell types and collective connections. During embryonic development simultaneous coordination of proliferation, differentiation and migration of numerous cell types requires a highly sophisticated strict regulatory system. In a process called axon guidance, neuronal protrusions sample the environment for membrane-bound or secreted attractive and repulsive cues in order to reach their innervation target. Whereas this happens naturally during development, in the adult brain these pathfinding capabilities are mostly lost. Upon injury to adult neurons, regeneration and regain of functionality is limited. This becomes clear in the detrimental effects of neuronal loss caused by neurodegenerative diseases but also for example as a result of injury, stroke or epilepsy. By studying the process of axon guidance in the embryo, our knowledge of axon guidance receptors and their ligands has increased exponentially in the past decades. It has become increasingly clear, however, that axon guidance does not end with merely the interaction of a ligand with a receptor. Sensitivity of a single receptor to a guidance cue may also depend on the correct balance of its interacting proteins and downstream signal transducers. This is one of the areas where our current knowledge remains poor but also where promising possibilities for therapeutic intervention lay.

This thesis contributes to our understanding of both neuronal development and disease, approached from three different levels: 1) at the protein level a molecular pathway controlling axon guidance is studied by unraveling the functioning of the axon guidance receptor Neogenin; 2) at the cellular level the process of neuronal migration involved in brain development is investigated using cerebellar granule neurons as a model system and; 3) at the tissue level a disease state responsible for neuronal rewiring and loss is characterized by identifying deregulated molecular pathways in epilepsy. These three approaches form the foundation of the results described in this thesis and will be introduced in the following sections.

# 1. Molecular pathway: RGM-Neogenin signaling

## 1.1 Axonal pathfinding

The adult central nervous system (CNS) contains millions of neurons each transmitting signals through a multitude of connections. To build this elaborate network, newly born neurons need to be able to find the correct regions within the brain and form their connections. They do this by extending an axon tipped with a highly motile growth cone that can sense guidance cues present in the surroundings. Upon encountering a repulsive cue, the growth cone will steer away, while the presence of an attractive cue will promote growth in that direction (fig 1A). These guidance cues can be membrane-bound, limiting their action to neighboring neurons; or secreted, which increases their range of receptivity. There are several classes of axon guidance molecules each binding to specific receptors (Chilton 2006; Kolodkin & Pasterkamp 2013). Binding of a guidance molecule to a receptor elicits an intracellular signaling cascade that ultimately results in cytoskeletal rearrangement and redirection of the axon (Huber et al. 2003). Growth cone sensitivity to a specific guidance cue depends not simply on the presence of the respective guidance receptor in the membrane. Rather, the functional outcome of ligand-receptor binding is dynamically regulated by extracellular and intracellular interactions with other proteins affecting for example membrane localization and downstream signaling pathways (Pasterkamp & Kolodkin 2013). Some classes of guidance molecules have been studied extensively, with great detail concerning their temporal and spatial regulation of sensitivity and their molecular pathways. For others, far less is known about how their signal is conveyed over the membrane and how cell type-specific sensitivity is accomplished. An example of the latter is the family of repulsive guidance molecules (RGMs), which has been shown to be important in neuronal development but is also implicated in neuronal regeneration and disease.

## 1.2 Repulsive guidance molecules (RGM)

In 1990, the presence of a protein that repelled axonal growth cones was discovered in the developing chick tectum (Stahl et al. 1990). This 33kDa protein was found to inhibit axon outgrowth and cause growth cone collapse which led to its name repulsive guidance molecule (RGM) (Müller et al. 1996). It was not until twelve years after its initial discovery that the molecular identity of RGM was first revealed in chicken (Monnier et al. 2002). RGM molecules have an Arg-Gly-Asp (RGD) motif, a partial von Willebrand (vWF) factor type D domain, two hydrophobic domains (one of which is a signal peptide), and a C-terminal glycosylphosphatidylinositol (GPI)-anchor tethering it to the plasma membrane

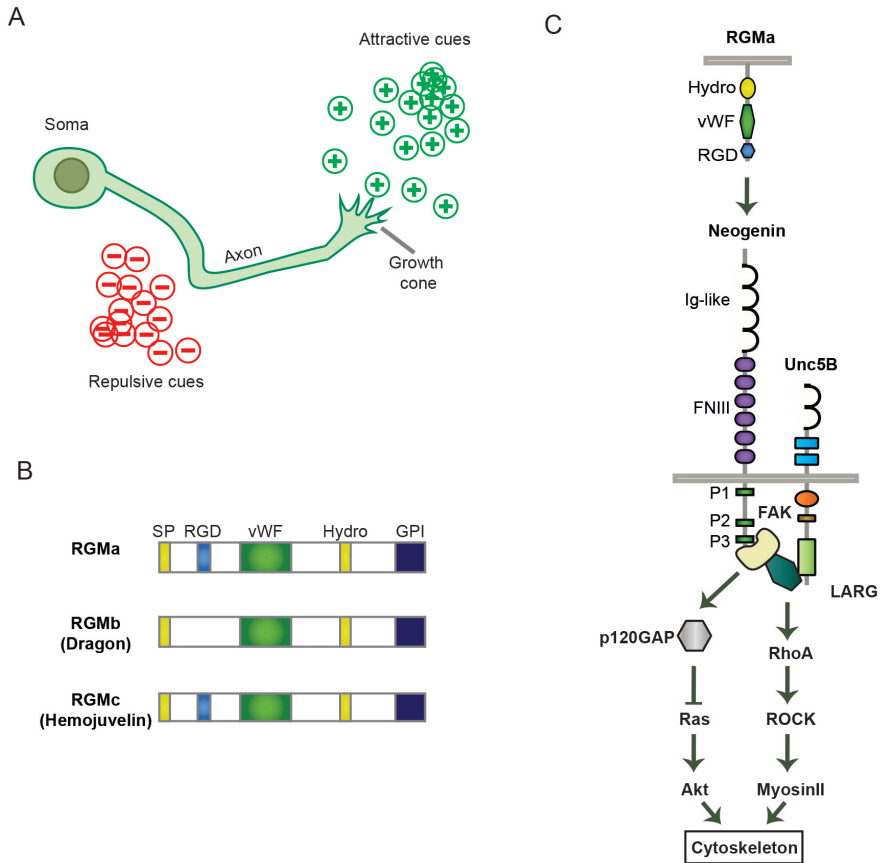


**Figure 1. Axonal repulsion mediated by RGM-Neogenin signaling**

**A.** Schematic of axon guidance. Developing neurons extend axons tipped with a growth cone sensing the environment. Repulsive cues (red) prompt the growth cone to steer away; attractive cues (green) promote growth in their direction. **B.** There are three mammalian RGM proteins; RGMa, RGMb (Dragon) and RGMc (Hemojuvelin). Their structure contains a signal peptide (SP), an RGD domain (conserved in RGMa and RGMc), a partial von Willebrand factor type D domain (vWf), a hydrophobic domain (hydro) and a GPI-link (GPI). **C.** RGMa binding to Neogenin initiates signaling resulting in growth cone collapse and neurite outgrowth inhibition. Focal adhesion kinase (FAK) associated with Neogenin P3 domain is phosphorylated and released upon RGMa binding. This releases interaction of FAK with p120GAP. The Ras-specific GTPase activating protein p120GAP subsequently inhibits Ras-mediated activation of Akt. Neogenin-associated FAK furthermore activates its interactor leukemia-associated Rho guanine nucleotide exchange factor (LARG) which is bound to the co-receptor Unc5B. LARG activation results in increased RhoA, Rho kinase (ROCK) and MyosinIII activity, leading to actin depolymerization.



(fig 1B). Later it was discovered that in mammals three RGM homologs exist; RGMa, b and c (Schmidtmer & Engelkamp 2004). RGMc (Hemojuvelin) is an essential regulator of systemic iron metabolism and is expressed in skeletal muscles, heart and liver (Oldekamp et al. 2004; Niederkofler et al. 2005; Zhang et al. 2009; Zhang et al. 2005). In contrast to RGMc, RGMa and RGMb (Dragon) are both primarily expressed in the developing and adult CNS, although their complementary expression patterns show little overlap within this system (Oldekamp et al. 2004; Schmidtmer & Engelkamp 2004). The biological function of RGMb is suggested to be closely related to that of RGMa, but remains largely uncharacterized (Liu et al. 2009). Of all three mammalian homologs, RGMa shares the highest sequence homology with chicken RGM. RGMa signaling is involved in a range of neuronal processes including differentiation, migration, adhesion, axon guidance and regeneration depending on cell type but also on spatial and temporal context (Key & Lah 2012). Little is known about how this wide variety of functions can be selectively regulated for specific cell types. This is especially intriguing since only one receptor capable of binding RGM has been identified; Neogenin.

### 1.3 Axon guidance receptor Neogenin

In a screen aimed at finding RGM binding partners, Neogenin was discovered to be the receptor responsible for mediating the axon repulsive effects of RGM (Rajagopalan et al. 2004). Neogenin is a close homolog of the axon guidance receptor deleted in colorectal cancer (DCC) and was first identified in the embryonic chick brain (Vielmetter et al. 1994). Similar to DCC, Neogenin is a transmembrane receptor consisting of six fibronectin type III (FNIII) and four immunoglobulin-like (Ig-like) extracellular domains, and three conserved intracellular domains (fig 1C). The FNIII domains are required for ligand binding (Tassew et al. 2012). However, detailed information regarding the molecular structure of this ligand-receptor interaction and the mode of signal transduction across the membrane is currently lacking. Neogenin expression is prominent throughout the CNS (Gad et al. 1997). Neuronal precursors and neural stem cell populations in the embryonic and adult brain, but also more mature neuronal populations express Neogenin (Gad et al. 1997; Keeling et al. 1997; Fitzgerald et al. 2007; van den Heuvel et al. 2013).

In the brain, RGM-mediated Neogenin signaling during development has been shown to be important in axon guidance, neuronal migration and differentiation. RGM-mediated axonal repulsion is involved in the development of several structures of the brain, including the retinotectal system, the supraoptic tract and the entorhinal-hippocampal system (Monnier et al. 2002; Rajagopalan et al. 2004; Brinks et al. 2004; Wilson & Key 2006). Both Neogenin and RGMa remain expressed during adulthood, suggesting they serve a specific, yet unknown,

---

role in adult neurons. Interestingly, increased RGMA expression has been found after neuronal injury, and this is thought to be an inhibiting factor for axonal regeneration of the adult CNS (Doya et al. 2006; Hata et al. 2006; Schnichels et al. 2011; Schwab et al. 2005). Therefore, understanding Neogenin-RGM ligand-receptor interactions and their downstream mechanism-of-action may benefit the search for therapeutic targets to increase neuronal regeneration after injury.

#### **1.4 Signal transduction pathways in repulsive RGM signaling**

Most of our knowledge about Neogenin signal transduction has come from studies focusing on RGMA. For efficient signal transduction the presence of Unc5B acting as a co-receptor is required (Hata et al. 2009). Unc5B directly interacts with both Neogenin and leukemia-associated Rho guanine-nucleotide exchange factor (LARG). When RGMA binds to Neogenin its intracellular binding partner focal adhesion kinase (FAK) phosphorylates and activates LARG (Hata et al. 2009; Ren et al. 2004). LARG directly activates the small GTPase RhoA which in turn activates its effector Rho kinase (ROCK). Activated ROCK phosphorylates MyosinII which mediates F-Actin depolymerization resulting in growth cone collapse and ultimately in neurite outgrowth inhibition (fig 1C).

Apart from inducing activation of RhoA, RGMA-mediated Neogenin signaling also results in inhibition of Ras, a GTPase that promotes axonal extension (Hall & Lalli 2010). RGMA binding causes dephosphorylation of Neogenin-associated FAK. This results in the release of Ras-specific GTPase-activating protein p120GAP that originally interacts with FAK. The binding of GTP-Ras to p120GAP released from FAK is increased, mediating the inactivation of Ras and its downstream effector Akt (Endo & Yamashita 2009) (fig 1C).

Neogenin sensitivity to RGMA can be altered by extracellular cleavage by the transmembrane protease ADAM17. Cleavage by ADAM17 has been shown to reduce responsiveness to RGMA, but the function underlying Neogenin ecto-domain shedding remains unclear (Okamura et al. 2011). The identification of a regulatory mechanism to acquire local sensitivity to RGMA may help explain the various cell type- and time point-dependent functions of its receptor Neogenin.

**Aims of this section:**

Receptivity to specific axon guidance cues depends on the correct balance between receptor and interacting proteins, and the presence and activation of downstream signal transducers. For the family of class 3 semaphorins the temporal and spatial regulation of responsiveness has been studied extensively. **Chapter 2** reviews some examples of molecular pathways controlling the axonal sensitivity to class 3 semaphorins. For the family of RGM proteins, data about molecular domains required for receptor binding and functioning are scarce. **Chapter 3** is aimed at increasing our basic understanding of RGM-mediated Neogenin signaling by solving the crystal structure of the RGM-Neogenin ligand-receptor complex. The aim of **Chapter 4** is to investigate how Neogenin sensitivity to RGMa is regulated at the neuronal cell membrane. The novel Neogenin interacting partner Lrig2, a transmembrane leucine-rich repeat protein, is identified as a regulator of axonal responsiveness to RGMa. Lrig2 is found to interact with Neogenin in a ligand-dependent manner to prevent proteolytic cleavage of Neogenin by the metalloprotease ADAM17.

## 2. Cellular process: cerebellar granule cell migration

### 2.1 Neuronal migration

Axon guidance refers to a process in which axons are guided to their synaptic targets that can be located in a different area of the brain several centimeters away (fig 1A). The first section of this thesis focuses on the molecular pathways regulating axon guidance receptor functioning. In this second section we move up a level to the cell and study the process of neuronal migration. This developmental process similarly involves guidance along attractive and repulsive cues but results in the movement of the entire cell. Proper neuronal migration is essential for correct development and ultimately formation of functional neural networks. In most cortical regions, neuronal migration takes place along the processes of glial cells. The migration of cerebellar granule neurons (CGNs) has long been used as a model system to study glia-guided neuronal migration for several reasons. First, migration of CGNs is very similar to that of neurons in other parts of the brain (Gasser & Hatten 1990; Nadarajah et al. 2001). Second, CGNs are the most abundant neuronal type in the brain, making it relatively easy to purify, culture, and study them. Third, the comparatively low number of different cell types in the cerebellum and the predictable mode and tempo of CGN migration provide a reliable model system. Fourth, in the cerebellum glial cells are derived from a different precursor cell than the CGNs, while in for example the cortex these cell types share common precursors. This makes it possible to dissect glia-

---

dependent phenotypes from neuron-dependent phenotypes in (conditional) functional genetics studies.

## 2.2 Cerebellar development

The three most prominent cell types of the cerebellum are Purkinje cells, Bergmann glia and glutamatergic interneurons or CGNs. Purkinje cells arise from progenitors in the ventricular zone from embryonic day (E)11 to E13 (Yuasa et al. 1991). In the postnatal cerebellum, their cell bodies are aligned in the Purkinje cell layer (PCL), with large dendritic trees that make up most of the molecular layer (ML) (fig 2A). Their axons project through the internal granule layer (IGL) into the white matter (WM) and ultimately form inhibitory synaptic contact with neurons in deep cerebellar nuclei and the brainstem (Altman & Bayer 1997). In the ML, Purkinje cell dendrites receive excitatory input from climbing fibers derived from the inferior olivary nucleus, and from parallel fibers derived from CGNs. CGNs originate in the embryonic rhombic lip from CGN precursor cells. Precursor cells migrate tangentially to the embryonic cerebellum to form the external granule layer (EGL). The outer EGL (oEGL) is a highly proliferative zone where precursor CGNs generate postmitotic CGNs between postnatal day (P)0 and P15 (Komuro et al. 2013). Postmitotic CGNs extend two processes and migrate tangentially in the inner EGL (iEGL) along the cerebellar surface in the direction of the thickest process which is called the leading process (fig 2A). At the border with the molecular layer (ML), CGNs slow down and almost come to a halt (Komuro et al. 2001). A new process directed at the ML emerges from the cell and the soma reorients to follow the newly formed leading process and radial migration into the ML commences (fig 2A). This part of CGN migration is glia-guided and has been studied most extensively. Bergmann glial cell bodies are intermixed with Purkinje cell bodies in the PCL and extend processes into the ML (fig 2A). The leading process of CGNs adheres to the glial process using it as a scaffold. The CGN cell body leaves behind a thinner trailing process that later becomes the parallel fiber (fig 2A). When CGN cell bodies reach the PCL, migration halts and the soma becomes rounded. The leading process remains present while highly motile lamellipodia emerging from its tip sample the environment. After a pause the CGN soma elongates again and radial migration is resumed into the IGL until it reaches the WM border (Komuro & Rakic 1998). Here, the CGN fully differentiates into a mature CGN (Mellor et al. 1998) (fig 2A). The entire migratory process takes on average 2 days and appears to be partly intrinsically regulated, since CGNs migrate in a strikingly similar way *in vitro* (Yacubova & Komuro 2002). However, extracellular cues such as secreted and membrane bound guidance molecules are essential *in vivo* to ensure proper migration by regulating and altering migration direction and speed. Over the past few years, several guidance cues involved



in the regulation of neuronal migration have been identified, including growth factors, adhesion molecules, and semaphorins (Renaud et al. 2008; Maier et al. 2010; Wilson et al. 2010). Yet, our knowledge about how these extracellular cues regulate neuronal migration is limited and several thus far unidentified intrinsic and extrinsic molecular mechanisms are expected to be involved.

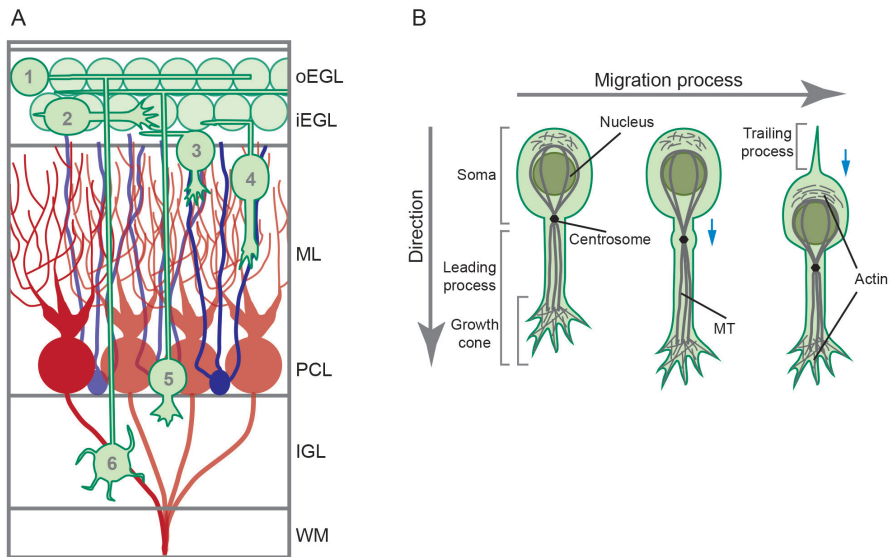


**Figure 2. Cerebellar granule neuron development and migration**

**A.** Three major cell types in the cerebellum are Purkinje cells (PC, red), Bergmann glia (BG, blue) and cerebellar granule neurons (CGNs, green). PC cell bodies are located in the Purkinje cell layer (PCL) intermixed with BG. The dendritic trees of PCs and BG processes reach into the molecular layer (ML). CGN proliferation occurs (1) in the outer external granule layer (oEGL) after which postmitotic CGNs extend a process and migrate tangentially (2) along the surface of the cerebellum in the inner (i)EGL. When CGNs reach the border of the ML, their soma rounds and another process emerges pointing towards the ML (3). The new leading process uses the BG fiber as a scaffold and radial migration commences (4). At the border with the internal granule layer (IGL) there is a pause where the CGNs detach from the BG and sample the environment with a short lamellipodia-like growth cone (5). Radial migration continues until CGNs reach the white matter (WM) border where they fully differentiate. **B.** When migration starts, the centrosome first moves ahead of the nucleus into the leading process while the leading process continues to grow forward. Next, the nucleus moves forward to catch up, by simultaneous pulling of the microtubules (MT) surrounding it and pushing of actin filaments in the rear, leaving behind a trailing process.

---

### 2.3 Neuronal migration: a look inside the cell

Migrating neurons extend a leading process which consists of a neurite-like structure tipped with a growth cone sampling the environment (fig 2B). Migration of the cell body is preceded by movement of the centrosome into the leading process (fig 2B). Next, the nucleus is moved forward, leaving behind a trailing process (fig 2B). The regulation of these steps of neuronal migration requires a tight coordination of several cellular processes, of which cytoskeletal rearrangement and intracellular transport are amongst the key elements (Sakakibara et al. 2013). Cytoskeletal rearrangement is one of the major propagators of neuronal migration. The cytoskeleton is not a static but a highly dynamic structure that gives shape to the cell. It consists of actin and microtubules (MTs). During migration, the nucleus is pulled into the leading process by MTs that surround the nucleus and converge in the centrosome (Tsai et al. 2007; Solecki et al. 2009) (fig 2B). Actin foci behind the nucleus are involved in pushing it in the direction of the centrosome (Bellion et al. 2005; Schaar & McConnell 2005) (fig 2B).

At the growth cone, a constant turnover of actin filament building and breakdown takes place as various environmental cues are encountered. These extracellular signals are conveyed across the membrane into the cell and reach the cytoskeleton to ultimately affect the cell's movement and direction. For guidance cues such as RGMs, the signaling cascade leading from ligand-receptor binding to migration represents a black box in our current knowledge.

Intracellular transport is another key element essential for migration. Extension and growth at the tip of the neuron requires the presence of basic cellular building blocks such as lipids, proteins and mitochondria. But also the temporal and spatial distribution of guidance receptors is regulated by intracellular transport. Moreover, signaling molecules are conveyed between growth cone and cell body to coordinate movement (Yap & Winckler 2012). The cytoskeleton is an important means of transport to reach the growth cone. Regulation of intracellular transport includes a range of specific motor- and cargo-proteins (Franker & Hoogenraad 2013). Motor- and cargo-proteins have highly specialized functions and the coordination of this elaborate network of transport remains largely unexplained.

**Aims of this section:**

RGMa-induced Neogenin signaling results in growth cone collapse *in vitro*. Little is known about the role of Neogenin in neuronal migration or its downstream signal transduction cascade resulting in cellular movement. **Chapter 5** is aimed at exploring the potential role of RGMa-induced Neogenin signaling in the regulation of radial CGN migration. We identify the cytoplasmic protein dedicator of cytokinesis 7 (Dock7) as a novel Neogenin interactor required for RGMa-induced neurite outgrowth inhibition. Moreover, we show that knockdown of Neogenin or Dock7 in CGNs intrinsically affects radial migration. Both intrinsic and extrinsic properties contribute to the regulation of CGN migration. The aim of **Chapter 6** is to investigate the intrinsic role of cargo-dynein transport protein BicD2 in neuronal development. BicD2 is found to be essential for radial CGN migration in the developing cerebellum. Interestingly, we discover that it is not BicD2 expression in the CGNs but in radial glial cells that is required.

### 3 Disease: microRNAs in temporal lobe epilepsy

Proteins work together as pathways to regulate cellular processes that ultimately shape the tissues of an organism. A single dysfunctional protein may disrupt an entire tissue leading to a diseased state. The first section of this thesis took a detailed look at axon guidance receptor structure and function at the protein level. In the second section the orchestrated movement of cells required to form a tissue was investigated. This migration is shown to require the correct functioning of not just neurons but also glial cells. The balance between these various cell types is essential to create a fully functional tissue, while imbalance may lead to disease. This third section examines such a disease at the tissue level.

#### 3.1 Temporal lobe epilepsy

Epilepsy is characterized by recurrent seizures that originate in the brain. Although there are cases of genetic sensitivity or inheritance of epilepsy, the most common cause of seizures is trauma to the brain. The initial insult can lead to a higher state of susceptibility to seizures which then sets into motion a cascade of events resulting in epilepsy. This process is called epileptogenesis and can extend over a period of months to years. The delay in onset of epilepsy makes it difficult to study epileptogenesis in humans. At the same time, however, it provides a period for intervention and disease prevention after initial injury. There are several processes simultaneously involved in creating the epileptogenic brain, including neuronal cell death, gliosis and inflammation (Rakhade & Jensen

---

2009). Since studies on epileptogenesis are limited to currently available animal models, little is known about the underlying mechanism(s) in humans. However, progress is being made in dissecting cause from consequence by pharmaceutical intervention in specific molecular or cellular pathways using a combination of experimental approaches and patient material (Pitkänen & Lukasiuk 2011).

### **3.2 Cellular mechanisms underlying epilepsy**

One of the best characterized aspects of the epileptogenic process is neuronal cell death. Loss of neuronal cell bodies is found in human surgically removed hippocampal tissue and in animal models after induction of status epilepticus (SE). However, it is unclear whether neuronal loss is a cause or the consequence of epileptogenesis, and intervention studies have had varying degrees of success (Brandt et al. 2003; Brandt et al. 2006). For instance, neuronal cell death is not a prerequisite for the development of spontaneous seizures and neuroprotection is not sufficient to inhibit epilepsy (Dubé et al. 2006; Brandt et al. 2003). Another major morphological change that takes place during epileptogenesis is gliosis. Paradoxically, the presence of glial cells can promote neuroprotection after injury but can also contribute to the process of epileptogenesis (Elkabes et al. 1996; Wetherington et al. 2008). The best-studied glial cells in relation to epilepsy are astrocytes and microglia. Microglial cells are considered to be the macrophages of the brain. Upon activation they proliferate and migrate towards the injury site. Activated microglia secrete pro-inflammatory molecules such as tumour necrosis factor alpha (TNF-alpha) that can be harmful to neurons, but they also produce neuroprotective factors such as brain derived neurotrophic factor (BDNF) (Kreutzberg 1996; Pitkänen & Lukasiuk 2009). Under normal circumstances astrocytes are important for the maintenance of the extracellular environment and they provide trophic support for neurons. However, injury can induce a process called reactive astrogliosis, a hallmark of epileptogenesis (Sofroniew & Vinters 2010). Reactive astrocytes produce factors that promote inflammation after initial injury and during epilepsy. As a consequence of microglial activation and astrogliosis, a strong immune response is triggered in the epileptogenic brain that may contribute to seizure susceptibility (Aronica et al. 2012). One of the effects of the production of pro-inflammatory cytokines by reactive astrocytes is the opening of the blood-brain barrier (BBB). This allows the infiltration of leukocytes and other potentially damaging factors. Another consequence of BBB breakdown is the accumulation of albumin in the brain. Albumin inhibits the neuroprotective properties of astrocytes and thus indirectly contributes to neuronal hyperexcitability (Friedman et al. 2009; van Vliet et al. 2014). Finally, albumin in the brain as a consequence of BBB leakage can bind and interfere with several anti-epileptic drugs contributing to the development



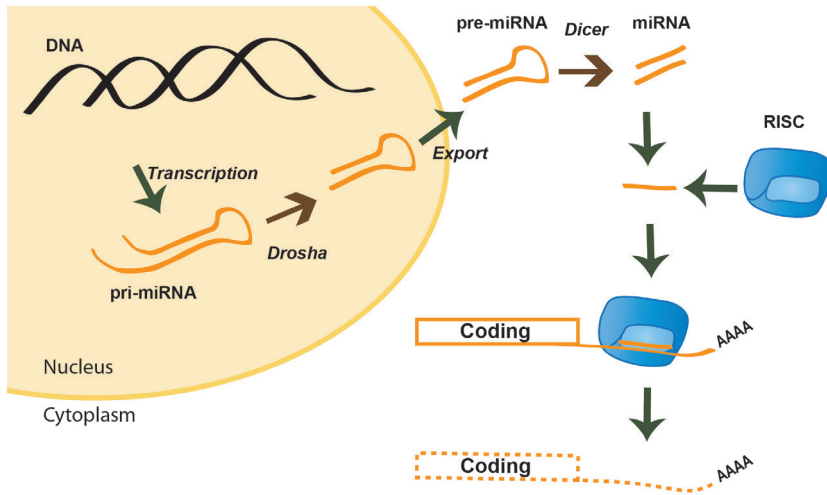


**Figure 3. MicroRNA biogenesis**

Pri-miRNAs are transcribed from genomic DNA and are cleaved by Drosha to create a hairpin pre-miRNA. Pre-miRNAs are exported out of the nucleus, where the hairpin loop is removed by Dicer. Mature miRNAs are loaded into the RNA induced silencing complex (RISC) and in the loaded RISC miRNAs interact with the untranslated region of target mRNAs. This interaction induces mRNA degradation or silencing of translation, thereby inhibiting protein expression.

of seizure pharmaco-resistance (Salar et al. 2014; van Vliet et al. 2014).

Thus, the accumulation of a combination of cellular processes and morphological changes contributes to the progression of epileptogenesis.

### 3.3 Gene expression changes during epileptogenesis

In order to identify candidate target pathways for potential intervention therapies, it is important to study the molecular changes that underlie epileptogenesis. Several studies have aimed at analyzing gene expression changes in both animal models and human brain tissue during epileptogenesis or epilepsy (Pitkänen & Lukasiuk 2011). Although numerous changes in gene expression have been identified, the translation of a single genetic target to a clinical application has not been made (Pitkänen & Lukasiuk 2011). Interestingly, however, gene expression profiling studies have revealed changes to groups of genes that are part of specific molecular pathways. For example, immune response genes are differentially expressed early during epileptogenesis, suggesting that these genes may share a common regulatory mechanism (Okamoto et al. 2010; Elliott et al. 2003; Gorter et al. 2006; Pitkänen & Lukasiuk 2009). Important regulators of gene expression control are microRNAs (miRNAs). MiRNAs have been discovered relatively recently, but they represent a highly relevant class of non-coding RNAs

---

involved in a large number of cellular processes in development and disease. Their post-transcriptional regulatory mechanism provides robustness and accuracy to protein translation of groups of genes in specific temporal and spatial cellular contexts (Ebert & Sharp 2012). The number of endogenous miRNAs in the genome increases with the evolutionary complexity of the organism (~400 in worm, over 2500 in humans) which indicates the importance of this sophisticated way of protein expression regulation (Kozomara & Griffiths-Jones 2014).

### **3.4 microRNA biogenesis**

MiRNAs are transcribed from intergenic or intronic regions in the genome, producing a pri-miRNA transcript (fig 3A). This transcript is cleaved in the nucleus by the enzyme Drosha to create a short hairpin pre-miRNA transcript that is subsequently exported into the cytoplasm (fig 3A). Next, the loop structure of the pre-miRNA is cleaved by the enzyme Dicer and the resulting mature miRNA is loaded into the RNA induced silencing complex (RISC) (fig 3A). Mature miRNAs are approximately 20 nucleotides (nt) long and can bind specific mRNA target sequences, thereby inducing mRNA degradation or inhibition of translation (fig 3A). MiRNA target sites in mRNAs are typically located in the 3' untranslated region (UTR). An important characteristic of miRNA target selection is the regulation of target site specificity. MiRNAs require a short ~8 nt sequence of homology, called the seed region. The seed region is located at the 5' end of the miRNA and conveys target specificity while mismatches in the remaining miRNA:mRNA sequence interaction are common if not essential for normal functioning. This imperfect basepairing combined with strong homology for a short sequence means that one miRNA can target a large number of mRNAs. Vice versa, one mRNA can be targeted by several unique miRNAs. Therefore, post-transcriptional regulation by miRNAs provides the cell with an extra level of control and greatly increases its adaptive possibilities. By using miRNAs as master-switches the cell can simultaneously control the translation of groups of genes. This is especially useful within the cellular and transcriptional complexity of the nervous system. MiRNAs are highly abundant in the brain and have an essential role in neuronal development and functioning (Kosik 2006; McNeill & Van Vactor 2012). Moreover, several animal studies have implicated miRNAs in the regulation of cellular processes associated with epileptogenesis, such as inflammation (Aronica et al. 2010; Liu et al. 2010). There is, however, limited information about the role of miRNA regulation in human epilepsy. An increased understanding about miRNA functioning in epilepsy may provide promising therapeutic targets. There are several possibilities for manipulating the expression and function of miRNAs *in vivo*, and successful clinical trials in human patients have been performed recently (Bhalala et al. 2013; Janssen et al. 2013).

**Aims of this section:**

The aim of **Chapter 7** is to increase our understanding of human miRNAs that may be affected in epilepsy. To achieve this, we perform genome-wide miRNA expression profiling on human brain tissue of epilepsy patients. Differences in both expression level and cellular localization of specific miRNAs are found to correlate with disease pathology. Finally, individual miRNAs are found to target modulators of the immune response, suggesting the involvement of miRNA deregulation in epileptogenic inflammation.

---

## References

- Altman, J. & Bayer, S.A., 1997. Development of the cerebellar system: in relation to its evolution, structure, and functions, CRC Press.
- Aronica, E. et al., 2012. Astrocyte immune responses in epilepsy. *GLIA*, 60, pp.1258–1268.
- Aronica, E. et al., 2010. Expression pattern of miR-146a, an inflammation-associated microRNA, in experimental and human temporal lobe epilepsy. *The European journal of neuroscience*, 31, pp.1100–1107.
- Bellion, A. et al., 2005. Nucleokinesis in tangentially migrating neurons comprises two alternating phases: forward migration of the Golgi/centrosome associated with centrosome splitting and myosin contraction at the rear. *The Journal of neuroscience : the official journal of the Society for Neuroscience*, 25, pp.5691–5699.
- Bhalala, O.G., Srikanth, M. & Kessler, J. a, 2013. The emerging roles of microRNAs in CNS injuries. *Nature reviews. Neurology*, 9, pp.328–39.
- Brandt, C. et al., 2003. N-methyl-D-aspartate receptor blockade after status epilepticus protects against limbic brain damage but not against epilepsy in the kainate model of temporal lobe epilepsy. *Neuroscience*, 118, pp.727–740.
- Brandt, C. et al., 2006. Treatment with valproate after status epilepticus: Effect on neuronal damage, epileptogenesis, and behavioral alterations in rats. *Neuropharmacology*, 51, pp.789–804.
- Brinks, H. et al., 2004. The repulsive guidance molecule RGMA is involved in the formation of afferent connections in the dentate gyrus. *The Journal of neuroscience : the official journal of the Society for Neuroscience*, 24, pp.3862–3869.
- Chilton, J.K., 2006. Molecular mechanisms of axon guidance. *Developmental Biology*, 292, pp.13–24.
- Doya, H. et al., 2006. Induction of repulsive guidance molecule in neurons following sciatic nerve injury. *Journal of Chemical Neuroanatomy*, 32, pp.74–77.
- Dubé, C. et al., 2006. Temporal lobe epilepsy after experimental prolonged febrile seizures: Prospective analysis. *Brain*, 129, pp.911–922.
- Ebert, M.S. & Sharp, P.A., 2012. Roles for MicroRNAs in conferring robustness to biological processes. *Cell*, 149, pp.505–524.
- Elkabes, S., DiCicco-Bloom, E.M. & Black, I.B., 1996. Brain microglia/macrophages express neurotrophins that selectively regulate microglial proliferation and function. *The Journal of neuroscience : the official journal of the Society for Neuroscience*, 16, pp.2508–2521.
- Elliott, R.C., Miles, M.F. & Lowenstein, D.H., 2003. Overlapping microarray profiles of dentate gyrus gene expression during development- and epilepsy-associated neurogenesis and axon outgrowth. *The Journal of neuroscience : the official journal of the Society for Neuroscience*, 23, pp. 2218–2227.

- Endo, M. & Yamashita, T., 2009. Inactivation of Ras by p120GAP via focal adhesion kinase dephosphorylation mediates RGMa-induced growth cone collapse. *The Journal of neuroscience: the official journal of the Society for Neuroscience*, 29, pp.6649–6662.
- Fitzgerald, D.P., Bradford, D. & Cooper, H.M., 2007. Neogenin is expressed on neurogenic and gliogenic progenitors in the embryonic and adult central nervous system. *Gene Expression Patterns*, 7, pp.784–792.
- Franker, M. a M. & Hoogenraad, C.C., 2013. Microtubule-based transport - basic mechanisms, traffic rules and role in neurological pathogenesis. *Journal of cell science*, 126, pp.2319–29.
- Friedman, A., Kaufer, D. & Heinemann, U., 2009. Blood-brain barrier breakdown-inducing astrocytic transformation: Novel targets for the prevention of epilepsy. *Epilepsy Research*, 85, pp.142–149.
- Gad, J.M. et al., 1997. The expression patterns of guidance receptors, DCC and Neogenin, are spatially and temporally distinct throughout mouse embryogenesis. *Developmental biology*, 192, pp.258–273.
- Gasser, U.E. & Hatten, M.E., 1990. Central nervous system neurons migrate on astroglial fibers from heterotypic brain regions in vitro. *Proceedings of the National Academy of Sciences of the United States of America*, 87, pp.4543–4547.
- Gorter, J.A. et al., 2006. Potential new antiepileptogenic targets indicated by microarray analysis in a rat model for temporal lobe epilepsy. *The Journal of neuroscience: the official journal of the Society for Neuroscience*, 26, pp.11083–11110.
- Hall, A. & Lalli, G., 2010. Rho and Ras GTPases in axon growth, guidance, and branching. *Cold Spring Harbor perspectives in biology*, 2.
- Hata, K. et al., 2006. RGMa inhibition promotes axonal growth and recovery after spinal cord injury. *The Journal of cell biology*, 173, pp.47–58.
- Hata, K. et al., 2009. Unc5B associates with LARG to mediate the action of repulsive guidance molecule. *The Journal of cell biology*, 184, pp.737–750.
- Van den Heuvel, D.M.A., Hellemons, A.J.C.G.M. & Pasterkamp, R.J., 2013. Spatiotemporal Expression of Repulsive Guidance Molecules (RGMs) and Their Receptor Neogenin in the Mouse Brain. *PLoS ONE*, 8.
- Huber, A.B. et al., 2003. Signaling at the growth cone: ligand-receptor complexes and the control of axon growth and guidance. *Annual review of neuroscience*, 26, pp.509–563.
- Janssen, H.L. a et al., 2013. Treatment of HCV infection by targeting microRNA. *The New England journal of medicine*, 368, pp.1685–94.
- Keeling, S.L., Gad, J.M. & Cooper, H.M., 1997. Mouse Neogenin, a DCC-like molecule, has four splice variants and is expressed widely in the adult mouse and during embryogenesis. *Oncogene*, 15, pp.691–700.
- Key, B. & Lah, G.J., 2012. Repulsive guidance molecule A (RGMa): A molecule for all seasons. *Cell Adhesion and Migration*, 6, pp.85–90.
- Kolodkin, A.L. & Pasterkamp, R.J., 2013. SnapShot: Axon guidance II. *Cell*, 153(3), p.722.
- Komuro, H. & Rakic, P., 1998. Distinct modes of neuronal migration in different domains of developing cerebellar cortex. *The Journal of neuroscience: the official journal of the Society for Neuroscience*, 18, pp.1478–1490.

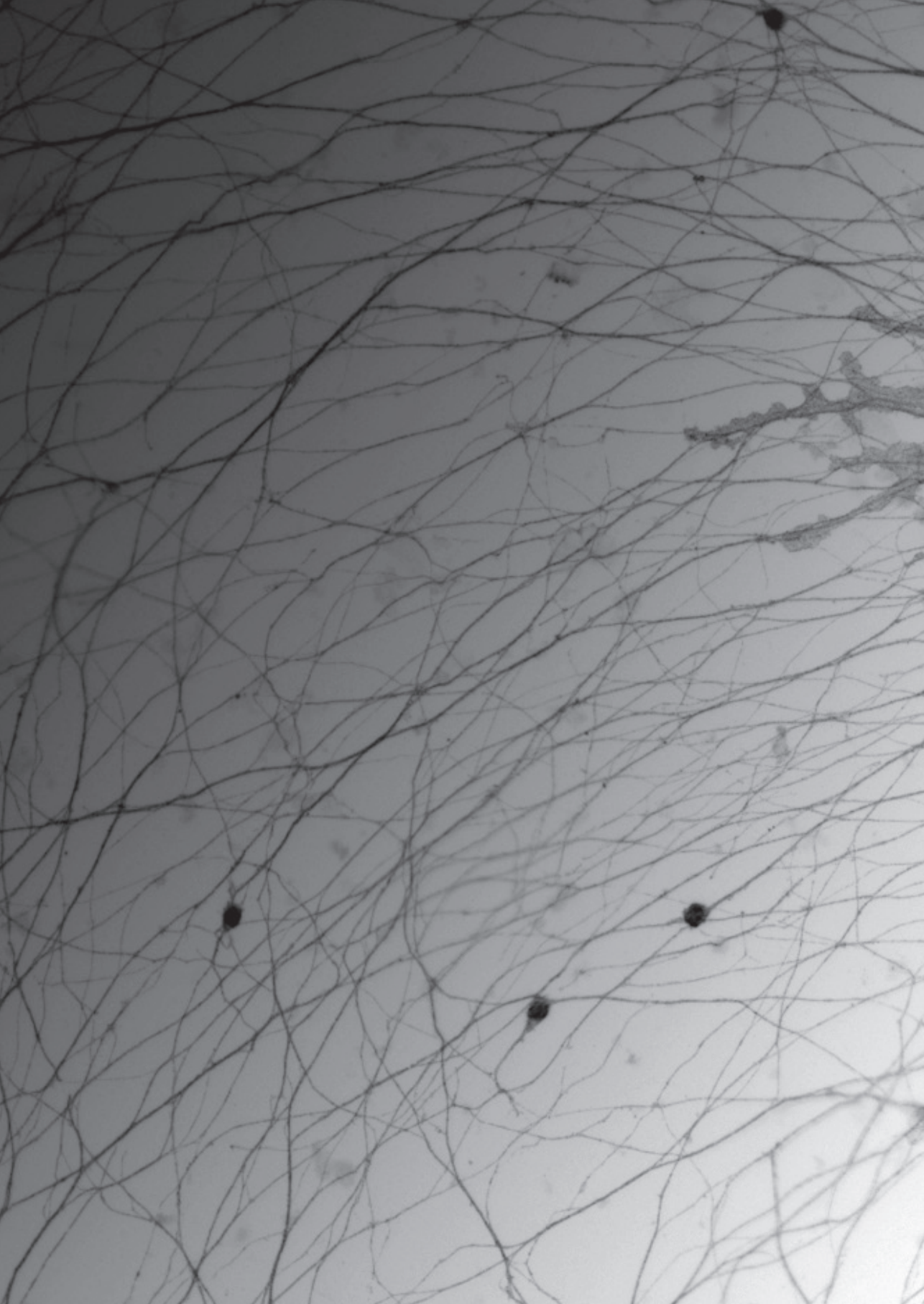
- 
- Komuro, H., Yacubova, E. & Rakic, P., 2001. Mode and tempo of tangential cell migration in the cerebellar external granular layer. *The Journal of neuroscience : the official journal of the Society for Neuroscience*, 21, pp.527–540.
  - Komuro, Y. et al., 2013. Granule Cell Migration and Differentiation. In *Handbook of the Cerebellum and Cerebellar Disorders*. Springer Netherlands, pp. 107–125.
  - Kosik, K.S., 2006. The neuronal microRNA system. *Nature reviews. Neuroscience*, 7, pp.911–920.
  - Kozomara, A. & Griffiths-Jones, S., 2014. MiRBase: Annotating high confidence microRNAs using deep sequencing data. *Nucleic Acids Research*, 42.
  - Kreutzberg, G.W., 1996. Microglia: A sensor for pathological events in the CNS. *Trends in Neurosciences*, 19, pp.312–318.
  - Liu, D.-Z. et al., 2010. Brain and blood microRNA expression profiling of ischemic stroke, intracerebral hemorrhage, and kainate seizures. *Journal of cerebral blood flow and metabolism : official journal of the International Society of Cerebral Blood Flow and Metabolism*, 30, pp.92–101.
  - Liu, X. et al., 2009. Repulsive guidance molecule b inhibits neurite growth and is increased after spinal cord injury. *Biochemical and Biophysical Research Communications*, 382, pp.795–800.
  - Maier, E. et al., 2010. Opposing Fgf and Bmp activities regulate the specification of olfactory sensory and respiratory epithelial cell fates. *Development (Cambridge, England)*, 137, pp.1601–1611.
  - McNeill, E. & Van Vactor, D., 2012. MicroRNAs Shape the Neuronal Landscape. *Neuron*, 75, pp.363–379.
  - Mellor, J.R. et al., 1998. Mouse cerebellar granule cell differentiation: electrical activity regulates the GABAA receptor alpha 6 subunit gene. *J Neurosci*, 18, pp.2822–2833.
  - Monnier, P.P. et al., 2002. RGM is a repulsive guidance molecule for retinal axons. *Nature*, 419, pp.392–395.
  - Müller, B.K., Jay, D.G. & Bonhoeffer, F., 1996. Chromophore-assisted laser inactivation of a repulsive axonal guidance molecule. *Current biology : CB*, 6, pp.1497–1502.
  - Nadarajah, B. et al., 2001. Two modes of radial migration in early development of the cerebral cortex. *Nature neuroscience*, 4, pp.143–150.
  - Niederkofler, V., Salie, R. & Arber, S., 2005. Hemojuvelin is essential for dietary iron sensing, and its mutation leads to severe iron overload. *Journal of Clinical Investigation*, 115, pp.2180–2186.
  - Okamoto, O.K. et al., 2010. Whole transcriptome analysis of the hippocampus: toward a molecular portrait of epileptogenesis. *BMC genomics*, 11, p.230.
  - Okamura, Y., Kohmura, E. & Yamashita, T., 2011. TACE cleaves neogenin to desensitize cortical neurons to the repulsive guidance molecule. *Neuroscience Research*, 71(1), pp.63–70.
  - Oldekamp, J. et al., 2004. Expression pattern of the repulsive guidance molecules RGM A, B and C during mouse development. *Gene Expression Patterns*, 4, pp.283–288.
  - Pasterkamp, R.J. & Kolodkin, A.L., 2013. SnapShot: Axon guidance. *Cell*, 153(2), pp.494–494.
  - Pitkänen, A. & Lukasiuk, K., 2011. Mechanisms of epileptogenesis and potential treatment targets. *The Lancet Neurology*, 10, pp.173–186.



- Pitkänen, A. & Lukasiuk, K., 2009. Molecular and cellular basis of epileptogenesis in symptomatic epilepsy. *Epilepsy and Behavior*, 14, pp.16–25.
- Rajagopalan, S. et al., 2004. Neogenin mediates the action of repulsive guidance molecule. *Nature cell biology*, 6, pp.756–762.
- Rakhade, S.N. & Jensen, F.E., 2009. Epileptogenesis in the immature brain: emerging mechanisms. *Nature reviews. Neurology*, 5, pp.380–391.
- Ren, X.-R. et al., 2004. Focal adhesion kinase in netrin-1 signaling. *Nature neuroscience*, 7, pp.1204–1212.
- Renaud, J. et al., 2008. Plexin-A2 and its ligand, Sema6A, control nucleus-centrosome coupling in migrating granule cells. *Nature neuroscience*, 11, pp.440–449.
- Sakakibara, A. et al., 2013. Microtubule dynamics in neuronal morphogenesis. *Open biology*, 3, p.130061.
- Salar, S. et al., 2014. Blood-brain barrier dysfunction can contribute to pharmacoresistance of seizures. *Epilepsia*, 55, pp.1255–1263.
- Schaar, B.T. & McConnell, S.K., 2005. Cytoskeletal coordination during neuronal migration. *Proceedings of the National Academy of Sciences of the United States of America*, 102, pp.13652–13657.
- Schmidtmer, J. & Engelkamp, D., 2004. Isolation and expression pattern of three mouse homologues of chick Rgm. *Gene Expression Patterns*, 4, pp.105–110.
- Schnichels, S., Heiduschka, P. & Julien, S., 2011. Different spatial and temporal protein expressions of repulsive guidance molecule a and neogenin in the rat optic nerve after optic nerve crush with and without lens injury. *Journal of Neuroscience Research*, 89, pp.490–505.
- Schwab, J.M. et al., 2005. Central nervous system injury-induced repulsive guidance molecule expression in the adult human brain. *Archives of neurology*, 62, pp.1561–1568.
- Sofroniew, M. V. & Vinters, H. V., 2010. Astrocytes: Biology and pathology. *Acta Neuropathologica*, 119, pp.7–35.
- Solecki, D.J. et al., 2009. Myosin II motors and F-actin dynamics drive the coordinated movement of the centrosome and soma during CNS glial-guided neuronal migration. *Neuron*, 63, pp.63–80.
- Stahl, B. et al., 1990. Biochemical characterization of a putative axonal guidance molecule of the chick visual system. *Neuron*, 5, pp.735–743.
- Tassew, N.G. et al., 2012. SKI-1 and Furin Generate Multiple RGMa Fragments that Regulate Axonal Growth. *Developmental Cell*, 22, pp.391–402.
- Tsai, J.-W., Bremner, K.H. & Vallee, R.B., 2007. Dual subcellular roles for LIS1 and dynein in radial neuronal migration in live brain tissue. *Nature neuroscience*, 10, pp.970–979.
- Vielmetter, J. et al., 1994. Neogenin, an avian cell surface protein expressed during terminal neuronal differentiation, is closely related to the human tumor suppressor molecule deleted in colorectal cancer. *The Journal of cell biology*, 127, pp.2009–2020.

- 
- Van Vliet, E.A., Aronica, E. & Gorter, J.A., 2014. Blood–brain barrier dysfunction, seizures and epilepsy. *Seminars in Cell & Developmental Biology*.
  - Wetherington, J., Serrano, G. & Dingledine, R., 2008. Astrocytes in the Epileptic Brain. *Neuron*, 58, pp.168–178.
  - Wilson, N.H. & Key, B., 2006. Neogenin interacts with RGMa and netrin-1 to guide axons within the embryonic vertebrate forebrain. *Developmental Biology*, 296(2), pp.485–498.
  - Wilson, P.M. et al., 2010. Astn2, a novel member of the astrotactin gene family, regulates the trafficking of ASTN1 during glial-guided neuronal migration. *The Journal of neuroscience : the official journal of the Society for Neuroscience*, 30, pp.8529–8540.
  - Yacubova, E. & Komuro, H., 2002. Intrinsic program for migration of cerebellar granule cells in vitro. *The Journal of neuroscience : the official journal of the Society for Neuroscience*, 22, pp.5966–5981.
  - Yap, C.C. & Winckler, B., 2012. Harnessing the Power of the Endosome to Regulate Neural Development. *Neuron*, 74, pp.440–451.
  - Yuasa, S. et al., 1991. Development and migration of Purkinje cells in the mouse cerebellar primordium. *Anatomy and Embryology*, 184, pp.195–212.
  - Zhang, A.S. et al., 2009. Hemojuvelin-neogenin interaction is required for bone morphogenic protein-4-induced hepcidin expression. *Journal of Biological Chemistry*, 284, pp.22580–22589.
  - Zhang, A.S. et al., 2005. Interaction of hemojuvelin with neogenin results in iron accumulation in human embryonic kidney 293 cells. *Journal of Biological Chemistry*, 280, pp.33885–33894.









---

# Chapter 2

## Semaphorin Signaling: Molecular Switches at The Midline

---

Alwin A.H.A. Derijck, Susan van Erp and R. Jeroen Pasterkamp

Department of Neuroscience and Pharmacology, Rudolf Magnus Institute of Neuroscience,  
University Medical Center Utrecht, Universiteitsweg 100, 3584CG Utrecht, the Netherlands

*Trends in Cell Biology*, 2010; 20(9), 568–576

# Semaphorin signaling: molecular switches at the midline

Alwin A.H.A. Derijck, Susan Van Erp and R. Jeroen Pasterkamp

Department of Neuroscience and Pharmacology, Rudolf Magnus Institute of Neuroscience, University Medical Center Utrecht, Utrecht, The Netherlands

**To establish axonal connections growth cones must navigate multiple intermediate targets before reaching their final target. During this journey growth cones are guided by extracellular repulsive and attractive signals. Although initially identified as repulsive molecules, members of the semaphorin family include both attractants and repellents. How a navigating growth cone responds to a specific semaphorin is not absolute but instead depends on the biological context in which this cue is encountered. Here we review recent breakthroughs in our understanding of the extrinsic signals and molecular processes that control growth cone responses to class 3 semaphorins (Sema3s) at a well-characterized intermediate target, the spinal cord midline.**

## Introduction

A challenging problem in biology is to understand how the billions of neurons in the mammalian nervous system 'wire up' to form functional neural circuits. This has been one of the most intensely studied areas of developmental neurobiology and a number of important proteins have been identified that instruct axons to project along multiple decision points to their specific synaptic targets. These so-called axon guidance proteins are detected by a highly motile structure at the tip of every growing axon, the growth cone. Receptor complexes at the growth cone surface detect guidance proteins and consequently trigger signal transduction events that affect the cytoskeleton and control growth cone navigation. Axon guidance proteins can act as attractants or repellents, that is, either directing axons towards a specific structure or preventing them from entering inappropriate regions. Furthermore, they can act as membrane-associated cues acting at short ranges or as secreted agents with longer-range effects [1,2].

Proper axon guidance depends crucially on the correct presentation of guidance proteins in the extracellular environment. Furthermore, it requires the regulated expression of guidance receptors and downstream signaling cues in growth cones. The response of a growth cone to an individual guidance protein is not fixed (i.e. repulsive or attractive) but instead depends on the biological context in which the cue is encountered. For example, retinal ganglion cell (RGC) growth cones change their response to the guidance cue Netrin-1 from attraction to repulsion upon reaching the optic nerve head. In

addition, spinal commissural axons become unresponsive to Netrin-1 following midline crossing [3,4]. Our understanding of the molecular mechanisms that underlie such changes, and especially of the signals that trigger them, is rather incomplete. Although progress has been made in defining the molecular events that control growth cone responses to members of the Netrin and Slit families [5], regulatory mechanisms for other axon guidance proteins remain largely unknown. Here we review recent work that provides insight into novel extrinsic signals and molecular processes that dynamically control growth cone responses to vertebrate members of the semaphorin family (i.e. secreted class 3 semaphorins; Sema3s). First we summarize the axon guidance functions and neuronal signaling mechanisms of Sema3s, with an emphasis on recent insights into the molecular basis of Sema3-mediated axon attraction which had remained poorly understood. Next we highlight examples of changes in growth cone responses to Sema3s at different intermediate targets. Finally we discuss how regulation of the activity of downstream effectors or of receptor levels is utilized to control growth cone sensitivity to Sema3s at a well-defined intermediate target, the spinal cord floorplate.

## Class 3 semaphorins

Sema3s are among the best-characterized semaphorins in vertebrate axon guidance. Seven Sema3 family members have been described (Sema3A–3G), all of which act as axon guidance cues [6,7]. To induce axon repulsion, Sema3s, with the exception of Sema3E, bind neuropilin proteins (Npn) on the growth cone surface to assemble and activate Npn–plexin holoreceptor complexes. In this complex, class A plexin proteins (PlexinA1–4) serve as a signal-transducing subunit. In addition, Npn–plexinA receptor complexes can require IgCAMs (immunoglobulin superfamily cell adhesion molecules) for specific repulsive events (e.g. Ref. [8]). Sema3E binds plexinD1 to mediate repulsive responses in cortical neurons [9]. The intracellular signal transduction pathways that function downstream of Sema3 receptor complexes in repulsive axon guidance are highlighted in several recent reviews [7,10,11]

Although initially identified as repulsive molecules, Sema3s include both attractants and repellents. In addition, individual Sema3s are bifunctional and can exert repulsive or attractive effects. For example, Sema3B is a repellent for cortical axons in the posterior part of the anterior commissure (AC), but is an attractant for axons in the anterior AC [12]. Several Sema3s can mediate

Corresponding author: Pasterkamp, R.J. (r.j.pasterkamp@umcutrecht.nl)



Table 1. Axon attraction by class 3 semaphorins

Semaphorin	<i>In vitro</i>	<i>In vivo</i>	Receptor	Ref.
Sema3A	Motor neurons <sup>a</sup>	nd	nd	[20]
	Cortical neurons <sup>b</sup>	nd	Npn-1	[68]
Sema3B	Cortical neurons	Anterior commissure patterning	Npn-2/NrCAM	[12]
	Olfactory bulb neurons	nd	nd	[69]
Sema3C	Dopaminergic neurons	nd	nd	[70]
	Cortical neurons	Corpus callosum formation	Npn-1	[51]
Sema3D	nd	Anterior commissure formation	Npn-1A/Npn-2B	[14]
Sema3E	Subicular neurons	Subiculo-mammillary tract formation	Npn-1/plexinD1/VEGFR2	[9]
Sema3F	Cerebellar granule cells	nd	Npn-2	[19]
	Dopaminergic neurons	Axon targeting in prefrontal cortex	Npn-2	[13]
Sema3G	nd	nd		

nd, not determined.

<sup>a</sup>Following manipulation of cyclic nucleotide signaling.<sup>b</sup>In the presence of soluble L1-Fc.

attractive axon guidance events *in vitro* and *in vivo* (Table 1) but the molecular pathways that underlie these effects are still not well known. Npns play at least two distinct roles in Sema3 attraction. First, Npn-1 and Npn-2 function as ligand-binding receptors. The formation of both the AC and the mesoprefrontal pathway depend on Npn receptor functions [12–14]. Sema3B attraction also requires the neuronal cell adhesion molecule (NrCAM) [12], suggesting that attractive Sema3 receptors, like their repulsive counterparts, consist of multiple distinct subunits (i.e. Npns and IgCAMs). Whether other Sema3s, other than Sema3E (see next section), display a similar dependency on IgCAMs or on plexins for evoking axon attraction will be an important issue to address in future research.

An alternative mode of action for Npns has been described for Sema3E-mediated axon attraction/elongation. Ventrolateral cortical axons express plexinD1 and display repulsive responses to Sema3E. By contrast, Sema3E attracts the axons of neurons residing in the subiculum, a part of the hippocampus, which express Npn-1 in addition to plexinD1. Unlike other Sema3s, Sema3E does not bind Npn-1 but instead directly interacts with plexinD1 (Figure 1). Nevertheless, both Npn-1 and plexinD1 are required for the positive effects of Sema3E on subicular axons [9]. Recent work further identifies vascular endothelial growth factor receptor 2 (VEGFR2, also known as Kdr/Flk1) as an additional, obligatory component of the attractive Sema3E receptor (Figure 1) [15]. Npn-1, plexinD1 and VEGFR2 associate through their extracellular parts, and the cytoplasmic domain of VEGFR2, but not of Npn-1 or plexinD1, is required for the effects of Sema3E [15]. Thus, plexinD1 and VEGFR2 serve as ligand-binding and signal-transducing subunits, respectively.

How does Npn-1 contribute to Sema3E axon attraction? Npn-1 is a key determinant for Sema3E attraction and, unlike plexinD1 and VEGFR2, is expressed in subicular but not in cortical neurons [9,15]. Such a restricted pattern of expression invites the speculation that Npn-1 might control the activity of the trimeric Sema3E receptor complex and thereby facilitate attractive responses. In endothelial cells, Npn-1 functions as a VEGFR2 coreceptor and enhances VEGF-induced VEGFR2 receptor signaling [16,17]. Similarly, VEGFR2 phosphorylation induced by Sema3E is more pronounced in the presence of Npn-1 [15]. Thus, Npn-1 could raise Sema3E-induced VEGFR2 activation to threshold levels for axon attraction. Alterna-

tively, Npn-1 might inhibit repulsive plexinD1 signaling and thereby allow VEGFR2 to induce attractive responses. This latter model is in line with (i) the observation that VEGFR2 inactivation blocks Sema3E attraction but that knockdown of Npn-1 protein levels converts attractive responses into repulsive ones [9–15], and (ii) the ability of Npn-1 to modulate the interaction of plexinA1 with some of its downstream effectors [18]. Further work is needed to examine whether and, if so, how Npn-1 silences repulsive plexinD1 signaling.

Which intracellular signaling events mediate attractive responses to Sema3s? Sema3B-mediated attraction of cortical axons, but not repulsion, is accompanied by the activation and membrane relocalization of FAK (focal adhesion kinase or Ptk2). Sema3B furthermore recruits the Src family kinase Fyn to FAK in the membrane compartment and Src kinase inhibitors abrogate Sema3B attraction [12]. Thus, FAK/Src signaling might play a central role in Sema3B attraction. cGMP can switch the axon-repulsive effects of several Sema3s to attraction [19,20] and its precise role and mechanism of action are under active investigation (e.g. Refs [21,22]). Sema3E stimulation of subicular neurons induces the autophosphorylation of VEGFR2 at Tyr1175 (and Tyr1214), and VEGFR2<sub>Y1175F</sub> mutants fail to transduce Sema3E signals [15]. Tyr1175 on VEGFR2 is important for PI 3-kinase (phosphoinositide 3-kinase) activation during VEGF-induced endothelial cell migration [23]. Sema3E treatment of subicular neurons also activates the PI 3-kinase pathway in a VEGFR2-dependent manner leading to the inactivation of GSK-3 $\beta$  (glycogen synthase kinase-3 $\beta$ ). Manipulation of PI 3-kinase signaling or of GSK-3 $\beta$  levels blocks the axon growth promoting effects of Sema3E [15]. In all, these findings support a model in which Sema3E induces VEGFR2 activation to enhance PI 3-kinase signaling and reduce GSK-3 $\beta$  activity, thereby stimulating axon elongation (Figure 1). Whether this pathway is also employed during Sema3E-mediated attraction remains to be addressed. Achieving a more complete understanding of the signaling pathways that dictate Sema3 axon attraction is clearly a major challenge for the future.

#### Changes in semaphorin responses at intermediate targets

Growth cones often travel long distances to reach their final synaptic targets and must therefore rely on many

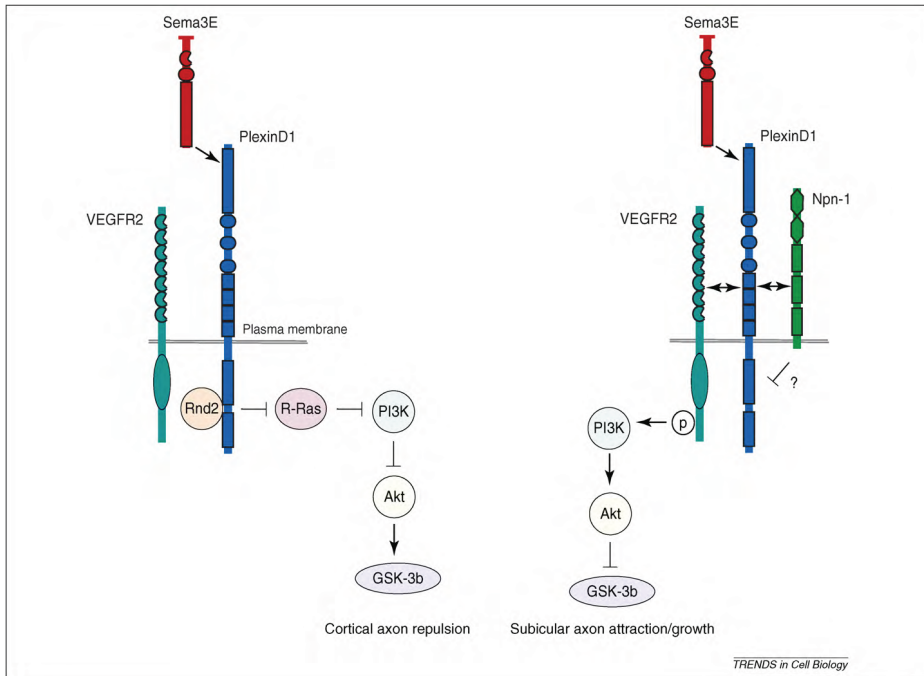


**Figure 1.** Sema3E signaling in axon attraction and repulsion. To induce cortical axon repulsion Sema3E binds its receptor plexinD1. This interaction leads to the activation of the intracellular plexinD1 RasGAP (Ras GTPase activating protein) domain and subsequently reduces R-Ras activity. Rnd2 (Rho family GTPase 2) is also required for Sema3E/plexinD1-mediated axon repulsion [67]. Sema3E stimulation of cortical neurons inhibits Akt (v-Akt murine thymoma viral oncogene homolog 1) phosphorylation [15] supporting a model in which Sema3E, by analogy to other semaphorin family members [11], ultimately activates GSK-3 $\beta$  (glycogen synthase kinase-3 $\beta$ ) through inhibition of the PI 3-kinase (phosphoinositide 3-kinase) pathway to induce repulsion. To induce attraction or growth of subicular axons Sema3E binds a trimeric receptor complex containing plexinD1 (ligand-binding subunit), Npn-1 (neuropilin-1; modulatory subunit), and VEGFR2 (vascular endothelial growth factor receptor 2; signal-transducing subunit). Binding of Sema3E to plexinD1 induces VEGFR2 autophosphorylation at Tyr1175 to enhance PI 3-kinase signaling and as a result reduces GSK-3 $\beta$  activity. Npn-1 could function to inhibit repulsive signaling by plexinD1 thereby facilitating attractive/growth promoting responses.

different attractive and repulsive guidance proteins. During this journey the response of a growth cone to an individual guidance cue is tightly controlled by a combination of intrinsic mechanisms and extrinsic signals. Examples of changes in growth cone responses to Sema3s during axon pathfinding have been reported in different neural systems.

#### Stage-dependent changes in the retinotectal system

In the developing visual system of non-mammalian vertebrates such as *Xenopus laevis*, RGC axons travel from the eye to their main contralateral target in the brain, the optic tectum. *En route*, RGC axons rely on different cues to guide them along multiple decision points [24]. Sema3A plays a key role in guiding RGC axons in the distal part of the optic tract and the tectum (Figure 2a) [25,26]. Interestingly, RGC growth cones acquire Sema3A responsiveness with age. Growth cones of young RGC neurons (stage 24; 26 hrs and 15 min post-fertilization), that have not passed the optic chiasm yet, do not express Npn-1 and fail

to collapse following Sema3A treatment. By contrast, more mature, post-crossing, growth cones (stage 33/34; 44 hrs and 30 min post-fertilization) express Npn-1 and display Sema3A-induced collapse responses. When young neurons are aged in culture they develop Npn-1 expression and Sema3A sensitivity in a similar manner, suggesting that an unknown, intrinsic mechanism of Npn-1 regulation mediates this age-dependent change [26] (Figure 2a,a').

#### From repulsion to attraction in the medial prefrontal cortex

Dopaminergic neurons in the midbrain that project axons to the prefrontal cortex (i.e. mesoprefrontal axons) mediate cognitive functions and are affected in psychiatric disorders [27]. Sema3F is a bifunctional guidance cue for Npn-2-expressing mesoprefrontal axons [13,28]. During the first part of the mesoprefrontal trajectory [embryonic day (E)~12–15], repulsion by Sema3F, which is expressed in regions surrounding the mesoprefrontal trajectory, is required for guidance, fasciculation, and rostrally oriented

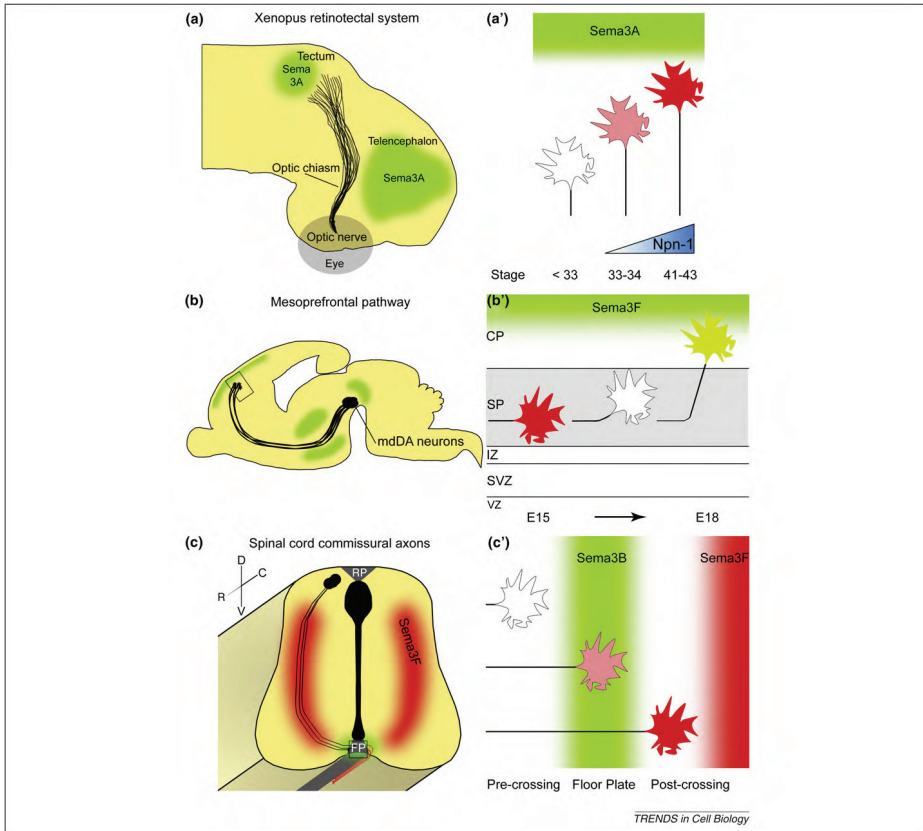


**Figure 2.** Changes in semaphorin responsiveness during axon pathfinding. **(a,a')** Axons of retinal ganglion cells (RGCs) gain responsiveness to Sema3A as they extend towards the optic tectum. **(a)** Schematic representation of the developing *Xenopus* retinotectal system at stage 41. Sema3A expression is indicated in green. **(a')** RGC growth cones are devoid of the Sema3A receptor Npn-1 (neuropilin-1, blue gradient) until stage 33 and fail to respond to Sema3A (Sema3A responsiveness is indicated in red). Npn-1 is first expressed around stage 33/34 and expression levels increase with time. Npn-1 expression enables axons to respond to Sema3A gradients in the telencephalon and, later on, in the tectum. **(b,b')** Axons from dopaminergic neurons in the midbrain (mdDA neurons) change their responsiveness to Sema3F from repulsion to attraction in the cortex. **(b)** Schematic representation of the developing mouse mesoprefrontal system (i.e. mdDA axon projections to the medial prefrontal cortex, mPFC). Gradients of Sema3F (in green) play an important role at different points during the establishment of the mesoprefrontal pathway [13]. **(b')** Schematic representation of the mPFC. Upon arrival in the subplate (SP) mesoprefrontal growth cones stall and change their responsiveness to Sema3F from repulsion (red) to attraction (light green). Extracellular matrix components (grey) could play an important role in this switch. A Sema3F gradient (green) in the overlying cortical plate (CP) subsequently pulls axons upwards. IZ, intermediate zone; SVZ, subventricular zone; VZ, ventricular zone. **(c,c')** Spinal commissural axons gain responsiveness to Sema3B and Sema3F at the floorplate (FP). **(c)** Schematic representation of developing commissural projections in the mouse spinal cord. Sema3F and Sema3B expression in red and green, respectively. Commissural axons grow from the dorsal horn of the spinal cord towards the floorplate (FP) after which they cross the midline and turn to grow rostrally. C, Caudal; D, Dorsal; RP, roofplate; R, Rostral; V, Ventral. **(c')** During midline crossing, growth cones gain responsiveness (in red) to Sema3B and Sema3F and this facilitates midline crossing and helps to guide commissural axons into their characteristic rostroventral trajectory.

growth of mesoprefrontal axons [13,28] (Figure 2b). When these axons reach the cortex, around E15, they wait for several days in the subplate (SP) before penetrating the overlying cortical plate (CP). During this period the responsiveness of mesoprefrontal axons to Sema3F switches from repulsion to attraction. Then, around E18, Sema3F attracts mesoprefrontal axons into the CP (Figure 2b') [13]. It is tempting to speculate that SP signals trigger changes in Sema3F responsiveness. Interestingly,

the SP is particularly rich in extracellular matrix (ECM) components such as proteoglycans [29–31] which can modulate semaphorin responses [32,33]. Alternatively, a preprogrammed intrinsic mechanism might induce the switch.

*Post-crossing responses at the spinal cord midline*

Commissural neurons in the dorsolateral spinal cord project their axons ventrally before redirecting them to the

### Box 1. Commissural axon guidance in the mouse spinal cord

The axons of commissural neurons in the dorsolateral spinal cord extend ventrally before being redirected towards the midline (the floorplate, FP) (Figure 2c). The ventrally directed growth of these axons is controlled by repulsion induced by BMPs (bone morphogenetic proteins) that are secreted by roof plate (RP) cells [58]. More ventrally, axons are guided towards the midline by attractive molecules released by FP cells (i.e. Netrin-1 and Shh, Sonic hedgehog) [42,44]. The effects of Netrin-1 depend on axonal expression of DCC (deleted in colorectal cancer) and DSCAM (Down's syndrome cell adhesion molecule) [59–61]. Boc (biregional Cdon-binding protein) mediates Shh attraction of pre-crossing axons [62].

The FP also expresses axon repellents, such as Slits and class 3 semaphorins (Sema3s) which ensure midline crossing and expulsion and prevent recrossing. Prior to midline crossing, repulsive responses to Slit proteins are repressed by Robo3.1, one of two splice variants of the *Robo3 (Rig1)* gene [39,63]. Robo3.1 inhibits Robo1 and Robo2 through an unknown mechanism. Axons lose Robo3.1 and initiate Robo3.2 expression post-crossing, hence acquiring Slit responsiveness [39]. Sema3B sensitivity is also suppressed at the pre-crossing stage and acquisition of post-crossing responsiveness involves FP-derived cues (Figures 3,4). Midline-derived ephrin-B3 repulsion functions in guiding a subset of ipsilateral commissural projections [64]. Midline crossing also requires the downregulation of sensitivity to FP attractants which would otherwise trap axons in the FP. Intriguingly, Robo receptors antagonize DCC thereby silencing attractive Netrin-1 signaling [4]. In addition to the synchronized regulation of FP attractants and repellents, FP crossing requires SCF (stem cell factor) and its receptor Kit [65]. SCF promotes the outgrowth of post-crossing axons thereby stimulating their midline exit.

Following midline expulsion, commissural axons make a sharp rostral turn to further extend along the anterior–posterior axis of the spinal cord. Anterior–posterior gradients of Wnt4 and Shh (in chicken) proteins in the ventral spinal cord function to attract and repel commissural axons, respectively, during their longitudinal journey [43,66]. Expression of Sema3F in the mantle zone of the spinal cord could also contribute to shaping the post-crossing trajectory [36]. Mediolateral positioning of longitudinal projections is controlled by Robo receptors [38]. The study of spinal commissural axons has provided a wealth of information on the function and regulation of axon guidance proteins. An important future challenge is to understand further how these different signals are integrated and how their effects are controlled in both time and space.

floorplate at the ventral midline. After crossing the midline, these axons turn rostrally into a longitudinal trajectory and neither recross to the ipsilateral side nor enter inappropriate regions of the more dorsal spinal cord (Figure 2c). Members of different axon guidance families have been implicated in spinal commissural axon guidance (Box 1). In the ventral spinal cord, commissural axons are guided to the midline by attractants in the floorplate. Once they reach the floorplate they switch off their responsiveness to these attractants and begin to respond to floorplate repellents that control midline crossing and expulsion and also prevent recrossing. Although pre-crossing commissural axons first traverse the ventral spinal cord to reach the midline (Figure 2c), the contralateral ventral spinal cord strongly repels post-crossing axons. Sema3s contribute to the repulsive properties of the floorplate and most likely of the ventral spinal cord. The semaphorin 3B gene (*sema3B*) is expressed in the floorplate and *sema3F* in the mantle layer of the spinal cord (Figure 2c,c') [34–37]. Both Sema3B and Sema3F can repel Npn-2-positive commis-

sural axons but, intriguingly, only post-crossing axons are sensitive to these guidance signals. Knockout mice *nfn-2*, *sema3B* or *plexinA1* have commissural axon guidance defects including axon stalling at the midline and randomized post-crossing projections along the anterior–posterior axis [36,37]. Thus, Sema3B is a midline repellent for post-crossing axons. Although it is unknown whether *sema3F* mutant mice display midline guidance defects, these observations also hint at a role for Sema3F as a ventral spinal cord-derived repellent (Figure 2c,c').

At the midline, Sema3B cooperates with Slits and their Robo receptors to guide axons across the floorplate [38,39]. Why these two repulsive guidance mechanisms coexist is unclear. It is possible that different subpopulations of commissural axons use different midline repellents or that Sema3B and Slits act in concert to increase the accuracy of the guidance process. Alternatively, these cues might act sequentially, mediating different aspects of midline guidance. This latter idea is supported by the occurrence of midline recrossing defects following loss of repulsive Slit but not of Sema3B signaling.

### Molecular switches at the midline

Spinal commissural axons express Npn-2 both pre- and post-crossing but only acquire responsiveness to Sema3B and Sema3F upon reaching the floorplate. This suggests that this switch (i) could be triggered by the floorplate, and (ii) does not involve regulation of Npn-2 levels. Two recent studies now provide a mechanistic insight into how commissural axons gain responsiveness to Sema3s upon reaching the floorplate [37,40].

### Sonic hedgehog reduces PKA activity

Parra and Zou tested the idea that acquisition of Sema3 responsiveness is induced by floorplate signals [40]. They compared the response of pre-crossing commissural axons to Sema3B and Sema3F in the presence or absence of two diffusible cues enriched in the floorplate, Sonic hedgehog (Shh) and Netrin-1 [41,42]. Intriguingly, Shh was able to switch on repulsive responses of pre-crossing axons. In addition, neutralization of Shh in 'open book' preparations of the spinal cord led to midline guidance defects some of which reflected the inability of axons to cross the midline or to turn rostrally post-crossing [40]. Shh has several functions during spinal cord development. It induces ventral cell types in the spinal cord, attracts pre-crossing commissural axons to the midline, and can guide post-crossing axons rostrally [43–45]. These functions are mediated by different receptors including Ptch1 (Patched1), Smo (Smoothened), Hhip (Hedgehog-interacting protein) and Boc (bi-regional Cdon-binding protein). The effect of Shh on midline crossing requires Ptch1 and Smo. Normally, Ptch1 inhibits Smo, and Shh binding to Ptch1 releases this inhibition. Ptch1 and Smo are both expressed by commissural axons [40,44] and overexpression of dominant-active Ptch1 or Smo knockdown induces midline guidance defects such as stalling, resembling the deficits found in *nfn-2* and *plexinA1* mice [36,37,40]. A model to explain the results of these various tissue culture experiments is that Shh–Ptch1–Smo signaling turns on Sema3 responses at the midline, thereby forcing axons (i) to cross the floorplate

(Sema3B), and (ii) to follow a rostroventral trajectory in the spinal cord (Sema3F)

In *Drosophila*, Smo can function as a G-protein-coupled receptor (GPCR), and in response to Hedgehog activates the G protein  $G_{\alpha_i}$  to reduce intracellular cyclic AMP levels [46]. The cAMP/cGMP ratio in a growth cone is a crucial determinant of axonal responses to guidance cues [20,47] and activity of the cAMP-dependent protein kinase PKA has been linked to semaphorin repulsion [48]. Treatment of dissociated commissural neurons with Shh reduces PKA activity. Furthermore, increasing cAMP levels (and thereby PKA activity) blocks the ability of Shh to switch on Sema3F responses and leads to midline guidance defects [40]. Inhibiting PKA activity in 'open book' preparations prevents large numbers of axons from entering the floorplate [40]. One of the models to explain this latter result is that reduced PKA activity renders pre-crossing axons sensitive to Sema3B. Alternatively, however, PKA inhibition could hamper the attractive effects of Netrin-1 [40]. Although it remains unresolved which of these two alternatives is correct, these results suggest that Shh released from the floorplate reduces PKA activity in commissural axons through Ptc1/Smo, thereby inducing responsiveness to Sema3s (Figure 3). Future experiments will undoubtedly continue to dissect this Shh-dependent pathway by for example testing the involvement of GPCR signaling or by examining whether these cAMP-dependent effects are direct or indirect.

*NrCAM inhibits plexinA1 cleavage*

Another recent study indicates that spinal commissural axons could employ multiple different strategies to control Sema3 responsiveness. In their study, Nawabi and colleagues hypothesized that Sema3B responsiveness could be gained through regulation at the receptor level [37]. They first identified plexinA1 as an obligatory component of the Sema3B receptor on commissural axons. PlexinA1 protein is enriched in post-crossing axon segments and growth cones, and *plexinA1* mutant mice display midline guidance defects. Knockdown of *plexinA1* blocks Sema3B responses in post-crossing axons, whereas *plexinA1* over-expression induces premature responses in pre-crossing axons [37]. These results together with earlier work implicating Npn-2 in Sema3B repulsion at the midline indicate that the receptor complex that mediates Sema3B responses in commissural axons is composed of Npn-2 [36] and plexinA1 [37]. NrCAM is also expressed in commissural neurons but its requirement in Sema3B repulsion [49], as has been reported for cortical axons [12], was unknown.

How is plexinA1 cell surface expression restricted to axon segments that are crossing or have already crossed the floorplate? Floorplate-conditioned medium can induce Sema3B responsiveness in pre-crossing axons *in vitro* and this effect is abrogated by pharmacological inhibition or knockdown of calpain1, a calcium-dependent cysteine protease [50]. Calpain1 is active at pre-crossing stages,

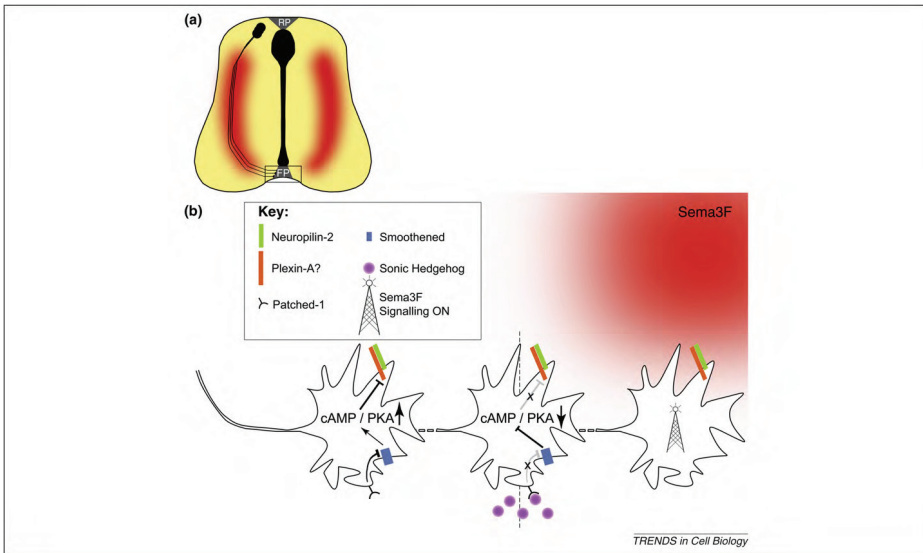


**Figure 3.** Sonic hedgehog reduces PKA activity at the midline. (a) Schematic representation of commissural axon projections approaching the floorplate (FP) in the mouse spinal cord. Sema3F in red; RP, roofplate. (b) As growth cones extend towards the FP they are not repelled by Sema3F and are characterized by high cAMP/PKA signaling (left growth cone). Upon entering the FP, Sonic hedgehog binds its receptor Patched-1 on commissural axons, inactivating the inhibitory effect of Ptc1 on Smoothed (middle growth cone). Activated Smoothed inhibits adenylate cyclase (through  $G_{\alpha_i}$  signaling) thereby reducing cAMP levels and consecutively PKA activity (middle growth cone). Dotted line indicates the midline. This drop in cAMP/PKA activity relieves the inhibition on plexin/neurophilin-2 receptor downstream signaling, allowing Sema3F in the ventral spinal cord to exert its function as a repellent (right growth cone).



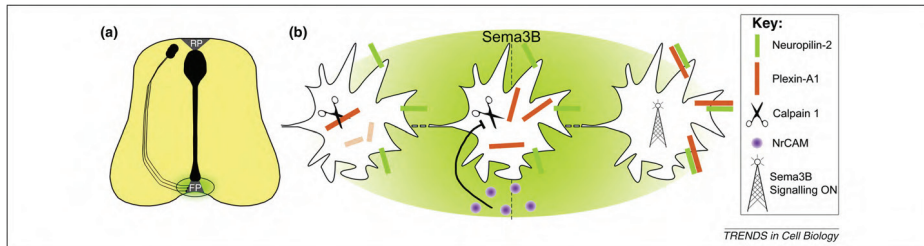


**Figure 4.** NrCAM inhibits proteolytic cleavage of plexinA1 at the midline. (a) Schematic representation of commissural axon projections approaching the floorplate (FP) in the mouse spinal cord. Sema3B in green. RP, roofplate. (b) As growth cones extend towards the FP Sema3B-mediated repulsion is prevented by proteolytic cleavage of plexinA1 by the calcium-dependent cysteine protease calpain1 (left growth cone). Neurophilin-2 expression is unaffected. At the midline, soluble NrCAM inhibits calpain1 through an as yet undetermined mechanism, triggering the accumulation of plexinA1 at the growth cone surface (middle growth cone). A fully active receptor complex (plexinA1/Neuropilin-2) then detects FP-derived Sema3B, forcing axons to cross and exit the floorplate (dotted line indicates midline) (right growth cone).

induces proteolytic cleavage of plexinA1, and inactivation of calpain1 raises plexinA1 levels in pre-crossing axons and results in midline guidance defects [37]. Thus, the selective activity of calpain1 at pre-crossing stages could contribute to restricting functional plexinA1 to post-crossing axon segments.

Which signals control the selective distribution of calpain1 activity? In their search for such a cue, Nawabi *et al.* focused on NrCAM [37], an IgCAM enriched in the floorplate. NrCAM is subjected to metalloprotease-mediated cleavage and therefore also exists in a secreted form. NrCAM ectodomain is produced by the floorplate and raises plexinA1 levels as well as Sema3B responsiveness in pre-crossing axons. Floorplate-conditioned medium devoid of NrCAM only induces weak Sema3B responses in pre-crossing axons, whereas NrCAM mutant mice show midline guidance defects resembling those found in *sema3B*, *npn2* and *plexinA1* knockout mice. Together these findings support a model in which floorplate NrCAM blocks the proteolytic cleavage of plexinA1 in commissural axons, thereby increasing cell surface plexinA1 and inducing Sema3B responsiveness (Figure 4). This effect of NrCAM on plexinA1 is likely to be mediated by calpain-1, although further experiments are needed to confirm this link. Furthermore, how soluble NrCAM suppresses calpain-1 activity remains to be unveiled. These findings support a novel role for NrCAM and suggest that this IgCAM is required both for floorplate entry, through interactions with axonin-1 [51,52], and for floorplate crossing/expulsion, by inducing Sema3B responsiveness [37].

#### Concluding remarks and future perspectives

Axon repulsion and attraction by Sema3s plays an essential role in midline guidance [36,37,40,53]. The recent implication of Shh and NrCAM as regulators of growth cone sensitivity to Sema3s at the midline provides a compelling insight into how Sema3 responses are controlled at intermediate targets. The selective embryonic distribution of NrCAM and Shh, together with the large number of intermediate targets that axons could need to navigate, supports the notion that many regulatory mechanisms of semaphorin responsiveness still await discovery (Box 2).

The coexistence of two signals for initiating Sema3 responses at the floorplate seems redundant but might be essential for safeguarding the accuracy of the midline guidance process. Alternatively, commissural axons could encounter Shh and NrCAM sequentially (i.e. the extents of their medio-lateral gradients could differ). This could contribute to a differential degree of Sema3 responsiveness across the floorplate region, with highest sensitivity at the midline, where both signals coexist, and decreasing laterally. In addition, different signals could control different aspects of midline guidance. Only a subset of the midline guidance defects observed in *plexinA1* deficient mice are present in *Nrcam* mutant mice or following calpain1 inhibition. This, coupled with the ability of floorplate-conditioned medium from *Nrcam* mutant mice to induce pre-crossing Sema3B responses, albeit far less efficiently

#### Box 2. Questions for future research

A major challenge for the future is to determine the multiple conserved and variable molecular players involved in regulating growth cone responses to semaphorins at intermediate targets in different parts of the developing embryo. Importantly, several distinct cellular processes and molecular pathways have been found to spatiotemporally control axonal responses to members of other axon guidance protein families (Ref. [5] for review) and we might be able to exploit this knowledge to begin to understand how semaphorin responsiveness is regulated in both time and space. *Vice versa*, insight into the control of semaphorin responses will undoubtedly also further our understanding of the regulation of other axon guidance proteins. Other important questions that need to be addressed to achieve significant conceptual progress include:

- Which receptors and signaling pathways underlie axon attraction induced by semaphorins other than Sema3E?
- How does Npn-1 contribute to Sema3E-induced axon attraction?
- Do *sema3F* knockout mice display commissural axon guidance defects?
- Does the effect of Shh on Sema3B responses involve GPCR signaling?
- Does NrCAM affect plexinA1 through calpain-1 and, if so, how can NrCAM regulate calpain-1 activity?
- Are Shh- and NrCAM-dependent mechanisms important for controlling axonal responsiveness to other axon guidance proteins at the midline?
- Why do two seemingly redundant regulatory mechanisms (Shh and NrCAM) coexist at the spinal cord midline?
- How specific is calpain-1 cleavage during commissural axon guidance and at which subcellular site is calpain-1 active?



than wild-type medium, hints at the existence of multiple floorplate signals. Simultaneous depletion of NrCAM and Shh from floorplate-conditioned medium will reveal whether this residual activity is mediated by Shh or by an as yet unidentified signal. An interesting point is that the function of Sema3B was assessed using growth cone collapse, but not axon repulsion assays. For example, it was not shown that NrCAM fragments can induce Sema3B repulsion in pre-crossing axons. Therefore, it is possible that Sema3B's main function is to slow down growth cone advance within the floorplate so that growth cones can detect other cues and be guided precisely.

Finally, it remains to be shown whether both the Sema3B and Sema3F responses are dependent on Shh (cAMP regulation) and NrCAM (calpain-1 proteolytic cleavage). Shh switches on axonal Sema3B responses in pre-crossing collagen matrix assays, but it is unknown whether reduced cAMP/PKA signaling is a prerequisite for Sema3B repulsion. Intriguingly, although Shh induces Sema3F responses in pre-crossing axons, lowering cAMP/PKA activity in the absence of Shh does not. This suggests that Shh activates additional mechanisms to complete this change. Calpain1 cleaves plexinA1, but not plexinA2, and its effect on plexinA3 (that is probably involved in mediating Sema3F responses) is unknown. The differential effect of calpain1 on plexins A1 and A2 is intriguing because tertiary structure elements rather than primary amino acid sequences are probably responsible for directing cleavage by calpains [54]. Calpain1 has numerous substrates, several of which function in axon guidance (e.g. Refs [55,56]); it will therefore be important to establish whether calpain1 selectively processes plexinA1 or whether it affects a wider array of Sema3 signaling cues.

Other open questions that will be a focus of future studies are: does calcium signaling play a role in the control of calpain1 activity by NrCAM or are other pathways involved? At which subcellular site does calpain1 cleavage of plexinA1 take place? Do NrCAM (calpain1) and Shh affect other guidance systems at the midline?

Aberrant function and expression of semaphorins and their downstream effectors has been proposed to trigger some of the neuronal structural changes observed during neurodegenerative, neurodevelopmental and psychiatric disorders [57]. In addition, semaphorins contribute to the regenerative failure of severed CNS axons [57]. Therefore, we can expect that experiments over the next few years will not only provide further insight into the mechanistic details of semaphorin signaling but also will contribute to conceptual and therapeutic advances in neural injury and disease.

#### Acknowledgements

We thank Fanny Mann, Valérie Castellani and Yimin Zou for critical reading of the manuscript. Work in the authors' laboratory on semaphorin signaling is supported by grants from the Netherlands Organization for Health Research and Development (ZonMW-VIDI/TOP), the Human Frontier Science Program (HFSP-CDA), and the ABC Genomics Center Utrecht (to R.J.P.).

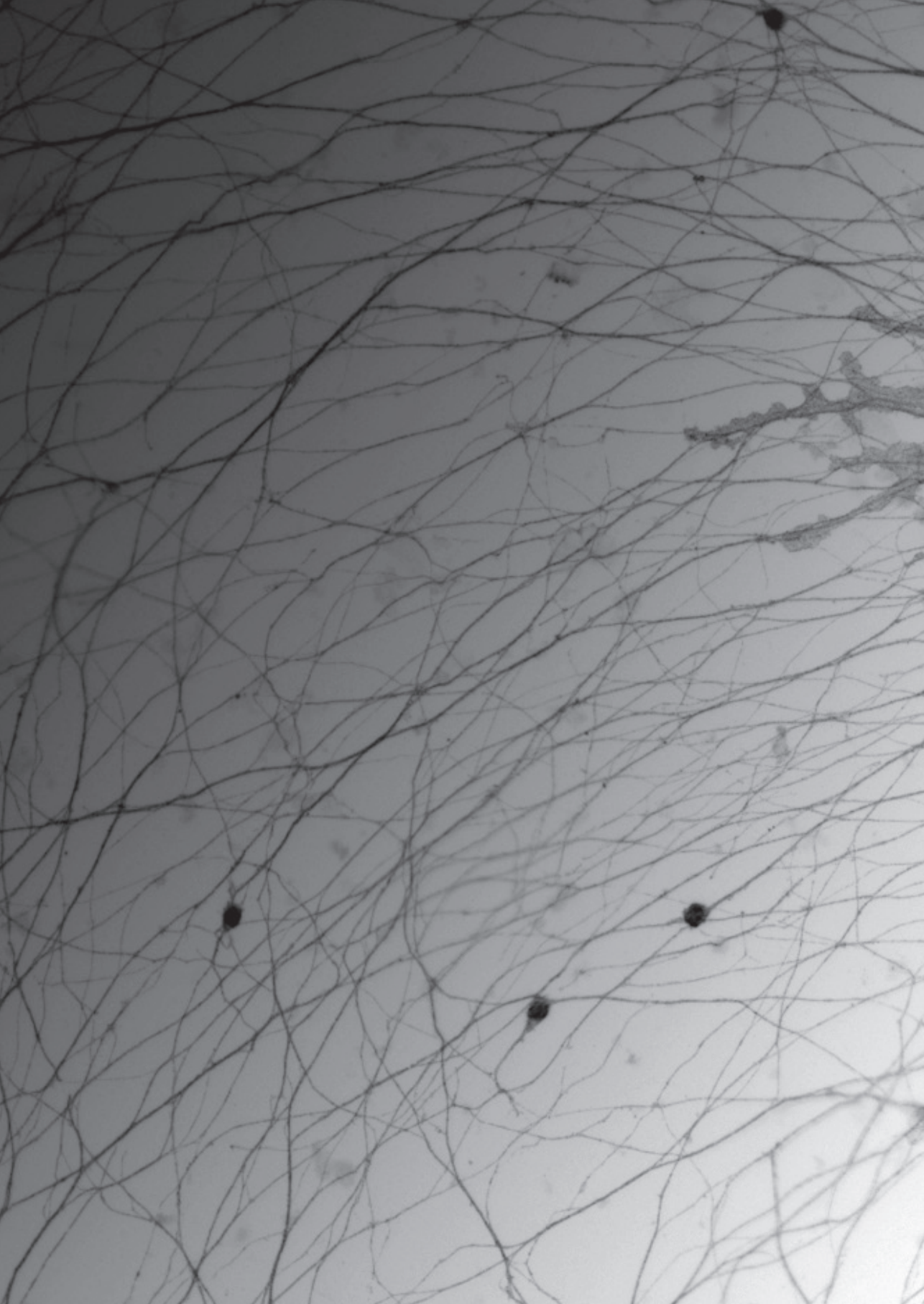
#### References

- Dickson, B.J. (2002) Molecular mechanisms of axon guidance. *Science* 298, 1959–1964

- Huber, A.B. *et al.* (2003) Signaling at the growth cone: ligand-receptor complexes and the control of axon growth and guidance. *Annu. Rev. Neurosci.* 26, 509–563
- Hopker, V.H. *et al.* (1999) Growth-cone attraction to netrin-1 is converted to repulsion by laminin-1. *Nature* 401, 69–73
- Stein, E. and Tessier-Lavigne, M. (2001) Hierarchical organization of guidance receptors: silencing of netrin attraction by slit through a Robo/DCC receptor complex. *Science* 291, 1928–1938
- O'Donnell, M. *et al.* (2009) Axon growth and guidance: receptor regulation and signal transduction. *Annu. Rev. Neurosci.* 32, 383–412
- Pasterkamp, R.J. (2007) *Semaphorins: Receptor and Intracellular Signaling Mechanisms*. Springer
- Tran, T.S. *et al.* (2007) Semaphorin regulation of cellular morphology. *Annu. Rev. Cell Dev. Biol.* 23, 263–292
- Bechara, A. *et al.* (2008) FAK-MAPK-dependent adhesion disassembly downstream of L1 contributes to semaphorin3A-induced collapse. *EMBO J.* 27, 1549–1562
- Chauvet, S. *et al.* (2007) Gating of Sema3E/PlexinD1 signaling by Neuropilin-1 switches axonal repulsion to attraction during brain development. *Neuron* 56, 807–822
- Jackson, R.E. and Eickholt, B.J. (2009) Semaphorin signalling. *Curr. Biol.* 19, R504–507
- Zhou, Y. *et al.* (2008) Semaphorin signaling: progress made and promises ahead. *Trends Biochem. Sci.* 33, 161–170
- Falk, J. *et al.* (2005) Dual functional activity of semaphorin 3B is required for positioning the anterior commissure. *Neuron* 48, 63–75
- Kolk, S.M. *et al.* (2009) Semaphorin 3F is a bifunctional guidance cue for dopaminergic axons and controls their fasciculation, channeling, rostral growth, and intracortical targeting. *J. Neurosci.* 29, 12542–12557
- Wolman, M.A. *et al.* (2004) Repulsion and attraction of axons by semaphorin3D are mediated by different neuropilins *in vivo*. *J. Neurosci.* 24, 8428–8435
- Bellon, A. *et al.* (2010) VEGFR2 (KDR/Flk1) signaling mediates axon growth in response to semaphorin 3E in the developing brain. *Neuron* 66, 205–219
- Soker, S. *et al.* (1998) Neuropilin-1 is expressed by endothelial and tumor cells as an isoform-specific receptor for vascular endothelial growth factor. *Cell* 92, 735–745
- Kawamura, H. *et al.* (2008) Neuropilin-1 in regulation of VEGF-induced activation of p38MAPK and endothelial cell organization. *Blood* 112, 3638–3649
- Toyofuku, T. *et al.* (2005) FARP2 triggers signals for Sema3A-mediated axonal repulsion. *Nat. Neurosci.* 8, 1712–1719
- Ding, S. *et al.* (2007) Semaphorin-3F attracts the growth cone of cerebellar granule cells through cGMP signaling pathway. *Biochem. Biophys. Res. Commun.* 356, 857–863
- Song, H. *et al.* (1998) Conversion of neuronal growth cone responses from repulsion to attraction by cyclic nucleotides. *Science* 281, 1515–1518
- Togashi, K. *et al.* (2008) Cyclic GMP-gated CNG channels function in Sema3A-induced growth cone repulsion. *Neuron* 58, 694–707
- Tedeschi, A. *et al.* (2009) The tumor suppressor p53 transcriptionally regulates cGKI expression during neuronal maturation and is required for cGMP-dependent growth cone collapse. *J. Neurosci.* 29, 15155–15160
- Holmqvist, K. *et al.* (2004) The adaptor protein shb binds to tyrosine 1175 in vascular endothelial growth factor (VEGF) receptor-2 and regulates VEGF-dependent cellular migration. *J. Biol. Chem.* 279, 22267–22275
- Erskine, L. and Herrera, E. (2007) The retinal ganglion cell axon's journey: insights into molecular mechanisms of axon guidance. *Dev. Biol.* 308, 1–14
- Atkinson-Leadbeater, K. *et al.* (2010) Dynamic expression of axon guidance cues required for optic tract development is controlled by fibroblast growth factor signaling. *J. Neurosci.* 30, 685–693
- Campbell, D.S. and Holt, C.E. (2001) Chemotropic responses of retinal growth cones mediated by rapid local protein synthesis and degradation. *Neuron* 32, 1013–1026
- Van den Heuvel, D.M. and Pasterkamp, R.J. (2008) Getting connected in the dopamine system. *Prog. Neurobiol.* 85, 75–93

- 28 Yamauchi, K. *et al.* (2009) FGF8 signaling regulates growth of midbrain dopaminergic axons by inducing semaphorin 3F. *J. Neurosci.* 29, 4044–4055
- 29 Franken, S. *et al.* (2003) Collapsin response mediator proteins of neonatal rat brain interact with chondroitin sulfate. *J. Biol. Chem.* 278, 3241–3250
- 30 Popp, S. *et al.* (2003) Localization of aggrecan and versican in the developing rat central nervous system. *Dev. Dyn.* 227, 143–149
- 31 Li, H.P. *et al.* (2005) Aberrant trajectory of thalamocortical axons associated with abnormal localization of neurocan immunoreactivity in the cerebral neocortex of reeler mutant mice. *Eur. J. Neurosci.* 22, 2689–2696
- 32 De Wit, J. *et al.* (2005) Semaphorin 3A displays a punctate distribution on the surface of neuronal cells and interacts with proteoglycans in the extracellular matrix. *Mol. Cell Neurosci.* 29, 40–55
- 33 Kantor, D.B. *et al.* (2004) Semaphorin 5A is a bifunctional axon guidance cue regulated by heparan and chondroitin sulfate proteoglycans. *Neuron* 44, 961–975
- 34 Cohen, S. *et al.* (2005) A semaphorin code defines subpopulations of spinal motor neurons during mouse development. *Eur. J. Neurosci.* 21, 1767–1776
- 35 Huber, A.B. *et al.* (2005) Distinct roles for secreted semaphorin signaling in spinal motor axon guidance. *Neuron* 48, 949–964
- 36 Zou, Y. *et al.* (2000) Squeezing axons out of the gray matter: a role for slit and semaphorin proteins from midline and ventral spinal cord. *Cell* 102, 363–375
- 37 Nawabi, H. *et al.* (2010) A midline switch of receptor processing regulates commissural axon guidance in vertebrates. *Genes Dev.* 24, 396–410
- 38 Long, H. *et al.* (2004) Conserved roles for Slit and Robo proteins in midline commissural axon guidance. *Neuron* 42, 213–223
- 39 Chen, Z. *et al.* (2008) Alternative splicing of the Robo3 axon guidance receptor governs the midline switch from attraction to repulsion. *Neuron* 58, 325–332
- 40 Parra, L.M. and Zou, Y. (2010) Sonic hedgehog induces response of commissural axons to Semaphorin repulsion during midline crossing. *Nat. Neurosci.* 13, 29–35
- 41 Chiang, C. *et al.* (1996) Cyclopia and defective axial patterning in mice lacking Sonic hedgehog gene function. *Nature* 383, 407–413
- 42 Kennedy, T.E. *et al.* (1994) Netrins are diffusible chemotropic factors for commissural axons in the embryonic spinal cord. *Cell* 78, 425–435
- 43 Bourikas, D. *et al.* (2005) Sonic hedgehog guides commissural axons along the longitudinal axis of the spinal cord. *Nat. Neurosci.* 8, 297–304
- 44 Charron, F. *et al.* (2003) The morphogen sonic hedgehog is an axonal chemoattractant that collaborates with netrin-1 in midline axon guidance. *Cell* 113, 11–23
- 45 Yamada, T. *et al.* (1993) Control of cell pattern in the neural tube: motor neuron induction by diffusible factors from notochord and floor plate. *Cell* 73, 673–686
- 46 Ogden, S.K. *et al.* (2008) G protein  $G_{\alpha_{\text{Ib}}}$  functions immediately downstream of Smoothened in Hedgehog signalling. *Nature* 456, 967–970
- 47 Nishiyama, M. *et al.* (2003) Cyclic AMP/GMP-dependent modulation of  $\text{Ca}^{2+}$  channels sets the polarity of nerve growth-cone turning. *Nature* 423, 990–995
- 48 Terman, J.R. and Kolodkin, A.L. (2004) Nerve links protein kinase A to plexin-mediated semaphorin repulsion. *Science* 303, 1204–1207
- 49 Matise, M.P. *et al.* (1999) Ventral midline cells are required for the local control of commissural axon guidance in the mouse spinal cord. *Development* 126, 3649–3659
- 50 Carragher, N.O. and Frame, M.C. (2002) Calpain: a role in cell transformation and migration. *Int. J. Biochem. Cell Biol.* 34, 1539–1543
- 51 Stoeckli, E.T. and Landmesser, L.T. (1995) Axonin-1, Nr-CAM, and Ng-CAM play different roles in the *in vivo* guidance of chick commissural neurons. *Neuron* 14, 1165–1179
- 52 Stoeckli, E.T. *et al.* (1997) Interference with Axonin-1 and Nr-CAM interactions unmasks a floor-plate activity inhibitory for commissural axons. *Neuron* 18, 209–221
- 53 Niquille, M. *et al.* (2009) Transient neuronal populations are required to guide callosal axons: a role for semaphorin 3C. *PLoS Biol.* 7, e1000230
- 54 Goll, D.E. *et al.* (2003) The calpain system. *Physiol. Rev.* 83, 731–801
- 55 Sheppard, A. *et al.* (1991) Proteolytic modification of neural cell adhesion molecule (NCAM) by the intracellular proteinase calpain. *Biochim. Biophys. Acta* 1076, 156–160
- 56 Chan, K.T. *et al.* (2010) Regulation of adhesion dynamics by calpain-mediated proteolysis of focal adhesion kinase (FAK). *J. Biol. Chem.* 285, 11418–11426
- 57 Pasterkamp, R.J. and Giger, R.J. (2009) Semaphorin function in neural plasticity and disease. *Curr. Opin. Neurobiol.* 19, 263–274
- 58 Augsburg, A. *et al.* (1999) BMPs as mediators of roof plate repulsion of commissural neurons. *Neuron* 24, 127–141
- 59 Keino-Masu, K. *et al.* (1996) Deleted in Colorectal Cancer (DCC) encodes a netrin receptor. *Cell* 87, 175–185
- 60 Liu, G. *et al.* (2009) DSCAM functions as a netrin receptor in commissural axon pathfinding. *Proc. Natl. Acad. Sci. U. S. A.* 106, 2951–2956
- 61 Ly, A. *et al.* (2008) DSCAM is a netrin receptor that collaborates with DCC in mediating turning responses to netrin-1. *Cell* 133, 1241–1254
- 62 Okada, A. *et al.* (2006) Boe is a receptor for sonic hedgehog in the guidance of commissural axons. *Nature* 444, 369–373
- 63 Sabatier, C. *et al.* (2004) The divergent Robo family protein rig-1/Robo3 is a negative regulator of slit responsiveness required for midline crossing by commissural axons. *Cell* 117, 157–169
- 64 Kadison, S.R. *et al.* (2006) EphB receptors and ephrin-B3 regulate axon guidance at the ventral midline of the embryonic mouse spinal cord. *J. Neurosci.* 26, 8909–8914
- 65 Gore, B.B. *et al.* (2008) Stem cell factor functions as an outgrowth-promoting factor to enable axon exit from the midline intermediate target. *Neuron* 57, 501–510
- 66 Lyuksyutova, A.I. *et al.* (2003) Anterior–posterior guidance of commissural axons by Wnt–frizzled signaling. *Science* 302, 1984–1988
- 67 Uesugi, K. *et al.* (2009) Different requirement for Rnd GTPases of R-Ras GAP activity of Plexin-C1 and Plexin-D1. *J. Biol. Chem.* 284, 6743–6751
- 68 Castellani, V. *et al.* (2000) Analysis of the L1-deficient mouse phenotype reveals cross-talk between Sema3A and L1 signaling pathways in axonal guidance. *Neuron* 27, 237–249
- 69 de Castro, F. *et al.* (1999) Chemoattraction and chemorepulsion of olfactory bulb axons by different secreted semaphorins. *J. Neurosci.* 19, 4428–4436
- 70 Hernandez-Montiel, H.L. *et al.* (2008) Semaphorins 3A, 3C, and 3F in mesencephalic dopaminergic axon pathfinding. *J. Comp. Neurol.* 506, 387–397







---

# Chapter 3

## Structure of the Repulsive Guidance Molecule (RGM)–Neogenin Signaling Hub

---

Christian H. Bell<sup>1</sup>, Eleanor Healey<sup>1,\*</sup>, Susan van Erp<sup>2,\*</sup>, Benjamin Bishop<sup>1</sup>, Chenxiang Tang<sup>1</sup>, Robert J. C. Gilbert<sup>1</sup>, A. Radu Aricescu<sup>1</sup>, R. Jeroen Pasterkamp<sup>2</sup>, Christian Siebold<sup>1</sup>

<sup>1</sup> Division of Structural Biology, Wellcome Trust Centre for Human Genetics, University of Oxford, Roosevelt Drive, Oxford OX3 7BN, United Kingdom.

<sup>2</sup> Department of Neuroscience and Pharmacology, Rudolf Magnus Institute of Neuroscience, University Medical Center Utrecht, Utrecht 3584 CG, The Netherlands.

\* These authors contributed equally

*Science*, 2013; 341(6141): 77-80

# Structure of the Repulsive Guidance Molecule (RGM)–Neogenin Signaling Hub

Christian H. Bell,<sup>1\*</sup> Eleanor Healey,<sup>1,†</sup> Susan van Erp,<sup>2,†</sup> Benjamin Bishop,<sup>1</sup> Chenxiang Tang,<sup>1,‡</sup> Robert J.C. Gilbert,<sup>1</sup> A. Radu Aricescu,<sup>1</sup> R. Jeroen Pasterkamp,<sup>2</sup> Christian Siebold<sup>1,§</sup>

Repulsive guidance molecule family members (RGMs) control fundamental and diverse cellular processes, including motility and adhesion, immune cell regulation, and systemic iron metabolism. However, it is not known how RGMs initiate signaling through their common cell-surface receptor, neogenin (NEO1). Here, we present crystal structures of the NEO1 RGM-binding region and its complex with human RGMB (also called dragon). The RGMB structure reveals a previously unknown protein fold and a functionally important autocatalytic cleavage mechanism and provides a framework to explain numerous disease-linked mutations in RGMs. In the complex, two RGMB ectodomains conformationally stabilize the juxtamembrane regions of two NEO1 receptors in a pH-dependent manner. We demonstrate that all RGM-NEO1 complexes share this architecture, which therefore represents the core of multiple signaling pathways.

The repulsive guidance molecule (RGM) family has three major, membrane-attached members: RGMA, RGMB (dragon), and RGMC (hemouvelin, HFE2). Their functions span biological phenomena ranging from cell

motility and adhesion (e.g., axon guidance, neural tube closure, and leucocyte chemotaxis) to immune cell regulation and systemic iron metabolism (1–5). Abnormal RGM expression or function has been linked to regenerative failure;

inflammation (3); and diseases such as multiple sclerosis (6), cancer (7), and juvenile hemochromatosis (JHH) (5). All RGMs bind directly to the cell surface receptor neogenin (NEO1) (8), triggering structural rearrangements of the actin cytoskeleton through the Rho family of small guanosine-5'-triphosphate (GTP)-hydrolyzing GTPases that mediate cell repulsion (1, 9, 10). RGM binding to NEO1 activates the bone morphogenetic protein (BMP)-regulated signaling involved in morphogenesis and iron homeostasis (11–14).

Human RGMs contain an Arg-Gly-Asp (RGD) motif (conserved in RGMA and RGMC), which is important for integrin-mediated adhesive function (15), and a region homologous to the von

<sup>1</sup>Division of Structural Biology, Wellcome Trust Centre for Human Genetics, University of Oxford, Roosevelt Drive, Oxford OX3 7BN, UK. <sup>2</sup>Department of Neuroscience and Pharmacology, Rudolf Magnus Institute of Neuroscience, University Medical Center Utrecht, CG Utrecht 3584, Netherlands.

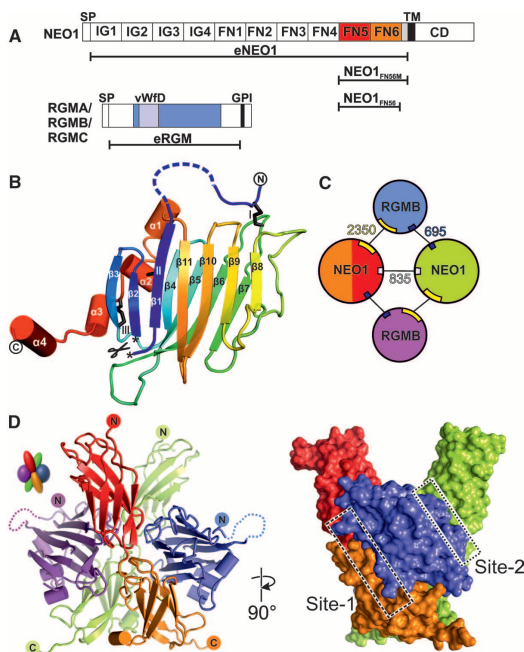
\*Present address: Roche Diagnostics GmbH, Nonnenfeld 2, 82377 Penzberg, Germany.

†These authors contributed equally to this work.

‡Present address: Molecular Biophysics and Biochemistry Department, Yale University, 260 Whitney Avenue, New Haven, CT 06520-8114, USA.

§Corresponding author. E-mail: christian@strubi.ox.ac.uk

**Fig. 1. Structure of the RGMB-NEO1 complex.** (A) Schematic of NEO1 and RGMs. SP indicates signal peptide; IG, Ig-like C2-type 1; TM, transmembrane; CD, C-terminal domain; GPI, glycosylphosphatidylinositol anchor; and vWFD, von Willebrand factor D domain-like. (B) eRGM ribbon diagram in rainbow coloring (blue, N terminus, red, C terminus). Disulfides (black sticks) are depicted with roman numerals. The autocatalytic cleavage site is marked with asterisks. (C) Schematics of the 2:2 RGMB-NEO1 complex. RGMB is blue and violet; NEO1 is red (FN5), orange (FN6), and green. Interface-buried surface areas ( $\text{\AA}^2$ ) are shown. (D) Ribbon (left) and surface representation of the 2:2 eRGM-NEO1<sub>FN56</sub> complex. Site-1 and site-2 interfaces are highlighted with boxes. Color coding is as in (C). Right image is 90° rotated around the y axis compared with the left representation.





## REPORTS

Willebrand factor type D (vWfD) domain, which contains an autocatalytic Gly-Asp-Pro-His cleavage site (1, 16) (Fig. 1A). NEO1 is a type-I transmembrane protein of the immunoglobulin (Ig) receptor superfamily related to the netrin-1 receptor DCC (deleted in colorectal cancer) (17, 18). Its extracellular region consists of four Ig domains followed by six fibronectin type III (FN) domains and 50 juxtamembrane residues that are predicted to be unstructured. The cytoplasmic region comprises three conserved motifs (P1, P2, and P3) containing several phosphorylation sites and is required for receptor oligomerization of DCC (18, 19). FN domains five and six contain the binding site for RGMs (20). However, the molecular mechanisms underlying extracellular RGM reception by NEO1 and the mode of signal transduction across the membrane are not known.

We solved a series of crystal structures of the fifth and sixth FN domains of NEO1 (NEO1<sub>FN56</sub>) in complex with the ectodomain of RGMb (eRGMb) (Fig. 1A, fig. S1, and table S1). In all of the NEO1-RGMb complexes, only the middle domain of RGMb (residues 134 to 338) could be resolved unequivocally. This domain represents a previously unknown protein fold consisting of a tightly packed  $\beta$  sandwich (Fig. 1B and fig. S2) extended by four short helices at the C terminus. The N and C termini, linked to the  $\beta$  sandwich by three disulfide bonds (fig. S3), point in opposite directions and into the solvent channels of the crystal, suggesting that the N- and C-terminal regions, which were disordered in the crystal, are flexible and do not associate with the middle domain. The autocatalytic cleavage site between Asp<sup>168</sup>-Pro<sup>169</sup> is located in the loop connecting  $\beta$  sheets 1 and 2 (Fig. 1B and figs. S3A and S4) and is conserved in all RGM family members (fig. S3A). Asp-Pro bonds are hydrolyzed in low pH environments, for example, in the Golgi and secretory vesicles (21). This autocatalytic cleavage allows Pro<sup>169</sup> to be deeply buried in the protein core (fig. S4A). Seven out of the 14 RGM disease mutations leading to JHH (5, 22, 23), a severe iron-overload condition, cluster at the cleavage site (fig. S5). Ten of these map onto the  $\beta$  sandwich (fig. S5A) and abolish protein secretion in mammalian cells (fig. S5B). These include Asp to Glu at position 172 (Asp172Glu<sup>RGMb</sup>) from the cleavage site itself (figs. S4 and S5), highlighting the importance of autocatalytic cleavage for the structural integrity of the middle domain and indeed the entire protein.

The eRGMb-NEO1<sub>FN56</sub> complex structure determined at neutral pH [(24), fig. S6, and table S1] has a 2:2 stoichiometry and exhibits twofold symmetry with both NEO1 C-termini oriented in the same direction (Fig. 1, C and D), as observed in two independent crystal forms (fig. S6). Each RGMb molecule acts as a staple, bringing two NEO1 receptors together with one major interaction site (site 1) and a minor site (site 2) (Fig. 1, C and D), positioning the NEO1 C-termini in close proximity to each other (Fig. 1C). Whereas

the two NEO1 molecules in the complex contact each other, the two RGMb molecules do not. Most of the site-1 contacts are formed between RGMb and the FN6 domain of NEO1, with the remainder of the interface made by the L3 loop of NEO1-FN5 (Fig. 2, A to C). The JHH-linked RGMb mutation Gly320Val<sup>RGMb</sup>, which cannot interact with NEO1 anymore (25), is located close to the site-1 interface (fig. S5D), thereby confirming the importance of the RGMb-NEO1 site-1 interface. We also solved three independent crystal structures of NEO1<sub>FN56</sub> alone (table S1). Together with a previously reported NEO1 structure (26), these reveal flexibility or disorder of the L3 loop as well as variation in the relative orientation of the FN5 and FN6 domains, in contrast to the rigidity of the NEO1 molecules in the RGMb complex structures (fig. S7). The site-2 interaction between RGMb and the neighboring NEO1 molecule (Fig. 2D and fig. S8) has a buried surface area one-fourth the size of site 1 (Fig. 1C). Therefore, the site-1 interaction is likely to be the driving force for the RGM-NEO1 complex formation, whereas site 2 has a supporting role because of its shallow geometry and predominantly hydrophobic nature.

Surface plasmon resonance (SPR) measurements revealed nanomolar equilibrium dissociation constants between the full-length ectodomains of NEO1 (eNEO1) and RGMa, RGMb, and RGMc, respectively (Fig. 3A and fig. S8). Furthermore, the truncated NEO1<sub>FN56</sub> and NEO1<sub>FN56M</sub> constructs (Fig. 1A) were necessary and sufficient for the RGM interaction [Fig. 3B, fig. S9, and (20)]. Site-directed mutagenesis of site-1 interface residues abolished or severely impaired the NEO1-RGM interaction, validating the observed binding mode (Fig. 3C and figs. S9 and S10). Mutations in the L3 loop of NEO1-FN5 and the corresponding RGMb surface did not abolish binding, consistent with NEO1-FN5 being important but not essential for interaction with RGMs. Unlike the majority of site-1 residues, the L3 loop residues are not conserved between NEO1 and DCC, possibly explaining why no binding between RGMs and DCC was observed in immunoprecipitation experiments (8, 25). Indeed, the interaction between RGMa, RGMb, or RGMc and the full-length DCC ectodomain was one-thousandth that observed for the equivalent NEO1 construct (fig. S11).

To test whether the RGMb-NEO1 complex observed in the crystal structures exists in

**Fig. 2. Detailed interactions of the RGMb-NEO1 complex.** Color coding is as Fig. 1D. (A) Ribbon representation of the RGMb-NEO1 site-1 complex. The L3 loop of NEO1 is marked. (B and C) Open-book view showing the solvent-accessible surface of the site-1 interface (formed by 17 hydrogen bonds and 147 nonbonded contacts). (B) Interface residues (I, Ile; L, Leu; Q, Gln; T, Thr). Cyan, hydrophilic interactions; yellow, nonbonded contacts. Residues tested by site-directed mutagenesis and functional experiments are labeled. (C) Residue conservation (from nonconserved, white, to conserved, black) based on sequence alignments from vertebrate NEO1 and RGM family members. (D) Ribbon representation of the RGMb-NEO1 site-2 complex. The site-2 interaction uses the RGMb  $\beta$ 5- $\beta$ 6 and  $\beta$ 10- $\beta$ 11 loop regions contacting the NEO1 FN5 and FN6 domains. K, Lys; V, Val.

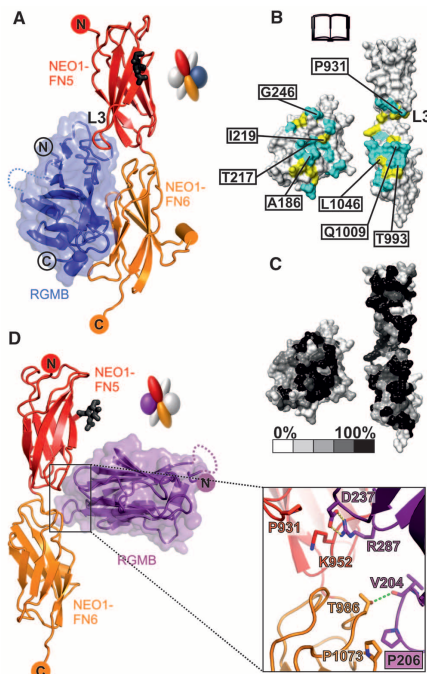
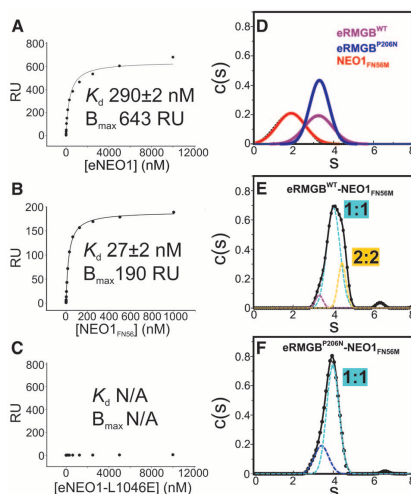


**Fig. 3. Biophysical characterization of the RGMB-NEO1 complex.** (A to C) SPR equilibrium binding. Different concentrations of eNEO1 (A), NEO1<sup>FNS56</sup> (B), and eNEO1-L1046E (where E is Glu) (C) were injected over surfaces coupled with eRGMB. RU, response units;  $K_d$ , dissociation constant;  $B_{max}$ , maximum binding capacity; and N/A, not applicable. (D to F) Sedimentation velocity AUC experiments of eRGMB-WT [(D) violet], eRGMB-P206N [(D) blue], NEO1<sup>FNS56M</sup> [(D) red], eRGMB-NEO1 (E), and eRGMB-P206N-NEO1 (F) complexes. Data fitted by using a continuous  $c(s)$  function (where  $s$  is the sedimentation coefficient) distribution model (solid line). Gaussian peaks contributing to the overall distributions (dotted lines) for eRGMB-NEO1 (E), root mean square deviation (RMSD) = 0.0038) and eRGMB-P206N-NEO1 (F, RMSD = 0.0063) complexes. Individual components run as monomeric species. The eRGMB-NEO1<sup>FNS56M</sup> complex shows two major species, indicating both 1:1 and 2:2 complexes. The eRGMB-P206N mutation introduces an N-linked glycan at the site-2 interface. The resulting eRGMB-P206N-NEO1 complex shows a single species corresponding to the 1:1 complex.



solution, we performed multiangle light scattering (MALS) measurements of purified proteins. At concentrations up to 3  $\mu$ M, we observed a 1:1 RGMB-NEO1 complex (fig. S12A). Sedimentation velocity analytical ultracentrifugation (AUC), allowing exploration of higher concentrations of eRGMB and NEO1<sup>FNS56M</sup> (up to 90  $\mu$ M), revealed that the individual components were monomeric (Fig. 3D), and the RGMB-NEO1 mixture showed both a major species, corresponding to the 1:1 stoichiometry, and a higher-order oligomer, likely the 2:2 complex (Fig. 3E). A mutation of RGMB-Pro<sup>206</sup> to asparagine in the site-2 interface (Fig. 2D), introducing an N-linked glycan, abolished the larger oligomer (Fig. 3F). The same AUC experiment performed with wild-type proteins at pH = 4.5 revealed only the 1:1 complex (fig. S12, B and C), suggesting that the site-2 interface is pH sensitive. This is in agreement with our structural data, because in a crystal form grown at pH = 4.5 to 5.0 (fig. S6C) the site-2 interface is absent, whereas site-1 is essentially identical to the neutral pH crystal form (fig. S7).

To explore the physiological relevance of the 2:2 oligomeric arrangement, we assessed the effect of RGMB mutants in neuronal explant cultures. Binding of RGMs to NEO1 inhibits neurite outgrowth from cerebellar granule neurons (CGNs) (27). To assess the functional consequences of site-1 and site-2 RGMB mutants, we cultured postnatal mouse CGN explants on substrates of control, RGMB-A186R (site-1 mutant with Ala changed to Arg at position 186), RGMB-P206N (site-2 mutant with Pro changed to Asn at position 206), and RGMB-WT (wild-type) proteins. As previously shown, neurite outgrowth was reduced on coverslips coated with RGMB-WT compared with control substrate (Fig. 4, A and B, and fig. S13). This inhibitory effect was not observed in neurons grown on RGMB-A186R and was reduced but not abolished by RGMB-P206N (Fig. 4 and fig. S13). These results support a functional role for RGMB-NEO1 interactions mediated through site-1 and to a lesser extent through site-2.

To investigate the RGM-NEO1 complex stoichiometry within a cellular context, we coexpressed full-length NEO1 tagged with either a His<sup>6</sup> or ID4 tag in human embryonic kidney 293T cells. We found that a specific antibody against NEO1-ID4 was able to coimmunoprecipitate NEO1-His<sup>6</sup>, indicating the presence of high-affinity NEO1 oligomers in the cellular lysate (fig. S14). This result suggests that NEO1 molecules may also be present in an RGM-independent, preclustered form at the cell surface.

The 2:2 stoichiometry of the RGM-NEO1 ectodomains may facilitate a common mechanism based on ligand-dependent receptor stabilization of NEO1 dimers within supramolecular signaling clusters (Fig. 4, C and D). Activation of the small GTPase RhoA and its downstream effectors Rho kinase and protein kinase C is a direct consequence of RGM-NEO1 interaction (9, 28). NEO1 can also interact with netrin-1 (NET1) (8), which

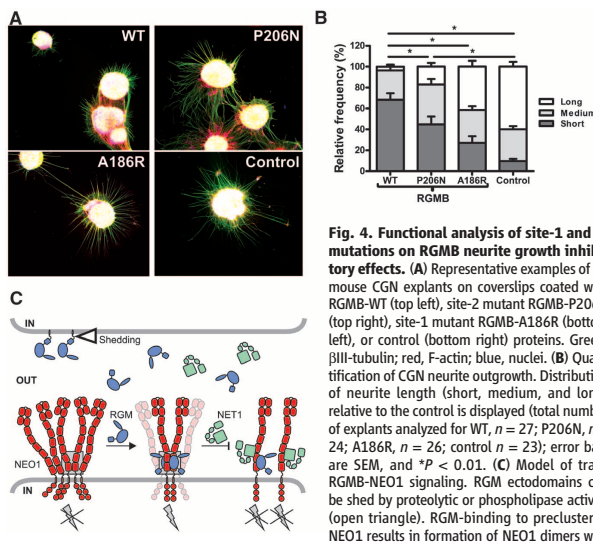


**Fig. 4. Functional analysis of site-1 and -2 mutations on RGMB neurite growth inhibitory effects.** (A) Representative examples of P9 mouse CGN explants on coverslips coated with RGMB-WT (top left), site-2 mutant RGMB-P206N (top right), site-1 mutant RGMB-A186R (bottom left), or control (bottom right) proteins. Green,  $\beta$ III-tubulin; red, F-actin; blue, nuclei. (B) Quantification of CGN neurite outgrowth. Distribution of neurite length (short, medium, and long) relative to the control is displayed (total number of explants analyzed for WT,  $n = 27$ ; P206N,  $n = 24$ ; A186R,  $n = 26$ ; control  $n = 23$ ); error bars are SEM, and  $*P < 0.01$ . (C) Model of trans RGM-NEO1 signaling. RGM ectodomains can be shed by proteolytic or phospholipase activity (open triangle). RGM-binding to preclustered NEO1 results in formation of NEO1 dimers with a defined, signaling-compatible orientation that may be part of a supramolecular clustered state. This arrangement leads to activation of downstream signaling via RhoA ( $\rho$ ) (gray lightning bolt). NET1 can inhibit RGM signaling by either simultaneous NEO1 binding or competing with the RGM-NEO1 interaction. The gray box highlights the RGM-NEO1 signaling hub observed in the crystal structure.

a defined, signaling-compatible orientation that may be part of a supramolecular clustered state. This arrangement leads to activation of downstream signaling via RhoA ( $\rho$ ) (gray lightning bolt). NET1 can inhibit RGM signaling by either simultaneous NEO1 binding or competing with the RGM-NEO1 interaction. The gray box highlights the RGM-NEO1 signaling hub observed in the crystal structure.

## REPORTS

functionally competes with RGMA, suppressing growth cone collapse in dorsal root ganglion axons (9). The NET1 binding site on the NEO1-related receptor DCC minimally involves the interface between its FN domains 4 and 5, including loop 5 of FN5 (29) occupied by a sucrose octasulphate (SOS) molecule in our apo-NEO1 structure (fig. S7B). This region, which borders the RGM interaction interface, is strictly conserved in NEO1 and DCC (fig. S3B), so NET1 might occupy the same position in NEO1, impairing the formation of an active 2:2 RGM-NEO1 complex and thus explaining the ability of NET1 to reduce RGM-induced growth cone collapse (Fig. 4C). An additional level of signaling control may be related to the subcellular localization of the RGM-NEO1 complex. The neutral pH at the cell surface allows an active 2:2 stoichiometry, whereas internalization and gradual acidification of the milieu promotes dissociation of the complex and signal termination. Such a signaling mechanism might prevent premature activation and allow dissociation upon internalization when RGM, NEO1, and associated proteins are expressed on the same cell.

Although diversity in the signaling triggered at downstream levels in a cell- and tissue-specific manner can be expected, our experimental evidence coupled with sequence conservation suggests that all RGM family members engage NEO1 in a similar way. Molecular details of the direct cross-talk between different receptors in signaling “supercomplexes,” such as RGM-NEO1-BMP ligand-BMP receptors (12–14), remain to be determined. However, we predict that the RGM-stapled NEO1 dimer provides a mode of pH-

dependent organization, which forms the signaling hub common to multiple extracellular guidance cues and morphogens.

## References and Notes

1. P. P. Mommier et al., *Nature* **419**, 392–395 (2002).
2. V. Niederhoffer, R. Salte, M. Signist, S. Arber, *J. Neurosci.* **24**, 806–818 (2004).
3. V. Mitrakaj et al., *Proc. Natl. Acad. Sci. U.S.A.* **108**, 6555–6560 (2011).
4. Y. Xia et al., *J. Immunol.* **186**, 1369–1376 (2011).
5. G. Papanikolaou et al., *Nat. Genet.* **36**, 77–82 (2004).
6. R. Muramatsu et al., *Nat. Med.* **17**, 488–494 (2011).
7. V. S. Li et al., *Gastroenterology* **137**, 176–187 (2009).
8. S. Rajagopalan et al., *Nat. Cell Biol.* **6**, 756–762 (2004).
9. S. Conrad, H. Genth, F. Hofmann, I. Just, T. Skutella, *J. Biol. Chem.* **282**, 16423–16433 (2007).
10. K. Hata et al., *J. Cell Biol.* **173**, 47–58 (2006).
11. J. L. Babitt et al., *Nat. Genet.* **38**, 531–539 (2006).
12. Z. Zhou et al., *Dev. Cell* **19**, 90–102 (2010).
13. D. H. Lee et al., *Blood* **115**, 3136–3145 (2010).
14. A. S. Zhang et al., *J. Biol. Chem.* **282**, 12547–12556 (2007).
15. J. P. Xiong et al., *Science* **296**, 151–155 (2002); 10.1126/science.1069040.
16. M. E. Lidell, M. E. Johansson, G. C. Hansson, *J. Biol. Chem.* **278**, 13944–13951 (2003).
17. N. H. Wilson, B. Key, *Int. J. Biochem. Cell Biol.* **39**, 874–878 (2007).
18. K. Lai Wing Sun, J. P. Correia, T. E. Kennedy, *Development* **138**, 2153–2169 (2011).
19. E. Stein, Y. Zou, M. Poo, M. Tessier-Lavigne, *Science* **291**, 1976–1982 (2001).
20. F. Yang, A. P. West Jr., G. P. Allendorph, S. Choe, P. J. Bjorkman, *Biochemistry* **47**, 4237–4245 (2008).
21. X. Landon, *Methods Enzymol.* **47**, 145–149 (1977).
22. C. Lanzara et al., *Blood* **103**, 4317–4321 (2004).
23. P. L. Lee, E. Beutler, S. V. Rao, J. C. Barton, *Blood* **103**, 4669–4671 (2004).
24. Materials and methods are available as supplementary materials on Science Online.
25. A. S. Zhang, A. P. West Jr., A. E. Wyman, P. J. Bjorkman, C. A. Enns, *J. Biol. Chem.* **280**, 33885–33894 (2005).
26. F. Yang, A. P. West Jr., P. J. Bjorkman, *J. Struct. Biol.* **174**, 239–244 (2011).
27. X. Liu et al., *Biochem. Biophys. Res. Commun.* **382**, 795–800 (2009).
28. K. Hata, K. Kailuchi, S. Inagaki, T. Yamashita, *J. Cell Biol.* **184**, 737–750 (2009).
29. B. V. Gettschreht, K. A. Dowd, R. W. Barfield, P. A. Longo, D. J. Leahy, *J. Biol. Chem.* **278**, 32561–32568 (2003).

**Acknowledgments:** We thank Diamond and European Synchrotron Radiation Facility beamline staff for assistance; T. Walter, K. Harlos, and G. Sutton for technical support; and M. Zebisch, E. Y. Jones, and D. I. Stuart for discussions. Work was funded by the Wellcome Trust (C.S.) and Human Frontier Science Program and the Netherlands Organization for Health Research and Development (R.J.P.). The Division of Structural Biology is supported by a Wellcome Trust Core Grant. R.J.C.G. was a Royal Society University Research Fellow. A.R.A. was a Medical Research Council Career Development Award Fellow. C.S. is a Cancer Research UK Senior Research Fellow. Structure coordinates of eRGM-NEO1<sub>FN56</sub>-Form 1, eRGM-NEO1<sub>FN56</sub>-Form 2, eRGM-NEO1<sub>FN56</sub>-Form 3, NEO1<sub>FN56</sub>-Form 1, NEO1<sub>FN56</sub>-Form 2, and NEO1<sub>FN56</sub>-SOS are deposited in the Protein Data Bank (identification codes 4BQ6, 4BQ7, 4BQ8, 4BQ9, 4BQB, and 4BQC, respectively).

## Supplementary Materials

www.sciencemag.org/cgi/content/full/science.1232322/DC1  
Materials and Methods  
Figs. S1 to S14  
Table S1  
References (30–59)

2 November 2012; accepted 23 May 2013  
Published online 6 June 2013;  
10.1126/science.1232322

---

# Supplemental Information

## Materials and Methods

### Expression and purification of RGM, NEO1 and DCC constructs and complexes.

Constructs of the extracellular region of human RGMA (GenBank ID AL136826; eRGMA: 47-423), human RGMB (GenBank ID AK074887, eRGMB: 53-412), human RGMC (GenBank ID AY372521; eRGMC: 36-400), mouse NEO1 (GenBank ID Y09535; NEO1FN56M: 883-1134, NEO1FN56: 883-1083 and eNEO1: 37-1134) and human DCC (GenBank ID AC011155; eDCC: 26-1129), as well as a full-length transmembrane construct of mouse NEO1 (fNEO1: 37-1493), fused C-terminally with a hexa-histidine (His6) tag, a C-terminal BirA recognition sequence or a 1D4 epitope-tag that can bind selectively the Rho 1D4 antibody (30), were cloned into the pHLsec or pHL-Avitag3 vectors (31) and expressed by transient transfection in HEK-293T cells (using an automated procedure (32) in the presence of the class I -mannosidase inhibitor, kifunensine, as described in (33)). Five days posttransfection, the conditioned medium was dialysed (for 48 hours at 4°C) and the proteins were purified by immobilised metal-affinity chromatography using TALON beads (Clontech) and treated with endoglycosidase F1 (75 µg mg<sup>-1</sup> protein, 12 h, 21°C) to cleave glycosidic bonds of N-linked sugars resulting in only one N-acetyl-glucosamine moiety bound to the corresponding asparagine side chain. The proteins were concentrated and further purified by size-exclusion chromatography (Superdex 200 16/60 column, GE Healthcare) in buffer containing 10mM HEPES, pH 7.5, 150 mM NaCl. The eRGMB-NEO1 complexes were formed by mixing a molar ratio of 1:1. The mixture was incubated for 1 h at room temperature and purified by size-exclusion chromatography (Superdex 200 16/60 column, GE Healthcare) in buffer containing 10 mM HEPES, pH 7.5, 150 mM NaCl.

### Site directed mutagenesis.

Site-directed mutagenesis to test specificity of protein-protein interactions or to stabilise the ectodomain of human RGMC (eRGMCAA: R326A/R329A/R332A) was carried out following a two-step, overlap-extension PCR using Pyrobest Polymerase (Takara). PCR products were cloned into the pHLsec or pHL-Avitag3 vectors resulting in protein constructs with a C-terminal hexa-histidine or with a C-terminal BirA recognition sequence (31). Mutant proteins were secreted at similar levels to the respective wildtype RGM and NEO1 constructs (data not shown). The stringent quality control mechanisms specific to the mammalian cell secretory pathway is likely to ensure that secreted proteins are correctly folded (34).

## Crystallization and data collection.

Protein samples were concentrated in size exclusion chromatography buffer by ultrafiltration to appropriate concentrations for crystallization experiments (NEO1FN56: 10 mg/ml, eRGMBNEO1FN56: 7 mg/ml). Nanolitre crystallization trials using a Cartesian Technologies robot (100 nl protein solution plus 100 nl reservoir solution) were setup in 96-well Greiner plates, placed in a TAP (The Automation Partnership) Homebase storage vault maintained at 295 K and imaged via a Veeco visualization system (35). NEO1FN56 Form 1 crystals were grown out of a mother liquor containing 0.1 M Tris-HCl, pH 8.5, 0.2 M sodium acetate, 30% PEG4000, NEO1FN56 Form 2 crystals out of mother liquor containing 0.13 M potassium nitrate, 13% PEG3350, eRGMB-NEO1FN56 Form 1 crystals out of mother liquor containing 0.1 M Tris Propane, pH 8.5, 0.2 M potassium nitrate, 20% PEG3350, eRGMB-NEO1FN56 Form 2 crystals out of mother liquor containing 0.1 M Tris-HCl, pH 8.5, 0.2 M lithium sulphate, 25% PEG3350 and eRGMB-NEO1FN56 Form 3 crystals out of mother liquor containing 0.1 M sodium acetate, pH 4.6, 0.18 M potassium acetate, 18% PEG3350. For the NEO1FN56-sucrose octasulphate (SOS) complex NEO1FN56 was mixed with 3 mM SOS prior to crystallization and crystals were grown out of mother liquor containing 0.15 M potassium nitrate, 15% PEG3350. Diffraction data were collected at 100 K. Prior to flash-freezing, crystals were treated with the appropriate cryo protectant solutions (NEO1FN56 Form 1, NEO1FN56 Form 2 and eRGMBNEO1FN56 Form 1: 25% (v/v) glycerol in mother liquor; eRGMB-NEO1FN56 Form 2, eRGMB-NEO1FN56 Form 3 and NEO1FN56-SOS: 28% (v/v) ethylene glycol in mother liquor). Data were collected at beamline I03 (eRGMB-NEO1FN56 Form 1, 2 and 3 and NEO1FN56 Form 2) at the Diamond Light Source, UK (equipped with a Pilatus 6M-F detector) and at beamline ID14-EH4 (NEO1FN56-SOS and NEO1FN56 Form 1) at the European Synchrotron Radiation Facility (ESRF), France (equipped with an ADSC Q315r detector). X-ray data were processed and scaled with the HKL suite (36) and XIA2 (37). Data collection statistics are shown in table S1.

## Structure determination and refinement.

The eRGMB-NEO1FN56 Form 3 complex was solved by molecular replacement in PHASER (38) using the structure of the fifth and sixth FNIII domain of human NEO1 (PDB ID: 3P4L (39)) as search model. Additional electron density for RGMB was immediately discernible. After density modification with PARROT as implemented in CCP4i (40) (figS1 A, B), the RGMB polypeptide chain was traced using Buccaneer(40). Iterative rounds of refinement in autoBUSTER (41), PHENIX(42), chain tracing in BUCCANEER (40) and manual building in COOT (43) resulted in a well-defined model for human RGMB that included residues 134-338 (Fig. 1B). The RGMB N- and C-terminal regions and the loop region between residues 143 and 157 could not be traced due to missing electron density and



---

were thus not included in the final model. All other structures were solved by molecular replacement in PHASER using the refined RGMB and NEO1 chains of the eRGMB-NEO1FN56 Form 3 complex. The models were refined using programs autoBUSTER (41) and PHENIX (42) and, where applicable, non-crystallographic symmetry restraints were used. As the test sets for all structures were chosen randomly the presence of non-crystallographic symmetry may artificially lower the value of R<sub>free</sub> by a small amount but will not render the metric invalid (44). The low resolution eRGMB-NEO1FN56 Form 2 complex structure was refined in PHENIX (42) only applying rigid body and TLS refinement. The resulting electron density maps are of reasonable quality and clearly show features, which are not present in the model used for molecular replacement (fig. S1D-F). Crystallographic and Ramachandran statistics are given in table S1. Stereochemical properties were assessed by MOLPROBITY (45). Superpositions were calculated using the program SHP (46) and COOT (43) and electrostatic potentials were generated using APBS (47). Buried surface areas of protein-protein interactions were calculated using the PISA webserver (48) for a probe radius of 1.4 Å.

### **Multiangle light scattering (MALS).**

MALS experiments were carried out using a DAWN HELEOS II from Wyatt Technology (equipped with a K5 flow cell and a 30 mW linearly polarized GaAs laser with a wavelength of 690 nm). Proteins used for MALS contained wildtype sugars. Prior to the experiments, proteins were purified by size exclusion chromatography and concentrated to approximately 2 mg/ml. Data were analysed using ASTRA (Wyatt Technologies) and molecular weights were calculated using the Debye fit method.

### **Surface plasmon resonance (SPR) binding studies.**

SPR experiments were performed using a Biacore T100 machine (GE Healthcare) at 25 °C in SPR running buffer (10 mM HEPES, pH 7.4, 150mM NaCl, 0.05% (v/v) polysorbate 20). All experiments were carried out using orientated protein immobilization by coupling biotinylated proteins to streptavidin coated biosensor chips (49). Proteins for surface attachment were engineered with a Cterminal recognition sequence for the enzyme BirA, allowing enzymatic biotinylation of a lysine residue within this sequence. Biotinylation of the C-terminus of NEO1 and RGMs replaces the transmembrane helix or the GPI-anchor, respectively, recapitulating the native topology of both proteins. Tagged proteins were secreted from HEK-293T cells with equivalent efficiency to their untagged counterparts. Proteins used as analytes were prepared as described above and underwent gel filtration in running buffer immediately prior to use. Experiments with the wildtype proteins were performed in both orientations and with the



mutant proteins in one orientation. Protein concentrations were determined from the absorbance at 280 nm using calculated molar extinction coefficients. Typically the ligands were bound to the surface at concentrations of 150-3,000 response units. After each binding experiment the chip was regenerated by short bursts of 2 M Magnesium sulphate. All experiments were done in duplicates with independently purified proteins. In all experiments analyzed, the experimental trace returned to baseline after each injection and the data fitted to a simple 1:1 Langmuir model of binding.  $K_d$  values were obtained by nonlinear curve fitting of the Langmuir binding isotherm ( $\text{bound} = C \cdot \text{max} / (K_d + C)$ , where  $C$  is analyte concentration and  $\text{max}$  is the maximum analyte binding) using the Biacore Evaluation software (GE Healthcare).

### **Analytical ultracentrifugation.**

Sedimentation velocity (SV) experiments were performed using a Beckman Optima XL-I analytical centrifuge and a run temperature of 20 °C. After gel filtration protein samples were concentrated to the following concentrations for SV analysis: eRGMB-WT and eRGMB-P206N: 3 mg/mL, NEO1FN56M: 2 mg/mL and for the complexes, the proteins were mixed in a 1:1 ratio with a final concentration of 6 mg/mL. For the pHdependent experiments, runs were conducted at pH 7 and pH 4. The samples were held in 3 mm path length Epon sector-shaped 2-channel centrepieces and were spun at 40,000 rpm, with 50 sample distribution scans being taken increments of 6 minutes apart. Data were collected using 280 nm absorbance optics. Data were analysed using Sedfit (50, 51), available from <http://www.analyticalultracentrifugation.com>. The scans 6-50 were used in the continuous  $c(s)$  distribution analysis, they were performed with a floating frictional ratio and baseline,  $s_{\text{min}} = 0.5$ ,  $s_{\text{max}} = 10$ , and a resolution of 100. A value of 0.73 ml/g was used for the partial specific volumes. Graphs were plotted and Gaussian distributions fitted to the curves using the plotting program PROFIT (Uetikon am See, Switzerland).

### **Co-immunoprecipitation**

Transfection and co-transfection of full-length fNEO1-His6 and fNEO-1D4 plasmids were performed using previously described methods (31). About 40 hours post-transfection the media (250 ml) was removed. The cells were washed in 2 x 50 mL PBS and lysed in 5 mL Lysis Buffer (10 mM Tris-HCl (pH 8.0), 150 mM NaCl, 1.5% DDM and protease inhibitor cocktail (Sigma)) for 2 hours at 4 °C. The lysate was cleared by centrifugation (100000 xg, 2 hours) and diluted 1:50 in lysis buffer containing 0.03 % DDM. Complexes were recovered on 1D4-antibody (University British Colombia)-conjugated sepharose beads (Amersham) and washed three times with lysis buffer (0.03 % DDM). Bound protein complexes

---

were eluted from the beads by incubation (12 hours, 4 °C) with 500 μM 1D4 peptide (TETSQVAPA, GenScript). Samples were analysed by Western blotting with a mouse anti-His6 antibody probe.

### **Neurite growth assays.**

Cerebellar external granule layer (EGL) explants were grown on RGMB coated coverslips. First, coverslips were coated with poly-D-lysine (100 μg/ml), washed and air-dried. Purified RGMB-WT, RGMB-P206N, RGMB-A186R or Fc control protein was then added to the coverslip at 50 μg/ml mixed with laminin (40 μg/ml, Invitrogen) in Neurobasal medium (NB, Gibco) overnight at 4 °C. Routinely, a 10% adsorption of input protein to poly-D-lysine-coated coverslips was observed (52). Shortly before plating the explants, coverslips were washed once in NB and incubated at 37 °C with culture medium (NB with penicillin/streptomycin, l-glutamine, 18 mM Hepes and 1xB27). Explants were obtained from postnatal day (P)9 mouse pups. In brief, the cerebellum was removed and dissected in ice cold L15, and coronal slices were cut using a MCillwain tissue chopper. Slices were further dissected to isolate the EGL and equally sized tissue explants were cut and placed onto the coated coverslips. After 3 days *in vitro* (DIV), the explants were fixed with 4% PFA for 20 min at room temperature. For immunohistochemistry, coverslips were washed with PBS and incubated in blocking buffer (PBS with 5% normal goat serum, 1% BSA, 1% glycine, and 0.4% Triton-X100) for 1 hour at RT. Primary (mouse anti  $\beta$ tubulin, T8660 Sigma) and secondary (goat anti mouse Alexa-488, A11029 Molecular Probes) antibodies were diluted in blocking buffer and incubated overnight at 4 °C. Nuclei and F-actin were stained using DAPI (Invitrogen) and Phalloidin-TRITC (Sigma-Aldrich), respectively, diluted in PBS. Pictures were taken with a Zeiss Scope A1 microscope with a 10x objective (Zeiss) and an Axiocam Mrm camera (Zeiss). Neurite outgrowth from the explants was analysed using ImageJ. The distance between explant and the growth cones of > 20 individual, nonfasciculated neurites was measured (three separate experiments, total explants analyzed per condition: WT n=27, P206N n=24, A186R n=26, control n=23) (fig. S13) and neurite lengths were normalized to the average neurite length of control explants per experiment. Three bins (short, medium, long) containing an equal proportion of measurements ranging from shortest to longest were created to establish the distribution of neurite lengths per explant. The percentage of neurites in each bin was calculated for each explant to obtain the average distribution of neurite lengths per condition. A twoway ANOVA with Bonferroni post-test was used to compare the distributions of neurite length between the experimental conditions.

### **Illustrations.**

Figures were produced using the programs PYMOL ([www.pymol.org](http://www.pymol.org)), Adobe Photoshop (Adobe Systems) and Corel Draw (Corel Corporation).

## Supplemental Figures

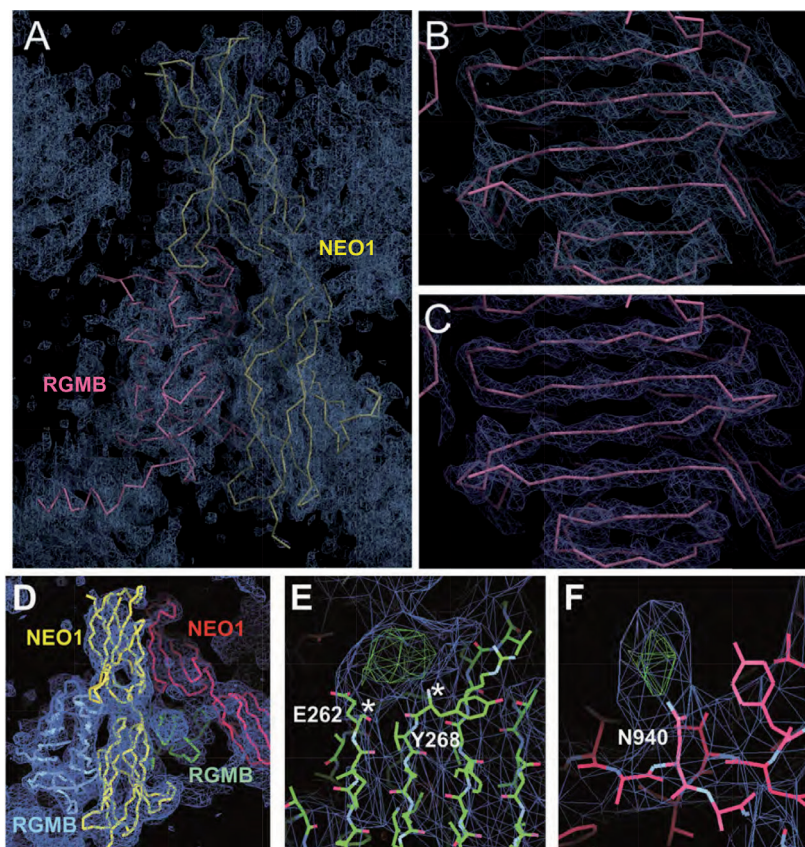


**Figure S1. Electron density of the RGMB-NEO1 complex.**

**A.** Initial electron density map of the low pH (Form 3) eRGMB-NEO1<sub>FN56</sub> complex contoured at 1.4 after molecular replacement in PHASER (38) (using the NEO1<sub>FN56</sub> structure (pdb 3P4L (39)) as search model) and density modification using PARROT (40). The additional electron density for the RGMB is clearly visible. The final model of the eRGMB-NEO1<sub>FN56</sub> complex is represented as ribbon with RGMB in pink and NEO1<sub>FN56</sub> in yellow. The orientation is similar to Fig. 2A. **B-C.** Detailed view onto one side of the RGMB  $\beta$ -sandwich. **B.** Initial electron density map as described in (A). **C.** SigmaA-weighted  $2Fo-Fc$  map of the final model from autoBUSTER (41) contoured at 1.4 $\sigma$ . **D-F.** SigmaA-weighted  $2Fo-Fc$  map (blue, 1.1  $\sigma$ ) and  $Fo-F\sigma$  map (green, +3.0  $\sigma$ ) from PHENIX (42) after rigid body and TLS refinement of the 6.6 Å neutral pH (Form 2) eRGMB-NEO1<sub>FN56</sub> complex. **D.** Overview of the eRGMB-NEO1<sub>FN56</sub> asymmetric unit. **E.** Close-up on the previously disordered RGMB loop between residues E262 and Y268. **F.** Close-up on the NEO1 N-linked glycosylation site at residue N940, which was excluded from the molecular replacement model. Additional features are clearly visible in the resulting electron density maps, e.g. the RGMB loop region spanning from residues 263-267 (E) as well as the NEO1 N-linked sugar moiety (F).

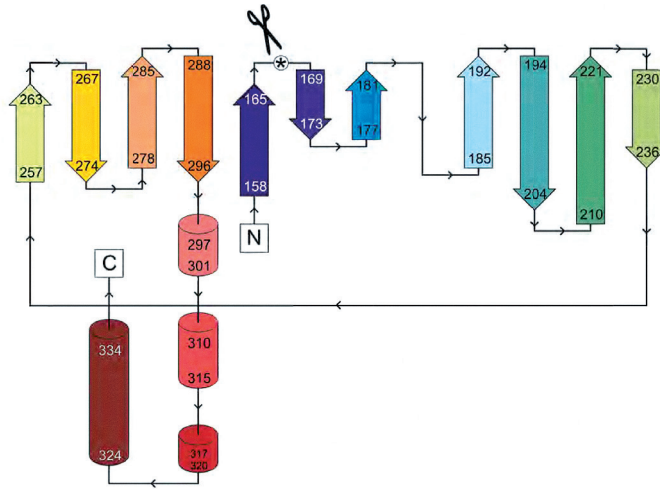


**Figure S2. Topology diagram of the RGM structure.**

Colouring is as in Fig 1B. The autocatalytic cleavage site is highlighted by an asterisk. The figure is adapted from PDBSUM (<http://www.ebi.ac.uk/pdbsum/>). RGMs comprise a novel protein fold consisting of a tightly packed  $\beta$ -sandwich with seven strands on one sheet and four strands on the other.



**A**

```

50      60      70      80      90      100     110
hRGMB ... QQPACROROKCTTDFVSLAH...LNSAVDGFDS...EFCAALRRYAGCORTSKACRGNLVYHSAVLGTS
mRGMB ... QQPACROROKCTTDFVSLAH...LNSAADGFDS...EFCAALRRYAGCORTSKACRGNLVYHSAVLGTS
cRGMB ... QQPACROROKCTTDFVSLAH...LNSALDGFDL...EFCAALRRYAGCORTSKACRGNLVYHSAVLGTS
xRGMB ... QQPACROROKCTTDFVSLAH...LNTGSDGFDS...EFCAALRRYAGCORTSKACRGNLVYHSAVLGTS
zRGMB ... QQPACROROKCTTDFVSLAH...LNPGLDGFDT...EFCAALRRYAGCORTSKACRGNLVYHSAVLGTS
hRGMA ... SPCKLHCNSEFWASARS...GSHAPASDDTP...EFCAALRRYALCRRRTARCCRDLLAYHSAVHGID
mRGMA ... SPCKLHCNSEFWASARS...GSHAPASDDVP...EFCAALRRYALCRRRTARCCRDLLAYHSAVHGID
cRGMA ... SPCKLHCNSEFWASARS...GSHALCAEETP...EFCAALRRYALCRRRTARCCRDLLAYHSAVHGID
xRGMA ... SCRLLKCRADYLAQTSN...PHHACPEDTV...EICALRRYALCRRRTARCCRDLLAYHSTVHGID
zRGMA ... SCRLLKHCNSEFWASARS...SSGPEE...EFCAALRRYALCRRRTARCCRDLLAYHSAVHGID
hRGMC ... CQKLCNAEYVSRPLS...LRGGGSGALRGGGGGRGGGVVSGGL...CALRRYSACRRRTARCCRDLLAYHSAVHGID
mRGMC ... CQKLCNAEYVSRPLS...LRGGGSDPTPRGGGRG...LASSGLS...CALRRYSACRRRTARCCRDLLAYHSAVHGID
cRGMC ... CQKLCNAEYVSRPLS...LRGGGSRNABIQK...LASSGLS...CALRRYSACRRRTARCCRDLLAYHSAVHGID
xRGMC ... CQKLCNAEYVSRPLS...LRGGGSRNABIQK...LASSGLS...CALRRYSACRRRTARCCRDLLAYHSAVHGID
zRGMC ... CQKLCNAEYVSRPLS...LRGGGSRNABIQK...LASSGLS...CALRRYSACRRRTARCCRDLLAYHSAVHGID

```

```

120     130     140     150     160     170
hRGMB D L M S Q R N C S K D G P T S S T N P F V ... T H P C M N H S H A G A R E H R G D Q N F P ... S T Y L C C I F G D P P H R F K D
mRGMB D L M S Q R N C S K D G P T S S T N P F V ... T H P C M N H S H G V R E H G G D R P P ... N Y L F C C I F G D P P H R F K D
cRGMB D L M S Q R N C S K D G P T S S T N P F V ... S H D C M N S G H T E A N E H O G G E K T P T ... T Y L F C C I F G D P P H R F K D
xRGMB D L M S Q R N C S K D G P T S S T N P F V ... T M O C M N H N R A T E R L L S G D Q T O P ... N Y L F C C I F G D P P H R F K D
zRGMB D L M S Q R N C S K D G P T S S T H P V I L ... F T C M N H S R H H H V S R G T V G E H P R L M Y L F C C I F G D P P H R F K D
hRGMA D L M S Q R N C S K D G P T S S T N P F V ... P R V T L P P A G S Q E R ... S D S P E L C H E K S F H K H S A P ... N Y L F C C I F G D P P H R F K D
mRGMA D L M V C H N C S K D G P T S S O P R L R T L P P G D S Q E R ... S D S P E L C H E K S F H K H S A P ... N Y L F C C I F G D P P H R F K D
cRGMA D L M S H N C S K D G P T S S P R I L P P G D S Q E R ... S D S P E L C H E K S F H K H S A P ... N Y L F C C I F G D P P H R F K D
xRGMA D L M S H N C S K D G P T S S P R I L P P G D S Q E R ... S D S P E L C H E K S F H K H S A P ... N Y L F C C I F G D P P H R F K D
zRGMA D L M S H N C S K D G P T S S P R I L P P G D S Q E R ... S D S P E L C H E K S F H K H S A P ... N Y L F C C I F G D P P H R F K D
hRGMC D L M I C H N C S R O G P T A P P P P G A L P G A G S G L P A ... P O R C D Y E G R F S R L H G R P P ... G F L H C C I F G D P P H R F H H
mRGMC D L M I C H N C S R O G P T A P P P A R G A L P G A G A P A L T ... P O R C D Y E G R F S R L H G R A P ... G F L H C C I F G D P P H R F H H
cRGMC D L M I C H N C S R O G P T A P P P A R G A L P G A G A P A L T ... P O R C D Y E G R F S R L H G R A P ... G F L H C C I F G D P P H R F H H
xRGMC D L L I L V R P K G A P P P P P L P Q A ... P L S ... C G E F E K G F I Q R E G A P ... P L H C C I F G D P P H R F N E
zRGMC D L L I L V R P K G A P P P P P L P Q A ... P L S ... C G E F E K G F I Q R E G A P ... P L H C C I F G D P P H R F N E

```

```

180     190     200     210     220     230     240     250     260
hRGMB N P Q C T C V I G A W P L D N N V L S V Q V T V P V P G S S A T A T K K T I F P R A H G C T D O K V Y A A T D D P A F A D G T G G G S D A S K S L R I
mRGMB H P Q T C V I G A W P L D N N V L S V Q V T V P V P G S S A T A T K K T I F P R A Q H C T D O K V Y A A T D D P A F A D G T G G G G N T K S L Q I
cRGMB H P Q T C V I G A W P L D N N V L S V Q V T V P V P G S S A T A T K K T I F P R E Y Q H C T D O K V Y A A T D D P A F A D G T G G G G N T K S L Q I
xRGMB H P Q T C V I G A W P L D N N V L S V Q V T V P V P G S S A T A T K K T I F P R E F Q D C T D O K V Y A A T D D P A F A D G T G G G S D S K S L R I
zRGMB Q P Q T C V I G A W P L D N N V L S V Q V T V P V P G S S A T A T K K T I F P R Y Q C T D O K V Y A A T D D P A F A D G T G G G S E T R S I W I
hRGMA R P Q T C V I G A W P L D N N V L S V Q V T V P V P G S S A T A T K K T I F P R F Q C T D O K V Y A A T D D P A F A D G T G G G K H G A N S L K I
mRGMA H P Q T C V I G A W P L D N N V L S V Q V T V P V P G S S A T A T K K T I F P R F Q C V I O K V Y A A T D D P A F A D G T G G G K H G A N S L K I
cRGMA T P Q T C V I G A W P L D N N V L S V Q V T V P V P G S S A T A T K K T I F P R E F Q C V I O K V Y A A T D D P A F A D G T G G G K H G A N S L K I
xRGMA T P Q T C V I G A W P L D N N V L S V Q V T V P V P G S S A T A T K K T I F P R F Q C V I O K V Y A A T D D P A F A D G T G G G K S G A N S L R I
zRGMA D P Q T C V I G A W P L D N N V L S V Q V T V P V P G S S A T A T K K T I F P R E F Q C V I O K V Y A A T D D P A F A D G T G G G H G A N T L R V I
hRGMC H P Q T C V I G A W P L D N N V L S V Q V T V P V P G S S A T A T K K T I F P R M Q C I D O K V Y A A T D D P A F A D G T G G G R P G S S L S T I
mRGMC Q P H T C V I G A W P L D N N V L S V Q V T V P V P G S S A T A T K K T I F P R M Q C I D O K V Y A A T D D P A F A D G T G G G R P G S S L S T I
cRGMC D P Q T C V I G A W P L D N N V L S V Q V T V P V P G S S A T A T K K T I F P R M Q C I D O K V Y A A T D D P A F A D G T G G G R A G G S M L K I
xRGMC E P Q C V I G A W P L D N N V L S V Q V T V P V P G S S A T A T K K T I F P R W R C A E O K V Y A A T D D P A F A D G T G G G R G H Q S L R I
zRGMC E P Q C V I G A W P L D N N V L S V Q V T V P V P G S S A T A T K K T I F P R W R C A E O K V Y A A T D D P A F A D G T G G G R G H Q S L R I

```

```

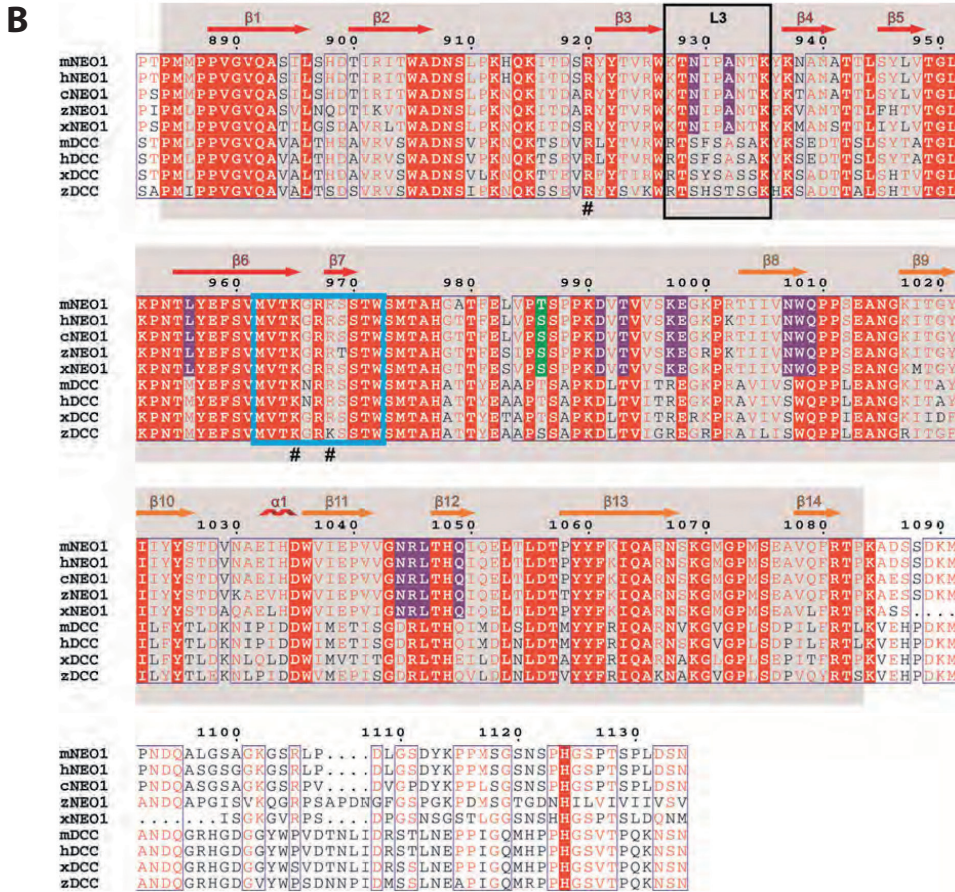
270     280     290     300     310     320     330
hRGMB V S R E S Q H V E H A R Y G T T V F V R Q V R Y L F L A I R M P E L M A Y E E ... S Q D L C L N C G C P S R I L D G G Q V S A I L G H S L P ...
mRGMB V S R E S Q R Y V E H A R Y G T T V F V R Q I G R Y L F L A I R M P E L M A Y E E ... S Q D L C L N C G C P S R I D G G Q V S A I L G H S L P ...
cRGMB V S R V S Q K Y V E H A R Y G T T V F V R O L G H Y L F L A I R M P E L M A Y E E ... S Q D L C L N C G C P S S R I D S G H L P L V R G O V L P ...
xRGMB I S R V G K H V E H A R Y G T T V R O L G N Y L F L A I R M P E L M A Y E E ... S Q D L C L N C G C P S R I E S G H L Q L P V T S S T H ...
hRGMA T S R V S Q H V E H A R Y G T T V I V R V G R Y L F F A V R M P E E V N A V E D W D S G G L V L C R G C P L N Q I F Q A F H T N A E G T G A R R L A A ...
mRGMA T S R V S Q H V E H A R Y G T T V I V R V G R Y L F F A V R M P E E V N A V E D R D S G G L V L C R G C P L N Q I F Q A F H A N E ... S P R P A A ...
cRGMA T S R V S Q H V E H A R Y G T T V I V R V G R Y L F F A V R M P E E V N A V E D R D S G G L V L C R G C P L N Q I F Q F R L A O A E G K A M K G P ...
zRGMA T S R V A Q H V E H A R Y G T T V I V R V G R Y L F F A V R M P E E V N A V E D K D G G L V L C H C C P N Q I F R F F H S O A P T G P L R L T S ...
hRGMC V S R V P Q H V E H A R Y G T T V I R V G H Y L F F A V R M P E E V N S V D Q D N Q D L V L C H C C P N Q I F R F F K A R A A E S H G V G R G R P ...
mRGMC Q P A N P G N H V E Q A A Y G T T I I R O T A G O L S F S I K V A E D V A M A F S A ... S Q D L C L C G C C P S R I L S ... R S E R N R R G A ...
cRGMA Q P A N P G S H V E R A A Y G T T I I R O T A G O L S F S I K V A E D V A R A F S A ... S Q D L C L C G C C P S R I L S ... R S E R N R R G A ...
xRGMC Y P R E P G S L I E R A A Y G T T I V R O L A K O L S F S L H M P E D I S L A F P S E ... S Q D L C L C G C C P A S F I S ... R T K D V G R T S S ...
zRGMC H S H D P G R H A B W A Y G T T I V R V G G S L S L V H S F R A L B S Y I P ... S Q D L C L C G C C P S R I L S ... R T K D V G R T S S ...

```

```

340     350     360     370     380     390     400     410
hRGMB ... R T S L V O A W P G Y T L E A T I C H E K M P V K D I Y F O S C F D L L T T O D A N F T A A H S L A D V E A D H P R K E R W H I F P S G N ...
mRGMB ... H T S V Q A W P G Y T L E A T I C H E K M P V K D I Y F O S C F D L L T T O D A N F T A A H S L A D V E A D H P R K E R W H I F P S C ...
cRGMB ... Q A G A A R P S A Y T L E A T I C H E K M L V K D I Y F O S C F D L L T T O D A N F T A A H S L A D V E A D H P R K E R W H I F P S G D ...
xRGMB ... D G S T V Q P A S I Y L T E A S A N K R E K L O V K H I Y F H S C F D L L T T O D A N F T A A P S A W E D M T L H P R K E R W O I F P K A C C ...
zRGMB ... Q Q P R V E A Q R G V F L T E A S A N K R D L E V K D I Y F H S C F D L L T T O D A N F T A A Y N A L K D V E T L H P R K E R W O I F P N ...
hRGMA ... A S P A P T A P E T F F Y E A V A K C R E K L P V E D I Y O A C F D L L T T O D V N F T L A A Y Y A L E G S M L H S N K D L H L V D T R D L P G R A ...
mRGMA ... A S P S P V P E T F F Y E A V A K C R E K L P V E D I Y O A C F D L L T T O D V N F T L A A Y Y A L E G S M L H S N K D L H L V D T R E L P G A V A A A A ...
cRGMA ... S L P A P ... P E A F Y E A T A K C R E K L P V E D I Y O S C F D L L T T O D V N F T L A A Y Y A F E V M L H S N K D L H L V D T R A L A P G N ...
xRGMA ... A S S A ... A S F P O A K C R E K L P V E D I Y O S C F D L L T T O D V N F T L A A Y F E V M L H S N K V H L E T T G L G P S N ...
zRGMA ... G N P S H ... G F T Y O S A M A K C R E R P V E D I Y O S C F D L L S S G I N F T L A A Y F E V M L H S N K N X H L E D T F P N ...
hRGMC ... N R R G A I T D A R L K C E G L P V E D A Y H E C F D V L S G D P N F T V A A Q A L E D A L P D L E L K H L P D ...
mRGMC ... N R R G A I T D A R L K C E G L P V E D A Y H E C F D V S Y S G D P N F T V A A Q T L D D A R I F L T D E L N L H P P D ...
cRGMC ... G R T S S I S T D A K M C R A K L P V E D A Y O S C F D V A I S G D A N M T N A Y Y A L E D A K D F L P E P G L H I F S G A A N ...
xRGMC ... G R T S S I S T D A K M C R A K L P V E D A Y O S C F D V O V T T D V N S S A S A V A L E D A R A M I S D P A R V H L V T G T G N ...
zRGMC ... L H A H P P D A Y H C S S L P G R D V Y P A C H F D V O V T T D V N S S A S A V A L E D A R A M I S D P A R V H L V T G T G N ...

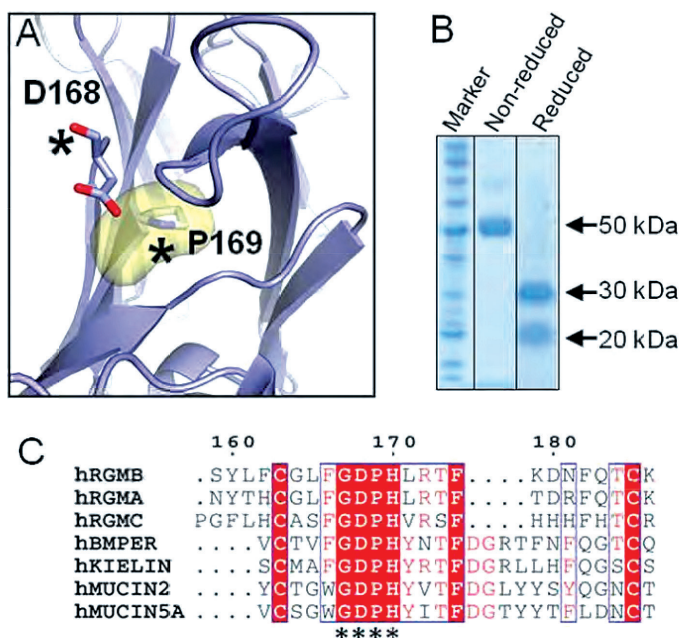
```



**Figure S3. Sequence alignments of the vertebrate RGM (A) and NEO1/DCC (B) family members.**

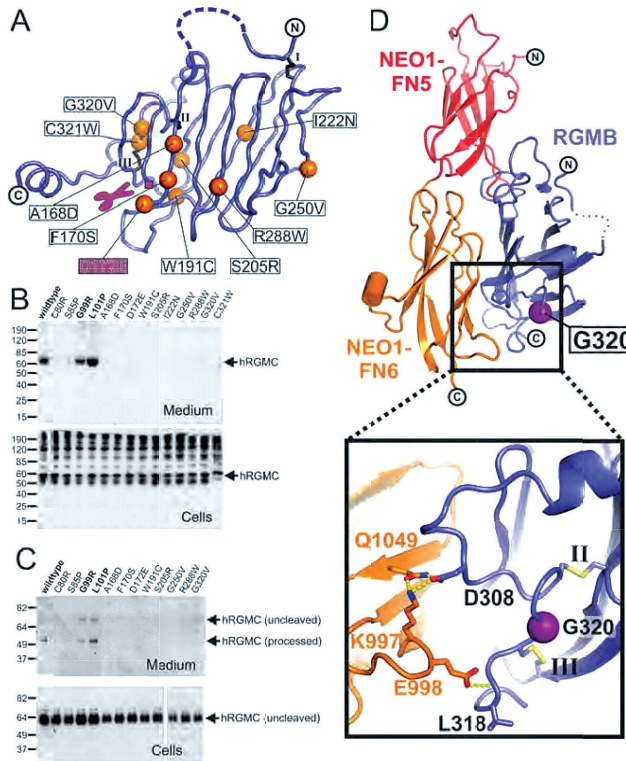
Sequences were aligned using MULTALIN ([bioinfo.genotoul.fr/multalin/multalin.html](http://bioinfo.genotoul.fr/multalin/multalin.html)) and formatted with ESPRIPT ([esprict.ibcp.fr/ESPrict/ESPrict/](http://esprict.ibcp.fr/ESPrict/ESPrict/)). Numbering corresponds to the full length human RGMb (A) and mouse NEO1 (B) (including the secretion signal). Secondary structure assignments are displayed above the alignment and colour-coded as in Fig. 1B (for RGMs) and Fig. 1D (for NEO1), respectively. Residues contributing hydrophilic interactions to the RGMb-NEO1 complex are highlighted in blue (site-1) and green (site-2). Residues forming the RGM autocatalytic cleavage site are shown in black. The potential furin cleavage site in RGMs is highlighted as yellow box. Disease-related residues identified in human RGMc are marked below the sequences with an asterisk (\*). Disulfide bridges are numbered in green. Hashtags mark the NEO1 residues interacting with SOS. The region of DCC identified to interact with glycosamino-glycans (53) and Netrin-1 (54) is boxed in light blue. The grey box in the background indicates the amino acid residues present in the structure. All residues involved in the NEO1-RGMb site-1 and site-2 interactions are conserved amongst RGMs, suggesting that the site-1 and site-2 interfaces reveal a common architecture for RGM-NEO1 interactions (see also Fig. 2C and Fig. S8C).





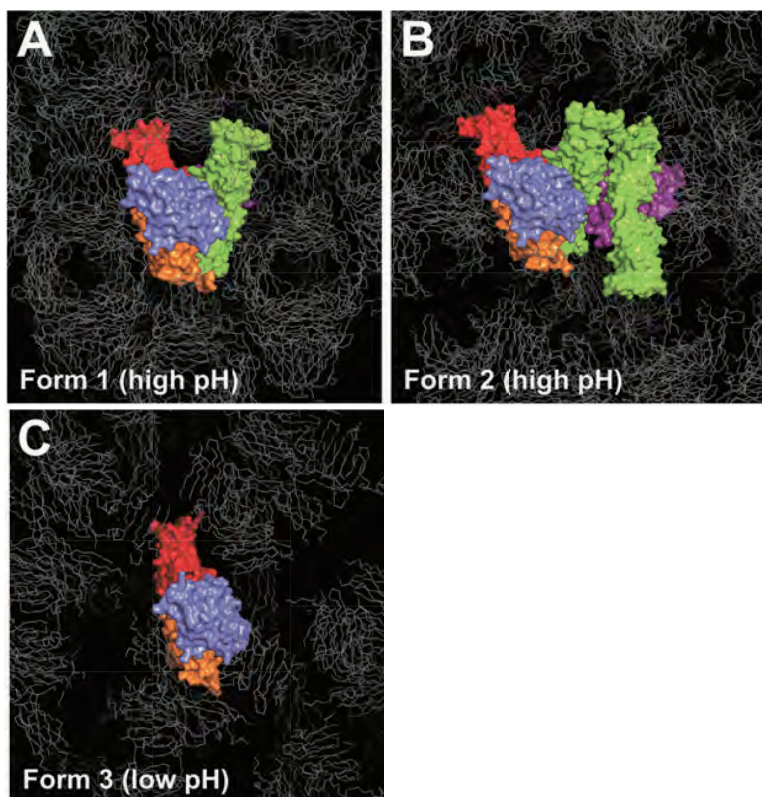
**Figure S4. The RGM autocatalytic cleavage site.**

**A.** Close-up view of the RGM autocatalytic cleavage site. Mechanistically, this involves intramolecular catalysis by aspartate carboxylate anion displacement of the protonated nitrogen of the peptide bond. Since the prolyl nitrogen has the strongest basicity of all amino acids, this enhances the peptide bond cleavage by increasing protonation of the leaving group which potentially occurs in lower pH environments (e.g. in the Golgi and secretory vesicles). The yellow sphere shows the solvent accessible surface of P169. **B.** SDS-PAGE of SEC-purified human RGMA. All transiently expressed and secreted RGMA and RGMB proteins from human HEK293T cells are ~100% processed. **C.** The RGM autocatalytic cleavage site ("GDPH") is conserved in various vWFD family members and has been functionally characterised in Mucins (55, 56) and BMPER (57). However, RGM family members are missing the characteristic Gly-Leu-Cys-Gly motif towards the C-terminus of the domain (29), which makes it difficult to predict if the other vWFD family members adopt a similar fold like RGMs. The sequence alignment was generated as in fig S3. Asterisks highlight the conserved autocleavage site residues. Human BMPER: Uniprot Q8N8U9, human Kielin: UniProt Q6ZWJ8, human Mucin 2: Uniprot Q02817, human Mucin 5A: UniProt P98088.



**Figure S5. Structural and functional characterisation of RGM mutations causing juvenile hemochromatosis.**

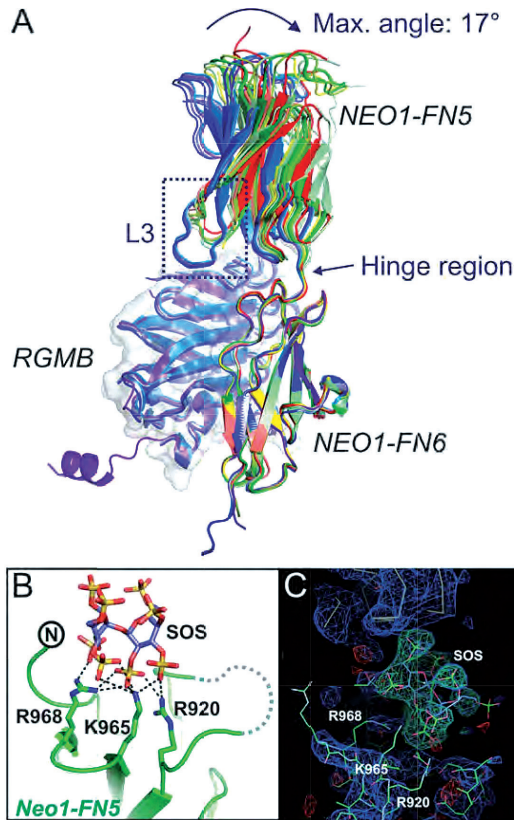
**A.** RGM mutations mapped onto the RGMB structure. Ten of the reported mutations map onto the domain of RGM observed in the crystal structure. Equivalent residues on RGMB are shown as orange sphere. The autocatalytic cleavage site is highlighted. **B-C.** Small scale expression test of the disease-related RGM mutants. All mutants were generated in the eRGM<sub>AAA</sub> background. Top panel: medium; lower panel: cells. Of the 14 mutants only two (G99R and L101P) were secreted at levels observed for the wildtype. G99R and L101P map to the N-terminal domain which is not present in the crystal structure. SDS-PAGE analysis was carried out under non-reducing (B) as well as reducing (C) conditions. Secreted human RGM exists in a major, processed and a minor, uncleaved form, which is in contrast to secreted RGM and RGMB proteins (fig S4). **D.** The RGM-G320V mutation. Colour coding is as in fig 1D. The Ca atom of G320 is shown as magenta sphere. Although all RGM mutations that may impact onto the site-1 interface impair secretion in this study, the JHH-linked RGM mutation Gly320Val<sup>RGM</sup> has been successfully expressed in a secreted form in a stable expression system (59). The authors showed that this mutant protein failed to interact with NEO1. Intriguingly, Gly-320 (corresponding to Gly-315 in human RGMB) is located close to the site-1 interface. A mutation of G320 to valine can potentially cause a rearrangement of RGM disulphide bridges II and III, as well as impair the site-1 NEO1-RGM interface including RGMB residues D308 and L318, which form hydrogen bonds with NEO1 residues K997, E998 and Q1049.



**Figure S6. Crystal packing of the different RGMB-NEO1 complex structures.**

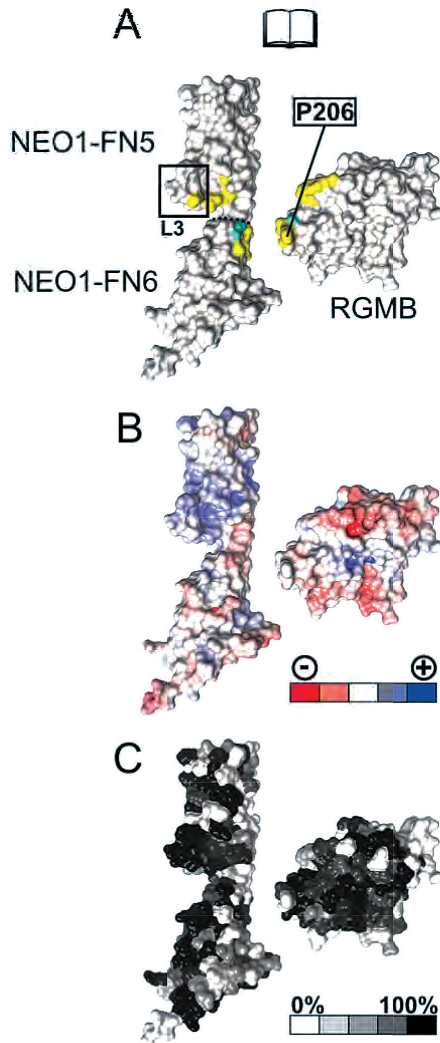
**A.** eRGMB-NEO1<sub>FN56</sub> Form 1. **B.** eRGMB-NEO1<sub>FN56</sub> Form 2 and **C.** eRGMB-NEO1<sub>FN56</sub> Form 3. Orientation and colour coding is as in Fig 1D, right panel. The neutral pH crystal form 1 contains the 2:2 complex in the asymmetric unit. In form 2 the 2:2 complex is built by a two-fold crystallographic axis. The low pH crystal form 3 contains only the 1:1 complex in the asymmetric unit. For crystallographic details see table S1.





**Figure S7. NEO1 structure comparison of apo and complex-bound forms.**

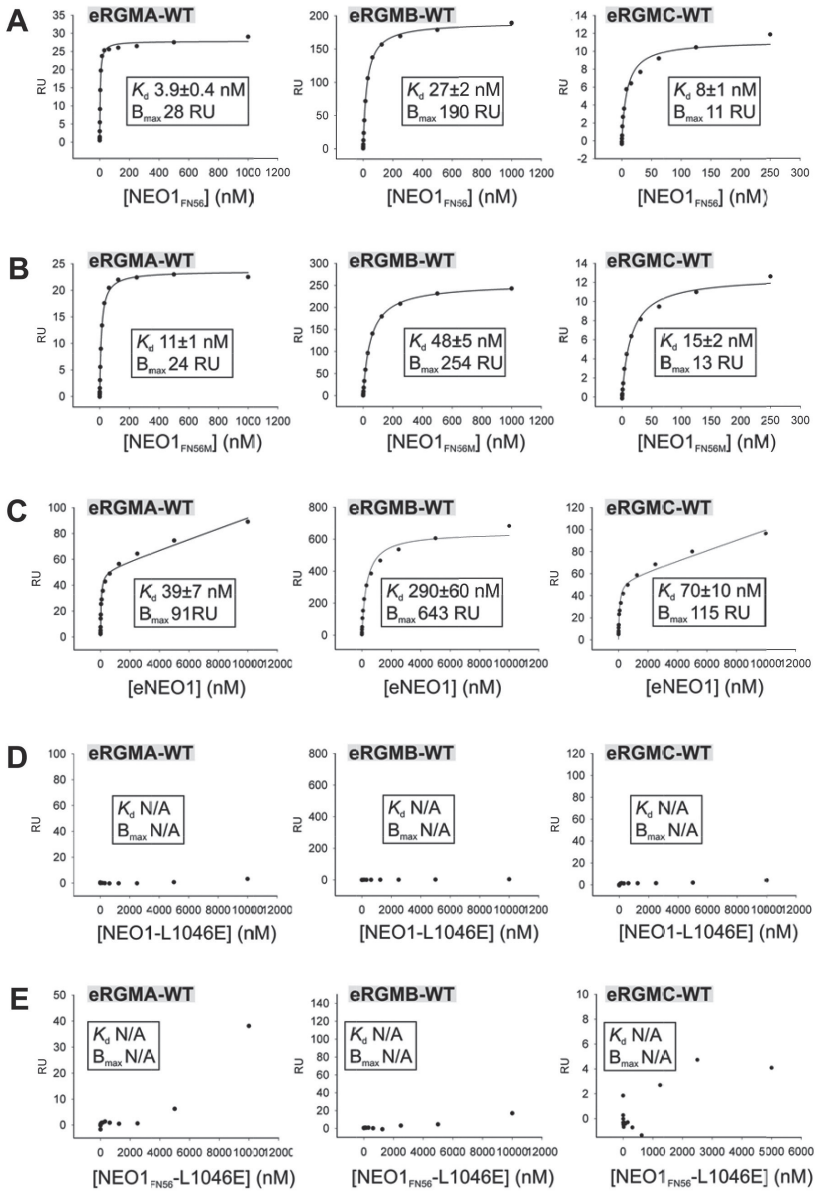
**A.** Superpositions calculated based on the NEO1-FN6 domain. NEO1<sub>FN56</sub> Form1 (4 molecules, coloured in different green shades), NEO1<sub>FN56</sub> Form 2 (2 molecules, coloured in different cyan shades), NEO1<sub>FN56</sub>-sucrose octasulphate (SOS) (2 molecules, coloured in different red shades) NEO1<sub>FN56</sub> previously reported (39) (PDB Id 3P4L, 1 molecule, coloured in yellow) eRGMB-NEO1<sub>FN56</sub> Form 1 (2 molecules NEO1 and RGMB coloured in dark blue), eRGMB-NEO1<sub>FN56</sub> Form 2 (2 molecules NEO1 and RGMB, coloured in light blue), eRGMB-NEO1<sub>FN56</sub> Form 3 (1 molecule NEO1 and RGMB, coloured in light violet). Superpositions of all 5 site-1 complex molecules result in a very good overall overlay, whereas the NEO1 apo structures show significant flexibility between the relative orientation of the FN5 and FN6 domains. The L3 loop, which forms the major interaction site of NEO1-FN5 with RGMB is flexible or disordered in the NEO1 apo structures, suggesting that RGMB adds rigidity towards the conformation of the NEO1 FN5-FN6 interface. **B.** Close-up of the NEO1-SOS binding site. The SOS molecule sits on top of the NEO1-FN5 domain. Interactions of the SOS sulphate groups involve the positively charged side chains of arginines 920 and 968 and lysine 965 (see also fig S3B). It is worth noting that the equivalent residues 965 and 968 in DCC have been previously implicated in glycosamino-glycan (53) and Netrin-1 binding (54). **C.** SigmaA-weighted  $2Fo-Fc$  map (bleu,  $1.0\sigma$ ) and  $Fo-Fc$  map (green/red,  $\pm 3.0\sigma$ ) from PHENIX (42) after rigid body and positional refinement calculated without the SOS molecule.



**Figure S8. The RGMB-NEO1 site-2 interactions.**

The eRGMB-NEO1<sub>FN56</sub> complex is shown in surface representation in an open book view.

**A.** Interface residues are highlighted (non-bonded interactions: yellow; hydrophilic interactions: cyan). The RGMB L3 loop is marked. In total the site-2 interface is composed of 1 hydrogen bond and 25 non-bonded contacts (see also fig 2D). **B.** Electrostatic potential from red (-8 kbT/ec) to blue (+8 kbT/ec). The majority of the interactions are formed by hydrophobic residues. **C.** The complex is colour-coded according to residue conservations (from non-conserved, white to conserved, black) based on alignments containing sequences from 17 NEO1 orthologues and 94 RGM orthologues and paralogues from vertebrates.



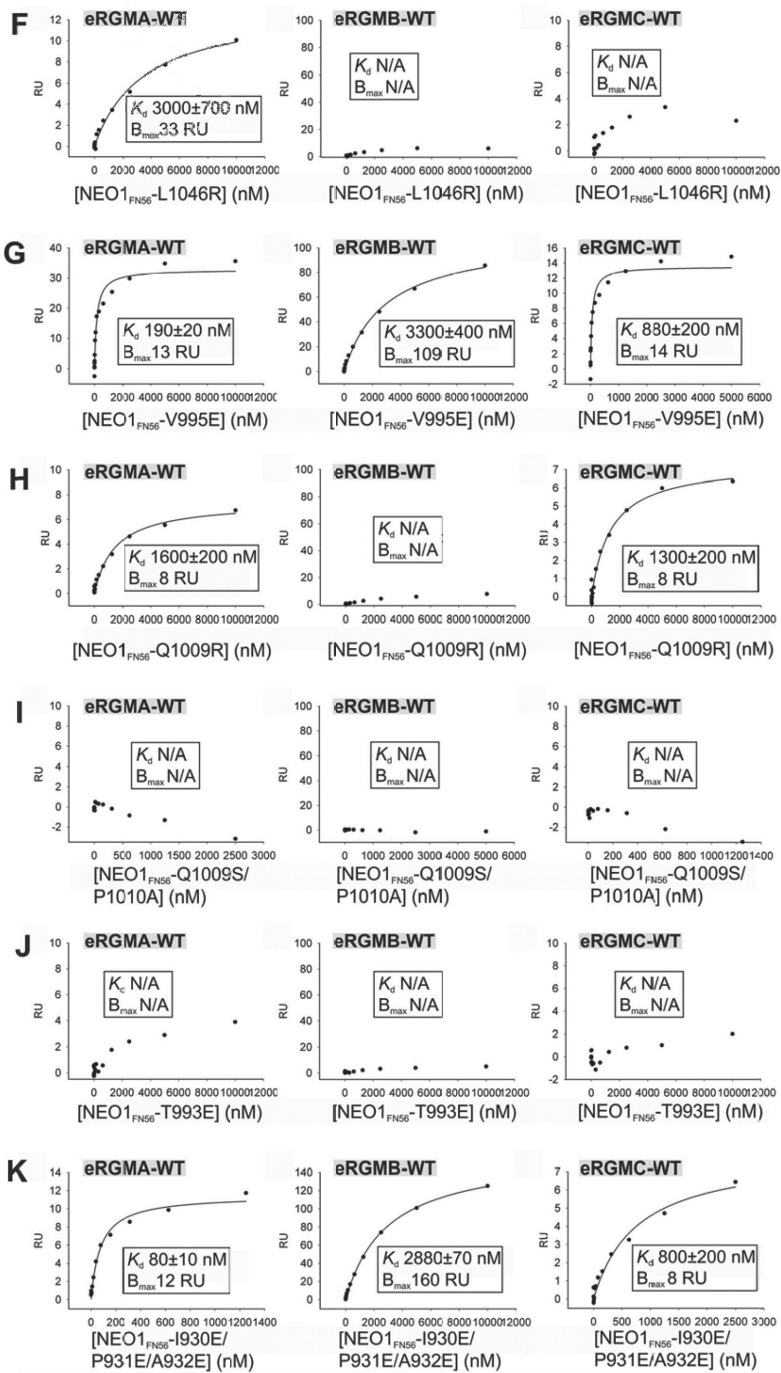


**Figure S9. SPR data of NEO1-RGM interactions.**

Binding of NEO1 constructs and mutants to the full-length ectodomains of RGMA (left panel), RGMB (middle panel) and RGMC (right panel), respectively. Graphs show a plot of the equilibrium binding response (response units (RU)) against concentration of the used NEO1 constructs. All experiments were performed in duplicate. Best-fit binding curves calculated using a 1:1 binding model are shown as lines. If not differently stated in the graph, the chip concentrations were 80 RU, 500 RU and 90 RU for eRGMA, eRGMB and eRGMC, respectively. Corresponding ligands (immobilised on the chip) are indicated in grey boxes. Binding constants ( $K_d$ ) are given as mean with the error representing the standard error of the mean. N/A: not applicable. NEO1 constructs comprising only the FN5 and FN6 domains (NEO1FN56 and NEO1FN56M) (Fig. 7A and B) showed even tighter binding to all RGMs compared to the full-length NEO1 ectodomain (Fig. 7C), possibly explained by better accessibility of the RGMs to the truncated constructs.

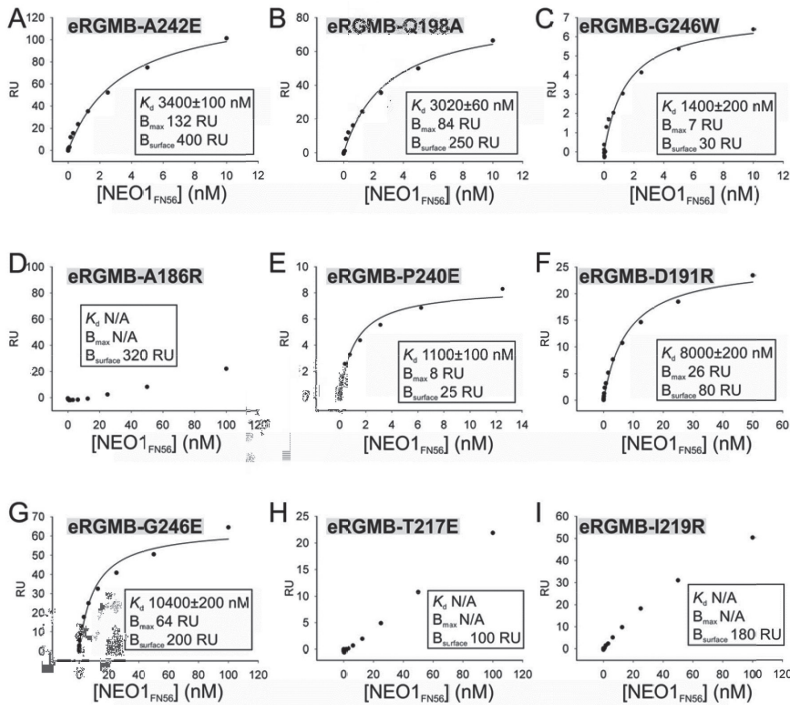


**Figure S10. Binding of NEO1 to different RGMB mutants.**

Graphs show a plot of the equilibrium binding response (response units (RU)) against NEO1<sub>FN56</sub> concentrations ranging from 6 nM to 100 nM. All experiments were performed in duplicate. Best-fit binding curves were calculated using a 1:1 binding model shown as lines. The chip concentrations of the RGMB constructs immobilised on the chip are given as  $B_{surface}$ . Binding constants ( $K_d$ ) are given as mean with the error representing the standard error of the mean. N/A: not applicable.

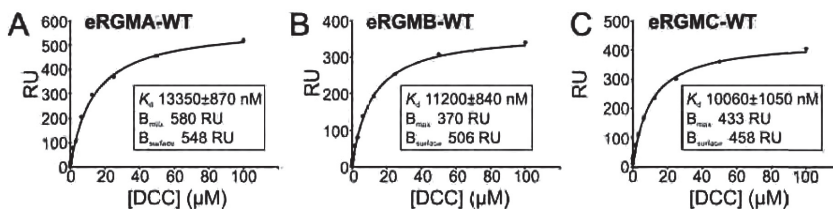


**Figure S11. Binding of DCC to RGMA (A), RGMB (B) and RGMC (C).**

Graphs show a plot of the equilibrium binding response (response units (RU)) against the concentration of the full-length ectodomain of DCC ranging from 6 nM to 100  $\mu$ M. All experiments were performed in duplicate. Best-fit binding curves were calculated using a 1:1 binding model shown as lines. The chip concentrations of the RGM constructs immobilised on the chip are given as  $B_{surface}$ . Binding constants ( $K_d$ ) are given as mean with the error representing the standard error of the mean.

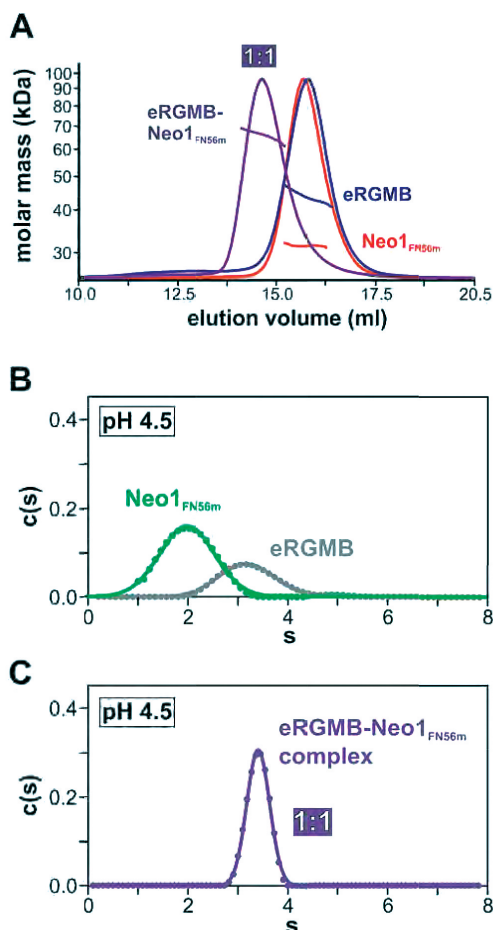




**Figure S12. Oligomeric behaviour of the RGMB-NEO1 complex.**

**A.** Multi-angle light scattering (MALS) analysis of the RGMB-NEO1 complex. eRGMB (blue) and NEO1<sub>FN56M</sub> (red) behave as monomers with the following molecular weights (measured/theoretical): eRGMB: 42.64 ±0.1/43.35kDa; NEO1<sub>FN56M</sub>: 31.04±0.1/31.05 kDa. The eRGMB-NEO1<sub>FN56M</sub> complex (magenta) behaves as a heterodimeric (one RGMB and one NEO1) complex (molecular weight measured/theoretical: 69.04±0.1/74.40 kDa) at concentrations up to 3 µM. Theoretical molecular weights of glycosylated proteins were calculated using PROTPARAM at the EXPASY server (www.expasy.ch). **B-C.** Analytical ultracentrifugation sedimentation velocity experiments of (B) eRGMB (grey) and NEO1FN56M (green) and (C) the eRGMB-NEO1FN56M complex at pH 45. Distribution plots obtained from the fitting of SV data using a continuous c(s) distribution model (solid line Gaussian fit to data plotted as symbols) are shown (compare to fig 3C-E). Individual Gaussian peaks contributing to the overall distributions are displayed in dotted lines from the eRGMB (B, RMSD: 0.0016), NEO1FN56M (B, RMSD: 0.0023) and the eRGMB-NEO1 (F, RMSD: 0.0027) complexes. The individual components run as discrete single, likely monomeric species. The eRGMB-NEO1FN56M complex shows a single species likely corresponding to the 1:1 complex.

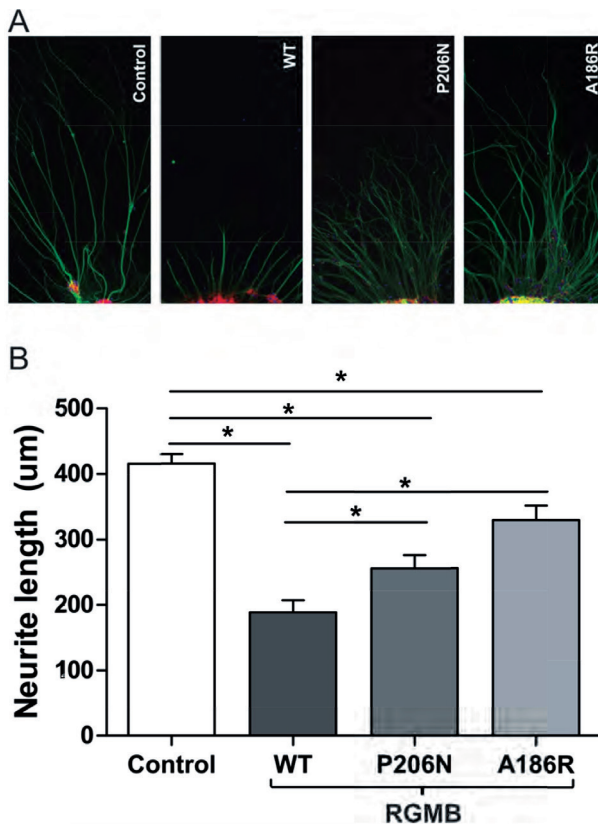


**Figure S13. Functional analysis of the effects of RGMB site 1 and 2 mutations on neurite growth.**

**A.** Higher magnification of representative neuronal explants used for the quantification of neurite length shown in fig 4. The length of individual, non-fasciculated neurites was determined by measuring the distance between the edge of the explant and the growth cone of >20 neurites per explant. **B.** Average neurite length per explant was calculated for each condition (three independent experiments, total number of explants analyzed per condition; WT n=27, P206N n=24, A186R n=26, control n=23), error bars are SEM, \*p<0.05.

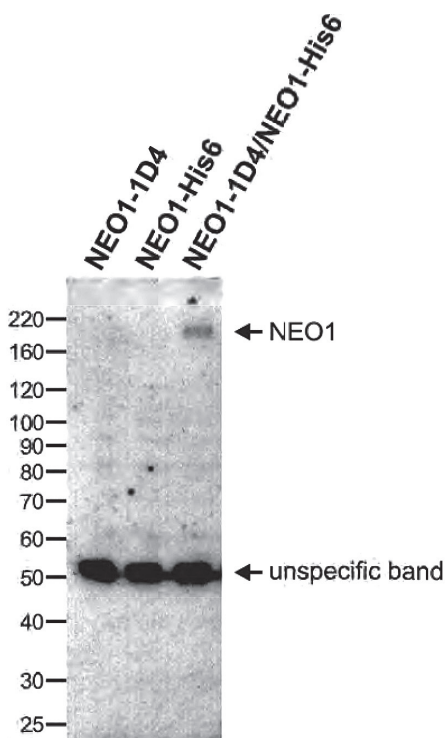


**Figure S14. Pre-formed NEO1 dimers can be isolated from the cell membrane.**

Full length NEO1-1D4 and NEO1-His6 proteins were extracted from the membranes of co-transfected cells. Proteins were solubilised in detergent-containing buffer and NEO1-1D4 proteins were immobilized on 1D4-antibody-conjugated sepharose beads. The beads were washed several times and the bound protein complexes were eluted from the beads by competition with high concentrations of 1D4 peptide. The eluted protein complexes were separated by SDS-PAGE (4-12% Bis Tris gradient gel), and analyzed by Western blotting with a mouse anti-His6 suggesting NEO1 dimers form in the membrane. Non-specific binding of NEO1-His6 to the 1D4-antibody-conjugated sepharose beads was not observed. Non-specific binding of the mouse anti-His6 antibody to NEO1-1D4 was also not observed.

**Table S1. Crystallographic data collection and refinement statistics**

r.m.s.d.: root mean square deviation from ideal geometry. Numbers in parentheses refer to the appropriate outer shell.

$aR_{\text{merge}} = \frac{\sum_i \sum_j |I(hkl;i) - \langle I(hkl) \rangle|}{\sum_i \sum_j I(hkl;i)}$ , where  $I(hkl;i)$  is the intensity of an individual measurement and  $\langle I(hkl) \rangle$  is the average intensity from multiple observations.

$bR_{\text{factor}} = \frac{\sum_i |F_{\text{obs}}| - k|F_{\text{calc}}|}{\sum_i |F_{\text{obs}}|}$ .

$cR_{\text{free}}$  equals the  $R$ -factor against 5% of the data removed prior to refinement.

NEO1 <sub>FN56</sub> <sup>-</sup> eRGM Form 1 (high pH)	NEO1 <sub>FN56</sub> <sup>-</sup> eRGM Form 2 (high pH)	NEO1 <sub>FN56</sub> <sup>-</sup> eRGM Form 3 (low pH)	NEO1 <sub>FN56</sub> Form 1	NEO1 <sub>FN56</sub> Form 2	NEO1 <sub>FN56</sub> <sup>-</sup> SOS
--	--	---	--------------------------------	--------------------------------	--

## DATA COLLECTION

<b>X-ray source</b>	DIAMOND-I03	DIAMOND-I03	DIAMOND-I03	ESRF-ID14-EH4	DIAMOND-I03	ESRF-ID14-EH4
<b>Resolution</b>	30.0-2.3 (2.4-2.3)	50.0-6.6 (6.8-6.6)	50.0-2.8 (2.9-2.8)	30.0-2.9 (3.0-2.9)	30.0-2.7 (2.8-2.7)	30.0- 3.2 (3.3-3.2)
<b>Space group</b>	P2 <sub>1</sub> 2 <sub>1</sub> 2 <sub>1</sub>	P3 <sub>2</sub> 12	P4 <sub>1</sub> 2 <sub>1</sub> 2	P3 <sub>1</sub> 21	P2 <sub>1</sub>	C222 <sub>1</sub>
<b>Cell dimensions [Å]</b>	a = 91.3 Å b = 100.4 Å c = 103.7 Å	a = 109.7 Å b = 109.7 Å c = 187.9 Å	a = 116.9 b = 116.9 c = 91.8	a = 103.6 Å b = 103.6 Å c = 110.8 Å	a = 59.0 Å b = 97.4 Å c = 91.3 Å β = 106.4°	a = 96.2 Å b = 157.8 Å c = 89.9 Å
<b>Solvent content [%] (mols per AU)</b>	55 (2 mols eRGM, 2 mols NEO1 <sub>FN56</sub> )	65 (2 mols eRGM, 2 mols NEO1 <sub>FN56</sub> )	68 (1 mol eRGM, 1 mol NEO1 <sub>FN56</sub> )	68 (2 mols NEO1 <sub>FN56</sub> )	56 (4 mols NEO1 <sub>FN56</sub> )	69 (2 mols NEO1 <sub>FN56</sub> )
<b>Wilson B factor [Å<sup>2</sup>]</b>	57	182	84	64	81	67
<b>Unique reflections</b>	42796 (2990)	2508 (181)	16223 (1167)	15545 (1531)	26660 (2518)	11572 (820)
<b>Completeness [%]</b>	99.3 (95.6)	97.7 (97.4)	99.9 (99.4)	99.9 (100.0)	97.7 (92.7)	99.4 (98.6)
<b>Rmerge [%]<sup>a</sup></b>	9.2 (84.1)	23.3 (78.9)	8.9 (90.8)	13.5 (86.8)	8.0 (82.9)	11.4 (83.0)
<b>I/σ</b>	10.2 (1.3)	7.5 (2.3)	15.5 (1.9)	10.8 (1.5)	11.3 (1.2)	16.3 (2.9)
<b>Redundancy</b>	6.0 (4.0)	6.0 (5.0)	8.4 (7.8)	4.2 (4.3)	2.3 (2.2)	10.0 (10.3)

## REFINEMENT

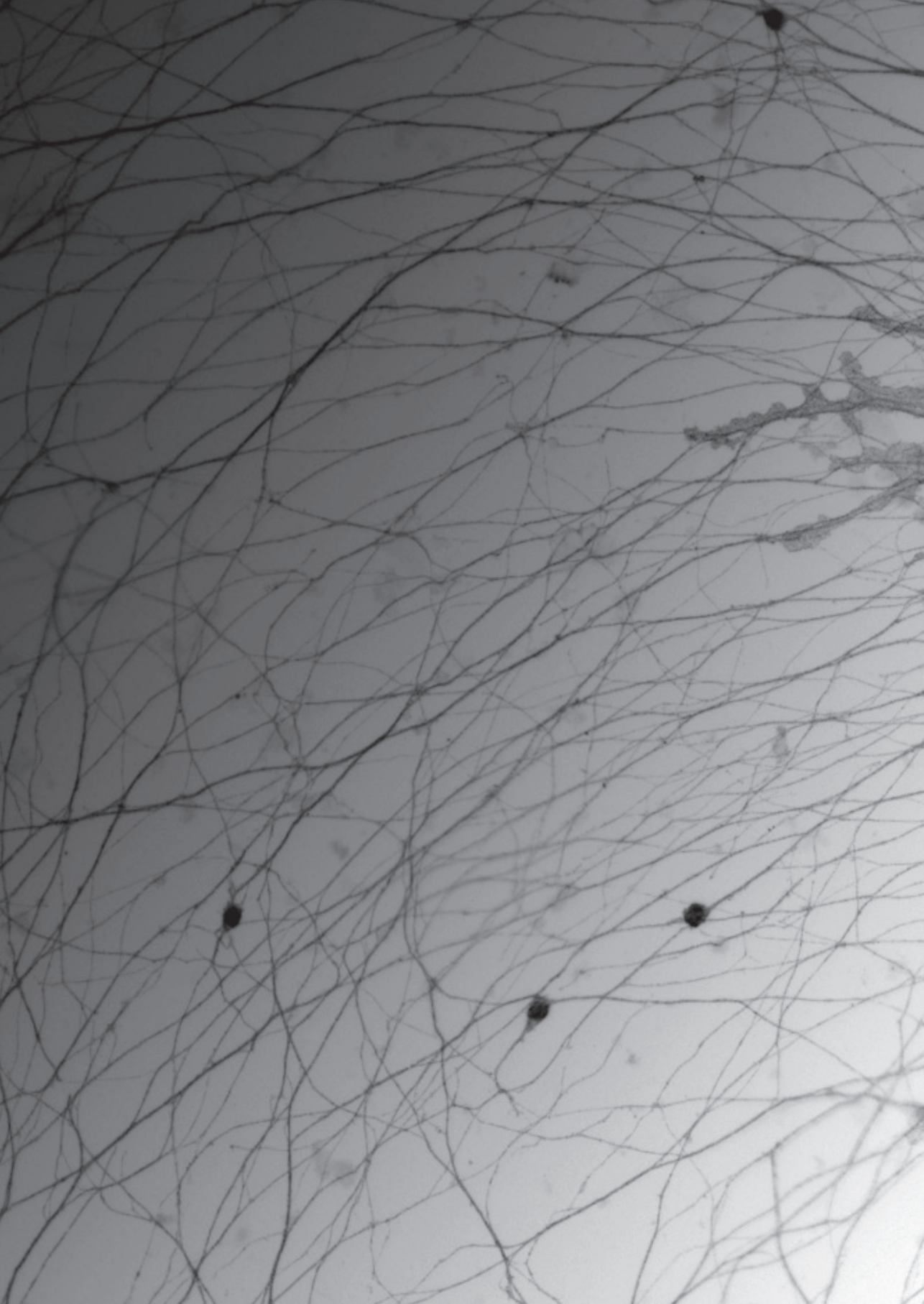
<b>Resolution range [Å]</b>	30.0-2.3 (2.36-2.30)	50.0-6.6 (8.3-6.6)	50.0-2.8 (3.0-2.8)	30.0-2.9 (3.1-2.9)	30.0-2.7 (2.8-2.7)	30.0- 3.2 (3.5-3.2)
<b>Number of reflections</b>	42757 (2852)	2488 (1116)	16180 (2854)	15443 (2737)	26625 (2837)	11548 (2686)
<b>No. of atoms (protein/NAG/SOS/ H<sub>2</sub>O)</b>	5771/28/0/329	5750/0/0/0	2905/14/0/0	3106/28/0/0	6277/56/0/0	2951/14/110/0
<b>B factors [Å<sup>2</sup>] (protein/NAG/SOS/ H<sub>2</sub>O)</b>	52/80/0/48	-	76/119/0/0	69/110/0/0	89/109/0/0	98/109/180/0
<b>R<sub>factor</sub> [%]c</b>	22.1 (21.0)	26.1 (28.9)	18.7 (21.9)	20.6 (27.2)	20.1 (24.5)	22.0 (24.2)
<b>R<sub>free</sub> [%] d</b>	26.6 (23.1)	27.2 (29.3)	20.3 (26.8)	23.2 (31.7)	22.4 (25.6)	26.5 (28.0)
<b>r.m.s.d. bonds [Å]</b>	0.010	0.019	0.009	0.010	0.010	0.010
<b>r.m.s.d. angles [deg]</b>	1.21	1.90	1.18	1.21	1.13	1.19
<b>Ramachandran statistics</b>						
<b>Favoured [%]</b>	94.6	94.0	96.1	96.6	97.6	95.9
<b>Disallowed [%]</b>	0	0.7	0	0	0	0

---

## Supplemental References

- 30. J. P. Wong, E. Reboul, R. S. Molday, J. Kast, A carboxy-terminal affinity tag for the purification and mass spectrometric characterization of integral membrane proteins. *J. Proteome Res.* 8, 2388 (2009). doi:10.1021/pr801008c Medline
- 31. A. R. Aricescu, W. Lu, E. Y. Jones, A time- and cost-efficient system for high-level protein production in mammalian cells. *Acta Crystallogr. D Biol. Crystallogr.* 62, 1243 (2006). doi:10.1107/S0907444906029799 Medline
- 32. Y. Zhao et al., Automation of large scale transient protein expression in mammalian cells. *J. Struct. Biol.* 175, 209 (2011). doi:10.1016/j.jsb.2011.04.017 Medline
- 33. V. T. Chang et al., Glycoprotein structural genomics: solving the glycosylation problem. *Structure* 15, 267 (2007). doi:10.1016/j.str.2007.01.011 Medline
- 34. E. S. Trombetta, A. J. Parodi, Quality control and protein folding in the secretory pathway. *Annu. Rev. Cell Dev. Biol.* 19, 649 (2003). doi:10.1146/annurev.cellbio.19.110701.153949 Medline
- 35. T. S. Walter et al., A procedure for setting up high-throughput nanolitre crystallization experiments. Crystallization workflow for initial screening, automated storage, imaging and optimization. *Acta Crystallogr. D Biol. Crystallogr.* 61, 651 (2005). doi:10.1107/S0907444905007808 Medline
- 36. Z. Otwinowski, W. Minor, Processing of X-ray diffraction data collected in oscillation mode. *Methods Enzymol.* 276, 307 (1997). doi:10.1016/S0076-6879(97)76066-X
- 37. G. Winter, xia2 : an expert system for macromolecular crystallography data reduction. *J. Appl. Cryst.* 43, 186 (2010). doi:10.1107/S0021889809045701
- 38. A. J. McCoy, R. W. Grosse-Kunstleve, L. C. Storoni, R. J. Read, Likelihood-enhanced fast translation functions. *Acta Crystallogr. D Biol. Crystallogr.* 61, 458 (2005). doi:10.1107/S0907444905001617 Medline
- 39. F. Yang, A. P. West, Jr., P. J. Bjorkman, Crystal structure of a hemojuvelin-binding fragment of neogenin at 1.8Å. *J. Struct. Biol.* 174, 239 (2011). doi:10.1016/j.jsb.2010.10.005 Medline
- 40. M. D. Winn et al., Overview of the CCP4 suite and current developments. *Acta Crystallogr. D Biol. Crystallogr.* 67, 235 (2011). doi:10.1107/S0907444910045749 Medline
- 41. E. Blanc et al., Refinement of severely incomplete structures with maximum likelihood in BUSTER-TNT. *Acta Crystallogr. D Biol. Crystallogr.* 60, 2210 (2004). doi:10.1107/S0907444904016427 Medline
- 42. P. D. Adams et al., PHENIX: building new software for automated crystallographic structure determination. *Acta Crystallogr. D Biol. Crystallogr.* 58, 1948 (2002). doi:10.1107/S0907444902016657 Medline
- 43. P. Emsley, K. Cowtan, Coot: model-building tools for molecular graphics. *Acta Crystallogr. D Biol. Crystallogr.* 60, 2126 (2004). doi:10.1107/S0907444904019158 Medline
- 44. G. J. Kleywegt, A. T. Brünger, Checking your imagination: applications of the free R value. *Structure* 4, 897 (1996). doi:10.1016/S0969-2126(96)00097-4 Medline
- 45. I. W. Davis et al., MolProbity: all-atom contacts and structure validation for proteins and nucleic acids. *Nucleic Acids Res.* 35, (Web Server), W375 (2007). doi:10.1093/nar/gkm216 Medline

- 46. D. I. Stuart, M. Levine, H. Muirhead, D. K. Stammers, Crystal structure of cat muscle pyruvate kinase at a resolution of 2.6 Å. *J. Mol. Biol.* 134, 109 (1979). doi:10.1016/0022-2836(79)90416-9 Medline
- 47. N. A. Baker, D. Sept, S. Joseph, M. J. Holst, J. A. McCammon, Electrostatics of nanosystems: application to microtubules and the ribosome. *Proc. Natl. Acad. Sci. U.S.A.* 98, 10037 (2001). doi:10.1073/pnas.181342398 Medline
- 48. E. Krissinel, K. Henrick, Inference of macromolecular assemblies from crystalline state. *J. Mol. Biol.* 372, 774 (2007). doi:10.1016/j.jmb.2007.05.022 Medline
- 49. C. A. O'Callaghan et al., BirA enzyme: production and application in the study of membrane receptor-ligand interactions by site-specific biotinylation. *Anal. Biochem.* 266, 9 (1999). doi:10.1006/abio.1998.2930 Medline
- 50. P. Schuck, P. Rossmanith, Determination of the sedimentation coefficient distribution by leastsquares boundary modeling. *Biopolymers* 54, 328 (2000). doi:10.1002/1097-0282(20001015)54:5<328:AID-BIP40>3.0.CO;2-P Medline
- 51. P. H. Brown, P. Schuck, Macromolecular size-and-shape distributions by sedimentation velocity analytical ultracentrifugation. *Biophys. J.* 90, 4651 (2006). doi:10.1529/biophysj.106.081372 Medline
- 52. R. J. Pasterkamp, J. J. Peschon, M. K. Spriggs, A. L. Kolodkin, Semaphorin 7A promotes axon outgrowth through integrins and MAPKs. *Nature* 424, 398 (2003). doi:10.1038/nature01790 Medline
- 53. K. L. Bennett et al., Deleted in colorectal carcinoma (DCC) binds heparin via its fifth fibronectin type III domain. *J. Biol. Chem.* 272, 26940 (1997). doi:10.1074/jbc.272.43.26940 Medline
- 54. B. V. Geisbrecht, K. A. Dowd, R. W. Barfield, P. A. Longo, D. J. Leahy, Netrin binds discrete subdomains of DCC and UNC5 and mediates interactions between DCC and heparin. *J. Biol. Chem.* 278, 32561 (2003). doi:10.1074/jbc.M302943200 Medline
- 55. M. E. Lidell, G. C. Hansson, Cleavage in the GDPH sequence of the C-terminal cysteine-rich part of the human MUC5AC mucin. *Biochem. J.* 399, 121 (2006). doi:10.1042/BJ20060443 Medline
- 56. M. E. Lidell, M. E. Johansson, G. C. Hansson, An autocatalytic cleavage in the C terminus of the human MUC2 mucin occurs at the low pH of the late secretory pathway. *J. Biol. Chem.* 278, 13944 (2003). doi:10.1074/jbc.M210069200 Medline
- 57. A. L. Ambrosio et al., Crossveinless-2 is a BMP feedback inhibitor that binds Chordin/BMP to regulate *Xenopus* embryonic patterning. *Dev. Cell* 15, 248 (2008). doi:10.1016/j.devcel.2008.06.013 Medline
- 58. J. E. Sadler, Biochemistry and genetics of von Willebrand factor. *Annu. Rev. Biochem.* 67, 395 (1998). doi:10.1146/annurev.biochem.67.1.395 Medline
- 59. A. S. Zhang, A. P. West, Jr., A. E. Wyman, P. J. Bjorkman, C. A. Enns, Interaction of hemojuvelin with neogenin results in iron accumulation in human embryonic kidney 293 cells. *J. Biol. Chem.* 280, 33885 (2005). doi:10.1074/jbc.M506207200 Medline





---

# Chapter 4

## Lrig2 Negatively Regulates Ectodomain Shedding of Axon Guidance Receptors by ADAM Proteases at the Neuronal Growth Cone

---

Susan van Erp<sup>1,\*</sup>, Dianne M.A. van den Heuvel<sup>1,\*</sup>, Yuki Fujita<sup>2</sup>, Anita J.C.G.M. Hellemons<sup>1</sup>, Marijn Kuijpers<sup>3</sup>, Jeroen Demmers<sup>4</sup>, Håkan Hedman<sup>5</sup>, Casper C. Hoogenraad<sup>3</sup>, Toshihide Yamashita<sup>2</sup>, and R. Jeroen Pasterkamp<sup>1</sup>

1 Department of Translational Neuroscience, Brain Center Rudolf Magnus, University Medical Center Utrecht, Universiteitsweg 100, 3584CG, Utrecht, The Netherlands

2 Department of Molecular Neuroscience, Graduate School of Medicine, Osaka University 2-2, Yamadaoka, Suita, Osaka 565-0871, Japan

3 Cell Biology, Faculty of Science, Utrecht University, 3584 CH, Utrecht, The Netherlands

4 Proteomics Centre and Department of Cell Biology, Erasmus University Medical Centre, Dr Molewaterplein 50, 3015 GE Rotterdam, The Netherlands

5 Oncology Research Laboratory, Department of Radiation Sciences, Umeå University, SE-90187, Umeå, Sweden

\* These authors contributed equally.

*Submitted*

---

## **Abstract**

Many axon guidance receptors are proteolytically cleaved by membrane-associated metalloproteases of the ADAM family leading to the shedding of their ectodomains. However, how ectodomain shedding is spatiotemporally controlled in neurons is poorly understood. Here we show that the transmembrane protein Lrig2 negatively regulates ADAM-mediated guidance receptor proteolysis in neurons. Lrig2 binds Neogenin, a receptor for Repulsive Guidance Molecules (RGMs), and inhibits Neogenin shedding by ADAM17 (TACE). This effect is ligand-dependent; RGMa binding reduces Lrig2-Neogenin interactions, providing ADAM17 access to Neogenin. Lrig2 is required for RGMa/Neogenin-mediated axon growth inhibition, and, accordingly, knockdown of Lrig2 improves axon regeneration. All three mammalian Lrigs reduce Neogenin shedding and Lrig2 also inhibits shedding of NCAM1 and Semaphorin4D suggesting that regulation of ADAM-mediated proteolysis is a general property of Lrigs. Together, our data identify a unique mechanism to control receptor shedding by ADAMs and reveal novel functions for Lrigs in axon growth inhibition and regenerative failure.

## Introduction

Leucine-rich repeats and immunoglobulin-like domains (Lrig) proteins are unique transmembrane proteins with an extracellular domain containing leucine-rich repeats (LRRs) and Ig-like domains, and a cytosolic region with no apparent homology to other proteins (Figure 1A). The Lrig family contains three vertebrate members, Lrig1 (Lig1), Lrig2 and Lrig3, while *Drosophila* and *C. elegans* each contain a single Lrig gene (Guo et al., 2004). Lrig1 has been best-characterized at the functional level and controls the activity of several growth factor receptors, including ErbB, Met, and Ret (e.g. (Gur et al., 2004; Laederich et al., 2004; Ledda et al., 2008)). Lrig1 deficiency in mice leads to a variety of phenotypes, including excess intestinal stem cell proliferation, tumor formation, impaired auditory responses, and psoriasis-like hyperplasia (Jensen and Watt, 2006; Page et al., 2013; Powell et al., 2012; Del Rio et al., 2013; Suzuki et al., 2002; Wong et al., 2012). Lrig1 has been described as a tumor suppressor in humans and is associated with tumor growth and patient survival (Lindquist et al., 2014). Unfortunately, our understanding of the function and mechanism-of-action of other Lrigs is rather rudimentary. Further, despite prominent neuronal expression, how Lrigs contribute to nervous system development or function is poorly understood.

Here we identify a role for Lrig2 in the proteolytic processing of axon guidance receptors. During embryonic development, axon guidance proteins provide instructive signals for growing axons and are detected by cell surface receptors at the axonal growth cone (Kolodkin and Pasterkamp, 2013; Yam and Charron, 2013). Many axon guidance receptors are proteolytically cleaved at their juxta-membrane region by membrane-associated metalloproteases of the ADAM (A Disintegrin And Metalloprotease) family, leading to the shedding of their ectodomains. This shedding is required for proper axon guidance and controls receptor levels, activation and the disassembly of ligand-receptor complexes (Chen et al., 2007; Coleman et al., 2010; Fambrough et al., 1996; Galko and Tessier-Lavigne, 2000; Hattori et al., 2000; Janes et al., 2005; Okamura et al., 2011; Romi et al., 2014). Despite these important roles of ADAMs, how their neuronal effects are controlled to spatiotemporally regulate axon guidance receptor signaling remains incompletely understood. For example, ADAM10 and ADAM17 (tumor necrosis factor- $\alpha$  converting enzyme; TACE), the principal sheddases in the neurons, are present in embryonic proprioceptive and cutaneous sensory axons but only induce cleavage of Neuropilin-1 in proprioceptive axons (Romi et al., 2014). Furthermore, shedding of Neogenin, a growth cone receptor for Repulsive Guidance Molecule a (RGMa) by ADAM17 desensitizes axons to RGMa, but how this cleavage event is spatiotemporally regulated to prevent premature cleavage is unknown (Okamura et al., 2011). Thus, unidentified regulatory mechanisms are in place to spatiotemporally control ADAMs in neurons.

---

RGMa is a GPI-anchored axon guidance protein that inhibits axon growth or induces axon repulsion by binding Neogenin, thereby contributing to the development of different axon tracts (Matsunaga et al., 2006; Tassew et al., 2008, 2012; Wilson and Key, 2006). In addition, it controls different aspects of neural development unrelated to axon guidance, such as neuron migration and survival (Kee et al., 2008; Matsunaga et al., 2004; Niederkofler et al., 2004). Intriguingly, injury-induced expression of repulsive guidance proteins contributes to the axon growth inhibitory environment of the injured adult central nervous system (CNS) and limits axon regeneration (Giger et al., 2010). Indeed, RGMa is upregulated in the injured CNS, and administration of function-blocking anti-RGMa antibodies to the injured rat spinal cord promotes functional recovery (Hata et al., 2006). This suggests that insight into RGMa function and signaling mechanisms may aid the development of therapeutic strategies to enhance CNS regeneration. Here, we identify Lrig2 as a binding partner of Neogenin and show that Lrig2 inhibits ADAM17-mediated ectodomain shedding of Neogenin in a RGMa-dependent manner. Lrig2 is required for the axon growth inhibitory effects of RGMa-Neogenin signaling, and, accordingly, knockdown of Lrig2 promotes optic nerve regeneration. These data reveal a previously uncharacterized neuronal role for Lrigs and unveil a novel mechanism in ADAM regulation that prevents premature receptor cleavage while retaining ligand responsiveness. Our observations that Lrig2 can prevent the shedding of multiple different substrates and that other Lrig family members may exert similar effects suggests that negative regulation of ADAM-mediated proteolysis is a general property of Lrigs.

## **Experimental Procedures**

### **Animals and Tissue Treatment**

All animal use and care were in accordance with institutional guidelines. C57BL/6 mice were obtained from Charles River. Timed-pregnant mice were killed by means of cervical dislocation. The morning on which a vaginal plug was detected was considered embryonic day 0.5 (E0.5). The day pups were born was defined as postnatal day (P)0. For *in situ* hybridization experiments, E16.5 embryos and P9 heads were frozen in 2-methylbutane (Merck). For immunohistochemistry, E16.5 heads and adult eyes were collected in phosphate-buffered saline (PBS, pH 7.4) and fixed by immersion for 3 hours (hrs) in 4% paraformaldehyde (PFA) in PBS at 4°C. Tissue was washed in PBS, cryoprotected in 30% sucrose at 4°C and frozen in 2-methylbutane. Sections (16 µm) were cut on a cryostat, mounted on Superfrost Plus slides (Fisher Scientific), air-dried and stored desiccated at -80°C for *in situ* hybridization and at -20°C for immunohistochemistry.



## ***In Situ* Hybridization**

Nonradioactive *in situ* hybridization was performed according to (Pasterkamp et al., 1998). In brief, probe sequences for *Neogenin* (NM\_008684.2: nt 2087-2587), *Lrig2* (NM\_001025067: nt 1149-1761) and *Lrig3* (Genepaint.org: probe 43) were polymerase chain reaction (PCR)-amplified from cDNA, using primer sequences listed in the Table below. The probe sequence for *Lrig1* (Genepaint.org: probe 90) was generated by reverse transcription-PCR (RT-PCR) on adult mouse whole brain RNA (primers listed in Table below). Digoxigenin (DIG)-labeled RNA probes were generated by an RNA polymerase reaction using 10x DIG RNA labeling mix (ENZO). Tissue sections were post-fixed in 4% PFA in PBS (pH 7.4) for 20 minutes (min) at room temperature (RT). To enhance tissue penetration and decrease non-specific background staining, sections were acetylated with 0.25% acetic anhydride in 0.1 M triethanolamine and 0.06% HCl for 10 min at RT. Sections were pre-hybridized for 2 hrs at RT in hybridization buffer (50% formamide, 5x Denhardt's solution, 5x SSC, 250 µg/ml baker's yeast tRNA and 500 µg/ml sonicated salmon sperm DNA). Hybridization was performed for 15 hrs at 68°C, using 400 ng/ml denatured DIG-labeled probe diluted in hybridization buffer. After hybridization, sections were first washed briefly in 2x SSC followed by incubation in 0.2x SSC for 2 hrs at 68°C. Sections were adjusted to RT in 0.2x SSC for 5 min. DIG-labeled RNA hybrids were detected with anti-DIG Fab fragments conjugated to AP (Boehringer) diluted in 1:2500 in TBS (pH 7.4) overnight at 4°C. Binding of AP-labeled antibody was visualized by incubating the sections in detection buffer (100 mM Tris-HCl, pH 9.5, 100 mM NaCl and 50 mM MgCl<sub>2</sub>) containing 240 µg/ml levamisole and nitroblue tetrazolium chloride/5-bromo-4-chloro-3-indolyl-phosphatase (NBT/BCIP, Roche) for 14 hrs at RT. Sections subjected to the entire *in situ* hybridization procedure, but with no probe or sense probe added, did not exhibit specific hybridization signals. The specificity of the *in situ* hybridization procedure was also inferred from the clearly distinct gene expression patterns observed. Staining was visualized using a Zeiss Axioskop 2 microscope.

## **Immunohistochemistry**

Sections were washed in PBS (pH 7.4), blocked in blocking buffer (PBS, 5% horse serum (Sigma-Aldrich), 1% bovine serum albumin (BSA), 1% glycine, 0.1% lysine and 0.4% Triton) for 1 hr at RT, and incubated with primary antibodies in blocking buffer overnight at 4°C. Antibodies were used at the following dilutions; rabbit anti-Lrig2-C antibody (1 µg/ml) (Holmlund et al., 2004), goat anti-Neogenin antibody (1:200; AF1079; R&D systems), and mouse anti-NeuN antibody (1:400; MAB377, Millipore). The next day, sections were washed in PBS and incubated with the appropriate Alexa Fluor-labeled secondary antibodies (1:500, Invitrogen) for 1 hr at RT. Sections were washed in PBS, counterstained with fluorescent Nissl

---

(1:500, NeuroTrace, Invitrogen) or DAPI (1:3,000, Invitrogen) for 15 min at RT, washed in PBS and embedded in Mowiol (Sigma-Aldrich). Staining was visualized using a Zeiss Axioskop 2 microscope and an Olympus FluoView FV1000 confocal microscope.

## **Dissociated Primary Neuron Cultures**

Mouse E14.5 cerebral cortices were dissected and dissociated in 0.25% trypsin (PAA) in DMEM/F12 (Gibco, Invitrogen) for 15 min at 37°C. Trypsin was inactivated by adding an equal volume of DMEM/F12 containing 20% fetal bovine serum (FBS, Lonza, BioWhittaker). The trypsinized cerebral cortices were further dissociated by trituration in DMEM/F12 containing 10% FBS and 20 µg/ml DNase I (Roche) using a fire-polished Pasteur pipette. Dissociated cortical neurons were cultured in Neurobasal medium (NB; Gibco, Invitrogen) containing 2 mM L-glutamine (PAA), 1x penicillin/streptomycin (pen/strep, PAA), and B-27 supplement (Gibco, Invitrogen) on 100 µg/ml poly-D-lysine (Sigma-Aldrich) and 40 µg/ml laminin (Invitrogen) coated, acid-washed coverslips in a humidified atmosphere with 5% CO<sub>2</sub> at 37°C. Neurons were transfected with DNA constructs and siRNA (mouse Lrig2 or scrambled non-targeting control pool, ON-TARGETplus, Dharmacon) at DIV1 using Lipofectamine 2000 (Invitrogen). In brief, 400 ng DNA and 40 pmol siRNA per well was mixed with 3 µl of Lipofectamine 2000 in 200 µl of NB, incubated for 30 min, and then added to the neurons in NB at 37°C in 5% CO<sub>2</sub> for 45 min. Next, neurons were washed with NB, transferred to the original medium, and kept for 2 days at 37°C in 5% CO<sub>2</sub>.

Primary hippocampal cultures were prepared from E18 rat embryos. Cells were plated on coverslips coated with poly-L-lysine (30 µg/ml) and laminin (2 µg/ml) at a density of 100,000 cells/well. Hippocampal cultures were grown in NB supplemented with B27, 0.5 mM glutamine, 12.5 µM glutamate and penicillin/streptomycin. Hippocampal neurons were co-transfected with DNA constructs and siRNAs (rat Lrig2 or scrambled non-targeting control pool, ON-TARGETplus, Dharmacon) using Lipofectamine 2000 (Invitrogen) as described above at DIV1 (live experiments) or at DIV4 (fixed experiments).

## **Immunocytochemistry**

Cells were fixed with 4% PFA for 15 min at RT and washed in PBS (pH 7.4). Cells were permeabilized and blocked in blocking buffer (PBS, 4% bovine serum albumin (BSA) and 0.1% Triton X-100) for 1 hr at RT. Cells were incubated with rabbit anti-Lrig2-C (0.5 µ/ml) in blocking buffer for 2 hrs at RT. Cells were washed in PBS and incubated with Alexa Fluor-labeled goat anti-rabbit secondary antibodies (1:500; Invitrogen) for 1 hr at RT. Dissociated E14.5 cortical neurons were fixed and incubated in blocking solution for 1 hr at RT and incubated with



rabbit anti-Lrig2-C antibody (1 µg/ml) and goat anti-Neogenin antibody (1:400; AF1079, R&D systems) in blocking solution overnight at 4°C. The next day, cells were washed in PBS and incubated with the appropriate Alexa Fluor-labeled secondary antibodies (1:500; Invitrogen) for 1 hr at RT. Staining was visualized using a Zeiss Axioskop 2 microscope and an Olympus FluoView FV1000 confocal microscope.

## Plasmid Construction

A biotin- and GFP-tagged full-length human Lrig2 cDNA (pcDNA3.1-Lrig2FL-GFP-Bio) was generated by subcloning a GFP-biotin tag (Groen et al., 2013) C-terminal to the full-length Lrig2 coding sequence amplified from wild type Lrig2 cDNA (pCMV-hLrig2) in a pcDNA3.1(-)/myc-his (Invitrogen) vector backbone. Similarly, biotin-GFP tagged Neogenin cDNA was generated (pcDNA3.1-NeoFL-GFP-Bio) by amplification from full-length mouse Neogenin cDNA (pCMVXL-6-Neogenin; a kind gift of Stephen Strittmatter, Yale School of Medicine). To generate pHLuorin-Neogenin full-length Neogenin was amplified and SacI/KpnI restriction sites were introduced, followed by cloning into the pHLuorin-C3 vector (a kind gift from Ruud Toonen, VU Amsterdam). The Neogenin intracellular domain (NeolCD; 1158-1492) was subcloned C-terminal to the GFP sequence of a modified pEGFP-C1 vector expressing a biotin-GFP fusion protein to generate a biotin-GFP-NeolCD-expression vector (pEGFP-Bio-GFP-NeolCD). Full-length and truncated myc-tagged mouse Neogenin constructs were created by subcloning fragments into the GW1-myc vector using AgeI/BglII restriction sites. Full-length mouse Lrig2 and Lrig2 truncation mutants were amplified from pCDH-Lrig2 (a kind gift from Dennis Selkoe, Harvard Medical School) and subcloned into the GW1-myc vector using HindIII/BglII restriction sites. The myc-tag was replaced by cloning a V5 tag into the GW1-myc backbone, using Sall/EcoRI restriction sites, to generate a GW1-Lrig2-FL-V5 vector.

For RNA interference experiments, DNA fragments encoding short hairpin (sh) RNAs directed against mouse Lrig2 (sequences listed in Table below) were cloned into pSuper, using BglII/HindIII restriction sites (Brummelkamp et al., 2002). A pSuper vector expressing a scrambled, non-targeting shRNA (sequence listed in Table below) was used as a control. A full-length Lrig2 rescue construct (GW1-Lrig2-RS-A-V5) insensitive to shLrig2-A was created by introducing non-coding point mutations into the GW1-Lrig2-FL-V5 vector (for the mutated target site see Table below). Primers containing the point mutations were used to amplify the construct, followed by DpnI digestion and transformation. The insertion of the mutation was confirmed by sequencing and loss-of-sensitivity to shLrig2-A was shown by Western Blot.

---

For production of Fc-tagged RGMa, the extracellular domain of RGMa lacking the GPI link was cloned into a pHLSec backbone vector (Aricescu et al., 2006). pEFBOS-Sema4D-Flag was a kind gift from Atsushi Kumanogoh (Osaka University) (Kumanogoh et al., 2000). NCAM1-GFP was as reported previously (Van Battum et al., 2014). The expression vector containing mouse ADAM17 (ADAM17/TACE-pcDNA3.1) was as reported previously (Okamura et al. 2011).

## **Immunoprecipitation**

Immunoprecipitation of biotin-tagged proteins was performed as described previously (Groen et al., 2013). HEK-293 cells co-transfected with a cDNA encoding the biotin ligase BirA and the indicated biotin-tagged cDNA constructs (1:1.5), were collected in ice-cold PBS and centrifuged at 300 rcf for 5 min in a pre-cooled centrifuge at 4°C. Cell pellets were lysed in lysis buffer (20 mM Tris-HCl, pH 8.0, 150 mM KCl, 1% Triton X-100, 0.2 µg/µl, phosphatase inhibitor cocktail (Sigma-Aldrich) and Complete protease inhibitor cocktail (Roche)), incubated on ice for 15 min and centrifuged at 14,000 rpm for 15 min at 4°C. Cleared supernatant was mixed with 25 µl (volume of original suspension) paramagnetic streptavidin beads (Dynabeads M-280, Invitrogen), which had been blocked in 125 µl blocking buffer (20 mM Tris-HCl, pH 8.0, 150 mM KCl, 20% glycerol and 200 ng/µl albumin from chick egg white (Sigma-Aldrich)) at 4°C. After 1 hr incubation at 4°C, beads were washed 4 times in washing buffer (20 mM Tris-HCl, pH 8.0, 150 mM KCl, 0.1% Triton X-100 and Complete protease inhibitor cocktail). Precipitated proteins were eluted by boiling the beads in NuPAGE LDS sample buffer (Invitrogen) containing 2.5% β-mercaptoethanol for 10 min at 70°C.

For endogenous-pull down and co-immunoprecipitation experiments, P0 mouse brains, N1E-115 or HEK293 cells were lysed in lysis buffer (20 mM Tris-HCl, pH 8.0, 150 mM NaCl, 1% NP-40, 10% glycerol and Complete protease inhibitor cocktail), incubated for 30 min (tissue) or 10 min (cells) rotating at 4°C and centrifuged at 14,000 rpm for 15 min at 4°C. Cleared supernatants or conditioned culture medium samples were incubated with 1 µg/ml sample of the indicated antibodies at 4° C. After 2 hrs, 10 µl/ml sample protein A/G Dynabeads (Invitrogen), which had been blocked in blocking buffer, were added and samples were incubated for 1 hr rotating at 4°C. Pull down samples were washed 3 times in washing buffer (20 mM Tris-HCl, pH 8.0, 150 mM NaCl, 1% NP-40 and 10% glycerol) and precipitated proteins were eluted by boiling in NuPAGE LDS sample buffer containing 2.5% β-mercaptoethanol for 10 min at 70°C.

## **In-Gel Analysis**

Pull-down samples were separated in a NuPAGE Novex 4-12% Bis-Tris gradient gel following the manufacturer's description (Invitrogen). For mass spectrometry

analysis, proteins were visualized using GelCode Blue Stain Reagent (Pierce). Silver staining was used to detect differential protein bands. The gel was soaked twice in 50% methanol, followed by 10 min incubation in 5% methanol. After 3 rinses in water, the gel was incubated in 10  $\mu$ M dithiothreitol (DTT) for 20 min, followed by 0.1% (w/v) AgNO<sub>3</sub> for 20 min. The gel was washed once in water and twice in developer solution (3% (w/v) Na<sub>2</sub>CO<sub>3</sub> and 0.02% (w/v) formaldehyde). The gel was incubated in the developer solution until protein bands appeared. The staining reaction was stopped by adding 5% (w/v) citric acid.

### **Gel Digestion and Nanoflow LC-MS/MS Analysis**

1D SDS-PAGE gel lanes were cut into 2-mm slices using an automatic gel slicer and subjected to in-gel reduction with DTT, alkylation with iodoacetamide and digestion with trypsin (Promega, sequencing grade), essentially as described previously (Wilm and Mann 1996). Nanoflow LC-MS/MS was performed on a CapLC system (Waters, Manchester, UK) coupled to a Q-TOF Ultima mass spectrometer (Waters, Manchester, UK) operating in positive mode and equipped with a Z-spray source. Peptide mixtures were trapped on a Jupiter<sup>TM</sup> C18 reversed phase column (Phenomenex; column dimensions 1.5 cm  $\times$  50  $\mu$ m, packed in-house) using a linear gradient from 0 to 80% B (A = 0.1 M acetic acid; B = 80% (v/v) acetonitrile, 0.1 M acetic acid) in 70 min and at a constant flow rate of 200 nl/min using a splitter. The column eluent was directly sprayed into the ESI source of the mass spectrometer. Mass spectra were acquired in continuum mode; fragmentation of the peptides was performed in data-dependent mode. Peak lists were automatically created from raw data files using the Protein Lynx Global Server software (version 2.0). The background subtraction threshold for noise reduction was set to 35% (background polynomial 5). Smoothing (Savitzky-Golay) was performed (number of interactions: 1, smoothing window: 2 channels). Deisotoping and centroiding settings were: minimum peak width: 4 channels, centroid top: 80%, TOF resolution: 5000, NP multiplier: 1. Mascot search algorithm (version 2.0, MatrixScience) was used for searching against the NCBI nr database that was available on the MatrixScience server. The peptide tolerance was typically set to 150 ppm and the fragment ion tolerance was set to 0.2 Da. A maximum number of 1 missed cleavage by trypsin was allowed and carbamidomethylated cysteine and oxidized methionine were set as fixed and variable modifications, respectively.

### **Western Blotting**

Cells were collected in ice-cold PBS (pH 7.4) with a cell scraper and centrifuged at 1,000 rpm for 5 min in a pre-cooled centrifuge at 4°C. The cell pellet was resuspended in ice-cold lysis buffer (20 mM Tris-HCl, pH 8, 150 mM KCl, 1%

.....

Triton X-100 and Complete protease inhibitor cocktail (Roche)), incubated on ice for 10 min, followed by centrifugation at 14,000 rpm for 10 min at 4°C. The supernatant was collected, NuPAGE LDS sample buffer (Invitrogen) containing 2.5%  $\beta$ -mercaptoethanol was added, and samples were boiled for 5 min at 95°C. Proteins were separated on an 8% SDS-PAGE gel and transferred onto nitrocellulose membrane (Hybond-C Extra; Amersham). Membranes were incubated in blocking buffer (TBS, 0.05% (v/v) Tween 20 and 5% milk powder) for 30 min at RT, followed by incubation with primary antibody in blocking buffer overnight at 4°C. Antibodies used were: goat anti-Neogenin antibody (1:2,000; AF1079; R&D systems); rabbit anti-GFP (1:3,000; A11122; Invitrogen); mouse anti-V5 antibody (1:5,000; R960-25; Novex, Invitrogen); mouse anti- $\alpha$ -Tubulin antibody (1:8,000; T5168; Sigma-Aldrich); rabbit anti-Lrig2-C antibody (0.1  $\mu$ g/ml); anti-Myosin X antibody; goat anti-ADAM17/TACE (1:500; sc-6416; Santa Cruz); mouse anti-c-myc (1:2,000; 9E10; Roche); mouse anti-Flag (1:1,000; 200472, Stratagene). The rabbit anti-Lrig3-207 antibody against the peptide CGTFGKPLRRPHLDA (single-letter amino acid code) in the cytosolic tail of mouse Lrig3 was developed and affinity-purified as previously described for LRIG1 (Nilsson et al., 2003)(5  $\mu$ g/ml). Membranes were incubated with appropriate peroxidase conjugated secondary antibodies in blocking buffer for two hrs at RT, followed by incubation with SuperSignal West Dura Extended Duration Substrate (Pierce) and exposure to ECL films (Pierce). Films were digitized and quantified by measuring background corrected band intensities using ImageJ. Intensities were normalized to the appropriate control band for each film. Every experiment was repeated and quantified at least three times.

## **Cell Culture and Transfection**

COS-7, HEK293 and N1E-115 cells were maintained in high glucose Dulbecco's modified Eagle's medium (DMEM; Gibco, Invitrogen). CHO and stable RGMa-expressing CHO (CHO- RGMa) cell lines were as described previously (Hata *et al.* 2006). CHO cells were cultured in Ham's F12 Nutrient Mixture (Gibco, Invitrogen). COS-7, HEK293 and CHO cell culture media were supplemented with 10% (v/v) heat-inactivated (FBS; Lonza, BioWhittaker), 2 mM L-glutamine (PAA), and 1x pen/strep (PAA). N1E-115 cell culture medium was supplemented with 2% FBS and 1x pen/strep. CHO cells were cultured in the presence of 300  $\mu$ g/ml hygromycin B (Roche). All cells were cultured in a humidified atmosphere with 5% CO<sub>2</sub> at 37°C. COS-7 cells and HEK293 cells were transfected using polyethylenimine (PEI; Polysciences). N1E-115 cells were transfected using Lipofectamine 2000 (Invitrogen).

## RGMa Protein Production

For alkaline phosphatase (AP)- and Fc-tagged protein production, HEK293 cells were transfected with AP-Fc (a kind gift from Roman Giger, University of Michigan), RGMa-AP (APtag5-RGMa-AP; a kind gift from Thomas Skutella, University Heidelberg), or RGMa-Fc and cultured in Opti-MEM reduced serum medium (Gibco, Invitrogen) supplemented with 3% FBS (Lonza, BioWhittaker), 2 mM L-glutamine (PAA), and 1x pen/strep (PAA). Cell culture medium containing AP-tagged proteins was collected after 5 days in culture, filter-sterilized and stored at 4°C. If required, culture medium was concentrated using Centriprep YM-50 centrifugal filter units (Millipore). The concentration of AP-tagged proteins was determined by measuring the spectrophotometric absorbance after incubation with SEAP detection buffer (20 mM 1-Homoarginine, 1 mg/ml BSA, 24 mM p-Nitrophenyl phosphate, 2 M diethanolamine, pH 9.8, 500  $\mu$ M MgCl<sub>2</sub>). Cell culture medium containing RGMa-Fc was collected after 5 days in culture and filter sterilized. RGMa-Fc-containing culture medium was incubated with protein A-agarose (Roche) on a roller overnight at 4°C. The next day, beads with bound RGMa-Fc were washed in ice-cold PBS. Beads were incubated with 100 mM glycine (pH 2.5) to elute RGMa-Fc from the beads. Eluted RGMa-Fc protein was neutralized through addition of 10 mM Tris-HCl (pH 9.5). RGMa-Fc was dialyzed against PBS using centrifugal filter units (Amicon Ultra, 0.5 ml, 10K, Ultracel-10K membrane; Millipore). Protein concentration was determined by in-gel analysis of GelCode Blue Stain Reagent (Pierce) stained SDS-PAGE gels using a BSA standard curve. As a control, human IgG Fc fragment (Calbiochem) was used.

## AP Cell Binding

COS-7 cells were transfected with wild type mouse Neogenin (pCMVXL-6-Neogenin) or GW1-Lrig2-V5. At DIV2, the culture medium was replaced by HBHA buffer (20 mM HEPES, pH 7.0, 1x Hank's balanced salt solution (HBSS; GIBCO, Invitrogen) and 0.5 mg/ml BSA) for 15 min at RT. Subsequently, cells were incubated with medium containing AP or RGMa-AP for 75 min, while gently rotating at RT, followed by 4 washes in HBHA buffer. Then, cells were incubated in fixative (20 mM HEPES, pH 7, 60% (v/v) acetone and 3.7% formaldehyde) for 30 seconds, followed by 2 washes in HBHA. HBHA was replaced by HBS (20 mM HEPES, pH 7.0, 150 mM NaCl) and endogenous phosphatase activity was heat-inactivated by incubation at 65°C for 90 min. Cells were equilibrated in detection buffer (100 mM Tris-HCl, pH 9.5, 100 mM NaCl and 5 mM MgCl<sub>2</sub>) and bound AP-protein was visualized by incubation in detection buffer containing levamisole and NBT/BCIP (Roche). The specificity of RGMa-AP protein binding was confirmed by competition with excess RGMa protein. Furthermore, no staining was observed for AP only.



---

## Neurite Growth Assay

Dissociated cortical mouse neurons (400,000 neurons/50  $\mu$ l sample) were electroporated with 4  $\mu$ g DNA in 50  $\mu$ l electroporation buffer (135 mM KCl, 2 mM MgCl<sub>2</sub>, 0.2 mM CaCl<sub>2</sub> and 5 mM EGTA, pH 7.3) using a BTX Electro Square Porator ECM 830 (BTX Harvard Apparatus; settings: 100 V, 3 pulses, 900  $\mu$ s pulse length, 2 s pulse interval). 170  $\mu$ l 37°C RPMI 1640 medium (Gibco, Invitrogen) was added to the electroporation sample and electroporated neurons were transferred to 4 wells of a 24-well plate. Electroporated neurons were cultured on a confluent layer of CHO-K1 (CHO-Control) or CHO-RGMA cells in DMEM/F12 (Gibco, Invitrogen) containing 2% FBS (Lonza, BioWhittaker), 2 mM L-glutamine (PAA), 1x pen/strep (PAA), and B-27 Supplement (Gibco, Invitrogen) in a humidified atmosphere with 5% CO<sub>2</sub> at 37°C. Where indicated, 10  $\mu$ M TAPI-1 (Millipore) dissolved in DMSO or DMSO alone was added 24 hrs before fixation. After 4 days, cells were fixed with 4% PFA for 15 min at RT and washed in PBS (pH 7.4). Cells were permeabilized and blocked in blocking solution (PBS, 4% BSA and 0.1% Triton X-100) for 1 hr at RT and incubated with rabbit anti-GFP (1:3,000; A11122; Invitrogen) and mouse anti- $\beta$ -III-Tubulin (1:5,000; T8660, Sigma) in blocking solution overnight at 4°C. The next day, cultures were washed in PBS and incubated with Alexa Fluor-594 goat anti-mouse and Alexa Fluor-488 goat anti-rabbit (1:750; Invitrogen) for 1 hr at RT. Images were taken using a Cellomics ArrayScan VTI HCS Reader (Thermo Scientific) and the length of the longest neurite was measured using NeuronJ. Three separate wells per condition were analyzed and >75 neurites per well were measured. Data were statistically analyzed by two-way ANOVA and represented as means  $\pm$  S.E.M.

## RhoA Pull-down Assay

Primary dissociated cortical neurons were prepared from the cortex of embryonic day 18 (E18) mice. Cells were gently dissociated after digestion with 0.25% trypsin (Gibco/Invitrogen, Paisley, UK) and DNase1 (Takara, Shiga, Japan) at 37°C for 15 min. Cells were washed and resuspended in mouse neuron nucleofector solution (Lonza Cologne AG, Cologne, Germany) to a final concentration of 5 x 10<sup>6</sup> cells/100  $\mu$ l. 500 pmol of siRNA was added to the cell-nucleofector solution complex, gently mixed and transferred into a cuvette, followed by nucleofection using the nucleofector program O-05. Immediately after electroporation, 500  $\mu$ l of DMEM/F12 containing 10% FBS was added to the cells, and the cell suspension was transferred into the poly-L-lysine-coated dishes. The medium was replaced with fresh DMEM/F12 containing B27 after 3 hrs, and the cells were incubated for an additional 72 hrs. The cells were treated with or without 2  $\mu$ g/ml RGMA (R&D systems) for 15 min, and subjected to the Rho pulldown assay.

The Rho pulldown assay was modified from a previously described protocol (Ren and Schwartz, 2000). Cells were lysed in lysis buffer containing 50 mM HEPES (pH 7.5), 1% Nonidet P-40, 150 mM NaCl, 30 mM MgCl<sub>2</sub>, 5% glycerol, 1 mM Na<sub>3</sub>VO<sub>4</sub>, 10 mM NaF, 1 mM DTT, 10 µg/ml leupeptin, and 10 µg/ml aprotinin, followed by centrifugation at 4°C at 15,000 rpm for 10 min. To collect active Rho protein, supernatants were incubated with 50 µg of Rho-binding domain of rhotekin beads at 4 °C for 45 min. The beads were washed four times with lysis buffer and subjected to SDS-PAGE followed by western blotting using anti-RhoA antibody. Whole cell lysates were also subjected to Western blotting for total RhoA. RhoA activation was assessed by comparing the band intensities of active RhoA bands with those of total RhoA in each lane using Multi Gauge software (Fuji Film Corporation, Tokyo, Japan). Results are shown as fold increase relative to control values. Data are shown as the means ± S.E.M. of four independent experiments. Statistical analyses were performed using one-way ANOVA, followed by Tukey-Kramer's test.

### Optic Nerve Injury

siRNA targeting mouse Neogenin and a scrambled control siRNA were obtained from Sigma-Aldrich (St Louis, MO, USA), as described previously (Hagihara et al., 2011). The siRNA targeting Lrig2 was as described above. 3-week-old C57BL/6J mice were obtained from Charles River Laboratories. Optic nerve injury was performed as previously described (Fujita et al., 2011). The left optic nerve was crushed with fine forceps for 10 sec approximately 1 mm posterior of the optic disc. 3 µl of a solution containing 1.5-2.0 µg of siRNA was injected intravitreally immediately following injury and on day 7 post-axotomy. At least 6 mice were used for each group. To visualize optic nerve axons, 1 µl of a solution containing cholera toxin β subunit (CTB) conjugated to Alexa Fluor-555 (2 µg/µl, Invitrogen) was injected intravitreally with a glass needle 12 days after the injury. On day 14 post-axotomy, mice were perfused with 4% PFA. The eye cups with the nerve segment were post-fixed, and immersed in 15–30% sucrose overnight at 4°C. Tissues were embedded in Tissue-Tek. Serial cross-sections (16 µm) were prepared using a cryostat and collected on MAS-coated glass slides (Matsunami, Osaka, Japan). CTB-labeled axons were visualized using DP Controller software (version 3.1.1.267; Olympus) on a microscope (BX51; Olympus) equipped with a camera (DP71; Olympus). Axonal regeneration was quantified by counting the number of CTB-labeled fibers extending 0.2, 0.5, and 1.0 mm from the distal end of the lesion site in 5 sections. The cross-sectional width of the optic nerve was measured at the point at which the measurements were taken and was used to calculate the number of axons per millimeter of nerve width. The number of axons per millimeter was then averaged over the 5 sections. Σad, the total number of

---

axons extending distance  $d$  in a nerve having a radius of  $r$ , was estimated by summing all the sections having a thickness  $t$  ( $16\ \mu\text{m}$ ):  $\Sigma ad = \pi r^2 \times [\text{average axons} / \text{mm}] / t$ . Statistical analysis were performed using Student's t-test.

### **Quantitative RT-PCR**

Total RNA was extracted from retinas by Trizol (Invitrogen). Gene specific quantitative RT-PCR was performed on 10 ng RNA per reaction in a 384 wells plate in triplicate using SYBR green RT-PCR kit (Qiagen) on a 7300 Fast Real-Time PCR system (Applied Biosystems). To control for (genomic DNA) contamination, samples with no template (water) and no reverse transcriptase (without enzyme mix) were run simultaneously for each RNA sample and each primer set. Primers for Neogenin and GAPDH were as described (Hagihara et al., 2011), primers for Lrig2 are listed in Table below. Ratios between GAPDH and Neogenin or Lrig2 were calculated to determine knockdown efficiency. RNA samples obtained from three retinas per condition were statistically analyzed using Student's t-test and shown as means  $\pm$ S.E.M.

### **Cell Surface Labeling and Internalization Assay**

Two days after transfection, coverslips with dissociated cortical mouse neurons were incubated on ice with anti-Neogenin antibody (1:200; AF1079, R&D) in conditioned medium for 20 min. Coverslips were returned to warm conditioned medium, where mentioned supplemented with  $3\ \mu\text{g}/\text{ml}$  RGMa-Fc or control Fc protein and incubated for 10 min in a humidified atmosphere with 5%  $\text{CO}_2$  at  $37^\circ\text{C}$ . For cell surface staining, coverslips were washed in warm NB medium and fixed in PBS with 4% PFA and 4% sucrose (4% PFA/suc) for 8 min at RT. For staining of internalized Neogenin, surface bound anti-Neogenin was stripped from the cell membrane by incubating in stripping buffer (0.5 M NaCl/0.2 M acetic acid) for three min on ice followed by a PBS wash, and fixation in 4% PFA/suc. After fixation, all coverslips were incubated in detergent free blocking buffer (PBS with 3% Normal Horse serum (NHS) and 1% BSA) containing donkey anti-goat Alexa Fluor-555 secondary antibody (1:500; Invitrogen) for 45 min (for surface staining) or with donkey anti-goat peroxidase conjugated antibody (for internalization assays). The coverslips were washed in PBS and fixed for 8 min in 4% PFA/suc, followed by 3 more PBS washes. Cells were permeabilized in blocking buffer supplemented with 0.1% Triton X-100 and incubated overnight at  $4^\circ\text{C}$  with primary antibody against GFP (1:3,000; A11122) only (for surface staining) or in combination with anti-Neogenin (1:200; AF1079; R&D). The following day, coverslips were washed with PBS and incubated with either donkey anti-rabbit Alexa Fluor-488 (1:500) alone (for surface staining) or both donkey anti-rabbit Alexa Fluor-488 and donkey anti-goat Alexa Fluor-555 (for internalization assays)

in blocking buffer for 1 hr at RT. Where mentioned, 10  $\mu\text{M}$  TAPI-1 (Millipore) dissolved in DMSO or DMSO alone was added to the culture medium 24 hrs prior to the experiment. Coverslips were mounted in Prolong Gold anti-fade reagent (Invitrogen). Pictures were taken using a Zeiss AxioScope microscope and 100x objective, with equal exposure times for all conditions within one experiment. The average fluorescence intensity of Neogenin staining in transfected growth cones was measured using ImageJ. Background was determined in areas without staining and subtracted from traced areas, after which mean signal intensity was determined. Per experiment at least 65 growth cones per condition were measured and normalized to the appropriate control condition. At least three separate experiments were performed and the normalized average was calculated for each condition. Data were statistically analyzed by two-way ANOVA and represented as means  $\pm$ S.E.M.

### FRAP Analysis

For quantitative fluorescence recovery after photobleaching (FRAP) experiments, neurons were transfected as described before, and imaged on an inverted research microscope Nikon Eclipse Ti-E (Nikon) equipped with Nikon CFI Apo TIRF 100x 1.49 N.A. oil objective (Nikon), CoolSNAP HQ2 CCD camera (Roper Scientific) and controlled with MetaMorph 7.7 software (Molecular Devices). The FRAP experiments were performed using the ILas2 system (Roper Scientific). Coverslips (18 mm) were mounted in metal rings and maintained at 37°C and 5% CO<sub>2</sub> in a stage top incubator INUBG2E-ZILCS (Tokai Hit). After acquisition of the baseline level, a circular area of  $\sim$ 1.5  $\mu\text{m}$  diameter was bleached with high laser power. To analyze the recovery of fluorescence, raw data were first adjusted by background subtraction at each time point and corrected for ongoing photobleaching. Recovery R was then calculated as  $R = (I(t) - I(\text{directly after bleaching})) / (I(\text{before bleaching}) - I(\text{directly after bleaching}))$ , with I denoting total intensity.

### ADAM17 Enzymatic Assay

Transfected HEK293 cells were lysed in lysis buffer (20 mM Tris-HCl, pH 7.4, 150 mM NaCl, 1% NP-40, and Complete protease inhibitor cocktail), incubated for 10 min rotating at 4°C and centrifuged at 14,000 rpm for 15 min at 4°C. Cleared supernatants were diluted in assay buffer (50 mM Tris, pH 7.4 and Complete protease inhibitor cocktail) and incubated with 2  $\mu\text{g}/\text{ml}$  recombinant mouse ADAM17 (r-ADAM17; 2978-AD-010, R&D Systems) for 10 min at 37°C. The enzymatic reaction was ended by adding NuPAGE LDS sample buffer containing 2.5%  $\beta$ -mercaptoethanol and heating for 5 min at 95°C. Control samples lacked r-ADAM17 but were otherwise treated equally. Blots were scanned and the intensity of full length Neogenin-bio-GFP and fragment was measured. The ratio

between full length and fragment was determined for each sample and Lrig2-FL samples were normalized to empty vector per experiment. Four separate experiments were performed and data were analyzed by One Sample t-test and represented as means  $\pm$ S.E.M.

## Statistical Analyses

To avoid observer bias, all quantitative measurements in this study were assessed while being unaware of experimental condition. During analysis, raw data were named in a descriptive way, without revealing experimental group information. (Fluorescent) microscopic imaging was always done with the same settings within experiments, and analyzing techniques were standardized. A single person analyzed all data obtained within the experiments. All experiments were replicated at least three times.

### Table Primer and shRNA Sequences.

In the upper part, primers used to create *in situ* hybridization (ISH) probes for *Lrig1*, *Lrig2* and *Lrig3*, and to detect *Lrig2* in quantitative PCR (q-PCR) are listed. The size of the resulting PCR product is indicated in base pairs (bp). In the lower part, target site sequence in *Lrig2* for shLrig2-A, -B, and -C, in *Lrig3* for shLrig3-D, -E, and -F, and the corresponding rescue site containing synonymous point mutations for Lrig2-RS-A (in bold) are given. All sequences are from '5 to '3. For information on siRNAs please see ON-TARGET plus siRNA library (<http://dharmacon.gelifsciences.com>).

Primer sequences:			
ISH	Forward	Reverse	Size(bp)
Lrig1	GACAGCTGCCCCACATACAA	TAGCTTCTCGGTGCCAATAGC	528
Lrig2	TGCCTTTGTGGGCTCTGAGCTTAC	CCATATGGTGACATGGGTG	613
Lrig3	ATGTGGAAGCCGCTTC	GATTGAGTCCAGCTCTG	508
q-PCR	Forward	Reverse	
Lrig2	CAGTGCATCGCTGGAGGAAGTC	TACAATGATGAGAAGCTGATTGGCTGCA	116
Knockdown sequences:			
shRNAs	Target site	Rescue site in Lrig2-RS-A	
shLrig2-A	GCTAGAAGATGCTGGAAAA	ATTGGAGGACGCAGGAAAA	
shLrig2-B	AGTTAATCTTGCAAGGAAA		
shLrig2-C	CATTGTAGATGCTGGGCTA		
shLrig3-D	GCAAAGAAAACGGAGTGACA		
shLrig3-E	GGGTACATCTCTCAGAAA		
shLrig3-F	GGAATAACAAAGTCAGCTA		
scrambled	GACAACCAATCGTAATACA		



## Results

### Expression of Lrig Proteins in the Developing Nervous System

Lrigs are expressed in the human and rodent brain (Guo et al., 2004; Homma et al., 2009), but how these proteins contribute to CNS development remains unexplored. To address this question, we determined neural Lrig expression patterns by using *in situ* hybridization. All three *Lrigs* were expressed in the developing mouse brain and spinal cord, displaying clearly distinct patterns of expression (Figure 1B, S1, S2A). Expression of *Lrig1* was strong in the ventricular zones of the embryonic nervous system, while at P9 *Lrig1* was detected in differentiated neurons. *Lrig2* and *Lrig3* displayed overlapping patterns of expression but expression of *Lrig2* was more widespread, and several structures showed *Lrig2* but no *Lrig3* labeling (Figure 1B, S1). Because of the abundant expression of *Lrig2* and the paucity of knowledge about its functional role, we further focused on Lrig2. At E16.5, immunohistochemistry with Lrig2-specific antibodies showed strong Lrig2 expression in neurons in the cortical plate (CP), marginal zone (MZ) and ventricular zone (VZ) of the cortex, and in sensory neurons in dorsal root ganglia and the olfactory epithelium (Figure 1C, S2B, C). Immunocytochemistry on dissociated cortical neuron cultures revealed strong expression in the cell body and punctate staining in neurites and growth cones (Figure 1D). Overall, these experiments reveal specific patterns of neuronal expression for individual Lrigs and suggest a role for Lrig2 in neurites and their growth cones.

### Lrig2 Binds the Guidance Receptor Neogenin in Neurons

As a first step towards determining the function of Lrig2, we used a biotin-streptavidin-based purification method to identify Lrig2-interacting proteins (Figure 1E, F) (Groen et al., 2013). This system allowed for highly specific pull-down of biotinylated full-length Lrig2 using streptavidin-coated beads (Figure 1G). Silver staining revealed multiple specific Lrig2 interacting proteins (Figure 1G). In line with this observation, mass spectrometry analysis of the pull-down samples revealed many proteins that were present in Lrig2-GFP-Bio complexes, but not in control Bio-GFP complexes. In line with the vesicular distribution of Lrig2 in axons and growth cones, several of the intra- and extracellular candidate interactors had reported roles in axon growth and guidance, cytoskeletal organization, and intracellular transport (Table S1).

One of the candidate interactors was Neogenin, a cell surface receptor for RGMs, bone morphogenetic proteins (BMPs), and Netrins. In the nervous system Neogenin's role has been best-characterized as a growth cone receptor for RGMA (Figure 2A). To examine whether or not Lrig2 contributes to Neogenin-RGMA

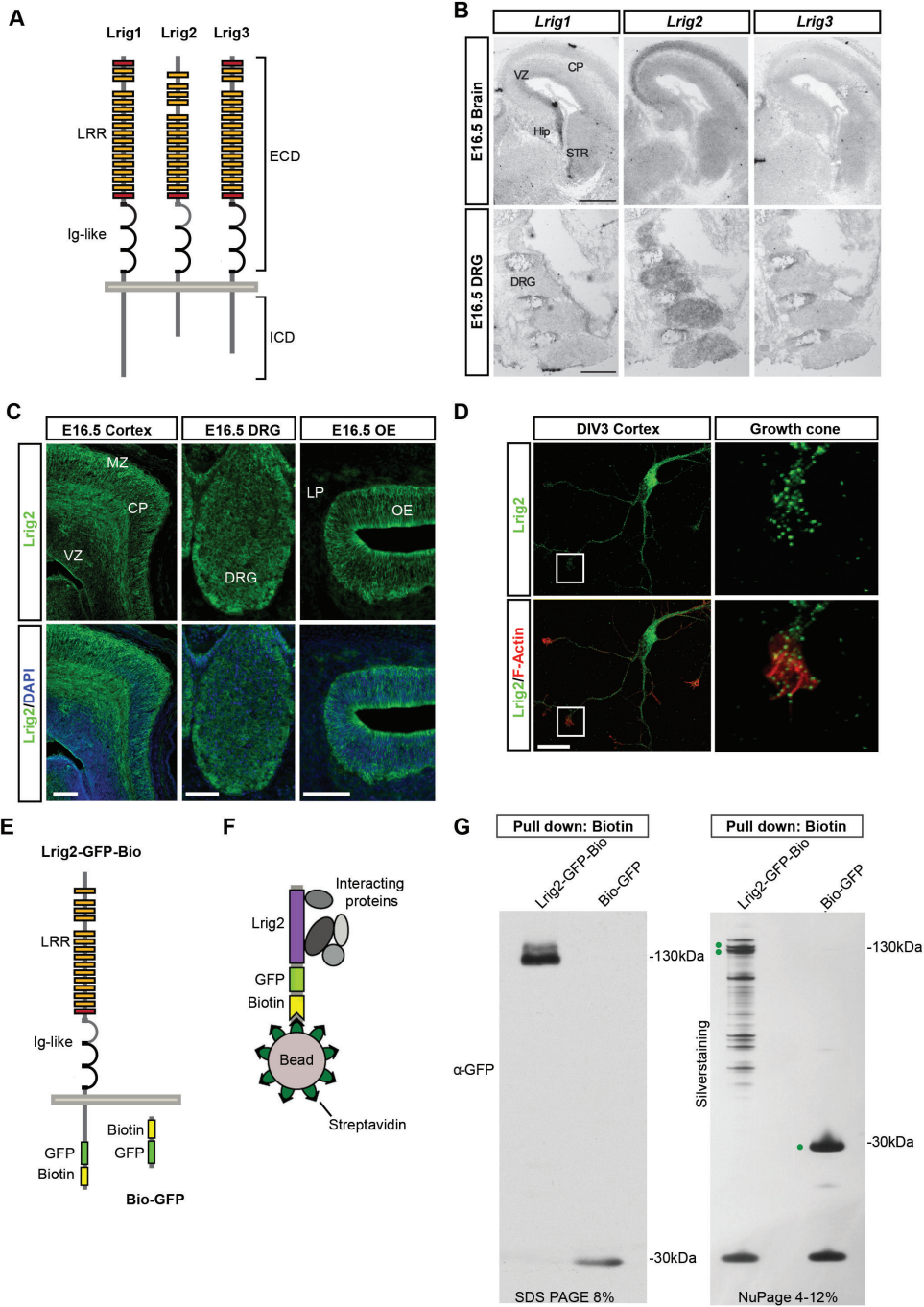


**Figure 1. Prominent Expression of Lrig2 During Neural Development.**

**A.** Schematic representation of the mouse leucine-rich repeats and immunoglobulin-like domains (Lrig) family. ECD, extracellular domain; ICD, intracellular domain; Ig, immunoglobulin; LRR, leucine-rich repeat. **B.** Representative images showing *in situ* hybridization for *Lrig1*, *Lrig2* or *Lrig3* on coronal (upper panels) and sagittal (lower panels) sections from E16.5 mouse embryos. Lrigs display distinct patterns of expression during neural development. CP, cortical plate; DRG, dorsal root ganglion; Hip, hippocampus; STR, striatum; VZ, ventricular zone. **C.** Representative images showing immunohistochemistry for Lrig2 in coronal sections of an E16.5 mouse embryo (green). Sections are counterstained with DAPI (blue, lower panels). LP, lamina propria; MZ, marginal zone; OE, olfactory epithelium. **D.** E14.5 mouse cortical neuron cultures analyzed at 3 days *in vitro* (DIV) by immunocytochemistry using anti-Lrig2 antibodies. Cultures were counterstained with phalloidin (red) to visualize F-actin. Right panels show a higher magnification of the boxed areas in the left panels. Lrig2 is expressed in a vesicular pattern in neurites and growth cones. **E.** Schematic representation of the biotin- and GFP-tagged Lrig2 proteins used in the streptavidin-based pull-down experiments in G. **F.** Schematic representation of the biotin-streptavidin pull-down assay. Lrig2-GFP-Bio or Bio-GFP are biotinylated by the co-transfected biotin ligase BirA and purified by precipitation using streptavidin-coated beads, along with interacting proteins. Purple region indicates full-length Lrig2. **G.** Streptavidin pull-down assays were performed on lysates of HEK293 cells co-expressing Bio-GFP or Lrig2-GFP-Bio and BirA. Proteins bound to streptavidin beads were analyzed by Western blotting using anti-GFP antibodies (left panel). The same samples were separated on a gradient gel followed by silver staining (right panel). Dots indicate Lrig2-GFP-Bio and Bio-GFP. Scale bars, B: 500  $\mu$ m, C: 100  $\mu$ m, D: 20  $\mu$ m. See also Figure S1, S2 and Table S1.

signaling, we first confirmed the interaction between Neogenin and Lrig2 in HEK293 cells transiently overexpressing full-length Neogenin (NeoFL-GFP-Bio) or the Neogenin intracellular domain (ICD; Bio-GFP-NeoICD). Lrig2 was detected following pull-down of NeoFL-GFP-Bio, but not Bio-GFP-NeoICD. In contrast, Myosin-X, which is known to interact with the Neogenin ICD (Zhu et al., 2007), co-precipitated with full-length Neogenin and the Neogenin ICD (Figure 2B). Next, we performed co-immunoprecipitation experiments from lysates derived from N1E-115 neuronal cells and also P0 brains using Neogenin- and Lrig2-specific antibodies. Endogenous Lrig2 co-precipitated with endogenous Neogenin from N1E-115 lysates, and vice versa (Figure 2C, D). Similarly, pull-down of Neogenin from P0 brain lysates resulted in co-precipitation of Lrig2 (Figure 2E). These results show that Neogenin and Lrig2 interact in endogenous protein complexes in the brain *in vivo*.

The interaction between Lrig2 and Neogenin in brain tissue suggests that both proteins co-localize in neurons. We therefore compared the expression patterns of both proteins in the mouse neocortex, in which Lrig2 (Figure 1) and Neogenin

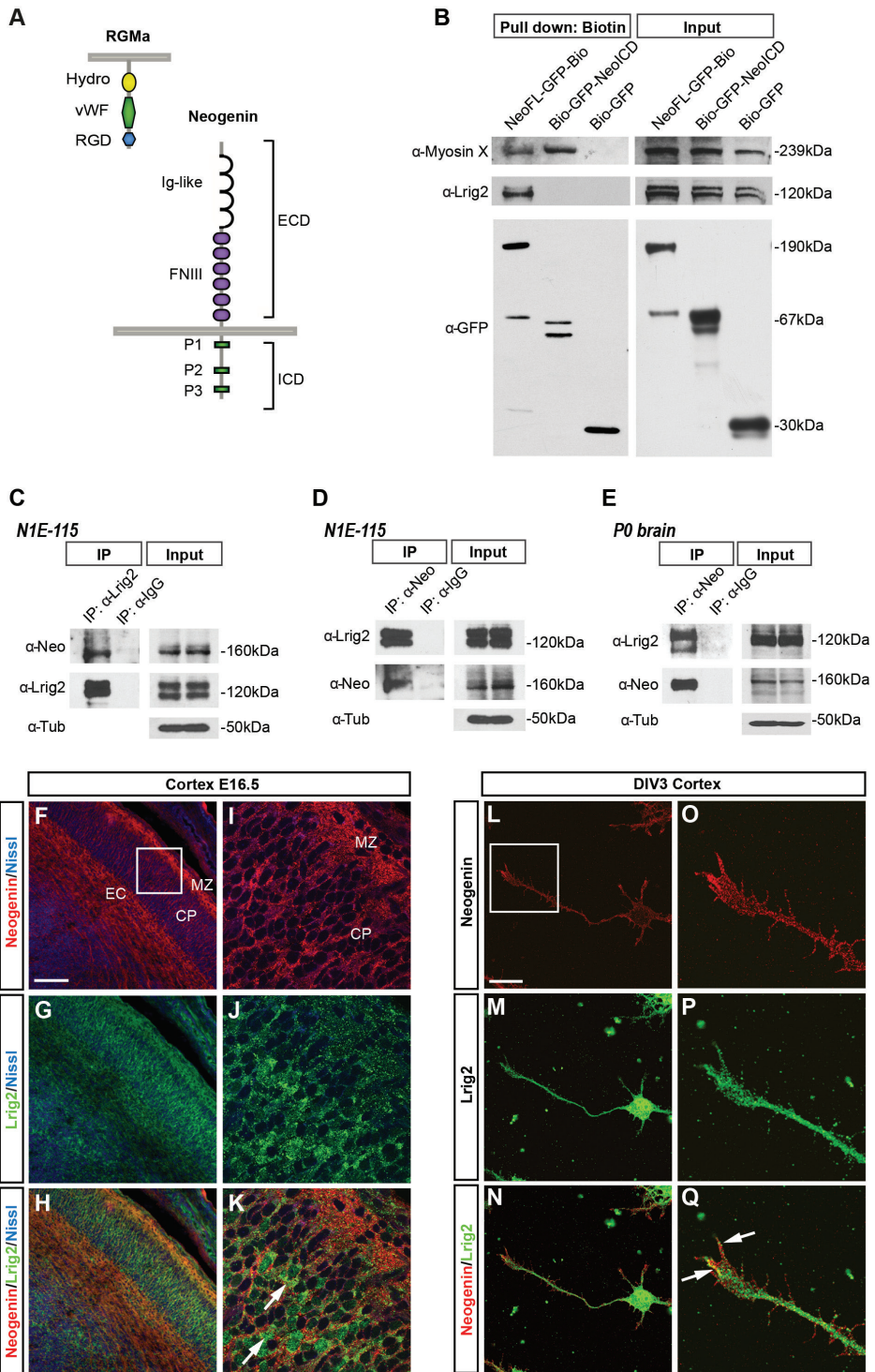


**Figure 2. Lrig2 Binds and Co-localizes with the RGMa Receptor Neogenin in Neurons.**

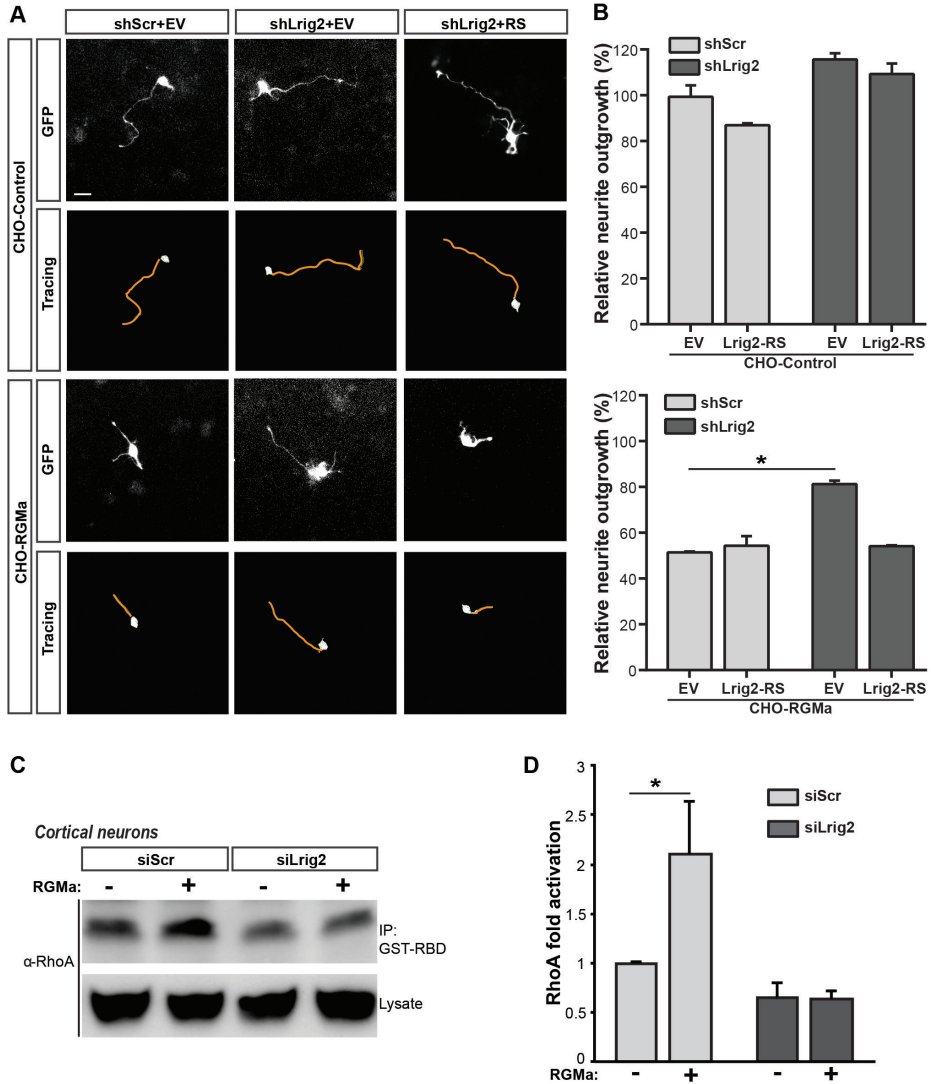
**A.** Schematic representation of Neogenin and its ligand RGMa (Repulsive Guidance Molecule a). ECD, extracellular domain; FNIII, fibronectin type III; Hydro, hydrophobic domain; ICD, intracellular domain; Ig, immunoglobulin; RGD, Arg-Gly-Asp; vWF, partial von Willebrand factor type D. **B.** Streptavidin pull-down assays were performed on lysates of HEK293 cells co-expressing Bio-GFP, NeogeninFL-GFP-Bio, or Bio-GFP-NeogeninICD together with BirA. Proteins bound to streptavidin beads were analyzed by Western blotting using the indicated antibodies. Myosin X is a known Neogenin interactor. Lrig2 binds full-length Neogenin, but not Neogenin ICD. **C, D.** Lysates of N1E-115 cells were immunoprecipitated with anti-IgG (control), anti-Lrig2 (C), or anti-Neogenin (D) antibodies. The immunoprecipitates were analyzed with the indicated antibodies. **E.** P0 mouse brain lysate was immunoprecipitated with anti-IgG and anti-Neogenin antibodies. The precipitates were analyzed with the indicated antibodies. Lrig2 and Neogenin bind in endogenous protein complexes. **F-K.** Immunohistochemistry for Neogenin (red) and Lrig2 (green) on E16.5 coronal mouse brain sections. Panels I-K show higher magnifications of the boxed area in F. Sections are counterstained with fluorescent Nissl (blue). Arrows indicate co-expression of Lrig2 and Neogenin in cortical neurons. CP, cortical plate; EC, external capsule; MZ, marginal zone. **L-Q.** Immunocytochemistry for Neogenin (red) and Lrig2 (green) on E14.5 dissociated cortical neurons at 3 DIV. Panels O-Q show higher magnifications of the boxed area in L. Arrows indicate areas of co-expression. Lrig2 and Neogenin are co-localized in cortical neurons *in vitro* and *in vivo*. All data represent at least three independent experiments. Scale bar, 20 µm.

(van den Heuvel et al., 2013) are known to be expressed. Immunohistochemistry revealed that at E16.5 the majority of neurons in the MZ and CP, and a subset of cortical axons in the external capsule (EC), co-expressed Neogenin and Lrig2 (Figure 2F-K). Immunostaining of dissociated cortical neurons showed punctate Neogenin and Lrig2 expression in the axon and growth cone. Although immunostaining for Neogenin and Lrig2 overlapped, vesicular structures expressing Neogenin but not Lrig2, and vice versa, were also observed (Figure 2L-Q). These results together with our biochemical data show that Lrig2 and Neogenin interact and partly co-localize in neurons.

**Neogenin and Lrig2 Interact Through Their Extracellular Domains**

To further define the interaction between Neogenin and Lrig2, a series of truncation mutants were generated for Lrig2 and Neogenin (Figure S3A, B) and used in pull-down assays from HEK293 cells. Lrig2 constructs containing the LRR and/or Ig-like domains showed binding to Neogenin (Figure S3C, E), indicating that at least two distinct regions in the Lrig2 ECD mediate its interaction with Neogenin. The Neogenin ICD region did not interact with Lrig2 (Figure 2B),





however, Neogenin proteins containing the Ig-like and/or FNIII regions bind Lrig2 (Figure S3D, F). Next we asked whether RGMa also binds Lrig2 by performing COS cell binding assays. Strong binding of alkaline phosphatase (AP)-tagged RGMa (RGMa-AP) was observed to cells expressing Neogenin but not to Lrig2-positive cells (Figure S3G). Thus, Neogenin-Lrig2 binding is mediated through interactions between at least two binding regions in the ECDs of each protein, with RGMa binding specifically to Neogenin (Figure S3H).

**Figure 3. Lrig2 is Required for RGMA-Induced Neurite Growth Inhibition and Signaling.**

**A.** Dissociated E14.5 cortical neurons were electroporated with GFP vector and different combinations of pSuper-shScr (shScr), pSuper-shLrig2 (shLrig2), empty GW1 vector (EV), or GW1-Lrig2-RS-A (RS) and grown on confluent layers of CHO-Control or CHO-RGMA cells. RS is a rescue construct that is not targeted by shLrig2. After 4 days *in vitro* DIV, cultures were fixed and immunostained with anti-GFP antibodies. Lower panels show tracing of the longest neurite in each example. Scale bar 50 $\mu$ m. **B.** Quantification of neurite length in cultures as in A. Graphs show average length of the longest neurite on CHO-Control cells (upper panel) and on CHO-RGMA cells (lower panel) normalized to control (shScr+EV on CHO-Control cells). Knockdown of Lrig2 blocks RGMA-induced neurite growth inhibition.  $n = 3$  experiments, >50 neurons per condition per experiment. \* $P < 0.05$ , two-way ANOVA. Data are presented as means  $\pm$  S.E.M. **C.** E18 cortical neurons electroporated with siScr or siLrig2 were incubated with 2  $\mu$ g/ml RGMA or control protein at DIV3. Cell lysates were subjected to active RhoA pull-down assays and cell lysates and pull-down samples were analyzed by Western blotting using anti-RhoA antibodies. **D.** Quantification of band intensities in experiments as shown in C. Signals from active RhoA bands are compared to those of total RhoA in each lane. Results are shown as fold change relative to control. Knockdown of Lrig2 inhibits RGMA-induced RhoA activation. \* $P < 0.05$ , one-way ANOVA followed by Tukey-Kramer's test. Data are presented as means (of four independent experiments)  $\pm$  S.E.M.

**Lrig2 Is Required for Neogenin-RGMA-Mediated Signaling and Neurite Growth Inhibition**

Binding of RGMA to Neogenin induces axon repulsion or growth inhibition, depending on the assay. To determine whether Lrig2 is required for RGMA-mediated neurite growth inhibition, we induced knockdown of Lrig2 in dissociated cortical neurons plated on a confluent layer of RGMA-expressing CHO cells (CHO-RGMA) or control CHO cells (CHO-Control), as described previously (Hata et al., 2006). Dissociated E14.5 mouse cortical neurons were electroporated with shLrig2 or scrambled control shRNA (shScr) in combination with GFP and either empty vector or Lrig2-RS, a rescue construct that is not targeted by shLrig2 (Figure S4A-D). Neurons were plated on CHO cells and visualized by anti-GFP immunostaining at 4 DIV (Figure 3A). Neurite outgrowth from cortical neurons electroporated with shScr and empty vector (EV) was significantly reduced on CHO-RGMA as compared to CHO-Control cells (Figure 3A, B). However, knockdown of Lrig2 significantly reduced this inhibitory effect of RGMA. Co-electroporation of shLrig2 and Lrig2-RS restored the sensitivity of neurites to RGMA, while electroporation of Lrig2-RS alone had no effect (Figure 3A, B).

Neurite growth inhibition by RGMA is dependent on the activation of RhoA downstream of Neogenin (Conrad et al., 2007; Hata et al., 2009). To query a role for Lrig2 in RGMA-dependent RhoA activation, Lrig2 knockdown was induced

---

in mouse cortical neuron cultures following which the activity of Rho was determined by affinity precipitation of GTP-bound RhoA. As reported previously, addition of 2  $\mu$ g/ml RGMa for 15 min to cultures electroporated with control siRNAs (siScr) led to a ~twofold increase in Rho activity. In contrast, no RGMa-induced increase in Rho activity was observed following knockdown of Lrig2 (siLrig2; Figure 3C, D, S4E). Thus, Lrig2 is required for RGMa-Neogenin-mediated signaling and neurite growth inhibition.

### **Lrig2 Regulates Neogenin Cell Surface Expression**

The next question we addressed was how Lrig2 influences RGMa-Neogenin signaling. A well-characterized effect of Lrigs is their ability to induce receptor ubiquitination and degradation (Gur et al., 2004; Laederich et al., 2004). However, knockdown of Lrig2 did not change Neogenin protein levels in total lysates from N1E-115 cells or Neogenin expression in somata or growth cones of primary cortical neurons (Figure 4A-C). Other previously reported effects of Lrigs, such as lipid raft recruitment (Ledda et al., 2008), were also unchanged for Neogenin following Lrig2 knockdown (data not shown). The cell surface levels of axon guidance receptors are tightly controlled to dictate signaling duration, magnitude and spatial activity. Therefore, we next explored the effect of Lrig2 on Neogenin cell surface expression. Dissociated cortical neurons were transfected at DIV1 with siRNAs together with GFP and immunolabeled with antibodies against Neogenin at DIV3 under non-permeabilizing conditions. Interestingly, a significant decrease in Neogenin surface intensity was observed in neurons transfected with siLrig2 as compared to siScr (Figure 4D, E). Thus, Lrig2 regulates Neogenin cell surface expression at the growth cone membrane.

### **Lrig2 Inhibits ADAM17-Mediated Cleavage of Neogenin**

Both Neogenin and Lrig2 are expressed in vesicular structures in the growth cone, which may represent exocytotic or endocytotic vesicles (Figure 2). Interestingly, defects in exocytosis or endocytosis may explain the reduction in Neogenin cell surface expression observed following Lrig2 knockdown. Therefore, we first examined a role for Lrig2 in the internalization of Neogenin. Antibodies directed against Neogenin were added to transfected cortical neurons and internalization of antibody-bound receptor complexes was allowed to occur. Next, cultures were fixed and the amount of internalized antibody was visualized. No differences in the amount of Neogenin internalization were detected between control or Lrig2 knockdown conditions (Figure 4F, G). To ask whether Lrig2 is involved in exocytosis of Neogenin receptors, hippocampal neurons were transfected with pHluorin-tagged Neogenin in combination with siRNAs following which we examined fluorescence recovery after photobleaching (FRAP) of pHluo-

Neogenin. In neurons cotransfected with scrambled siRNAs, pHLuo-Neogenin fluorescence recovered to  $50\% \pm 5\%$  of prebleached intensity after  $\sim 8$  seconds with an average recovery half-time of  $1.16 \pm 0.03$  seconds. A similar recovery was observed following knockdown of Lrig2 (Figure 4H-J, S4F). Overall, these data suggest that exo-endocytic recycling of Neogenin is independent of Lrig2.

An alternative explanation for the effect of Lrig2 on Neogenin cell surface expression is that Lrig2 regulates Neogenin ectodomain shedding. Cleavage by ADAM17 releases the Neogenin ECD and desensitizes cortical neurons to the repulsive effects of RGMa (Goldschneider et al., 2008; Okamura et al., 2011). Because Lrig2 and Neogenin interact through their ECDs, we hypothesized that Lrig2 physically interferes with ADAM17-mediated cleavage of Neogenin. If so, knockdown of Lrig2 would lead to enhanced shedding and reduced Neogenin cell surface expression. To test this model, dissociated cortical neurons were transfected with siRNAs and cultured in the presence of TAPI-1, an inhibitor of ADAM17 and other metalloproteases, or vehicle. Knockdown of Lrig2 induced a significant decrease in cell surface Neogenin expression, but this effect was not observed in the presence of TAPI-1. Further, TAPI-1 did not affect Neogenin growth cone cell surface expression in control neurons (Figure 4K, L). This latter effect is intriguing since TAPI-1 was previously reported to reduce constitutive Neogenin shedding in primary cortical neuron cultures (Okamura et al., 2011). One explanation for this difference is that ADAM17 mediates constitutive Neogenin shedding in some but not all subcellular compartments. Next, HEK293 cells were transfected with Neogenin-Bio-GFP and a combination of ADAM17 and/or Lrig2 constructs. HEK293 cells express ADAM17, and Neogenin-bio-GFP was cleaved by endogenous ADAM17 (e.g. Figure 5E). However, co-transfection of ADAM17 greatly enhanced Neogenin cleavage and was therefore used. ADAM17-mediated Neogenin cleavage was reduced by co-transfection of full-length LLrig2 or the Lrig2 ECD but not by the Lrig2 ICD (Figure 5A-D). Furthermore, while Lrig1 is an ADAM17 substrate (Yi et al., 2011) no Lrig2 cleavage by ADAM17 was observed (Figure 5B). These data show that binding of Lrig2 to Neogenin blocks ADAM17-induced cleavage and that the Lrig2 ECD mediates this inhibitory effect.

The activity of ADAM17 can be regulated through extra- and intracellular mechanisms (Scheller et al., 2011). Lrig2 binds the ECD of Neogenin, and the Lrig2 ECD is sufficient to block cleavage of Neogenin. This suggests that Lrig2 is an extracellular regulator of ADAM17. To provide further support for this model, we incubated lysates of HEK293 cells transfected with Neogenin-Bio-GFP and empty vector (EV) or Lrig2-FL with recombinant ADAM17 extracellular domain (r-ADAM17). As predicted, addition of r-ADAM17 enhanced Neogenin cleavage in the absence, but not presence, of Lrig2 (Figure 5E, F).

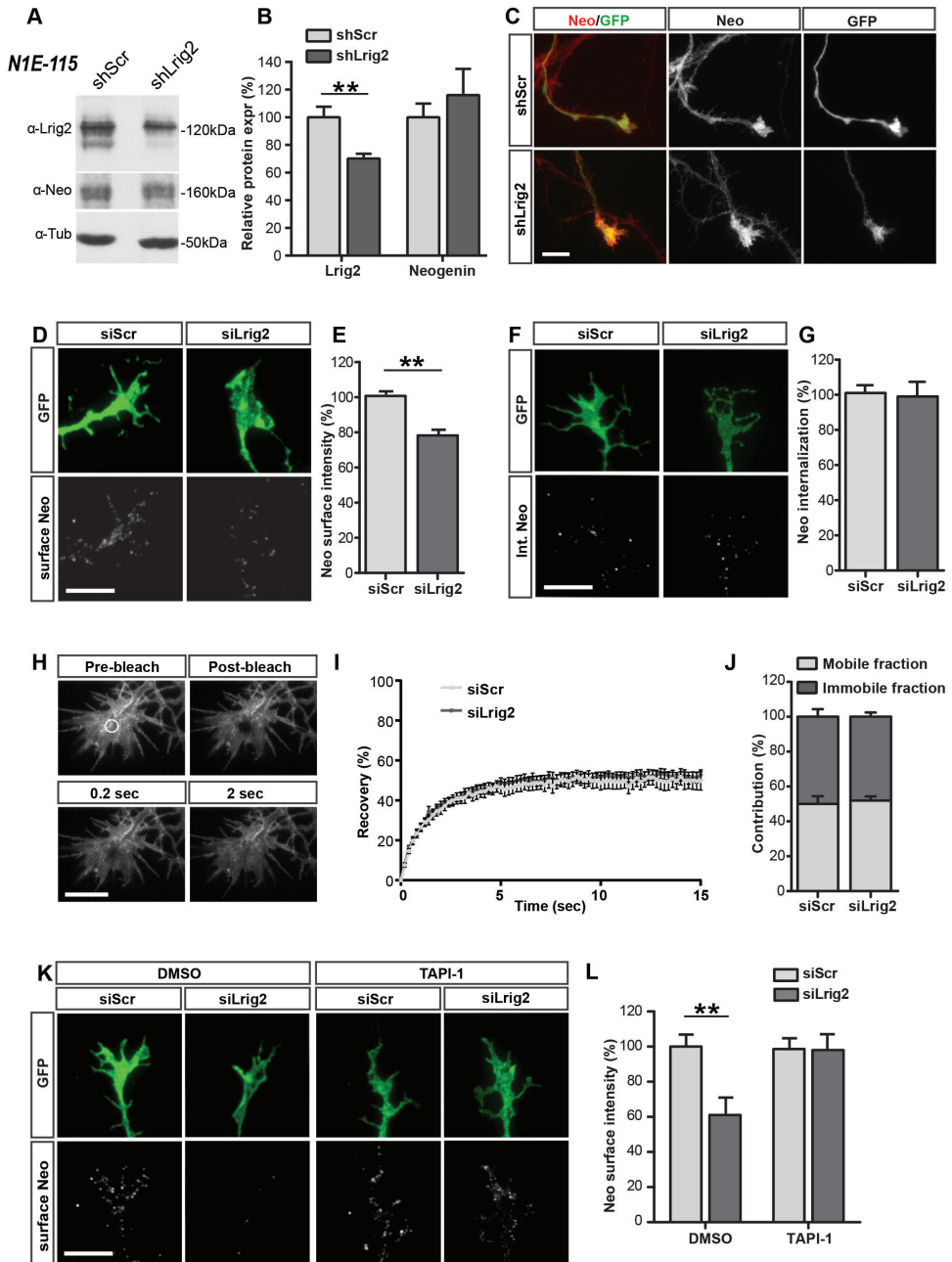




**Figure 4. Lrig2 Regulates Neogenin Cell Surface Expression at the Growth Cone.**

**A.** Lysates of N1E-115 cells transfected with pSuper-shScr or pSuper-shLrig2 were subjected to Western blotting using the indicated antibodies. **B.** Quantification of band intensities in experiments as shown in A. Results are normalized to control. Knockdown of Lrig2 decreases total Lrig2 but not Neogenin expression.  $**P < 0.01$ , Student's t-test. Data are presented as means (of three independent experiments)  $\pm$  S.E.M. **C.** Representative images showing E14.5 dissociated cortical neurons transfected at 1 DIV with pSuper-shScr or pSuper-shLrig2 and immunostained using anti-GFP and anti-Neogenin antibodies at 3 DIV. Lrig2 knockdown does not affect Neogenin levels or localization. **D.** Immunocytochemistry was performed to visualize intracellular GFP expression and cell surface Neogenin expression in growth cones of E14.5 cortical neurons transfected with siRNAs at 1 DIV and analyzed at 3 DIV. **E.** Growth cone fluorescent intensity of experiments as in D was measured. Data were normalized to siScr control. Knockdown of Lrig2 reduces Neogenin cell surface expression.  $n = 3$  experiments,  $>60$  growth cones per condition per experiment.  $**P < 0.01$ , Student's t-test. Data are presented as means  $\pm$  S.E.M. **F.** Immunocytochemistry showing internalized Neogenin in growth cones of E14.5 cortical neurons transfected with siRNAs at 1 DIV and analyzed at 3 DIV. Transfected live neurons were incubated with anti-Neogenin antibodies for 10 min at 37°C to allow antibody internalization. Surface bound antibody was removed and internalized antibody was visualized by incubation with fluorescent secondary antibody in permeabilizing buffer. **G.** Growth cone fluorescent intensity of experiments as in F was measured. Data were normalized to siScr control. No effect of Lrig2 knockdown on Neogenin internalization.  $n = 3$  experiments,  $>60$  growth cones per condition per experiment.  $P = 0.80$ , Student's t-test. Data are presented as means  $\pm$  S.E.M. **H.** Still images from a time-lapse recording of a fluorescence recovery after photobleaching (FRAP) experiment at 3 DIV on growth cones of E18 hippocampal neurons transfected with pHluorin-Neogenin at 1 DIV. **I.** Fluorescent recovery plots showing the mean rates of pHluorin recovery in photobleached growth cones (at  $t=0$ ) of neurons transfected with pHluorin-Neogenin in combination with siScr or siLrig2.  $n = 11$  neurons per condition. Data are presented as means  $\pm$  S.E.M. **J.** Calculation of Neogenin mobile and immobile pools from the FRAP experiments in I. Data are presented as means  $\pm$  S.E.M. **K.** Immunocytochemistry was performed to visualize intracellular GFP expression and cell surface Neogenin expression in growth cones of E14.5 cortical neurons transfected with siRNAs at 1 DIV and cultured in the presence of vehicle (DMSO) or TAPI-1. **L.** Growth cone fluorescent intensity of experiments as in K was measured. Data were normalized to siScr control. Knockdown of Lrig2 reduces Neogenin cell surface expression but this effect is rescued by TAPI-1 incubation.  $n = 3$  experiments,  $>60$  growth cones per condition per experiment.  $**P < 0.01$ , Student's t-test. Data are presented as means  $\pm$  S.E.M. Scale bar, C, D, F, J: 10  $\mu$ m, H: 5  $\mu$ m.

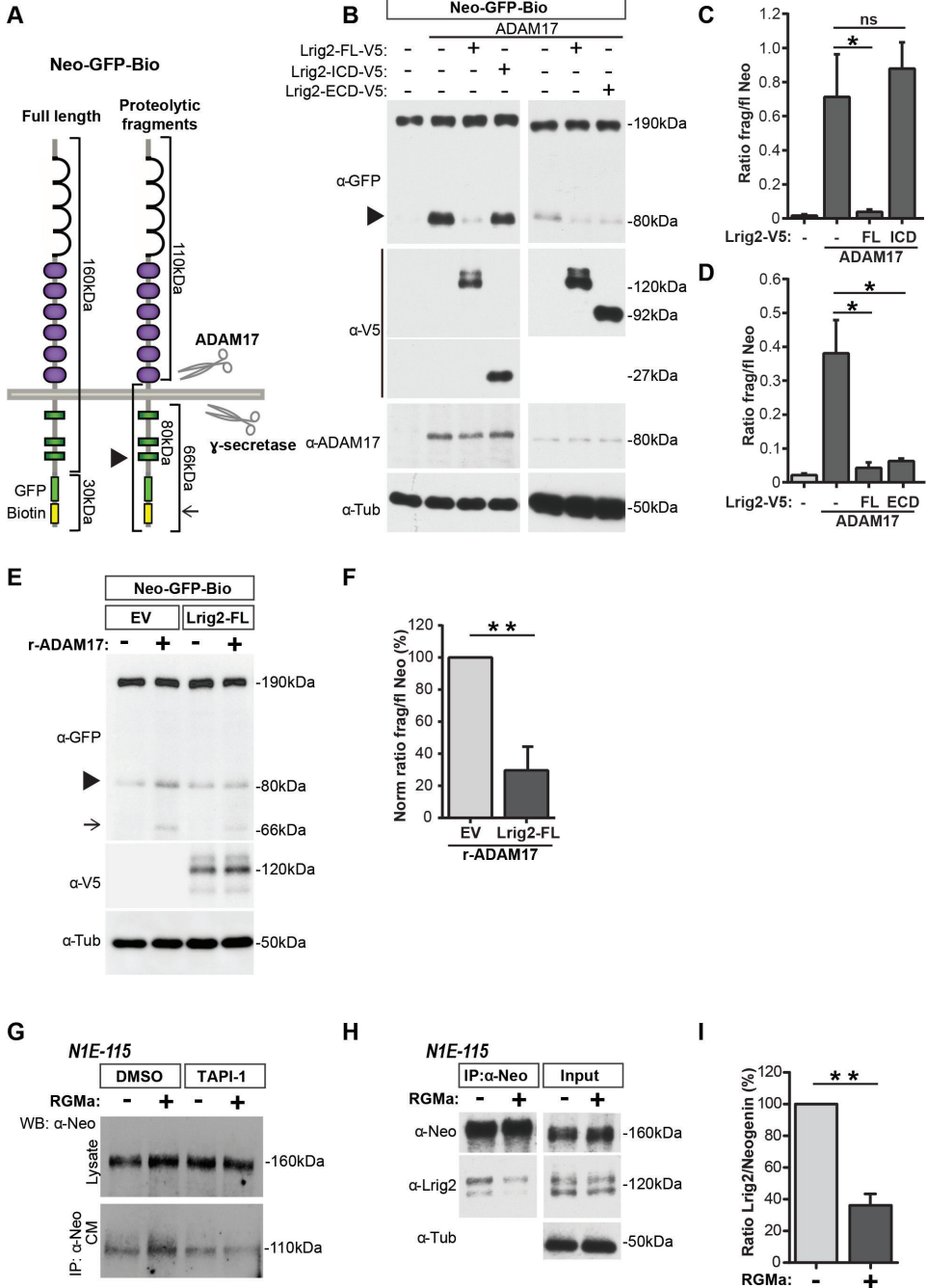
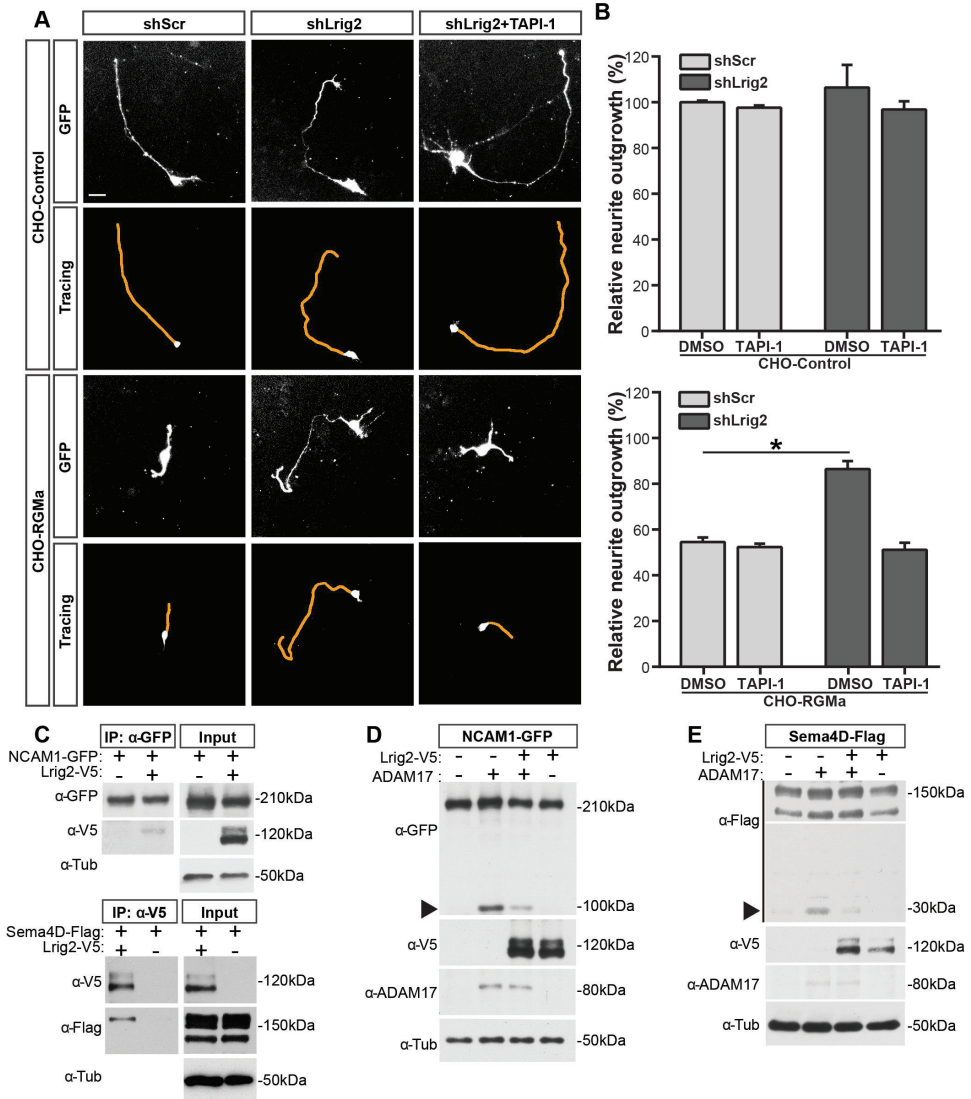


**Figure 5. Lrig2 Inhibits Cleavage of Neogenin by ADAM17.**

**A.** Schematic representation of the Neogenin fragments generated by proteolytic cleavage. Neogenin can be proteolytically processed by ADAM17 and  $\gamma$ -secretase leading to protein fragments of the indicated size. Arrowhead and arrow are used in panels B and E to indicate these fragments. **B.** Streptavidin pull-down assays were performed with lysates of HEK293 cells co-expressing the indicated constructs together with BirA. Proteins bound to streptavidin beads were analyzed by Western blotting using the indicated antibodies. Processing by ADAM17 leads to an 80 kDa cleavage fragment (arrowhead). ECD, extracellular domain; FL, full-length; ICD, intracellular domain. **C, D.** Quantification of band intensities in experiments as shown in B. Ratio between cleaved (frag; 80 kDa) and full-length Neogenin (fl Neo) was calculated. \* $P < 0.05$ , One Sample t-test. Data are presented as means (of four independent experiments)  $\pm$  S.E.M. Full-length Lrig2 and the Lrig2 ectodomain (ECD) block ADAM17-mediated cleavage of Neogenin. **E.** Lysates of HEK293 cells transfected with Neogenin-GFP-Bio and empty vector (EV) or Lrig2-FL-V5 were incubated at 37°C with or without recombinant ADAM17 (r-ADAM17) and subjected to Western blot analysis with the indicated antibodies. Arrowhead indicates ADAM17-induced Neogenin fragment and arrow indicates fragment produced by  $\gamma$ -secretase cleavage. In intact cells the  $\gamma$ -secretase fragment is rapidly degraded (Goldschneider et al., 2008) but in lysates it is visible due to treatment with protease inhibitor. **F.** Quantification of band intensities in experiments as shown in E. Ratio between full length and cleaved Neogenin was calculated in r-ADAM17 experiments and data were normalized to control. Lrig2 inhibits cleavage of Neogenin by ADAM17. \*\* $P < 0.01$ , One Sample t-test. Data are presented as means (of four independent experiments)  $\pm$  S.E.M. **G.** N1E-115 cells were incubated with Fc control or 2  $\mu$ g/ml RGMa-Fc in the presence of vehicle (DMSO) or TAPI-1. Western blot analysis was performed on cell lysates or on anti-Neogenin immunoprecipitates from conditioned N1E-115 cell medium (CM). RGMa enhances ectodomain shedding of Neogenin (110 kDa fragment). **H.** Immunoprecipitation of Neogenin from lysates of N1E-115 cells treated with Fc control or 2  $\mu$ g/ml RGMa-Fc protein. Immunoprecipitates were analyzed with the indicated antibodies. RGMa inhibits the interaction between Lrig2 and Neogenin. **I.** Quantification of band intensities in experiments as shown in H. Ratio between Lrig2 and Neogenin bands was calculated in pull-down samples and data were normalized to control. \*\* $P < 0.01$ , Student's t-test. Data are presented as means (of three independent experiments)  $\pm$  S.E.M.

Ectodomain shedding of receptors is a common mechanism for signal termination. Cleavage of Neogenin by ADAM17 reduces growth cone sensitivity to RGMa, but it is unknown whether this cleavage event is ligand-dependent. Therefore, N1E-115 cells were treated with RGMa-his in combination with TAPI-1 or DMSO vehicle. Conditioned medium was collected from the cells and immunoprecipitated using antibodies directed against Neogenin. This antibody recognizes the Neogenin ECD and allowed us to detect the cleaved endogenous Neogenin ECD. Incubation with RGMa-his increased the amount of Neogenin ectodomain in the medium, and



this effect was nullified by addition of TAPI-1 (Figure 5G). These results suggest that ectodomain shedding of Neogenin is ligand (RGMa)-dependent. A possible explanation for this result is that RGMa induces a reduction in the interaction between Lrig2 and Neogenin, providing ADAM17 access to Neogenin. In line with this model, the interaction between Neogenin and Lrig2 was significantly reduced in the presence of RGMa, though Lrig2 and Neogenin levels are unchanged (Figure 5H, I). Finally, to examine whether regulation of shedding by Lrig2 contributes

**Figure 6. Lrig2 Can Protect Multiple Distinct ADAM17 Substrates from Shedding.**

**A.** Dissociated E14.5 cortical neurons were electroporated with GFP vector and pSuper-shScr (shScr) or pSuper-shLrig2 (shLrig2), cultured on CHO-Control or CHO-RGMA cell layers, and incubated with vehicle or TAPI-1. After 4 DIV, cultures were fixed and immunostained with anti-GFP antibodies. Lower panels show tracing of longest neurite in each example. Scale bar 50 $\mu$ m. **B.** Quantification of neurite length in cultures as in A. Graphs show average length of the longest neurite on CHO-Control cells (upper panel) or on CHO-RGMA cells (lower panel) normalized to control (shScr+EV on CHO-Control cells). TAPI-1 blocks the inhibitory effect of Lrig2 knockdown on RGMA-induced neurite growth inhibition.  $n = 3$  experiments, >75 neurons per condition per experiment. \* $P < 0.05$ , two-way ANOVA. Data are presented as means  $\pm$  S.E.M. **C.** HEK293 cells were cotransfected with Lrig2 and NCAM1 or Sema4D constructs followed by anti-GFP or anti-V5 pull-downs, respectively, and subjected to Western blot analysis using the indicated antibodies. Lrig2 binds NCAM1 and Sema4D. **D, E.** HEK293 cells were co-transfected with different combinations of ADAM17, Lrig2-FL-V5, NCAM1-GFP or Sema4D-Flag. Cell lysates were subjected to Western blot analysis using the indicated antibodies. Arrowhead indicates ADAM17-induced cleavage products. Lrig2 blocks the ADAM17-mediated cleavage of NCAM1 and Sema4D.

to RGMA-Neogenin signaling at the functional level, dissociated cortical neurons were electroporated with shLrig2 or shScr and cultured on confluent CHO cells in the presence of TAPI-1 or vehicle (Figure 6A). Neurons grown on CHO-RGMA cells had significantly shorter neurites, and knockdown of Lrig2 restored neurite length towards control levels. This effect of Lrig2 knockdown was rescued by treatment with TAPI-1 (Figure 6A, B). These results show that regulation of Neogenin ectodomain shedding by Lrig2 is required for neurite growth inhibition by RGMA.

Since Lrigs can bind various other proteins, we hypothesized that Lrig2-mediated regulation of ADAM proteolysis may be a more general mechanism. We tested the ability of Lrig2 to negatively regulate cleavage of two other ADAM17 substrates, neural cell adhesion molecule 1 (NCAM1) and Semaphorin 4D (Sema4D), after we confirmed their ability to bind Lrig2 (Fig. 6C). Interestingly, cleavage of NCAM1-GFP by ADAM17 was reduced by co-expression of Lrig2 (Figure 6D). Similarly, Lrig2 reduced ADAM17-induced cleavage of FLAG-tagged Sema4D (Figure 6E). Thus, Lrig2 can negatively regulate the ADAM17-dependent processing of multiple, distinct, cell surface proteins. Since Lrig1 and Lrig3 bind Neogenin (data not shown), we also tested whether these Lrigs inhibit ADAM17-mediated cleavage of Neogenin. Indeed, expression of Lrig1 or Lrig3 reduced cleavage of Neogenin (Fig. S5). Thus, negative regulation of ADAM-mediated ectodomain shedding may be a general property of Lrigs.



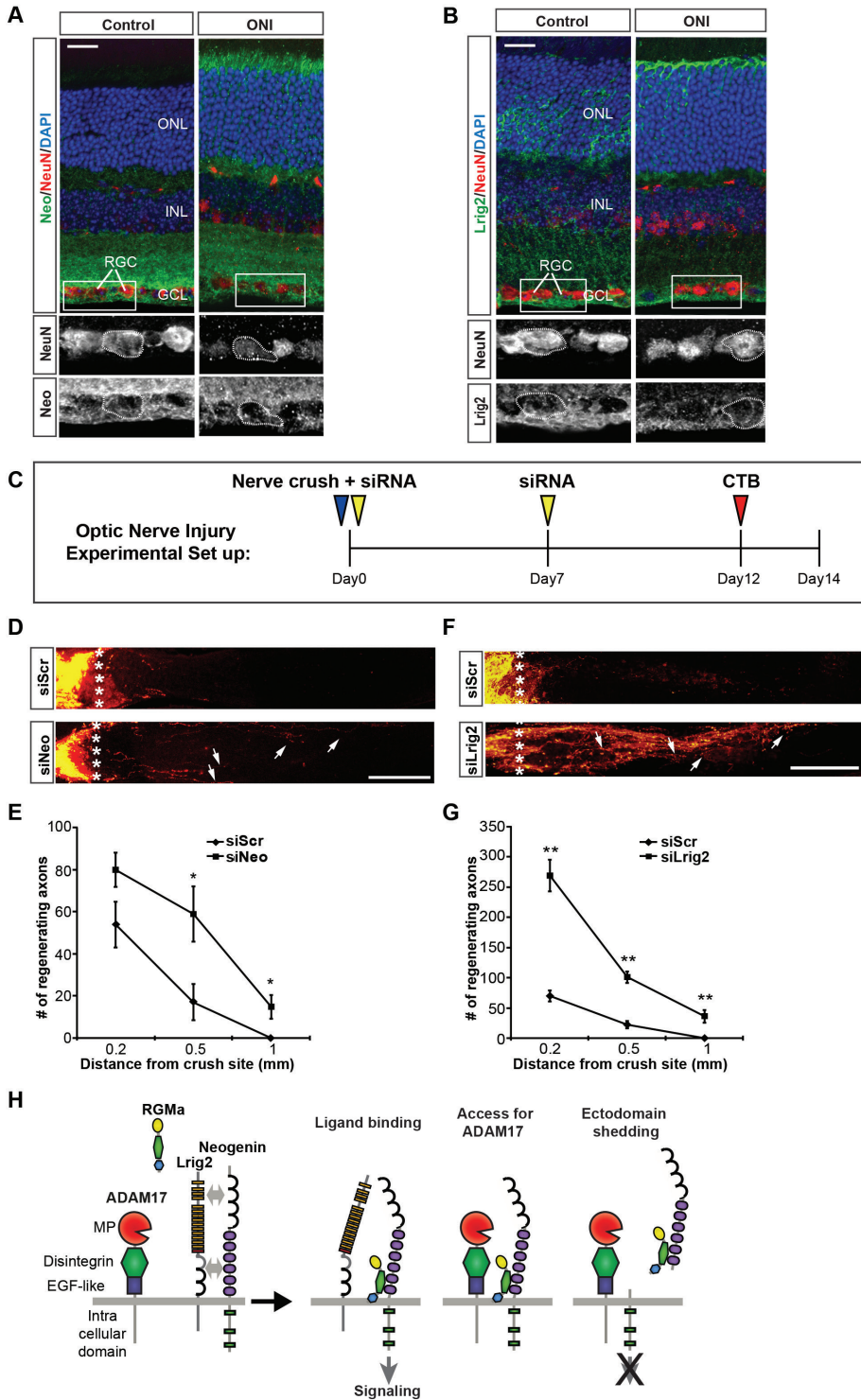


**Figure 7. *In Vivo* Knockdown of Lrig2 Promotes Optic Nerve Regeneration.**

**A, B.** Representative images showing immunohistochemistry for Neogenin (A) or Lrig2 (B) in green and NeuN (red) on adult mouse control retinas and at 14 days after optic nerve crush (ONI). Antibodies against NeuN were used to identify retinal ganglion cells (RGC). DAPI counterstaining is in blue. Boxed areas in the RGC layer (GCL) are shown at higher magnification in lower panels. Neogenin and Lrig2 are expressed in intact and injured adult RGCs. INL, inner nerve layer; ONL, outer nerve layer. **C.** Experimental setup of the ONI studies. siRNAs and CTB were injected in the eye and mice were sacrificed at day 14 post-injury. CTB, Alexa Fluor-555 conjugated cholera toxin subunit B. **D, F.** Confocal images of optic nerve axons labeled by CTB at 14 days post-injury. *In vivo* transfection with control siRNA, *Neogenin* siRNA, or *Lrig2* siRNA was performed. Asterisks indicate distal border of injury site. Arrows indicate regenerating axons. Scale bar, A, B: 20  $\mu$ m, D, F: 200  $\mu$ m. **E, G.** Quantitative analysis of regenerating axons extending at different distances from the distal end of the crush site at 14 days post-injury as in D, F. At least five sections per animal were quantified. Knockdown of Neogenin or Lrig2 significantly enhances optic nerve regeneration.  $n = 6$  animals per condition. \* $P < 0.05$ ; \*\* $P < 0.01$ , Student's t-test. Data are presented as means  $\pm$  S.E.M. **H.** In our model, binding of RGMa induces signaling downstream of Neogenin and the dissociation of the Lrig2-Neogenin complex. This latter event provides ADAM17 with access to the Neogenin ectodomain resulting in ectodomain shedding and signal termination.

**Knockdown of Lrig2 Promotes Axon Regeneration**

Studies in chick and *Xenopus* indicate that axon repulsion by RGMa is required for the development of different axonal connections *in vivo*. Evidence for a similar role in mice *in vivo* is still lacking, but RGMa contributes to the axon growth inhibitory environment of the injured mammalian CNS, and intrathecal application of antibodies directed against RGMa significantly promotes axon regeneration after rat spinal cord injury (Hata et al., 2006). Our data showing a requirement for Lrig2 in repulsive RGMa-Neogenin signaling support the intriguing possibility that manipulation of Lrig2 may also enhance axon regeneration. To test this model, we used the optic nerve crush model. siRNAs can be efficiently targeted to retinal ganglion cells (RGCs), and optic nerve regeneration can be reliably quantified (Dickendesher et al., 2012). A recent study shows that removal of Neogenin from lipid rafts promotes optic nerve regeneration (Tassew et al., 2014). To confirm and extend these findings, we first used immunohistochemistry to show expression of Neogenin in RGCs in the uninjured mouse retina and at 14 days after optic nerve injury (ONI; Figure 7A). Next, we performed knockdown of Neogenin in combination with ONI. At day 0, optic nerve crush was performed followed by intravitreal injection of scrambled siRNAs or siRNAs targeting Neogenin (siNeo). At day 7 the animals received another injection with siRNAs, and after 12 days cholera toxin subunit B (CTB) conjugated to AlexaFluor-555

---

was injected intravitreally to label regenerating RGC axons (Figure 7C). Mice were sacrificed at day 14 and the number of regenerating axons at 0.2, 0.5 and 1 mm from the crush site was quantified. To confirm knockdown efficiency, *Neogenin* levels were determined by quantitative (q) PCR using RNA collected from retinas injected with siRNAs, revealing that injection of siNeo markedly reduced *Neogenin* expression *in vivo* (Figure S4G). Following electroporation of siScr, most CTB-labeled axons stopped abruptly at the crush site and only few fibers crossed the lesion into the distal nerve. In contrast, siNeo induced significant regeneration beyond the lesion site and more pronounced sprouting in the distal segment of the nerve (Figure 7D, E). On basis of these results and our cell biological experiments (Figure 3), we predicted that knockdown of *Lrig2* in RGCs would also promote optic nerve regeneration. Immunohistochemistry confirmed the expression of *Lrig2* in intact and injured adult mouse RGCs (Figure 7B). Next, we combined ONI with knockdown of *Lrig2* using a similar experimental strategy as described for Neogenin (Figure 7C). *Lrig2* knockdown efficiency was confirmed by qPCR (Figure S4H). In stark contrast to the siScr condition, knockdown of *Lrig2* in RGCs induced pronounced regeneration of numerous CTB-labeled RGC axons beyond the lesion site and into the distal nerve (Figure 7F,G). Together, these data show that knockdown of *Lrig2* markedly improves CNS regeneration.

## Discussion

Neural circuit development and regeneration critically depend on precise regulation of growth and guidance receptors at the growth cone membrane. Different mechanisms control growth cone receptor expression, including proteolysis by ADAM proteases. However, how ADAMs themselves are regulated to spatiotemporally control growth cone receptor signaling remains incompletely understood. Here we show that *Lrig2* binds the RGMa receptor Neogenin and negatively regulates Neogenin ectodomain shedding by ADAM17. *Lrig2* is required for the axon repulsive effects of RGMa-Neogenin signaling, and accordingly, knockdown of *Lrig2* promotes optic nerve regeneration. Our data unveil a unique mechanism for ADAM regulation that acts to control premature receptor shedding while retaining ligand responsiveness. Further, our findings reveal a previously uncharacterized function for *Lrig* proteins and identify *Lrig2* as a potential target for promoting axon regeneration.

### Negative Regulation of Ectodomain Shedding by *Lrig2*

The shedding of axon guidance receptors by ADAMs regulates receptor cell surface expression, activates signaling upon ligand binding, and induces the disassembly of ligand-receptor complexes (Bai and Pfaff, 2011). These effects

require tight spatiotemporal control of the proteolytic actions of ADAMs so as to prevent premature cleavage. Numerous molecular mechanisms have been reported for ADAM regulation in non-neuronal cell types and these affect ADAM expression, activity or substrates (Blobel, 2005; Scheller et al., 2011; Weber and Saftig, 2012). In contrast, much less is known about ADAM regulation in neurons. Here, we identify a novel regulatory mechanism for ADAMs by showing that Lrig2 negatively controls ADAM-mediated receptor shedding through substrate interactions. Our data indicate that Lrig2 binds Neogenin and thereby inhibits shedding of this receptor by ADAM17. Intriguingly, the Neogenin ligand RGMA dissociates the Lrig2-Neogenin complex, providing ADAM17 access to Neogenin (Fig. 7H). Multiple lines of evidence support this model. First, knockdown of Lrig2 in cortical neurons leads to reduced Neogenin cell surface expression and a concomitant decrease in RGMA responsiveness. Application of the metalloprotease inhibitor TAPI-1 rescues these defects. Second, overexpression of Lrig2 in non-neuronal cells reduces cleavage of Neogenin by ADAM17. Third, exogenous application of RGMA reduces Lrig2-Neogenin binding and increases shedding of an ADAM17-dependent proteolytic Neogenin fragment. Treatment with TAPI-1 inhibits this effect. Fourth, Lrig2 and Neogenin interact through their ECDs and the Lrig2 ECD is sufficient to inhibit Neogenin shedding by ADAM17. Although our data do not formally exclude all previously reported modes of ADAM regulation, the most parsimonious explanation for our results is that binding of Lrig2 to Neogenin renders Neogenin inaccessible for cleavage in the absence of RGMA (Fig. 7H).

### **A Novel Mechanism-of-Action for Lrig Proteins**

Despite prominent neuronal expression, how Lrigs contribute to nervous system development and function is poorly understood. Lrig1 negatively regulates glial cell line-derived neurotrophic factor (GDNF)-induced neurite growth *in vitro* by binding the GDNF receptor Ret (Ledda et al., 2008). In addition, sensory innervation of the cochlea is disrupted in *Lrig1;Lrig2* double knockout mice, hinting at axonal defects (Del Rio et al., 2013). Our data extend these findings by revealing a novel neuronal function for the poorly characterized Lrig family member *Lrig2* and by showing that Lrigs not only regulate cellular responses to chemotrophic growth factors (e.g. EGF, GDNF) but also to chemotropic guidance cues (RGMA). This new insight is interesting in light of the identification of *LRIG2* mutations as a cause of urofacial syndrome (UFS), a congenital autosomal recessive disorder characterized by aberrant urinary bladder innervation (Stuart et al., 2013). How UFS mutations affect Lrig2 function is unknown, but it is tempting to speculate that they impair guidance of Lrig2-positive axons that target the bladder.

---

Lrigs act through different molecular mechanisms to control growth factor receptors. Lrigs enhance receptor degradation, inhibit ligand-receptor interactions, and recruit receptors to lipid rafts (e.g. (Gur et al., 2004; Laederich et al., 2004; Ledda et al., 2008; Wong et al., 2012)) Our study demonstrates an additional level of complexity of Lrig-dependent receptor regulation by identifying Lrig2 as an inhibitor of receptor ectodomain shedding. Several growth factor receptors such as Met and ErbB4, are Lrig binding partners and ADAM substrates (Blobel, 2005; Scheller et al., 2011). This raises the intriguing possibility that ectodomain shedding represents an additional mechanism through which Lrigs control growth factor receptors. However, our work, and that of others, indicates that the role of Lrigs is not restricted to growth factor receptors. In *C. elegans*, sma-10/Lrig binds BMP receptors, while Lrig3 modulates Wnt signaling in *Xenopus* (Gumienny et al., 2010; Zhao et al., 2008). Furthermore, we report here that Lrig2 inhibits shedding of Neogenin, NCAM1, and Sema4D that serve important roles in embryonic development and immune function (Maness and Schachner, 2007; Suzuki et al., 2008). This wide array of Lrig binding partners with diverse functions suggests that Lrig-dependent regulation of ectodomain shedding is a common mechanism in normal physiology and disease.

### **Lrig2 is Required for Repulsive RGMa-Neogenin Signaling**

RGMa is critical for the development of axonal connections in chick and *Xenopus* (Matsunaga et al., 2006; Tassew et al., 2012; Wilson and Key, 2006). While evidence for a similar role in mice *in vivo* is still lacking, axon growth inhibition by RGMa contributes to the failure of axon regeneration in the mammalian CNS (Hata et al., 2006; Tassew et al., 2014). Therefore, further insight into how RGMa functions and signals may aid the development of therapeutic strategies towards CNS regeneration. Previous work implicated ADAM17 in RGMa-Neogenin signaling by showing that this protease cleaves the Neogenin ectodomain *in cis* and thereby terminates, rather than activates, repulsive Neogenin signaling (Okamura et al., 2011). However, whether this cleavage is constitutive or tightly regulated remained unknown. Here we show that shedding of Neogenin by ADAM17 at the growth cone is negatively controlled by Lrig2 and that this process is, at least in part, ligand-dependent. We propose that this mechanism provides a way to limit premature Neogenin cleavage in the presence of active proteases while retaining immediate RGMa responsiveness. A small pool of Neogenin receptors may be subjected to ligand-independent constitutive shedding; Neogenin is shed from primary cortical neurons in the absence of exogenous RGMa and this shedding is reduced by knockdown of ADAM17 (Okamura et al., 2011). It should be noted, however, that primary cortical neurons express RGMa and that RGMa can bind Neogenin *in cis* (van den Heuvel et al., 2013; Tassew et al., 2014). It is

therefore possible that 'constitutive' Neogenin shedding results from auto- or paracrine exposure to RGMa. In our study, exogenous Lrig2 reduced Neogenin cleavage (Fig. 5) but did not enhance axon growth inhibition by RGMa (Fig. 3). It is plausible that this apparent discrepancy is caused by the assay used to detect axonal responses to RGMa. Due to the strong inhibitory effect of RGMa in the CHO assay, manipulations that further increase RGMa sensitivity are likely to escape detection.

Previous work has shown that proteolysis of repulsive Ephrins by ADAM10 is also regulated by ligand-receptor binding (Hattori et al., 2000; Janes et al., 2005). Our data are, however, conceptually distinct from these previous results: we find that ligand binding induces the dissociation of a substrate inhibitor leading to shedding, rather than inducing a new molecular recognition motif for effective cleavage. RGMs were originally identified as axon repulsive cues, but are now known to control a plethora of unrelated (non-)neuronal processes via Neogenin (Severyn et al., 2009). In addition, Neogenin not only binds RGMs but also functions as a cell surface receptor for BMPs and Netrin-1 in processes such as myotube formation and endochondral bone development (Kang et al., 2004; Zhou et al., 2010). Therefore, it will be important to determine whether Lrig2 regulates RGMa-Neogenin signaling events unrelated to axon growth inhibition or Neogenin signaling in response to non-RGM ligands.

## **Knockdown of Lrig2 Promotes Axon Regeneration in the Adult CNS**

Lrigs are promising therapeutic targets for cancer treatment since soluble forms of Lrig1 and knockout of Lrig2 inhibit tumorigenesis *in vivo* (Johansson et al., 2013; Rondahl et al., 2013). Our data support the exciting possibility that Lrigs may also serve as therapeutic targets for promoting axon regeneration in the injured CNS. Two intravitreal injections of *Lrig2* siRNAs, one at the time of injury and a second one seven days post-injury, induced significant regenerative axon growth into the distal, denervated, portion of the optic nerve. This effect is in line with the reported role of RGMa as an inhibitor of axon regeneration (Hata et al., 2006; Tassew et al., 2014) and the functional requirement for Lrig2 in repulsive RGMa-Neogenin signaling. While it is tempting to speculate that knockdown of Lrig2 decreases the sensitivity of injured axons to scar tissue-associated RGMa and thereby promotes regeneration, it should be noted that although *Neogenin* and *Lrig2* siRNAs induced a similar reduction in RGC gene expression *in vivo*, a far larger number of regenerating optic nerve fibers was observed following Lrig2 knockdown. A plausible explanation for this apparent discrepancy is that knockdown of Lrig2 could block the effects of multiple, distinct, regeneration inhibiting proteins or could enhance positive factors. For example, Lrig2 not



---

only binds and reduces shedding of Neogenin but also of Sema4D, a repulsive cue upregulated at CNS lesion sites (Moreau-Fauvarque et al., 2003). Future experiments will dissect the roles and mechanisms-of-action of Lrig2 in injured neurons and will explore whether manipulation of Lrig2 can contribute to combinatorial strategies aimed at promoting axon regeneration. Recent studies have successfully explored neuron intrinsic mechanisms as targets for enhancing regenerative axon growth (Lu et al., 2014; Stuessi and Bradke, 2011), but our findings are, to our knowledge, the first to show that targeting the intrinsic regulation of receptor proteolysis may help to improve regeneration.

Together, our findings highlight an important role for Lrig2 in neurons and unveil a novel mechanism that negatively controls ADAM proteases. The regulatory mechanism described here may provide new ways to understand or manipulate other cleavage events mediated by ADAM proteases with roles in development, physiology and disease.

## **Acknowledgements**

We thank members of the Pasterkamp laboratory for assistance and helpful discussions, and Alex Kolodkin and Joost Verhaagen for comments on the manuscript. We thank Christian Siebold, Stephen Strittmatter, Dennis Selkoe, Thomas Skutella, Atsushi Kumanogoh, and Ruud Toonen for providing antibodies and DNA constructs. This work was supported by the Netherlands Organization for Health Research and Development (ZonMW-VIDI), the Human Frontier Science Program (HFSP-CDA), Hersenstichting Nederland, and Neuroscience and Cognition Utrecht to R.J.P. This study was partly performed within the framework of Dutch Top Institute Pharma project T5-207 (R.J.P.). R.J.P. was a Henry and William Test National Alliance for Research on Schizophrenia and Depression Investigator.



# Supplemental Information

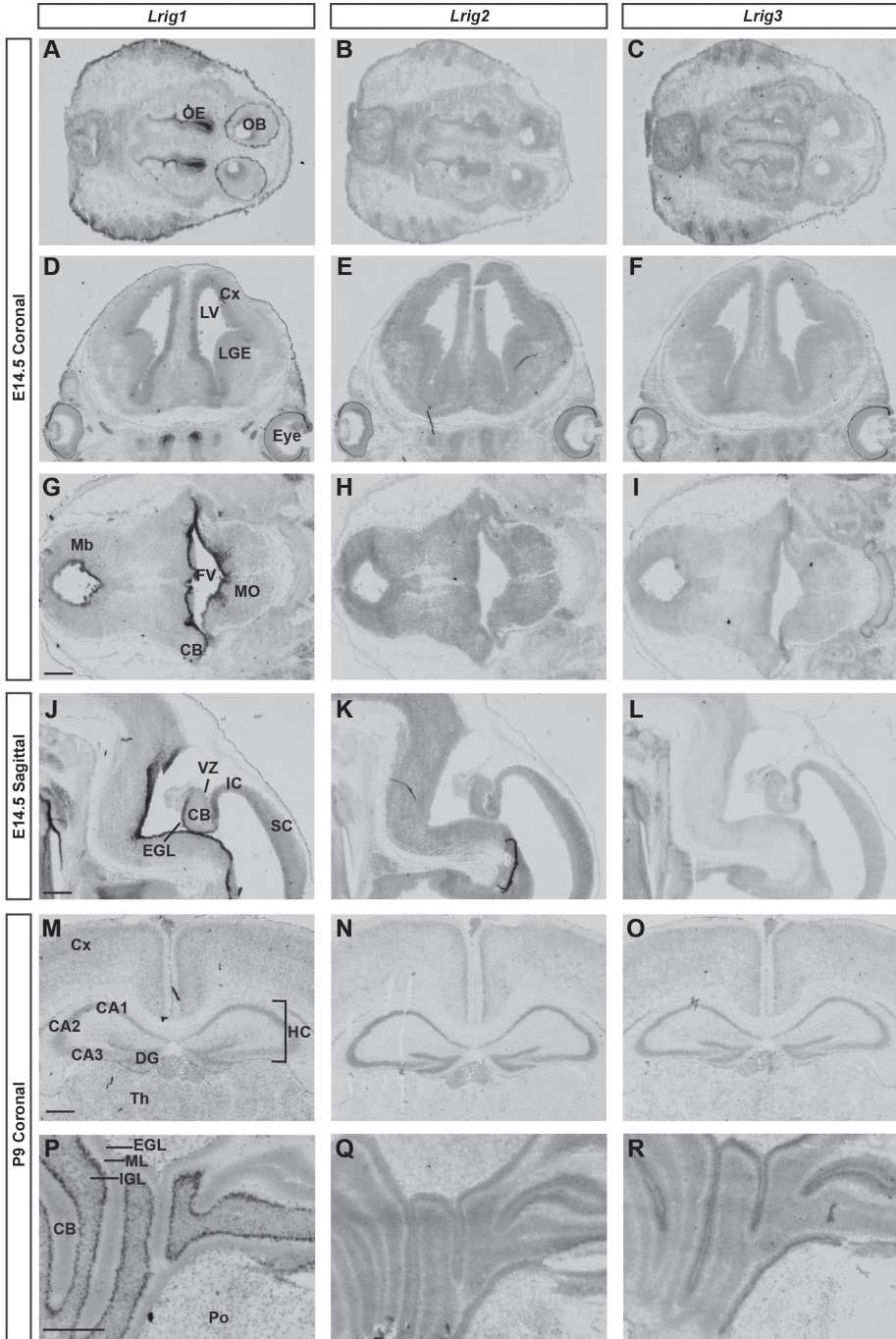


**Figure S1. *Lrig* Expression in the Developing Nervous System. Related to Figure 1.**

Our understanding of the spatiotemporal expression of *Lrig*s during mouse neural development is rather rudimentary. Therefore, *in situ* hybridization was used to examine the expression of *Lrig1*, *Lrig2*, and *Lrig3* in the nervous system at different developmental stages. E14.5 coronal (A-I), sagittal (J-L), E16.5 (see Figure 1), and P9 coronal (M-R) mouse sections were analyzed. Partially overlapping but clearly distinct patterns of expression were detected for each of the three *Lrig* family members. CA, cornu amonis; CB, cerebellum; Cx, cortex; DG, dentate gyrus; EGL, external granule layer; FV, fourth ventricle; IGL, internal granule layer; LGE, lateral ganglionic eminence; HC, hippocampus; IC, inferior colliculus; LV, lateral ventricle; Mb, midbrain; ML, molecular layer; MO, medulla oblongata; OB, olfactory bulb; Po, pons; SC, superior colliculus; Th: thalamus; VZ, ventricular zone. Scale bar, 500  $\mu$ m.

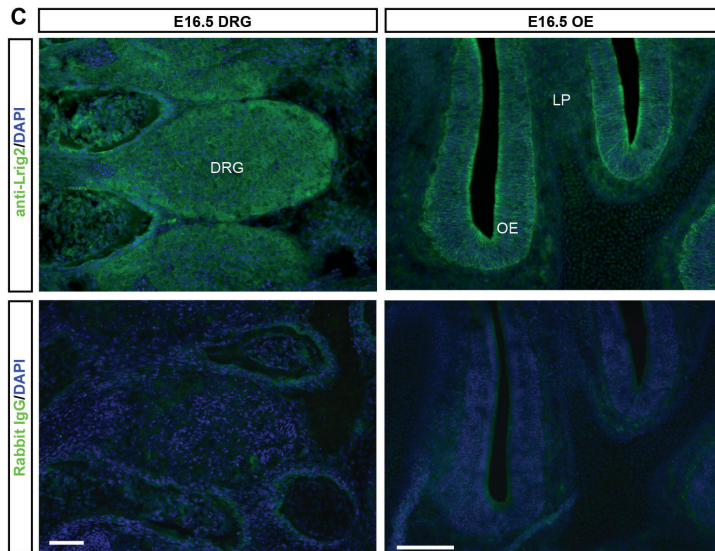
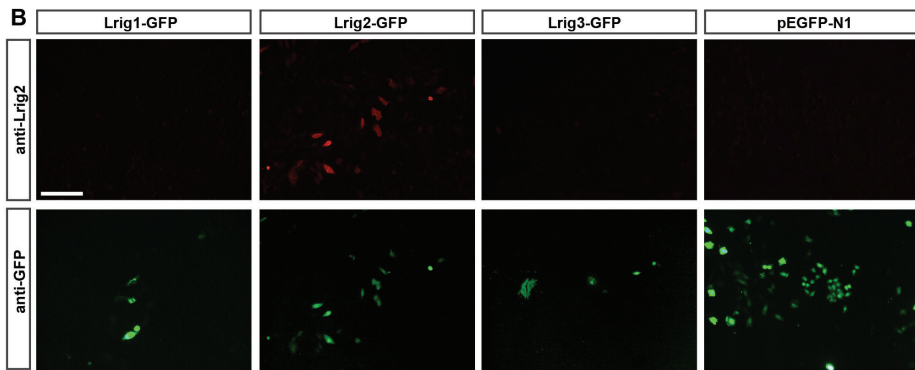
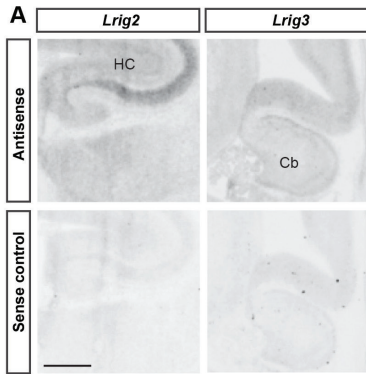


**Figure S2. Specificity Controls for the *In Situ* Hybridization and Immunohistochemical Experiments. Related to Figure 1.**

**A.** The specificity of *in situ* hybridization probes used to detect *Lrig1-3* was established using E18.5 mouse sections. *Lrig* antisense probes and corresponding control sense probes were incubated on adjacent sections and subjected to the same *in situ* hybridization procedure. Antisense probes revealed distinct expression patterns for *Lrig2* and *Lrig3* (see also Figure 1), but no specific staining was observed after incubation with sense control probes. Cb, cerebellum; HC, hippocampus. Scale bar, 500  $\mu$ m. **B.** COS7 cells were transfected with *Lrig1*-GFP, *Lrig2*-GFP, *Lrig3*-GFP or pEGFP-N1 vector and co-immunostained with anti-GFP and anti-*Lrig2* antibodies. GFP expression revealed transfected cells in each condition, but *Lrig2* antibody binding was only present in *Lrig2*-GFP transfected cells. **C.** E16.5 mouse sections were incubated with anti-*Lrig2* or rabbit-IgG control antibody and subsequently with fluorescent secondary anti-rabbit antibodies and counterstained with DAPI to visualize nuclei. Specific immunostaining was present in dorsal root ganglia (DRG) and olfactory epithelium (OE) in anti-*Lrig2* sections but no binding was observed in control sections. LP, lamina propria. Scale bars, B: 300 $\mu$ m, C: 500 $\mu$ m.



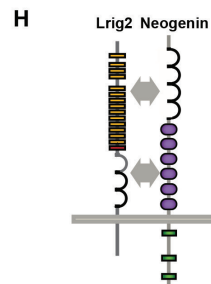
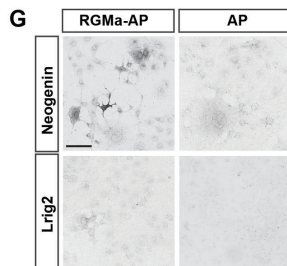
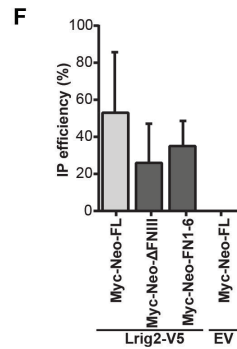
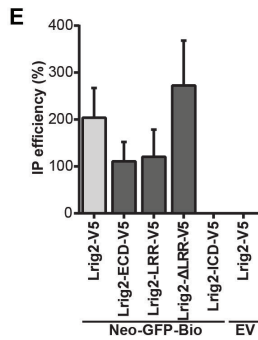
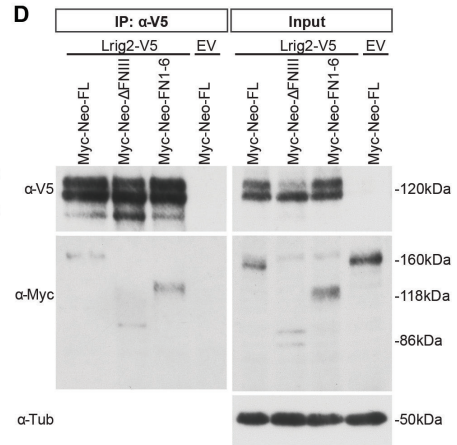
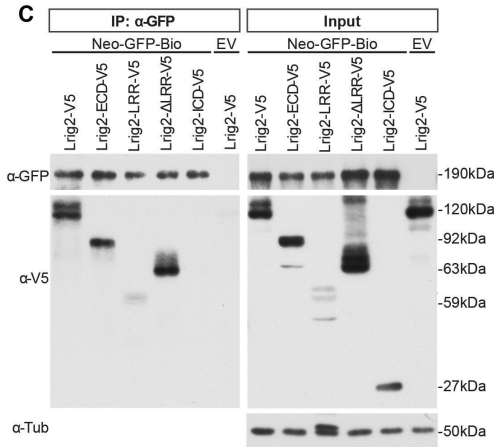
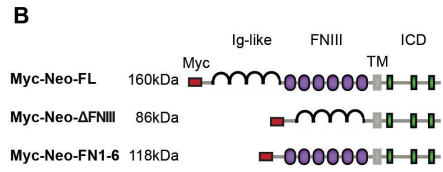
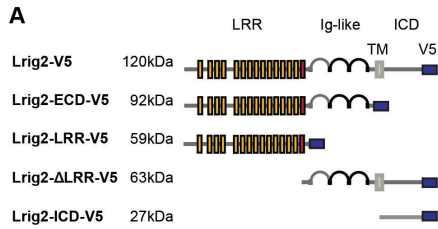


**Figure S3. Neogenin and Lrig2 Extracellular Domains Interact. Related to Figure 2.**

**A, B.** Schematic representation of full length and truncated V5-tagged Lrig2 constructs (A) and full length and truncated Myc-tagged Neogenin construct (B). Predicted molecular weights based on amino acid sequences are indicated. ECD, extracellular domain; ICD, intracellular domain; FL, full length; FN, fibronectin; Ig, immunoglobulin; LRR, leucine-rich repeat; TM, transmembrane. **C.** Anti-GFP pull down on HEK293 cell lysates co-transfected with pcDNA3.1-Neogenin-Bio-GFP and GW1-Lrig-V5 truncation constructs revealed that the LRR and Ig-like domains of Lrig2 interact with Neogenin. **D.** Anti-V5 pull down on HEK293 cell lysates co-transfected with GW1-Lrig2-FL-V5 and GW1-myc-Neogenin truncation constructs, revealed that both the FNIII and Ig-like domains of Neogenin interact with Lrig2. **E, F.** Quantification of band intensities in experiments as shown in C and D, respectively. The ratio between Neo-GFP-Bio bait and (truncated) Lrig2-V5 (E) or Lrig2-V5 bait and (truncated) Myc-Neo (F) in respective IP samples in C and D was determined. To calculate the relative interaction, the ratio in IP samples was normalized to each corresponding input sample. Data are presented as means (of three independent experiments)  $\pm$  S.E.M. **G.** COS-7 cells were transfected with either full length Neogenin or Lrig2 and incubated with alkaline phosphatase (AP)-tagged RGMa or AP only as a control. RGMa-AP binding was detected when Neogenin was present but no binding to Lrig2 was observed. No staining was detected after incubation with AP control protein. Scale bar, 50  $\mu$ m **H.** Schematic representation of Lrig2-Neogenin binding. Arrows indicate potential interacting regions.

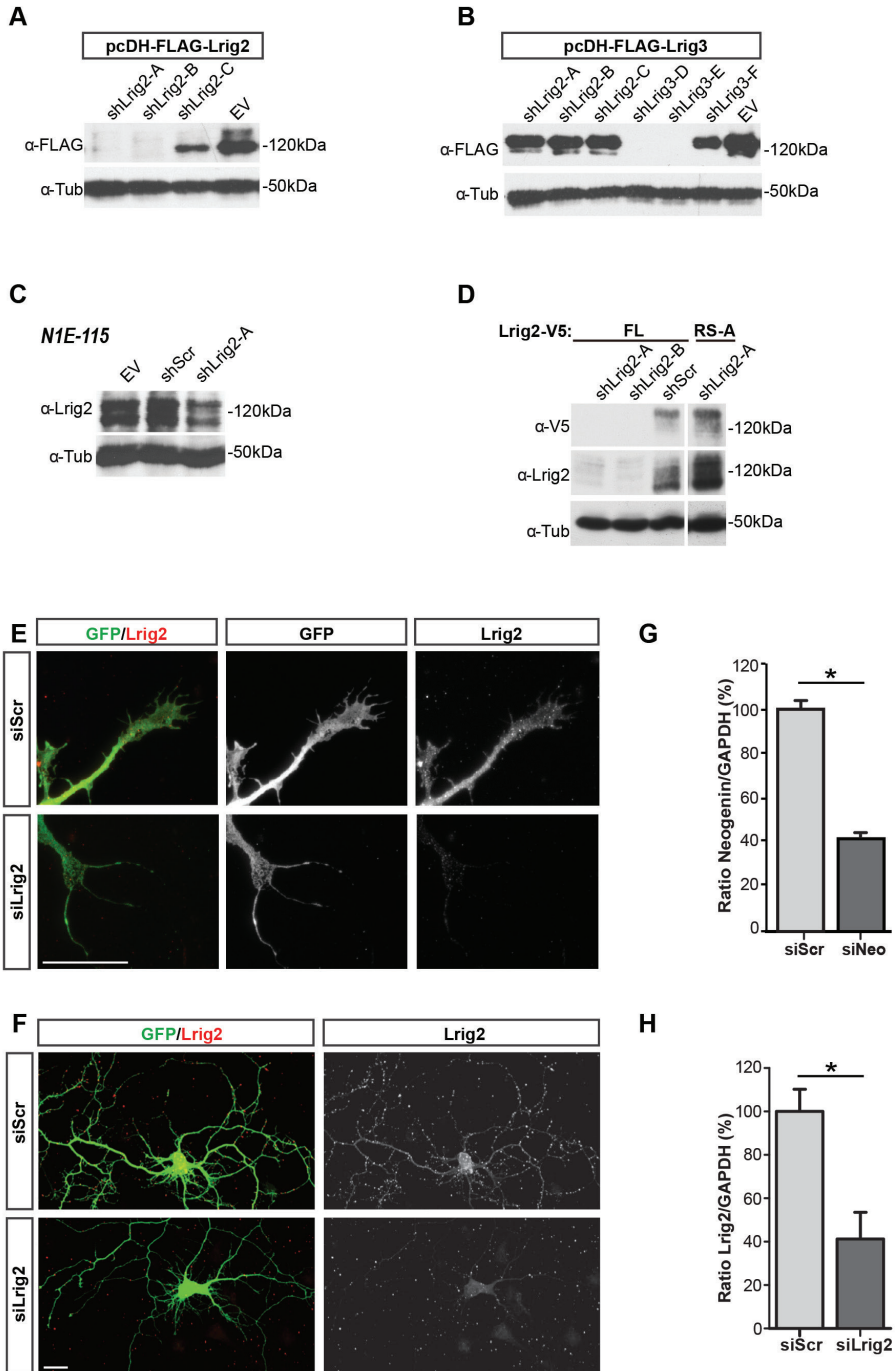


**Figure S4. Confirmation of Knockdown Efficiency. Related to Figures 3, 4, 6 and 7.**

**A.** Immunoblotting of HEK293 cell lysates co-transfected with pcDH-FLAG-Lrig2 and pSuper-shLrig2-A, shLrig2-B or shLrig2-C, or pSuper empty vector (EV) with anti-FLAG antibodies revealed strong shLrig2-mediated knockdown by shLrig2-A and shLrig2-B. Anti- $\alpha$ -tubulin immunoblotting was used as loading control. **B.** Immunoblotting of HEK293 cell lysates cotransfected with pcDH-FLAG-Lrig3 and pSuper-shLrig2-A-C, shLrig3D-F or pSuper empty vector (EV) with anti-FLAG antibodies revealed strong knockdown of FLAG-Lrig3 by shLrig3D and shLrig3E but not by shLrig2-A-C. Anti- $\alpha$ -tubulin immunoblotting was used as loading control. **C.** Transfection of N1E-115 cells with either empty pSuper expression vector (EV), scrambled shRNA pSuper expression vector (shScr) or Lrig2 targeting shRNA pSuper expression vector (shLrig2-A) showed specific knockdown of endogenous Lrig2 by shLrig2-A. Anti- $\alpha$ -tubulin antibody was used as loading control. **D.** A full length, V5-tagged Lrig2 construct containing non-coding point mutations in the target site for shLrig2-A was created (Lrig2-RS-A). HEK293 cells were cotransfected with wildtype Lrig2-FL-V5 or the Lrig2 rescue construct Lrig2-RS-A, along with pSuper containing shLrig2-A, shLrig2-B, or shScr. Both shLrig2-A and shLrig2-B induce knockdown of Lrig2-FL-V5 as shown by anti-V5 and anti-Lrig2 detection. Expression of Lrig2-RS-A was unaffected by shLrig2-A. **E, F.** Dissociated cultured mouse cortical neurons (E) or rat hippocampal neurons (F) were transfected at 1 DIV (E) or 4 DIV (F) with GFP plasmid and siRNAs targeting Lrig2 (siLrig2) or scrambled control siRNAs (siScr). Two days after transfection, neurons were fixed and immunostained with anti-GFP (green) and anti-Lrig2 (red) antibodies. Knockdown of Lrig2 resulted in reduced Lrig2 immunostaining. Scale bar, 20  $\mu$ m. **G, H.** Graphs showing *Neogenin* or *Lrig2* levels as determined by quantitative PCR following knockdown of *Neogenin* or *Lrig2*, respectively, at 14 days after intravitreal siRNA injections in adult mice. *Neogenin* and *Lrig2* levels were normalized to internal *GAPDH* control. \* $P < 0.05$ , Student's t-test. Data are presented as means (of three independent experiments,  $n = 3$  retinas per condition)  $\pm$  S.E.M.

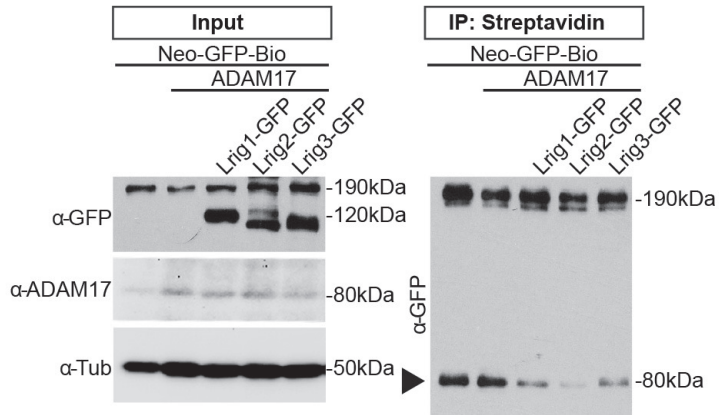


**Figure S5. Lrig1, Lrig2 and Lrig3 Inhibit Neogenin Ectodomain Shedding by ADAM17. Related to Figure 6.**

HEK293 cells were co-transfected with different combinations of ADAM17, Neo-GFP-Bio, Lrig1-GFP, Lrig2-GFP or Lrig3-GFP. Immunoprecipitation was performed using streptavidin beads. Precipitates and cell lysates were subjected to Western blot analysis using the indicated antibodies. Arrowhead indicates ADAM17-induced Neogenin cleavage products. Lrig1, Lrig2 and Lrig3 reduced the ADAM17-mediated cleavage of Neogenin. Tub,  $\alpha$ -tubulin.

**Table S1. Overview of Lrig2-interacting Proteins.**

List of gene symbols for proteins identified in a pull down experiment using Streptavidin-coated beads on lysates from HEK293 cells transfected with Lrig2-GFP-Bio and BirA. Listed proteins for the selected GO-categories were detected with a Mascott score of >40 and are unique for Lrig2-GFP-Bio precipitates. Non-specific proteins interacting with Bio-GFP were removed. Neogenin is in bold. Note: LRIG1 and LRIG3 were also identified as Lrig2-Bio-GFP interactors but are not assigned to any of the selected GO-categories.

Category	Proteins identified		Category	Proteins identified		
<b>Actin &amp; microtubule cytoskeleton</b>	FLNA	PPP4C	<b>(m)RNA processing</b>	RBM26	RBM27	
	HSP90B1	DYNLL1		STRAP	RBM10	
	TUBB	ALDOA		DHX15	CHERP	FIP1L1
	FLNB	DPYSL3		RBM17	KHSRP	
	CAPZB	BCR		U2SURP	MAGOHB	
	EPB41L2	CALD1		SART3	BCAS2	
	EPB41L3	PEX14		DDX46	SMN1	
	EPB41	CORO1B		SSB	SRSF8	
	CAPZA1	MYH9				
	ADD1	KIF2A				
	CAPZA2	DLG1				
	FAM101B	FHL3				
		SHROOM3				
<b>Cell adhesion &amp; axon guidance</b>	MYCBP2	STIP1	<b>Apoptosis</b>	PRKDC	SLK	
	<b>NEO1</b>	CSNK2A1		WWOX	OGT	
	TLN1			YWHAE	NBN	
<b>Intracellular transport</b>	ZBTB33	C15orf38-	PUF60	VDAC1		
	RAN	AP3S2	SAP30BP	FAM32A		
	DVL2	ARCN1				
	RANBP3	DVL3				
	COPB2	COPB1				
		RANBP1				
<b>Axon cargo transport</b>	NEFL	AP3S1	<b>Cell division</b>	CKAP5	SEPT2	
	AP3B1	KIF4A		TUBB	SMC4	
<b>Proteolysis</b>	PSMB3	PSMB7		RUVBL1	HAUS2	
	PSMA4	PSMA5		MAP4	KNSTRN	
	CLPP			CD2AP	WAPAL	
		NEK9		HAUS7		
		PPP1CC	SMC2			
		HAUS4				



---

## References

- Antczak, C., Radu, C., and Djaballah, H. (2008). A profiling platform for the identification of selective metalloprotease inhibitors. *J. Biomol. Screen.* 13, 285–294.
- Aricescu, A.R., Hon, W.-C., Siebold, C., Lu, W., van der Merwe, P.A., and Jones, E.Y. (2006). Molecular analysis of receptor protein tyrosine phosphatase mu-mediated cell adhesion. *EMBO J.* 25, 701–712.
- Bai, G., and Pfaff, S.L. (2011). Protease Regulation: The Yin and Yang of Neural Development and Disease. *Neuron* 72, 9–21.
- Blobel, C.P. (2005). ADAMs: key components in EGFR signalling and development. *Nat. Rev. Mol. Cell Biol.* 6, 32–43.
- Brummelkamp, T.R., Bernards, R., and Agami, R. (2002). A system for stable expression of short interfering RNAs in mammalian cells. *Science* (80-.). 296, 550–553.
- Chen, Y.Y., Hehr, C.L., Atkinson-Leadbeater, K., Hocking, J.C., and McFarlane, S. (2007). Targeting of retinal axons requires the metalloproteinase ADAM10. *J. Neurosci.* 27, 8448–8456.
- Coleman, H.A., Labrador, J.-P., Chance, R.K., and Bashaw, G.J. (2010). The Adam family metalloprotease Kuzbanian regulates the cleavage of the roundabout receptor to control axon repulsion at the midline. *Development* 137, 2417–2426.
- Conrad, S., Genth, H., Hofmann, F., Just, I., and Skutella, T. (2007). Neogenin-RGMA signaling at the growth cone is bone morphogenetic protein-independent and involves RhoA, ROCK, and PKC. *J. Biol. Chem.* 282, 16423–16433.
- Dickendesher, T.L., Baldwin, K.T., Mironova, Y.A., Koriyama, Y., Raiker, S.J., Askew, K.L., Wood, A., Geoffroy, C.G., Zheng, B., Liepmann, C.D., et al. (2012). NgR1 and NgR3 are receptors for chondroitin sulfate proteoglycans. *Nat. Neurosci.* 15, 703–712.
- Fambrough, D., Pan, D., Rubin, G.M., and Goodman, C.S. (1996). The cell surface metalloprotease/disintegrin Kuzbanian is required for axonal extension in *Drosophila*. *Proc. Natl. Acad. Sci. U. S. A.* 93, 13233–13238.
- Fujita, Y., Endo, S., Takai, T., and Yamashita, T. (2011). Myelin suppresses axon regeneration by PIR-B/SHP-mediated inhibition of Trk activity. *EMBO J.* 30, 1389–1401.
- Galko, M.J., and Tessier-Lavigne, M. (2000). Function of an axonal chemoattractant modulated by metalloprotease activity. *Science* 289, 1365–1367.
- Giger, R.J., Hollis, E.R., and Tuszynski, M.H. (2010). Guidance molecules in axon regeneration. *Cold Spring Harb. Perspect. Biol.* 2, a001867.
- Groen, E.J.N., Fumoto, K., Blokhuis, A.M., Engelen-Lee, J.Y., Zhou, Y., van den Heuvel, D.M.A., Koppers, M., van Diggelen, F., van Heest, J., Demmers, J.A.A., et al. (2013). ALS-associated mutations in FUS disrupt the axonal distribution and function of SMN. *Hum. Mol. Genet.* 22, 3690–3704.
- Gumienny, T.L., Macneil, L., Zimmerman, C.M., Wang, H., Chin, L., Wrana, J.L., and Padgett, R.W. (2010). *Caenorhabditis elegans* SMA-10/LRIG is a conserved transmembrane protein that enhances bone morphogenetic protein signaling. *PLoS Genet.* 6, e1000963.

- Guo, D., Holmlund, C., Henriksson, R., and Hedman, H. (2004). The LRIG gene family has three vertebrate paralogs widely expressed in human and mouse tissues and a homolog in Ascidiacea. *Genomics* 84, 157–165.
- Gur, G., Rubin, C., Katz, M., Amit, I., Citri, A., Nilsson, J., Amariglio, N., Henriksson, R., Rechavi, G., Hedman, H., et al. (2004). LRIG1 restricts growth factor signaling by enhancing receptor ubiquitylation and degradation. *EMBO J.* 23, 3270–3281.
- Hagihara, M., Endo, M., Hata, K., Higuchi, C., Takaoka, K., Yoshikawa, H., and Yamashita, T. (2011). Neogenin, a receptor for bone morphogenetic proteins. *J. Biol. Chem.* 286, 5157–5165.
- Hata, K., Fujitani, M., Yasuda, Y., Doya, H., Saito, T., Yamagishi, S., Mueller, B.K., and Yamashita, T. (2006). RGMa inhibition promotes axonal growth and recovery after spinal cord injury. *J. Cell Biol.* 173, 47–58.
- Hata, K., Kaibuchi, K., Inagaki, S., and Yamashita, T. (2009). Unc5B associates with LARG to mediate the action of repulsive guidance molecule. *J. Cell Biol.* 184, 737–750.
- Hattori, M., Osterfield, M., and Flanagan, J.G. (2000). Regulated cleavage of a contact-mediated axon repellent. *Science* 289, 1360–1365.
- Van den Heuvel, D.M.A., Hellemons, A.J.C.G.M., and Pasterkamp, R.J. (2013). Spatiotemporal Expression of Repulsive Guidance Molecules (RGMs) and Their Receptor Neogenin in the Mouse Brain. *PLoS One* 8.
- Holmlund, C., Nilsson, J., Guo, D., Starefeldt, A., Golovleva, I., Henriksson, R., and Hedman, H. (2004). Characterization and tissue-specific expression of human LRIG2. *Gene* 332, 35–43.
- Homma, S., Shimada, T., Hikake, T., and Yaginuma, H. (2009). Expression pattern of LRR and Ig domain-containing protein (LRRIG protein) in the early mouse embryo. *Gene Expr. Patterns* 9, 1–26.
- Janes, P.W., Saha, N., Barton, W.A., Kolev, M. V., Wimmer-Kleikamp, S.H., Nievergall, E., Blobel, C.P., Himanen, J.P., Lackmann, M., and Nikolov, D.B. (2005). Adam meets Eph: An ADAM substrate recognition module acts as a molecular switch for ephrin cleavage in trans. *Cell* 123, 291–304.
- Jensen, K.B., and Watt, F.M. (2006). Single-cell expression profiling of human epidermal stem and transit-amplifying cells: Lrig1 is a regulator of stem cell quiescence. *Proc. Natl. Acad. Sci. U. S. A.* 103, 11958–11963.
- Johansson, M., Oudin, A., Tiemann, K., Bernard, A., Golebiewska, A., Keunen, O., Fack, F., Stieber, D., Wang, B., Hedman, H., et al. (2013). The soluble form of the tumor suppressor Lrig1 potently inhibits in vivo glioma growth irrespective of EGF receptor status. *Neuro. Oncol.* 15, 1200–1211.
- Kang, J.-S., Yi, M.-J., Zhang, W., Feinleib, J.L., Cole, F., and Krauss, R.S. (2004). Netrins and neogenin promote myotube formation. *J. Cell Biol.* 167, 493–504.
- Kee, N., Wilson, N., De Vries, M., Bradford, D., Key, B., and Cooper, H.M. (2008). Neogenin and RGMa control neural tube closure and neuroepithelial morphology by regulating cell polarity. *J. Neurosci.* 28, 12643–12653.
- Kolodkin, A.L., and Pasterkamp, R.J. (2013). SnapShot: Axon guidance II. *Cell* 153, 722.

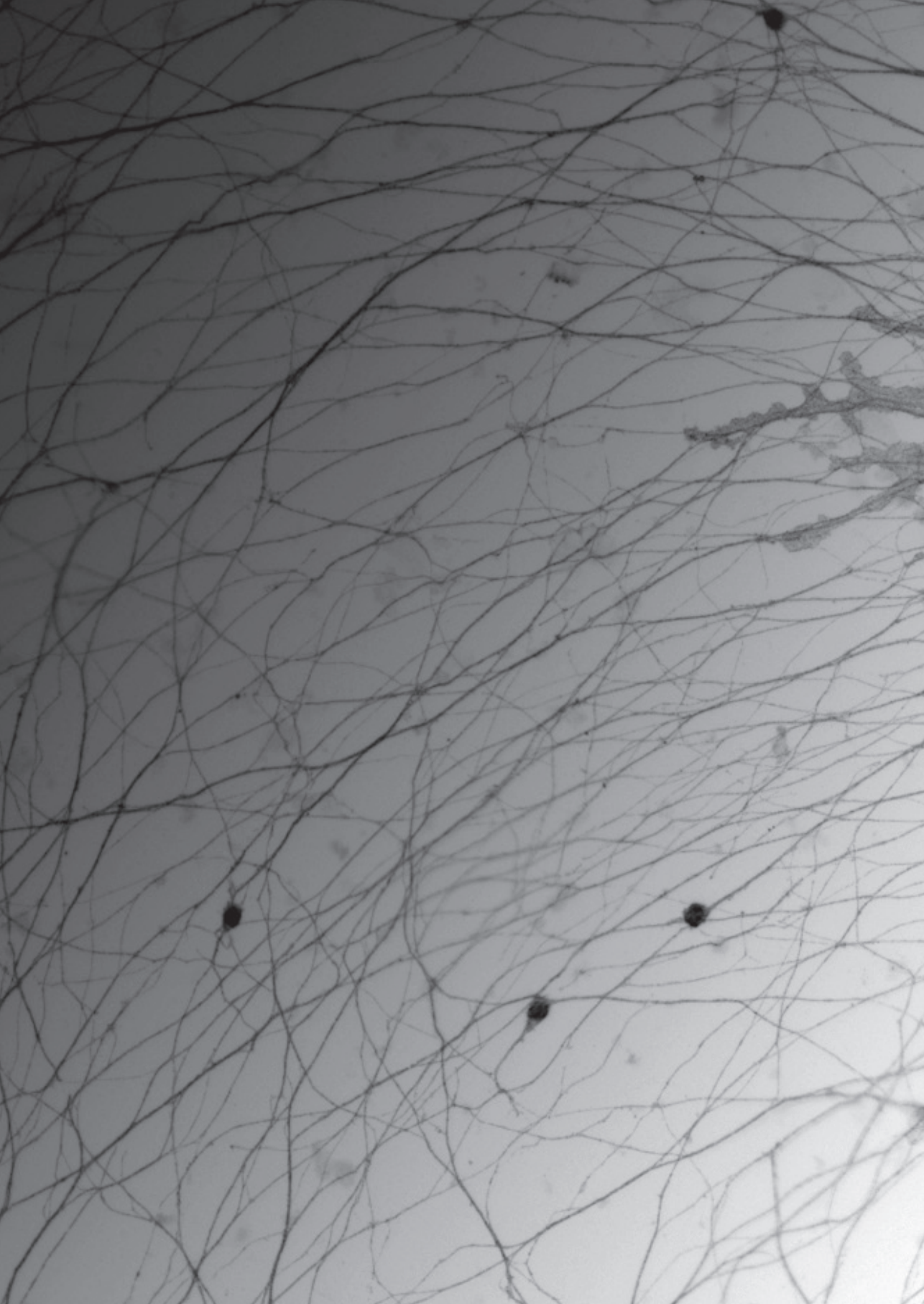
- 
- Kumanogoh, A., Watanabe, C., Lee, I., Wang, X., Shi, W., Araki, H., Hirata, H., Iwahori, K., Uchida, J., Yasui, T., et al. (2000). Identification of CD72 as a lymphocyte receptor for the class IV semaphorin CD100: a novel mechanism for regulating B cell signaling. *Immunity* 13, 621–631.
  - Laederich, M.B., Funes-Duran, M., Yen, L., Ingalla, E., Wu, X., Carraway, K.L., and Sweeney, C. (2004). The leucine-rich repeat protein LRIG1 is a negative regulator of ErbB family receptor tyrosine kinases. *J. Biol. Chem.* 279, 47050–47056.
  - Ledda, F., Bieraugel, O., Fard, S.S., Vilar, M., and Paratcha, G. (2008). Lrig1 is an endogenous inhibitor of Ret receptor tyrosine kinase activation, downstream signaling, and biological responses to GDNF. *J. Neurosci.* 28, 39–49.
  - Lindquist, D., Kvarnbrink, S., Henriksson, R., and Hedman, H. (2014). LRIG and cancer prognosis. *Acta Oncol.* 53, 1135–1142.
  - Maness, P.F., and Schachner, M. (2007). Neural recognition molecules of the immunoglobulin superfamily: signaling transducers of axon guidance and neuronal migration. *Nat. Neurosci.* 10, 19–26.
  - Matsunaga, E., Tauszig-Delamasure, S., Monnier, P.P., Mueller, B.K., Strittmatter, S.M., Mehlen, P., and Chédotal, A. (2004). RGM and its receptor neogenin regulate neuronal survival. *Nat. Cell Biol.* 6, 749–755.
  - Matsunaga, E., Nakamura, H., and Chédotal, A. (2006). Repulsive guidance molecule plays multiple roles in neuronal differentiation and axon guidance. *J. Neurosci.* 26, 6082–6088.
  - Moreau-Fauvarque, C., Kumanogoh, A., Camand, E., Jaillard, C., Barbin, G., Boquet, I., Love, C., Jones, E.Y., Kikutani, H., Lubetzki, C., et al. (2003). The transmembrane semaphorin Sema4D/CD100, an inhibitor of axonal growth, is expressed on oligodendrocytes and upregulated after CNS lesion. *J. Neurosci.* 23, 9229–9239.
  - Nakamura, T., Hamuro, J., Takaishi, M., Simmons, S., Maruyama, K., Zaffalon, A., Bentley, A.J., Kawasaki, S., Nagata-Takaoka, M., Fullwood, N.J., et al. (2014). LRIG1 inhibits STAT3-dependent inflammation to maintain corneal homeostasis. *J. Clin. Invest.* 124, 385–397.
  - Niederkofler, V., Salie, R., Sigrist, M., and Arber, S. (2004). Repulsive guidance molecule (RGM) gene function is required for neural tube closure but not retinal topography in the mouse visual system. *J. Neurosci.* 24, 808–818.
  - Nilsson, J., Starefeldt, A., Henriksson, R., and Hedman, H. (2003). LRIG1 protein in human cells and tissues. *Cell Tissue Res.* 312, 65–71.
  - O'Donnell, M., Chance, R.K., and Bashaw, G.J. (2009). Axon growth and guidance: receptor regulation and signal transduction. *Annu. Rev. Neurosci.* 32, 383–412.
  - Okamura, Y., Kohmura, E., and Yamashita, T. (2011). TACE cleaves neogenin to desensitize cortical neurons to the repulsive guidance molecule. *Neurosci. Res.* 71, 63–70.
  - Pasterkamp, R.J. (2012). Getting neural circuits into shape with semaphorins. *Nat. Rev. Neurosci.* 13, 605–618.
  - Pasterkamp, R.J., De Winter, F., Holtmaat, A.J., and Verhaagen, J. (1998). Evidence for a role of the chemorepellent semaphorin III and its receptor neuropilin-1 in the regeneration of primary olfactory axons. *J. Neurosci.* 18, 9962–9976.

- Powell, A.E., Wang, Y., Li, Y., Poulin, E.J., Means, A.L., Washington, M.K., Higginbotham, J.N., Juchheim, A., Prasad, N., Levy, S.E., et al. (2012). The pan-ErbB negative regulator Lrig1 is an intestinal stem cell marker that functions as a tumor suppressor. *Cell* 149, 146–158.
- Rafidi, H., Mercado, F., Astudillo, M., Fry, W.H.D., Saldana, M., Carraway, K.L., and Sweeney, C. (2013). Leucine-rich repeat and immunoglobulin domain-containing protein-1 (Lrig1) negative regulatory action toward ErbB receptor tyrosine kinases is opposed by leucine-rich repeat and immunoglobulin domain-containing protein 3 (Lrig3). *J. Biol. Chem.* 288, 21593–21605.
- Del Rio, T., Nishitani, A.M., Yu, W.M., and Goodrich, L. V. (2013). In Vivo Analysis of Lrig Genes Reveals Redundant and Independent Functions in the Inner Ear. *PLoS Genet.* 9.
- Romi, E., Gokhman, I., Wong, E., Antonovsky, N., Ludwig, A., Sagi, I., Saftig, P., Tessier-Lavigne, M., and Yaron, A. (2014). ADAM metalloproteases promote a developmental switch in responsiveness to the axonal repellent Sema3A. *Nat. Commun.* 5, 4058.
- Rondahl, V., Holmlund, C., Karlsson, T., Wang, B., Faraz, M., Henriksson, R., and Hedman, H. (2013). Lrig2-deficient mice are protected against PDGFB-induced glioma. *PLoS One* 8, e73635.
- Scheller, J., Chalaris, A., Garbers, C., and Rose-John, S. (2011). ADAM17: A molecular switch to control inflammation and tissue regeneration. *Trends Immunol.* 32, 380–387.
- Schimmelpfeng, K., Gögel, S., and Klämbt, C. (2001). The function of leak and kuzbanian during growth cone and cell migration. *Mech. Dev.* 106, 25–36.
- Severyn, C.J., Shinde, U., and Rotwein, P. (2009). Molecular biology, genetics and biochemistry of the repulsive guidance molecule family. *Biochem. J.* 422, 393–403.
- Stuart, H.M., Roberts, N.A., Burgu, B., Daly, S.B., Urquhart, J.E., Bhaskar, S., Dickerson, J.E., Mermerkaya, M., Silay, M.S., Lewis, M.A., et al. (2013). LRIG2 mutations cause urofacial syndrome. *Am. J. Hum. Genet.* 92, 259–264.
- Suzuki, K., Kumanogoh, A., and Kikutani, H. (2008). Semaphorins and their receptors in immune cell interactions. *Nat. Immunol.* 9, 17–23.
- Suzuki, Y., Miura, H., Tanemura, A., Kobayashi, K., Kondoh, G., Sano, S., Ozawa, K., Inui, S., Nakata, A., Takagi, T., et al. (2002). Targeted disruption of LIG-1 gene results in psoriasiform epidermal hyperplasia. *FEBS Lett.* 521, 67–71.
- Tassew, N.G., Chestopolava, L., Beecroft, R., Matsunaga, E., Teng, H., Chedotal, A., and Monnier, P.P. (2008). Intraretinal RGMa is involved in retino-tectal mapping. *Mol. Cell. Neurosci.* 37, 761–769.
- Tassew, N.G., Charish, J., Seidah, N.G., and Monnier, P.P. (2012). SKI-1 and Furin Generate Multiple RGMa Fragments that Regulate Axonal Growth. *Dev. Cell* 22, 391–402.
- Tassew, N.G., Mothe, A.J., Shabanzadeh, A.P., Banerjee, P., Koeberle, P.D., Bremner, R., Tator, C.H., and Monnier, P.P. (2014). Modifying lipid rafts promotes regeneration and functional recovery. *Cell Rep.* 8, 1146–1159.
- Weber, S., and Saftig, P. (2012). Ectodomain shedding and ADAMs in development. *Development* 139, 3693–3709.
- Wilson, N.H., and Key, B. (2006). Neogenin interacts with RGMa and netrin-1 to guide axons within the embryonic vertebrate forebrain. *Dev. Biol.* 296, 485–498.

- 
- Wong, V.W.Y., Stange, D.E., Page, M.E., Buczacki, S., Wabik, A., Itami, S., van de Wetering, M., Poulsom, R., Wright, N.A., Trotter, M.W.B., et al. (2012). Lrig1 controls intestinal stem-cell homeostasis by negative regulation of ErbB signalling. *Nat. Cell Biol.* 14, 401–408.
  - Xiao, Q., Tan, Y., Guo, Y., Yang, H., Mao, F., Xie, R., Wang, B., Lei, T., and Guo, D. (2014). Soluble LRIG2 Ectodomain Is Released from Glioblastoma Cells and Promotes the Proliferation and Inhibits the Apoptosis of Glioblastoma Cells In Vitro and In Vivo in a Similar Manner to the Full-Length LRIG2. *PLoS One* 9, e111419.
  - Yi, W., Holmlund, C., Nilsson, J., Inui, S., Lei, T., Itami, S., Henriksson, R., and Hedman, H. (2011). Paracrine regulation of growth factor signaling by shed leucine-rich repeats and immunoglobulin-like domains 1. *Exp. Cell Res.* 317, 504–512.
  - Zhao, H., Tanegashima, K., Ro, H., and Dawid, I.B. (2008). Lrig3 regulates neural crest formation in *Xenopus* by modulating Fgf and Wnt signaling pathways. *Development* 135, 1283–1293.
  - Zhou, Z., Xie, J., Lee, D., Liu, Y., Jung, J., Zhou, L., Xiong, S., Mei, L., and Xiong, W.C. (2010). Neogenin Regulation of BMP-Induced Canonical Smad Signaling and Endochondral Bone Formation. *Dev. Cell* 19, 90–102.
  - Zhu, X.-J., Wang, C.-Z., Dai, P.-G., Xie, Y., Song, N.-N., Liu, Y., Du, Q.-S., Mei, L., Ding, Y.-Q., and Xiong, W.-C. (2007). Myosin X regulates netrin receptors and functions in axonal path-finding. *Nat. Cell Biol.* 9, 184–192.







---

# Chapter 5

## Neogenin and its Novel Binding Partner Dock7 are required for RGMa-regulated Radial Cerebellar Granule Neuron Migration

---

Susan van Erp, Dianne M.A. van den Heuvel, M. Renate Buijink, Anita J.C.G.M. Hellemons, Stephen Horan, R. Jeroen Pasterkamp

Department of Translational Neuroscience, Brain Center Rudolf Magnus, University Medical Center Utrecht, 3584 CG Utrecht, The Netherlands.

*Manuscript in preparation*

---

## Abstract

The axon guidance receptor Neogenin and its ligand repulsive guidance molecule a (RGMa) have been implicated in neuronal migration. The novel Neogenin binding partner dedicator of cytokinesis 7 (Dock7) is involved in cytoskeleton remodeling and cellular migration. Here we show that Dock7 is required for RGMa-induced neurite outgrowth inhibition *in vitro*. Immunohistological staining reveals that Neogenin and Dock7 are co-expressed in migrating cerebellar granule neurons (CGNs) of the external granule layer (EGL) and internal granule layer (IGL) *in vitro* and *in vivo*. RGMa is detected on Bergmann glia cells and is strongest at the border of the molecular layer (ML) and IGL. The role of Neogenin in CGN migration was further investigated in explants and ex vivo cerebellar electroporation experiments. Selective knockdown of *Neogenin* or *Dock7* in CGNs stalled radial migration. In addition, CGN migration from EGL-derived explants is inhibited by extracellular RGMa, but this inhibition is attenuated after *Dock7* knockdown. Our data provide evidence that RGMa-induced Neogenin signaling is involved in CGN migration. Furthermore, they suggest that Dock7 functions downstream of Neogenin signaling during RGMa-induced neuronal migration.



## Introduction

In the central nervous system, the most prominent function of Neogenin is as an axon guidance receptor in neurite outgrowth and steering. Neogenin can act as a chemoattractive receptor (following Netrin-1 binding) and as a chemorepulsive receptor (following binding of Repulsive Guidance Molecule a (RGMa)) (Rajagopalan et al. 2004; Wilson & Key 2006). RGM-induced Neogenin signaling has recently also been implicated in cellular migration and adhesion ((Conrad et al. 2010; Lah & Key 2012; Mirakaj et al. 2012). Here we investigated the signal transduction pathway of Neogenin in neuronal migration. In differentiating neurons, Neogenin activation has been shown to lead to F-actin depolymerization by the RhoA kinase (ROCK) signal cascade through RhoA activation, ultimately resulting in growth cone collapse and reduced neurite outgrowth (Hata et al. 2006; Conrad et al. 2007; Kubo et al. 2008). Our previous results identified Dock7 as a potential Neogenin interactor (Van den Heuvel and Pasterkamp, unpublished observations). Transgenic mice expressing green fluorescent protein (GFP)-tagged Neogenin specifically in neurons under the control of the synapsin-I promotor was used to discover interacting proteins *in vivo*. Immunoprecipitation and subsequent mass spectrometry analysis revealed Dock7 as a specific GFP-Neogenin interactor.

Dock7 (dedicator of cytokinesis 7) is a member of the Dock family of guanine exchange factors (GEF), specific for Rho GTPase family member Rac1 and Cdc42 (Watabe-Uchida et al. 2006; Yamauchi et al. 2008). GEFs are responsible for the activation of GTPases by catalyzing the exchange of GDP for GTP (Schmidt & Hall 2002). The Rho family of small GTPases is active when bound to GTP and inactive when bound to GDP (Bar-Sagi & Hall 2000).

In unpolarized neurons, Dock7 is expressed predominantly in the developing axon. In these neurons, knockdown of Dock7 leads to loss of axonal specification. When Dock7 is overexpressed multiple axons are formed. This axonal regulation occurs through phosphorylation of Stathmin/Op18. This microtubule destabilizing protein is deactivated by Dock7 through the activation of Rac (Watabe-Uchida et al. 2006). Like Dock7, Stathmin/Op18 is also enriched in the destined axon. Apart from proliferative zones where populations of unpolarized neurons reside, Stathmin/Op18 is also highly expressed in neuronal migratory pathways (Camoletto et al. 1997). In migrating GnRH neurons knockdown of Stathmin/Op18 reduces cellular motility and leads to the formation of multipolar processes, while overexpression leads to increased motility and proliferation (Giampietro et al. 2005).

---

*In vivo*, Dock7 is involved in nucleokinesis in radial glial progenitors, by interacting with and antagonizing TACC3 function (Yang et al. 2012). TACC3 is a tubulin depolymerizing protein, associated with the centrosome. Knockdown of TACC3 or overexpression of Dock7 results in uncoupling of the centrosome from the cell body, causing increased interkinetic nuclear migration which results in increased neurogenesis. A Dock7 deletion mutant lacking the DHR2 domain, which is responsible for GEF functionality, is still able to control interkinetic nuclear migration and neurogenesis (Yang et al. 2012). This study therefore directly links Dock7 to a microtubule binding protein independent of its function as a GEF.

In the peripheral nervous system, Dock7 is important in the migration, differentiation and myelination of Schwann cells (Yamauchi et al. 2008; Yamauchi et al. 2011). In Schwann cells, expression of Dock7 is associated with the regulation of two distinct developmental stages. First, Dock7 positively regulates Schwann cell migration through Rac1/Cdc42-mediated activation of the JNK pathway (Yamauchi et al. 2008). The next developmental step for Schwann cells after migration is differentiation and myelination. Dock7 negatively regulates these processes as knockdown of Dock7 results in increased differentiation and myelination (Yamauchi et al. 2011). During Schwann cell development, Dock7 is tyrosine phosphorylated and thereby activated by the ErbB2 receptor. This activation leads to increased activity of Rac1 and its downstream signal transduction cascade involved in the differentiation of Schwann cells (Yamauchi et al., 2008).

Here we show that Dock7 regulates RGMa-Neogenin signaling during neuronal migration. We perform an extensive analysis of Neogenin and RGMa expression in the developing cerebellum, and show that Neogenin and Dock7 expression colocalizes at specific stages of CGN development. *In vivo* radially migrating CGNs encounter RGMa and loss of either Neogenin or Dock7 leads to impaired radial CGN migration. Finally, knockdown of Dock7 renders CGN insensitive to extracellular RGMa, suggesting that the interaction of Neogenin with Dock7 is required for efficient RGMa-induced signaling during CGN migration.

## **Materials & Methods**

### **Plasmids**

For Neogenin knockdown experiments, a DNA fragment encoding a short hairpin (sh) RNA directed against mouse Neogenin (GAAACAACCTGCTAACATA) was cloned into pSuper, using BglIII/HindIII restriction sites (Brummelkamp et al. 2002). A pSuper vector containing a DNA fragment encoding a short hairpin (sh) RNA directed against mouse *Dock7* (GCTAATCGGGATGCAAAGA) was used (pSuper-Dock7#1; a kind gift of Linda Van Aelst). A pSuper vector expressing a

scrambled non-targeting shRNA was used as control (GACAACCAATCGTAATACA). For production of Fc-tagged RGMa, the extracellular domain of RGMa lacking the GPI link was cloned into a pHLSec backbone vector, creating pHLSec-RGMa-Fc (Zhao et al. 2011).

### **Animals and tissue treatment**

All animal use and care were in accordance with institutional guidelines. C57BL/6 mice were obtained from Charles River. The day that pups were born was designated postnatal day (P)0. Pups were killed by decapitation and the cerebellum was dissected. For *in situ* hybridization experiments, cerebella were directly frozen in 2-methylbutane (Merck). For immunohistochemistry, cerebella were rinsed in phosphate-buffered saline (PBS; pH 7.4) and fixed by immersion for 2 hours (hrs) in 4% paraformaldehyde (PFA) in PBS at room temperature (RT). After fixation, cerebella were immersed in 30% sucrose solution in PBS overnight at 4°C and frozen on dry ice the next day. Sections were cut on a cryostat (16 µm), mounted on Superfrost Plus slides (Fisher Scientific), air-dried and stored at -80°C for *in situ* hybridization and at -20°C for immunohistochemistry.

### **Cell culture and transfection**

HEK293 cells were maintained in high glucose Dulbecco's Modified Eagle Medium (DMEM; Gibco, Invitrogen) supplemented with 10% heat-inactivated fetal calf serum (FCS, Lonza, BioWhittaker), 2mM L-glutamine (PAA) and 1x penicillin/streptomycin (pen/strep; PAA). CHO and stable RGMa-expressing CHO (CHO-RGMa) cell lines were a kind gift of Toshihide Yamashita (Hata *et al.* 2006). CHO cells were cultured in Ham's F12 nutrient mixture (Gibco, Invitrogen) supplemented with 10%FCS, 2mM L-glutamine and 1xpen/strep. Cell culture medium for CHO-RGMa cells was additionally supplemented with 300 µg/ml hygromycin B (Roche). N1E-115 cells were maintained in high glucose DMEM supplemented with 2% FCS, 2mM L-glutamine and 1xpen/strep. All cells were cultured in a humidified atmosphere with 5% CO<sub>2</sub> at 37°C. HEK293 cells were transfected using polyethylenimine (PEI; Polysciences) (Reed et al. 2006).

### **Immunoprecipitation and Western blot**

For endogenous pull down and co-immunoprecipitation experiments, P0 mouse brains or cells (10cm plates) were lysed in lysis buffer (20 mM Tris-HCl, pH 8.0, 150 mM NaCl, 1% NP-40, 10% glycerol and Complete protease inhibitor cocktail (Roche)) and incubated for 30 min in a rotor and centrifuged at 14,000 rpm for 15 min at 4°C. Cleared supernatants were incubated with 1 µg of the indicated antibodies at 4° C. After 2 hrs, 10 µl protein A/G Dynabeads (Invitrogen), which had been blocked in blocking buffer (20 mM Tris-HCl, pH 8.0, 150 mM KCl, 20%



---

glycerol and 200 ng/ $\mu$ l albumin from chick egg white (Sigma-Aldrich)) were added and samples were incubated for 1 hour rotating at 4°C. Pull down samples were washed 3 times in washing buffer (20 mM Tris-HCl, pH 8.0, 150 mM NaCl, 1% NP-40 and 10% glycerol) and precipitated proteins were eluted by incubating the beads in 2x NuPAGE LDS sample buffer (Invitrogen) with 2.5%  $\beta$ -mercaptoethanol for 10 min at 70°C.

Proteins were separated in 8% SDS-PAGE gels and transferred onto nitrocellulose membrane (Hybond-C Extra; Amersham). Membranes were incubated in blocking buffer (PBS, 0.05% (v/v) Tween 20 and 5% milk powder) for 30 min at RT followed by incubation with primary antibodies in blocking buffer overnight at 4°C. Antibodies used: rabbit anti-Dock7 antibody (28057; IBL, 1:500); mouse anti-FLAG (Stratagene, 1:2000); goat anti-Neogenin antibody (AF1079; R&D systems, 1:2000); mouse anti- $\alpha$ -Tubulin antibody (T5168; Sigma-Aldrich, 1:8000). Blots were incubated with SuperSignal West Dura Extended Duration Substrate (Pierce) and exposed to ECL films (Pierce).

### **Neurite outgrowth assay**

Dissociated E14.5 cortical neurons (400.000/50  $\mu$ l sample) were electroporated with 4  $\mu$ g DNA in 50  $\mu$ l electroporation buffer (135 mM KCl, 2 mM MgCl<sub>2</sub>, 0.2 mM CaCl<sub>2</sub> and 5 mM EGTA, pH 7.3) using a BTX Electro Square Porator ECM 830 (BTX Harvard Apparatus; settings: 100 V, 3 pulses, 900  $\mu$ s pulse length, 2 s pulse interval). 170  $\mu$ l 37°C RPMI 1640 medium (Gibco, Invitrogen) was added to the electroporation sample and electroporated neurons were transferred to 4 wells of a 24-well plate. Electroporated neurons were cultured on a confluent layer of CHO or CHO-RGMA cells in DMEM/F12 (Gibco, Invitrogen) containing 2% FBS (Lonza, BioWhittaker), 2 mM L-glutamine (PAA), 1x pen/strep (PAA) and B-27 Supplement (Gibco, Invitrogen) in a humidified atmosphere with 5% CO<sub>2</sub> at 37°C. After 4 days cells were fixed with 4% PFA for 15 min at RT and washed in PBS (pH 7.4). Cells were permeabilized and blocked in blocking solution (PBS, 4% BSA and 0.1% Triton) for 1 hr at RT and incubated with rabbit anti-GFP (A11122; Invitrogen) at 1:3000 and mouse anti- $\beta$ III tubulin (MMS-435P; Covance) at 1:2000 in blocking solution overnight at 4°C. The next day, wells were washed in PBS and incubated with Alexa Fluor 594 goat anti-mouse and Alexa Fluor 488 goat anti-rabbit (Invitrogen) at 1:500 for 1 hr at RT. Images were taken using a Cellomics ArrayScan VTI HCS Reader (Thermo Scientific) and the length of the longest neurite was measured using NeuronJ (Meijering *et al.* 2004). Data were statistically analyzed by two-tailed Student's t-test and represented as means  $\pm$  SEM.

## RGMaFc protein production and purification

For RGMa-Fc protein production, HEK293 cells were transfected with pHSec-RGMa-Fc plasmid DNA and cultured in Opti-MEM Reduced Serum Medium (Gibco, Invitrogen) supplemented with 3% FCS (Lonza, BioWhittaker), 2 mM L-glutamine (PAA) and 1x pen/strep (PAA). Cell culture medium containing Fc-tagged ligands was collected after 5 days in culture, filter-sterilized and incubated with Protein A Agarose beads (Roche) overnight at 4°C. The next day, beads with bound RGMa-Fc were washed four times in ice-cold PBS. To elute RGMa-Fc beads were incubated with 100 mM glycine (pH 2.5). Eluted RGMa-Fc protein was neutralized by adding 10mM Tris-HCl (pH 9.5), followed by dialysis and concentration in PBS using Centrifugal filter units Amicon Ultra 0.5 ml 10K Ultracel-10K membrane (Millipore). To determine the final concentration of RGMa-Fc, samples were run on SDS-PAGE gel together with a BSA standard series. Proteins were visualized with GelCode Blue Stain Reagent (Pierce) and in-gel comparison of band intensity was used to estimate protein concentration. For Fc control protein, human IgG Fc fragment (Calbiochem) was used.

## *In situ* hybridization

Probe sequences were amplified from *RGMa*, *Neogenin* and *Dock7* cDNA using the primers listed in Table 1 and subsequently Digoxigenin (DIG)-labeled complementary (c)RNA probes were created by RNA polymerase reaction using 10x DIG RNA labeling mix (ENZO). Nonradioactive *in situ* hybridization was performed as described previously (Pasterkamp et al. 1998). Fresh frozen tissue sections were post-fixed in 4% PFA in PBS (pH 7.4) for 20 minutes (min) at RT. To enhance tissue penetration and decrease nonspecific background staining, sections were acetylated with 0.25% acetic anhydride in 0.1 M triethanolamine and 0.06% HCl for 10 min at RT. Sections were prehybridized for 2 hrs at RT in hybridization buffer (50% formamide, 5x Denhardt's solution, 5x SSC, 250 µg/ml baker's yeast tRNA and 500 µg/ml sonicated salmon sperm DNA). Denatured DIG-labeled cRNA probe diluted in hybridization buffer (400ng/ml) was applied to the sections and incubated overnight at 68°C. Next, sections were rinsed briefly in 2x SSC followed by a stringency wash in 0.2x SCC for 2 hrs at 68°C. Sections were adjusted to RT in 0.2x SSC for 5 min and blocked in Tris buffered saline (TBS) pH 7.4 with 10% FCS for one hour at RT. Anti-DIG Fab fragments conjugated to alkaline phosphatase (Boehringer) were diluted in TBS pH.4 (1:2500) and incubated with sections overnight at 4°C. Binding of antibody to DIG-labeled probes was visualized by incubating the sections in alkaline phosphatase substrate containing detection buffer (100 mM Tris-HCl, pH 9.5, 100 mM NaCl, 50 mM MgCl<sub>2</sub>, 240 µg/ml levamisole and nitro-bluetetrazolium chloride/5-bromo-4-chloro-3-indolylphosphatase (NBT/BCIP, Roche)) at RT until staining

was clearly visible (approximately 14 hrs). Sections subjected to the entire *in situ* hybridization procedure, but with no probe or with sense probe added, did not exhibit specific hybridization signals. The specificity of the *in situ* hybridization procedure was also inferred from the clearly distinct gene expression patterns observed. Staining was visualized using a Zeiss Axioskop 2 microscope.

**Table 1. Sense and antisense primer sequences for *RGMa*, *Neogenin* and *Dock7* *in situ* hybridization probes.**

Gene	Sense primer	Antisense primer	Size
<i>RGMa</i>	5'-TCAGCTGCCCCAACTACT-3'	5'-TCCTCCACGGCGTTGACTACC-3'	454 bp
<i>Neogenin</i>	5'-ACACCGTTATCTGGCAATGG-3'	5'-TTCAGCAGACAGCCAATCAG-3'	501 bp
<i>Dock7</i>	5'-AAGATCAGCAGAAGCTGTTGC-3'	5'-AAGTCAAAGATACTGCAGGC-3'	566 bp

## Immunocytochemistry

P8 cerebellar granule neurons were cultured as explants or dissociated on coverslips and fixed at DIV2 or DIV5 with 4% PFA for 15 min at RT followed by a wash in PBS (pH 7.4). Neurons were permeabilized and blocked in blocking buffer (PBS, 3% goat serum (Sigma-Aldrich), 2% horse serum, 1% bovine serum albumin (BSA), 1% glycine, 0.1% lysine, 0.4% Triton) for 1 hr at RT. Primary antibodies were diluted in blocking buffer and incubated with coverslips overnight at 4°C. Antibodies used: rabbit anti-Dock7 (28057, IBL; 1:100), goat anti-Neogenin (AF1079, R&D systems; 1:400), mouse anti-βIII tubulin (T8660, Sigma; 1:5000) and rabbit anti-GFP (A11122, Invitrogen; 1:2000). The next day, neurons were washed in PBS and incubated with the appropriate Alexa Fluor-labeled secondary antibodies (Invitrogen) at 1:750 for 1 hr at RT. After subsequent washes, coverslips were incubated for 10min in PBS with DAPI (Invitrogen, 1:3000) to visualize nuclei and where mentioned Alexa-594 conjugated phalloidin (1:250) to visualize F-actin. The coverslips were mounted on microscope slides embedded in Prolong Gold Antifade (Invitrogen). Staining was visualized using a Zeiss Axioskop 2 microscope.

## Immunohistochemistry

Prefixed tissue cryo-sections were washed in PBS (pH 7.4) and incubated in horse blocking buffer (PBS, 5% Horse Serum (Sigma-Aldrich), 1% BSA, 1% glycine, 0.1% lysine, 0.4% Triton) for 1 hr. Primary antibodies were diluted in blocking buffer and incubated with coverslips overnight at 4°C. Antibodies used: rabbit anti-Dock7 (28057, IBL; 1:100), goat anti-Neogenin (AF1079, R&D systems; 1:200), mouse anti-Calbindin (D-28, Swant; 1:2000), guinea pig anti-Doublecortin (AB2253, Millipore;

1:1000), mouse anti-TAG1 (4D7, DSHB; 1:100) and rabbit anti-Ki67 (ab15580, Abcam; 1:1000). The next day, sections were washed in PBS and incubated with the appropriate Alexa Fluor-labeled secondary antibodies (Invitrogen) at 1:750 for 1 hr at RT. Slides were washed in PBS, counterstained with fluorescent Nissl (NeuroTrace, Invitrogen; 1:500) or DAPI (Invitrogen, 1:3000) for 15 min at RT, washed in PBS and embedded in Mowiol (Sigma-Aldrich). Staining was visualized using a Zeiss Axioskop 2 microscope and an Olympus FluoView FV1000 confocal microscope.

After four days in culture, electroporated cerebellar slices in culture inserts were fixed in 4% PFA overnight at 4°C. The following day, slices were washed three times for 20 min on a rocking platform at RT. The membrane holding the slices was excised from the insert and incubated for 5-6 hours in Goat Blocking Buffer (GBB; PBS, 5% Normal Goat Serum (NGS), 1% BSA, 1% glycine, 0.4% Triton-X100) on a rocking platform at RT. Buffer was replaced with GBB containing rabbit anti-GFP (1:2000) and mouse anti-Calbindin (1:1000) antibody and membranes incubated overnight at 4°C. The next day the membranes were washed 3 times 30 min with PBS on a rocking platform at RT. Membranes were incubated in GBB containing the appropriate AlexaFluor labeled secondary antibodies (Invitrogen, 1:750) overnight at 4°C. Membranes were washed 3 times 30min in PBS and then incubated in DAPI solution (1:3000) for 20 minutes on a rocking platform at RT followed by a PBS wash. Membranes were mounted on microscope slides, embedded in FluorSave Reagent (Merck Millipore) and covered with glass coverslips for fluorescent microscopy analysis on an Olympus FluoView FV1000 confocal microscope.

### ***Ex vivo* cerebellar electroporation**

*Ex vivo* electroporation of mice cerebella was adapted from (Ruiz de Almodovar et al. 2011). P9 mice were decapitated, scalp and skull were stripped, and the cerebellum and brainstem were dissected in dissection medium (Leibovitz L15, Life Technologies, Invitrogen; 5 mM HEPES, Sigma-Aldrich). Meninges and blood vessels were carefully removed and DNA mixture (500 ng/ $\mu$ L DNA, 0.02% FastGreen in PBS) was injected into the EGL via heat-pulled capillary tubes pressured by a 1 mL syringe. Injected cerebella were electroporated with 5 pulses of 85 V for 50 ms each, with 1 s intervals (ECM830 ElectroSquare Porator, BTX, Harvard Apparatus). The sample was returned to dissection medium, and bubbles, remaining meninges, blood vessels, and the brainstem were removed. The cleaned and electroporated cerebella were cut into 300  $\mu$ m sections (McIlwain Tissue Chopper, The Mickle Laboratory Engineering Co., Ltd.) and the slices separated in dissection medium. Slices were kept in culture on cell culture inserts (0.4 mm, Millipore) in a humidified atmosphere at 37°C for four days, with

---

slice culture medium (50% Basal Medium Eagle (Sigma-Aldrich), 25% Hank's Balanced Salt Solution (Life Technologies, Invitrogen), 25% Horse Serum, 1 mM L-glutamine and 1x Pen/Strep) replaced after two days.

### **Explant migration assay**

Coverslips were coated with poly-D-lysine (100 µg/mL), rinsed and airdried. Next, coverslips were incubated with mouse laminin (40 µg/mL, Invitrogen) and purified RGMa-Fc (50 µg/mL) or control Fc protein (50 µg/mL) diluted in Neurobasal medium (Life Technologies, Invitrogen) overnight at 4°C. Shortly before plating, coverslips were washed once with Neurobasal medium (NB) and then equilibrated in explant culture medium (1xB27 supplement (Gibco, Invitrogen), 5 mM HEPES, 2 mM L-glut, 1x Pen/Strep in NB) in a humidified atmosphere at 37°C with 5% CO<sub>2</sub>. Cerebella were dissected, and where mentioned electroporated, and sliced as described above. The external granule layer (EGL) of the slices was further dissected in ice-cold L15 medium supplemented with 5% HI-FCS. Where mentioned, electroporated, Fastgreen-stained EGL was dissected specifically. Explants were collected with a P1000 pipet tip and plated on coated coverslips. Explants were cultured for 3 days in a humidified atmosphere at 37°C and 5% CO<sub>2</sub>.

### **Migration analysis**

For analysis of CGN migration in cerebellar slices the molecular layer was outlined in microscope images using ImageJ based on anti-Calbindin staining of Purkinje cells and laminar architecture as defined by DAPI nuclear staining. The number of CGNs present in each layer was counted with ImageJ and the relative distribution per image was determined. The average distribution of over ~20 images per animal was calculated per experiment, with each experiment consisting of an shRNA knockdown and scrambled control electroporated animal in parallel (n = 4 separate experiments for Neogenin knockdown, n = 3 separate experiments for Dock7 knockdown).

The migration of CGNs from EGL explants was analyzed using ImageJ. The distance between the cell body of the migrating CGNs as determined by DAPI staining and the explant was measured. In case of electroporation experiments, only GFP-positive cell bodies were analyzed. The average migration distance per explant was calculated (with at least 10 cells per explants), for at least 10 explants per condition. Each experiment consisted of an shRNA knockdown and scrambled control electroporated animal dissected in parallel, and for each animal the explants were divided equally between RGMa-Fc and control Fc coated coverslips (n = 3 separate experiments).

## Results

### **Dock7 interacts with Neogenin and is required for RGMa-induced neurite outgrowth inhibition**

Co-immunoprecipitation experiments were used to verify the interaction between Neogenin and Dock7, which was identified previously through *in vivo* pull-down experiments followed by mass spectrometry (Van den Heuvel and Pasterkamp, unpublished observations). An anti-GFP pull down on lysates of HEK293 cells transfected with GFP-Neogenin and FLAG-Dock7 precipitated GFP-Neogenin and immunoblotting using anti-FLAG antibodies confirmed that FLAG-Dock7 co-precipitated with GFP-Neogenin (fig. 1A). Additionally, endogenous pull down experiments on N1E-115 neuroblastoma and mouse P0 whole brain lysates specifically detected the presence of Neogenin in Dock7 pull down samples. Neogenin was not detected in a control pull down experiment using a non-specific anti-IgG rabbit antibody (fig. 1B-C).

Next, the functional contribution of Dock7 to RGMa-induced signaling was investigated. We confirmed that Dock7 shRNA (Watabe-Uchida et al. 2006) induced specific knockdown of endogenous Dock7 in N1E-115 neuroblastoma cells, as compared to a scrambled control shRNA (fig 1D). Dissociated primary cortical neurons were electroporated with pSuper vector containing shRNA targeting Dock7 (shDock7) and cultured on a monolayer of wild type CHO cells (CHO-control) or CHO cells stably expressing RGMa (CHO-RGMa). Control neurons electroporated with non-targeting scrambled shRNA (shScr) showed a strong reduction in neurite length when cultured on CHO-RGMa cells. Knockdown of Dock7 restored neurite length on CHO-RGMa to control levels, i.e. neurite length of neurons grown on CHO-control cells (fig 1E). Thus, Dock7 is required for RGMa-induced neurite outgrowth inhibition.

### **Neogenin and Dock7 but not RGMa expression patterns overlap *in vivo* in the EGL and IGL**

Neogenin and RGMa expression in the developing cerebellum has been shown previously (van den Heuvel et al. 2013). The cerebellum has a unique laminar architecture, which is recognizable by visualizing the presence of three of its most prominent cell types; Purkinje neurons, Bergmann glia and cerebellar granule neurons (CGNs). Purkinje neurons have large dendritic trees ascending through the molecular layer (ML) to the border of the external granule layer (EGL). The monolayer of Purkinje cell bodies forms the Purkinje cell layer (PCL) which demarcates the border to the internal granule layer (IGL) (fig 2A). Bergmann glial processes extend to the top of the EGL, providing a scaffold for radially migrating CGNs (fig 2A). Their cell bodies are located between the much larger



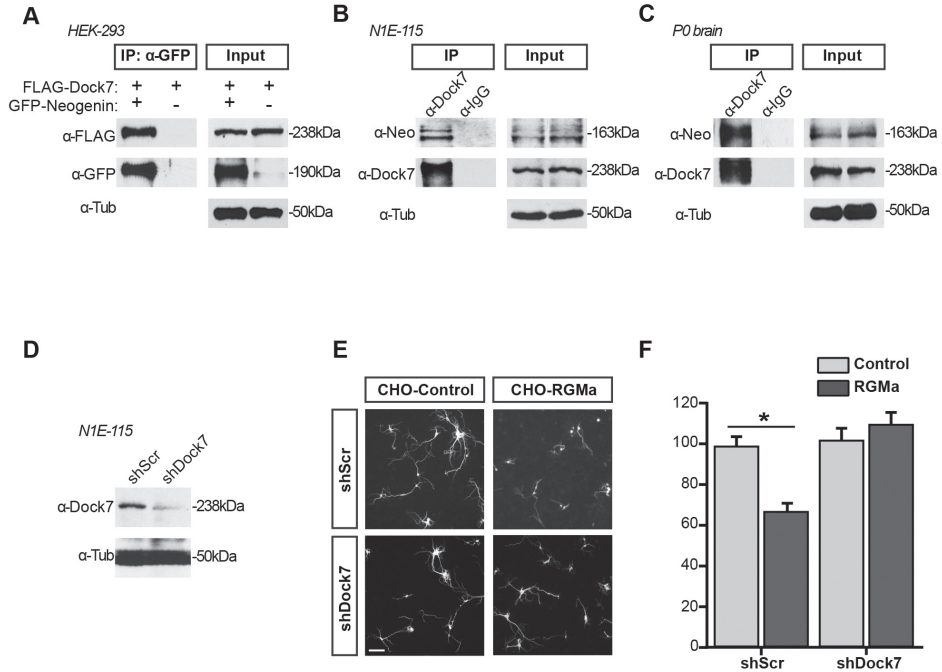


**Figure 1. Dock7 is an *in vivo* binding partner of Neogenin and is required for RGMA-induced neurite outgrowth inhibition**

**A.** Anti-FLAG immunoblotting detects FLAG-Dock7 in an anti-GFP pull down experiment for GFP-Neogenin, both transiently expressed in HEK293 cells. **B-C.** Immunoblotting shows co-immunoprecipitation of Neogenin in an endogenous pull down experiment for Dock7 in N1E-115 neuroblastoma cells (**B**) and P0 mouse brain lysate (**C**). **D.** Dock7 shRNA (shDock7) induces a strong knockdown of endogenous Dock7 in N1E-115 neuroblastoma cells, as compared to non-targeting scrambled shRNA (shScr). **E.** Neurite outgrowth of dissociated cortical neurons electroporated with GFP and shScr is reduced when cultured on a confluent layer of CHO-RGMa cells, as compared to CHO-control cells. No reduction in neurite length is observed in shDock7-electroporated dissociated cortical neurons cultured on CHO-RGMa cells. Immunocytochemistry using anti-βIII tubulin antibodies was used to visualize neurons. Scale bar is 100μm. **F.** Dissociated cortical neurons were electroporated with shScr or shDock7 and cultured on a confluent layer of CHO-control or CHO-RGMa cells for 4 days. Graph shows average length of the longest neurite per neuron ±SEM, \*p<0.001, Student T-test. Average neurite length of shScr-transfected cells on control CHO cells was set to 100%. sh, short hairpin; Dock7, dedicator of cytokinesis 7; GFP, green fluorescent protein; IP, immunoprecipitation; Neo, Neogenin; Tub, alpha-tubulin.

Purkinje neurons. At P15, CGNs can be seen at their final location in the IGL, while radial migration is still taking place for others. To visualize CGNs specifically, an inducible *Math1-Cre* mouse was crossed with a *lox-stop-lox YFP* mouse. At E16.5, *Math1* is expressed by precursor CGNs and induction of Cre activity at that time point provides specific labeling of CGNs at P15 (MacHold & Fishell 2005). The stop codon preceding the YFP gene is selectively recombined upon activation of Cre in these mice, ensuring stable expression of YFP in targeted cells (fig 2A).

The structure of the cerebellum changes dramatically during postnatal development because its most abundant cell type, the CGN, is undergoing proliferation, migration and differentiation in the period from approximately P4 to P21. Proliferation takes place in the outer (o)EGL as can be visualized at P8 by immunostaining for Ki67 (fig 2B-C). Postmitotic CGNs start migrating tangentially through the inner (i)EGL along the surface of the cerebellum. When they reach the border with the ML, they switch direction and commence radial migration (fig 2C). Radial migration can be visualized by immunolabeling for TAG-1, which is expressed on the surface of developing axons (fig 2B) (Yamamoto et al. 1990). When the CGN reaches the border of the PCL and the IGL, it switches from glia-guided to non-glia guided radial migration. Around P20, all CGNs are fully differentiated and reside in the IGL as shown by NeuN staining (fig 2B-C).

To explore a potential role for *Dock7* in Neogenin signaling during CGN migration, we performed *in situ* hybridization and immunohistochemistry at several stages. During postnatal development, *Neogenin* was expressed at P5 and P10 in the EGL, PCL and sparser labeling was present in the IGL (fig 3A). Staining was absent in the ML (fig 3A). At protein level the distribution of this transmembrane protein appeared more diffused than the mRNA staining (fig 3B). However, strong *Neogenin* mRNA expression in the EGL was reflected at protein level at both P5 and P10. *Neogenin* protein levels were low but not absent in the ML (fig 3B). In the PCL and IGL of P5 cerebella, *Neogenin* staining was strong which is in line with high levels of mRNA expression in this cell layer (fig 3A-B). *Neogenin* expression in the PCL could originate from Purkinje cells, Bergmann glia or migrating CGNs present in this layer. In the IGL, *Neogenin* staining was present at P5 and at lower levels at P10 but the relatively high density of CGNs in the IGL made it impossible to determine if this staining originated from a subset of cells highly expressing *Neogenin*, or from low expression in all CGNs.

*RGMa* mRNA was expressed in Bergmann glia cells and in a subset of cells in the IGL at both P5 and P10 (fig 3A). Co-immunostaining with GFAP has previously shown that *RGMa* is localized on Bergmann glia fibers extending into the ML (Van den Heuvel et al., 2012). At P5, the protein expression pattern of *RGMa* resembled that of GFAP, confirming these previous findings (fig 3B). Furthermore, *RGMa* mRNA staining at P5 and P10 was most prominent in cells estimated

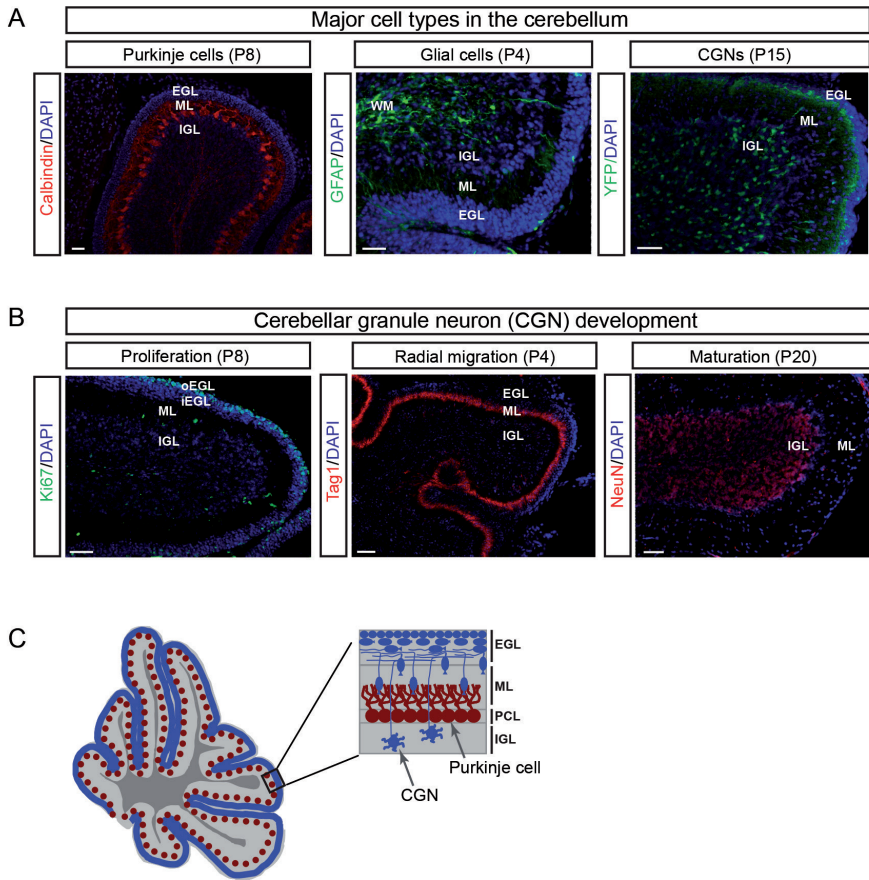


**Figure 2. Cell types and cellular processes in the postnatal mouse cerebellum.**

**A.** Postnatal mouse cerebella were stained for a Purkinje cell marker (anti-Calbindin) at P8, a glia cell marker (anti-GFAP) at P4, and tissue from a P15 transgenic Math1-cre:YFP mouse conditionally expressing YFP in CGNs was stained with anti-GFP. **B.** Several aspects of CGN development were visualized using immunohistochemistry. Proliferating CGNs are present in the EGL as shown by anti-Ki67 staining at P8; radial migration takes place in the ML at P4 as shown by anti-Tag1 staining; and mature CGNs are visualized in the IGL at P20 by anti-NeuN staining. **C.** Schematic of the developing cerebellum. Precursor CGNs (blue) proliferate in the EGL, after which post-mitotic cells tangentially migrate, leaving long trailing processes behind which will later become parallel fibers. After a switch in migration, CGNs continue radially through the ML to the Purkinje cell (red) layer (PCL) along the processes of Bergmann glia cells. CGNs continue to migrate into the IGL where they fully mature and extend dendritic processes. Scale bars are 50 $\mu$ m.

to be Bergmann glia residing in the PCL (fig 3A). At P10, RGMA protein levels were high in the ML and in the white matter, but no specific cellular structures could be detected in the ML by immunostaining. RGMA can be attached to the membrane by its GPI, link but its extracellular domain can also be released into the intercellular space (Tassew et al. 2012). The pattern of immunostaining at P10 suggests that RGMA may predominantly exist as a secreted protein in these structures (fig 3B).

The mRNA and protein expression pattern of Dock7 partially overlapped with that of Neogenin at both P5 and P10 (fig 3A-B). Interestingly, strong *Dock7* mRNA expression was detected in CGNs in the EGL and in the IGL (fig 3B). Moreover, strong *Dock7* mRNA staining was seen in the PCL at P5 and P10, and immunostaining suggested that Dock7 was present in several cell types in this layer, including but not limited to Purkinje cells (fig 3B).

### **Migrating CGNs co-express Neogenin and Dock7 *in vitro***

Immunostaining of cerebellar tissue sections indicates that Neogenin and Dock7 are coexpressed in the EGL and IGL. To provide further insight into the cell types in these layers that express Neogenin, tissue from P8 EGL and IGL was dissected and cultured 5 days *in vitro* (DIV) as explants followed by co-immunostaining for Neogenin and neuronal marker  $\beta$ III tubulin. This revealed that Neogenin is expressed in CGNs that migrate out of the explants (fig 3C). Both EGL- and IGL-derived migrating CGNs express Neogenin, in line with our observation that Neogenin is expressed in the EGL and IGL *in vivo* (fig 3B-C). Next, we determined whether Dock7 and Neogenin are co-expressed in CGNs derived from P8 EGL and IGL. Tissue was dissected followed by dissociation and immunostaining after 2 DIV. Neogenin was strongly expressed in both EGL- and IGL-derived CGNs, with strong staining in the growth cone of the leading process and the cell body (fig 3D). Dock7 was also present in both EGL- and IGL- derived CGNs, with lower expression levels in the growth cone, and was found in punctae along the neurite of the leading process. Again, strong staining of the cell body was observed (fig 3D). Taken together, immunostaining of cerebellar tissue, explants, and dissociated granule cells revealed co-expression of Neogenin and Dock7 in migrating CGNs.

### ***Ex vivo* electroporation enables gene expression manipulation and analysis of CGN migration**

Because of the colocalizing expression of Dock7 and Neogenin in migrating CGNs, we investigated whether Neogenin signaling is dependent on Dock7 in these cells. To do this, we used an *ex vivo* cerebellar electroporation assay. P9 mouse cerebella were injected with DNA solution in the EGL specifically, followed

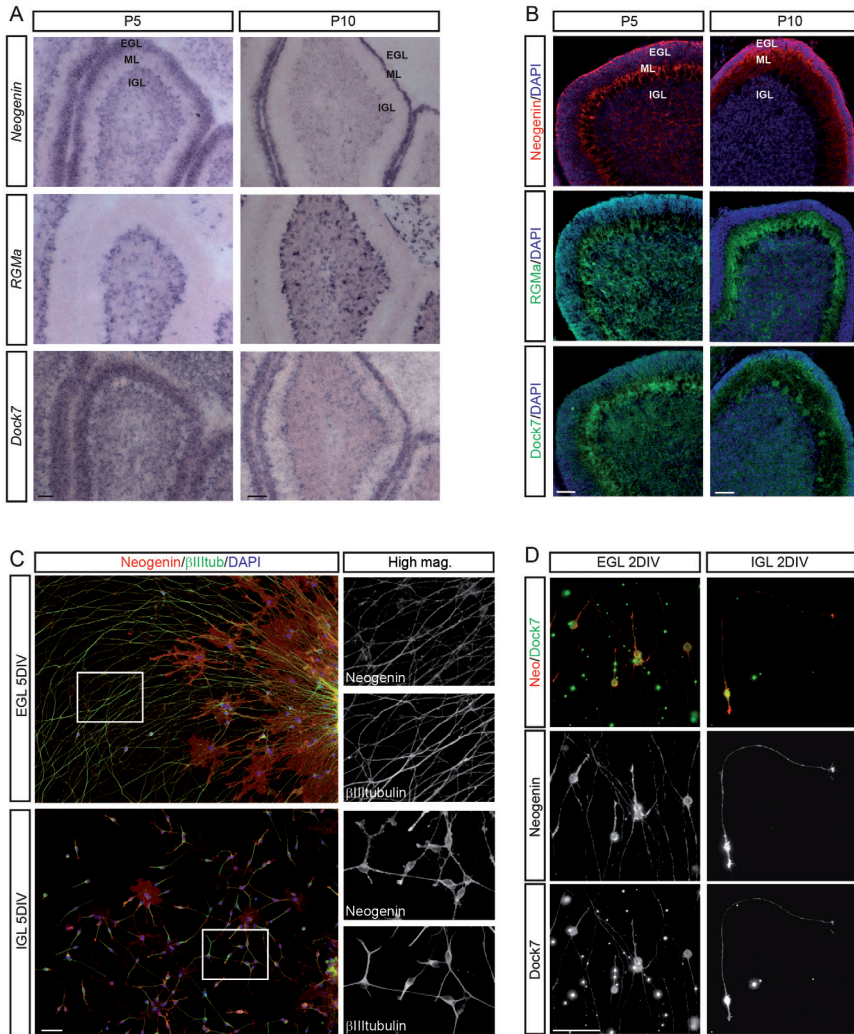


**Figure 3. Neogenin and Dock7 expression partly overlaps in the developing cerebellum.**

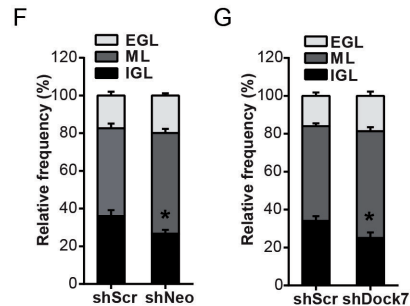
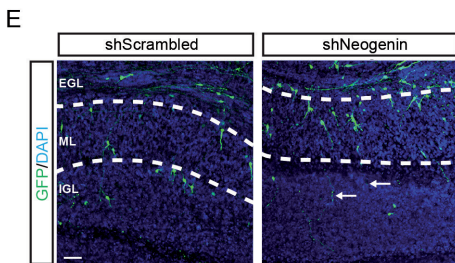
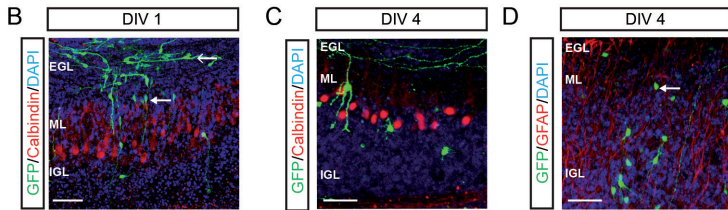
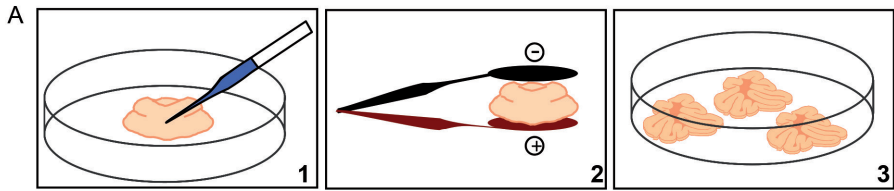
**A.** P5 and P10 mouse cerebella were used for *in situ* hybridization to detect *Neogenin*, *Dock7* and *RGMa*. *Neogenin* and *RGMa* show mostly complementary staining at both P5 and P10, while *Dock7* expression partly overlaps with *Neogenin* signals. **B.** Immunohistochemistry was performed to analyze the expression of Neogenin, Dock7 and RGMA protein in P5 and P10 mouse cerebella. Neogenin and Dock7 expression is strongest in the EGL, PCL and IGL. RGMA is found in the ML and IGL. **C.** EGL- and IGL- derived explants were cultured for 5 days *in vitro* (DIV) and immunostained for Neogenin and  $\beta$ III tubulin. Both EGL- and IGL- migrating neurons express Neogenin. Higher magnifications of the boxed areas are shown at the right. **D.** To investigate the subcellular localization of Neogenin and interactor Dock7, immunocytochemistry on dissociated CGNs was performed. CGNs from either EGL or IGL were cultured for 2 DIV and double-labeled using anti-Neogenin and anti-Dock7 antibodies. Scale bars are 50 $\mu$ m.

by electroporation to induce DNA uptake in proliferating CGNs (fig 4A). Next, organotypic coronal slices were cut and cultured for 4 DIV to allow CGNs to follow their normal migratory route (fig 4A). This method induces uptake of plasmid DNA in a subset of EGL neurons, which can then be visualized by immunostaining. Hence, this approach allows visualization of tangential and radial CGN migration *in vitro*. It takes on average 50 hours for a postmitotic CGN to reach its final target in the IGL (Komuro & Rakic 1995; Komuro & Rakic 1998a; Komuro & Rakic 1998b; Komuro et al. 2001). In line with this, when slices were stained at 1 DIV, the targeted cells resided mostly in the EGL and ML where tangential and radial migration occurs (fig 4B). To ensure that normal tissue organization is maintained in the *ex vivo* cultures, we performed immunostaining on 4 DIV slices *ex vivo* electroporated with GFP plasmid, using anti-Calbindin or anti-GFAP antibodies to detect Purkinje and glial cells, respectively. Anti-GFP antibodies were used to label electroporated cells and the general laminar architecture of the tissue was visualized using a nuclear stain (DAPI) (fig 4C). Calbindin staining revealed the characteristic morphology of Purkinje cells in the targeted area with large dendritic trees projecting into the ML after 4 DIV, representing ~P12 *in vivo* (fig 4C). At this time point, most GFP-positive CGNs were found in the IGL and ML and very few cells were present in the EGL (fig 4C-D). Notably, where the Purkinje cell layer *in vivo* consists of a strict layer of single cell bodies, in 4 DIV cultured slices the cell bodies were more dispersed. GFAP staining revealed that glial cells were present throughout the *ex vivo* cultured slices at 4 DIV (fig 4D). In the ML, staining was present as a meshwork of fibers extending perpendicular to the tissue surface, most likely representing Bergmann glial fibers. These fibers are used as a scaffold for CGN migration, and examples of GFP-positive CGNs aligned to GFAP-positive fibers were found (fig 4D). These results establish that CGNs can be specifically targeted with shRNA and their migration followed *in vitro* in a way that closely resembles the *in vivo* situation. Therefore, we next used this model to analyze the role of Neogenin and Dock7 in CGN migration.

### **Loss of Neogenin or Dock7 impairs *ex vivo* radial CGN migration**

To determine the effect of loss of Neogenin function on CGN migration, we induced Neogenin knockdown by electroporation using shRNA expressing plasmids in combination with GFP to visualize targeted cells in *ex vivo* slices. Because RGMA is present along Bergmann glia and in the IGL (fig 3B), we hypothesized that Neogenin receptor signaling takes place during radial migration. We therefore chose to analyze CGN migration at 4 DIV, when most but not all targeted cells have reached the IGL and ML in control slices (fig 4C-D). The number of GFP-positive cells in the EGL, PCL-ML (starting at the bottom of the Purkinje cell bodies and ending at the EGL) and IGL was determined in slices electroporated





with Neogenin targeting shRNA (shNeo) or scrambled control shRNA (shScr) (fig 4E). In slices electroporated with shScr, 17.4% (+/-2.0 SEM) of the targeted CGNs resided in the EGL, while 46.5% (+/- 2.5 SEM) were present in the ML and 36.1% (+/-3.1 SEM) in the IGL (fig 4F). Knockdown of Neogenin had no significant effect on the number of CGNs in the EGL (19.9% +/-1.2 SEM), but the distribution of cells in the ML and IGL was shifted. Significantly fewer cells were detected in the IGL (26.7% +/-2.0 SEM) and as a result an increased number of CGNs were found in the ML (53.4% +/-2.2 SEM) (fig 4F). Interestingly, Neogenin knockdown induced long leading processes in CGNs that projected far into the IGL while the cell body stalled in the ML (fig 4E). This suggests that migration rather than outgrowth was affected in these cells.

Next, we asked whether Dock7 is required for Neogenin signaling during CGN migration. We electroporated the EGL of P8 cerebella with shRNA targeting Dock7 (shDock7) or shScr and assessed the migration of GFP-positive CGNs at

**Figure 4. Targeted electroporation allows *ex vivo* analysis of cerebellar granule cell migration in organotypic slice culture and reveals reduced radial migration after knockdown of Neogenin or Dock7.**

**A.** Schematic of the experimental design. Mouse P9 cerebella were dissected and the EGL was injected with DNA solution (1). Tweezer electrodes were used to induce DNA uptake through electroporation (2). Coronal slices were cut and kept in culture for 4 days (3). **B.** GFP staining reveals that CGNs were correctly targeted. At 1 DIV, both tangentially (open arrow) and radially (closed arrow) migrating CGNs can be seen. Slices were stained using anti-Calbindin antibodies to visualize Purkinje cells and DAPI was used to visualize tissue morphology. **C-D.** Cerebellar morphology and structure of *ex vivo* electroporated slices is maintained at 4 DIV. Purkinje cells are visualized by anti-Calbindin (**C**) and Bergmann glia by anti-GFAP (**D**) immunostaining. The laminar structure of the cerebellum is intact as revealed by DAPI nuclear staining. Anti-GFP immunostaining reveals targeted CGNs, and arrow in **D** indicates an example of a radially migrating GFP-positive CGN aligned with a GFAP-positive fiber. **E.** P9 cerebella were *ex vivo* electroporated with GFP and shRNA coding plasmid targeting Neogenin (shNeo), Dock7 (shDock7) or non-targeting scrambled control (shScr). Slices were fixed at 4 DIV and GFP expression was visualized by immunostaining. Laminar structure as revealed by DAPI nuclear staining was used to determine CGN migration. Arrows indicate long leading processes in the IGL after Neogenin knockdown. **F-G.** The ratio of the number of cell bodies in the EGL, ML and IGL was quantified for shNeo and shDock7 and compared to shScr for each experiment. There are significantly fewer cell bodies in the IGL after Neogenin knockdown (**F**), while the number of cells in the EGL is unchanged. Knockdown of Dock7 has a similar effect (**G**). Graphs show average distribution of GFP-positive neurons in EGL, ML and IGL per picture per condition  $\pm$ SEM normalized to shScr-transfected cells per experiment, \* $p < 0.05$ , Two-way ANOVA with multiple comparisons. Scale bars are 50  $\mu$ m.

4 DIV. The distribution of control cells was similar to that in the previous set of experiments (fig 4 F), with 16.0% ( $\pm$ 1.8 SEM) of the CGNs in the EGL, 50.0% ( $\pm$  1.5 SEM) in the ML, and 34.0% in the IGL ( $\pm$  2.6 SEM) (fig 4G). Similar to knockdown of Neogenin, knockdown of Dock7 shifted the distribution of cells in the IGL. The number of CGNs in the IGL was significantly reduced to 25% ( $\pm$  2.8 SEM) while the distribution of cells in the EGL (18.6%  $\pm$ 2.3 SEM) and ML (56.2%  $\pm$ 2.1 SEM) was statistically unchanged (fig 4G).

The striking similarity between the CGN migration defects observed following Neogenin and Dock7 knockdown, indicates that Dock7 is a downstream mediator of Neogenin signaling during CGN migration.

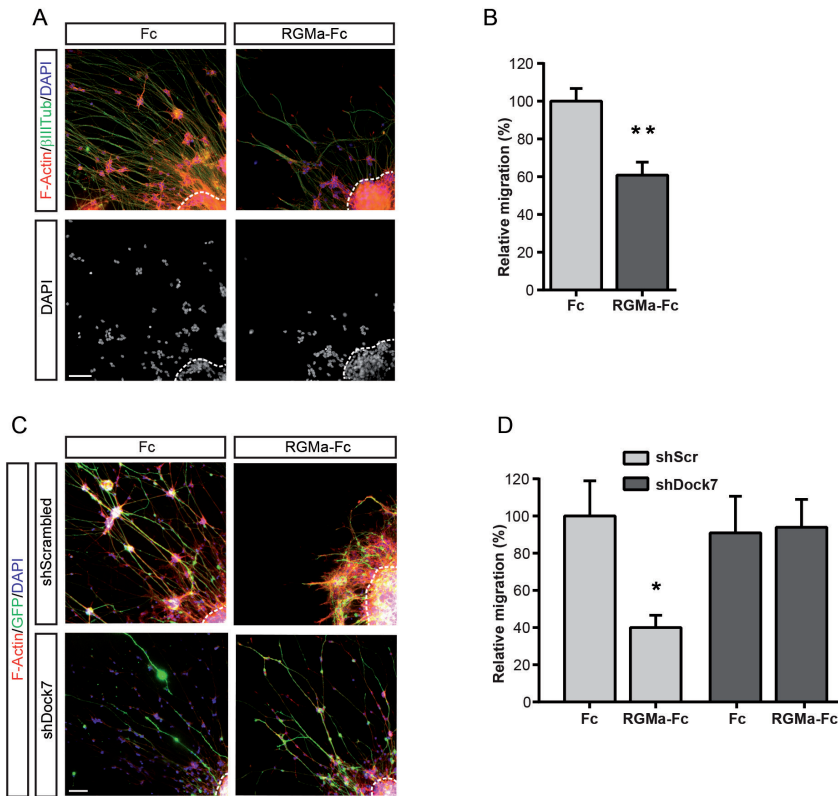


**Figure 5. Inhibition of CGN migration by RGMa is dependent on Dock7.**

**A.** The migration of EGL-derived CGNs is inhibited by RGMa. P8 EGL explants were cultured on RGMa-Fc- or Fc control protein-coated coverslips for 2 DIV. Neuronal outgrowth, visualized by  $\beta$ III tubulin and F-actin immunostaining (top), and cell body migration, visualized by DAPI nuclear staining (bottom), were strongly inhibited by RGMa-Fc, as compared to Fc control. Dashed lines in bottom right corners outline the explants. **B.** The average distance that the cell body traveled from the explant was measured and normalized to control (Fc) condition. The presence of RGMa-Fc significantly reduces the distance migrated. Graph shows average distance migrated per explant  $\pm$ SEM, \*\* $p=0.001$ , Student T-test. **C.** P8 cerebella were electroporated with shDock7 or shScr and GFP plasmid followed by dissection of the targeted EGL. Explants were cultured on RGMa-Fc- or control Fc-coated coverslips for 2 DIV, followed by immunostaining for GFP to visualize targeted cells, F-actin to visualize all cells and DAPI to visualize nuclei. Dashed lines in bottom right corners outline the explants. RGMa-Fc (right) inhibited outgrowth from EGL explants compared to Fc control (left) for GFP-positive shScr-transfected cells, but shDock7 transfection resulted in loss of migration inhibition. **D.** The average distance that GFP-positive cell bodies migrated from the EGL explant was measured and normalized to control condition (shScr on Fc control). A significant reduction of distance migrated was found in shScr cells, but this reduction was not seen in shDock7 cells. Graph shows average distance migrated per explant  $\pm$ SEM, \* $p=0.03$ , Student T-test. Scale bars are 50 $\mu$ m.

## **Knockdown of Dock7 results in loss of CGN sensitivity to RGMa *in vitro***

RGMa expression colocalizes with Bergmann glia (van den Heuvel et al. 2013) and is strongest in the ML (fig 3B). We therefore hypothesized that RGMa is involved in Neogenin signaling during radial CGN migration. To further investigate the role of RGMa in CGN migration, we designed an explant assay. First, we determined the sensitivity of explant-derived CGNs to RGMa by culturing P8 EGL explants on RGMa-Fc coated coverslips and analyzing the migration of CGNs from the explant at 2 DIV. As revealed by  $\beta$ III tubulin and F-actin staining, the outgrowth of CGNs cultured on RGMa-Fc was inhibited, as compared to Fc control (fig 5A). To quantify the effect of RGMa-Fc on migration, we measured the distance traveled from the explant for cell bodies using a DAPI nuclear stain (fig 5A-B). The presence of RGMa-Fc substrate strongly reduced CGN migration from the explant (fig 5B). As Neogenin is the only known receptor for RGMa (Rajagopalan et al., 2004), the observed inhibitory effect of RGMa on CGN outgrowth and migration confirmed that Neogenin signaling occurs in these cells. To explore the role of Dock7 in RGMa-induced Neogenin signaling, we used a modified version of the *ex vivo* electroporation assay. Instead of culturing organotypic slices after electroporation, the targeted EGL area was dissected and cultured on RGMa-Fc- or control Fc-coated coverslips.

At 2 DIV, explants were stained for GFP and F-actin and the migration of GFP-positive CGNs from the explant was measured (fig 5C). Control targeted CGNs cultured on RGMa-Fc-coated coverslips showed reduced migration (fig 5C-D) similar to untransfected CGNs (fig 5A-B). However, the migration of CGNs electroporated with shDock7 was not inhibited by the presence of RGMa, indicating that Dock7 is required for RGMa sensitivity. Together with our previous observations that Neogenin and Dock7 interact and that their expression patterns overlap in radially migrating CGNs, this suggests that Dock7 is a downstream mediator of Neogenin signaling. Moreover, we show for the first time that Neogenin and RGMa are involved in the migration of CGNs and that Neogenin expression by CGNs is an intrinsic requirement to sense extracellular RGMa. Loss of Neogenin in radially migrating CGNs leads to altered migration which is possibly caused by loss of sensitivity to RGMa.

## **Discussion**

Our data suggest that RGMa-induced Neogenin signaling is involved in the phase of radial CGN migration that occurs after CGNs have passed the border between the PCL and the IGL. After a short pause when the CGN cell body reaches the PCL, the leading process 'samples' the environment, in search for thus far

---

unidentified cues. The CGN then continues to migrate, its soma elongates and the leading process extends into the IGL (Komuro & Rakic 1998a). After Neogenin knockdown, the CGN cell body apparently fails to follow the extended leading process, resulting in long leading processes in the IGL with cell bodies stalling at the ML.

CGNs first encounter RGMA on Bergmann glia when their expression level of Neogenin is low. The expression of RGMA increases in the ML and after they have reached the PCL the CGNs detach from the glial fibers and continue to migrate radially into the IGL. At this switch from glia-guided migration to non-glial migration, Neogenin expression is upregulated, while RGMA is detected only at low levels in the IGL. It is therefore tempting to speculate that RGMA-induced repulsion drives the CGN cell body away from the Bergmann glia in the ML and into the IGL.

This hypothesis is in line with our intuitively paradoxical results that whereas knockdown of Neogenin or Dock7 in organotypic slice culture leads to reduced migration, it results in increased migration in explants exposed to RGMA. In the first experimental setup loss of Neogenin or Dock7 prevents the repulsion of CGN cell bodies from glial fibers in the ML. In the second experiment loss of sensitivity to RGMA prevents RGMA-induced inhibition of CGN migration.

Dock7 has been reported to have a large array of cell type-dependent functions and the mechanism involved in Neogenin signaling remains to be further elucidated. If Neogenin binding to Dock7 has a functional effect on Rac activation, this would be the first indication that Neogenin could affect both RhoA and Rac GTPases. However, it is also possible that Dock7 functions in Neogenin signaling independent from its role as a GEF. Dock7 is involved in directly antagonizing TACC3 and thereby modulates the tubulin cytoskeleton (Yang et al. 2012). The interaction of Dock7 with TACC3 may provide an indirect link between Neogenin and modulation of the microtubule cytoskeleton. Another recent study has shown a different role for Dock7 separate from its GEF function. In Chandelier cells, it was shown that Dock7 binds with tyrosine receptor ErbB4, thereby phosphorylating and activating it (Tai et al. 2014). Dock7 may have a similar direct effect on Neogenin or could serve to couple the signal transduction cascades of Neogenin to that of ErbB4.

To resolve the molecular mechanism(s) of Dock7 in Neogenin signaling, future experiments aimed at testing the involvement of different pathways downstream of that Dock7 are needed. For example, Dock7 truncation constructs containing a deletion of a specific functional domain could be introduced in combination with knockdown of endogenous Dock7 in ex vivo cerebellar electroporation. If the introduction of a truncation construct rescues the effect on CGN migration, it would reveal the redundancy of that domain in Neogenin signaling. If, however,

a truncation construct does not rescue, it is likely that the deleted domain is required for Neogenin signaling during CGN migration.

Interestingly, knockdown of Dock7 has been implicated in reduced migration of Schwann cells. In these cells, Dock7 GEF function is required for migration. Activation of Dock7 through binding of tyrosine receptor ErbB2 results in increased Rac1 activation and subsequently increased Schwann cell migration (Yamauchi et al. 2008). It is possible that Dock7 activation occurs downstream of Neogenin signaling, which would link Neogenin to Rac1 signaling in CGN migration. An alternate possibility is that Dock7 has a similar but independent effect on CGN migration and is involved in a signaling pathway separate from Neogenin. An experiment to explore this possibility would be to perform simultaneous knock down of Dock7 and Neogenin. No additive effect of double knockdown would be anticipated if the genes interact in the same pathway. However, if Dock7 functions independently of Neogenin, a cumulative loss of outgrowth inhibition or reduction of migration would be expected.

Our data provide some additional hints about the molecular pathway linked to Neogenin-Dock7 signaling. Migrating CGNs have relatively long leading processes, making it possible to separate effects on growth cone motility and neurite outgrowth from those on nuclear migration. Interestingly, in migrating neurons, Rac1/Cdc42 and RhoA are involved in the dynamics of different cellular compartments. Inhibition of Rac1/Cdc42 results in impaired neurite outgrowth, but does not affect nuclear migration. RhoA activation is required for cell body migration, but is dispensable for neurite outgrowth (Causeret et al. 2004). CGNs express only Rac family member Rac1 (and not Rac2 or Rac3) (Bolis et al. 2003). Dock7 selectively binds Rac1 (Watabe-Uchida et al. 2006). Moreover, Rac1<sup>-/-</sup> mice show less neuronal migration and outgrowth (Tahirovic et al. 2010). Dock7 acts as a Rac1/Cdc42 activator and knockdown of Dock7 would consequently be expected to affect neurite outgrowth but not cell body migration. However, our results show that knockdown of Dock7 affects CGN cell body migration. Since RGMA binding to Neogenin results in RhoA activation, knockdown of Neogenin would be expected to affect cell body migration which is in agreement with our results. Together, these results suggest that in radially migrating CGNs, the role of Dock7 is independent of its Rac GEF functionality.

Another unexplored possibility is that Dock7 might function as an upstream regulator rather than downstream signal transducing partner of Neogenin. For example, MyosinVI, a confirmed Dock7 binding partner, has been implicated in intracellular transport, secretion and endocytosis through its interaction with the actin cytoskeleton (Majewski et al. 2012; Buss et al. 2002). Myosin VI is a unique member of its protein family because it is the only known myosin motor protein to travel from the plus to the minus end of actin filaments. Dock7 could be involved



---

in MyosinVI-mediated transport of Neogenin from or to the growth cone. Loss of Dock7 would in this case lead to potential mislocalization of Neogenin.

Taken together, our results for the first time reveal a role for Neogenin in CGN migration, and implicate Dock7 as a novel effector in RGMa-mediated Neogenin signaling during neuronal migration.

## **Acknowledgements**

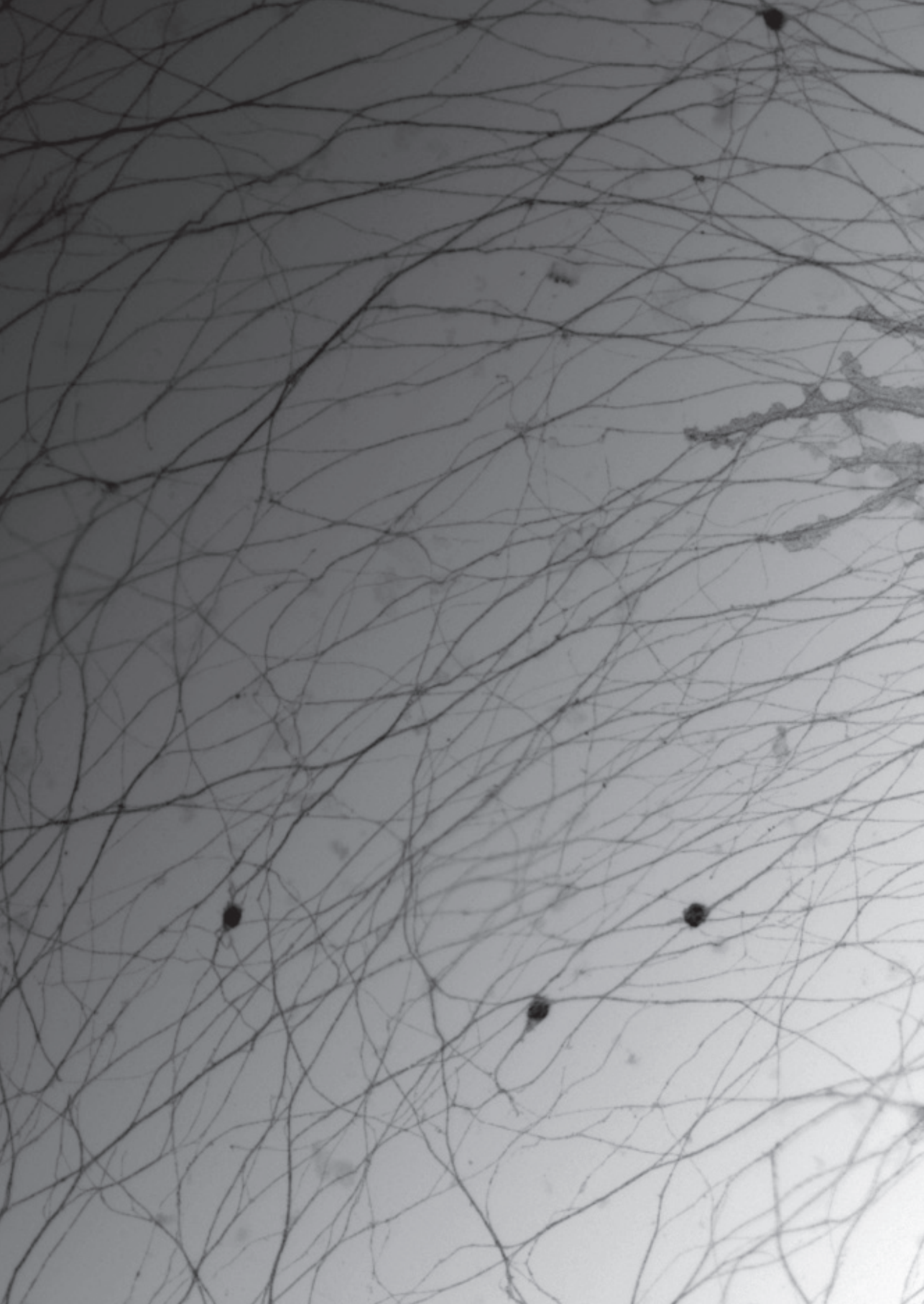
We are thankful to Toshihide Yamashita (Osaka University, Japan) for providing us with CHO and CHO-RGMa cell lines and to Linda van Aelst (CSHL, USA) for her gift of pcDNA3.1/CMV-Flag-Dock7 and pSuper-Dock7#1. We would like to thank Peter Carmeliet (KU Leuven, Belgium) for sharing his protocol for *ex vivo* cerebellar electroporation. This work was supported by HFSP (CDA) and NWO (VIDI) grants to R.J.P.

## References

- Bar-Sagi, D. & Hall, A., 2000. Ras and Rho GTPases: a family reunion. *Cell*, 103, pp.227–238.
- Bolis, A. et al., 2003. Differential distribution of Rac1 and Rac3 GTPases in the developing mouse brain: Implications for a role of Rac3 in Purkinje cell differentiation. *European Journal of Neuroscience*, 18, pp.2417–2424.
- Brummelkamp, T.R., Bernards, R. & Agami, R., 2002. A system for stable expression of short interfering RNAs in mammalian cells. *Science*, 296, pp.550–553.
- Buss, F., Luzio, J.P. & Kendrick-Jones, J., 2002. Myosin VI, an actin motor for membrane traffic and cell migration. *Traffic (Copenhagen, Denmark)*, 3, pp.851–858.
- Camoletto, P. et al., 1997. The cytosolic phosphoprotein stathmin is expressed in the olfactory system of the adult rat. *Neuroreport*, 8, pp.2825–2829.
- Causeret, F. et al., 2004. Distinct roles of Rac1/Cdc42 and Rho/Rock for axon outgrowth and nucleokinesis of precerebellar neurons toward netrin 1. *Development (Cambridge, England)*, 131, pp.2841–2852.
- Conrad, S. et al., 2007. Neogenin-RGMA signaling at the growth cone is bone morphogenetic protein-independent and involves RhoA, ROCK, and PKC. *The Journal of biological chemistry*, 282, pp.16423–16433.
- Conrad, S. et al., 2010. RGMB controls aggregation and migration of Neogenin-positive cells in vitro and in vivo. *Molecular And Cellular Neurosciences*, 43(2), pp.222–231.
- Giampietro, C. et al., 2005. Stathmin expression modulates migratory properties of GN-11 neurons in vitro. *Endocrinology*, 146, pp.1825–1834.
- Hata, K. et al., 2006. RGMA inhibition promotes axonal growth and recovery after spinal cord injury. *The Journal of cell biology*, 173, pp.47–58.
- Van den Heuvel, D.M.A., Hellemons, A.J.C.G.M. & Pasterkamp, R.J., 2013. Spatiotemporal Expression of Repulsive Guidance Molecules (RGMs) and Their Receptor Neogenin in the Mouse Brain. *PLoS ONE*, 8.
- Komuro, H. & Rakic, P., 1998. Distinct modes of neuronal migration in different domains of developing cerebellar cortex. *The Journal of neuroscience: the official journal of the Society for Neuroscience*, 18, pp.1478–1490.
- Komuro, H. & Rakic, P., 1995. Dynamics of granule cell migration: a confocal microscopic study in acute cerebellar slice preparations. *The Journal of neuroscience: the official journal of the Society for Neuroscience*, 15, pp.1110–1120.
- Komuro, H. & Rakic, P., 1998. Orchestration of neuronal migration by activity of ion channels, neurotransmitter receptors, and intracellular Ca<sup>2+</sup> fluctuations. *Journal of Neurobiology*, 37, pp.110–130.
- Komuro, H., Yacubova, E. & Rakic, P., 2001. Mode and tempo of tangential cell migration in the cerebellar external granular layer. *The Journal of neuroscience: the official journal of the Society for Neuroscience*, 21, pp.527–540.
- Kubo, T. et al., 2008. Myosin IIA is required for neurite outgrowth inhibition produced by repulsive guidance molecule. *Journal of Neurochemistry*, 105, pp.113–126.
- Lah, G.J. & Key, B., 2012. Novel roles of the chemorepellent axon guidance molecule RGMA in cell migration and adhesion. *Molecular and Cellular Biology*, 32(5), pp.968–80.

- 
- MacHold, R. & Fishell, G., 2005. Math1 is expressed in temporally discrete pools of cerebellar rhombic-lip neural progenitors. *Neuron*, 48, pp.17–24.
  - Majewski, Ł. et al., 2012. Dock7: A GEF for Rho-family GTPases and a novel myosin VI-binding partner in neuronal PC12 cells. *Biochemistry and Cell Biology*, 90, pp.565–574.
  - Mirakaj, V. et al., 2012. The guidance receptor neogenin promotes pulmonary inflammation during lung injury. *The FASEB Journal*, 26, pp.1549–1558.
  - Pasterkamp, R.J. et al., 1998. Evidence for a role of the chemorepellent semaphorin III and its receptor neuropilin-1 in the regeneration of primary olfactory axons. *The Journal of neuroscience: the official journal of the Society for Neuroscience*, 18, pp.9962–9976.
  - Rajagopalan, S. et al., 2004. Neogenin mediates the action of repulsive guidance molecule. *Nature cell biology*, 6, pp.756–762.
  - Reed, S.E. et al., 2006. Transfection of mammalian cells using linear polyethylenimine is a simple and effective means of producing recombinant adeno-associated virus vectors. *Journal of Virological Methods*, 138, pp.85–98.
  - Ruiz de Almodovar, C. et al., 2011. VEGF Mediates Commissural Axon Chemoattraction through Its Receptor Flk1. *Neuron*, 70, pp. 966–978.
  - Schmidt, A. & Hall, A., 2002. Guanine nucleotide exchange factors for Rho GTPases: turning on the switch. *Genes & development*, 16, pp.1587–1609.
  - Tahirovic, S. et al., 2010. Rac1 regulates neuronal polarization through the WAVE complex. *The Journal of neuroscience: the official journal of the Society for Neuroscience*, 30, pp.6930–6943.
  - Tai, Y. et al., 2014. Regulation of chandelier cell cartridge and bouton development via DOCK7-mediated ErbB4 activation. *Cell Reports*, 6, pp.254–263.
  - Tassew, N.G. et al., 2012. SKI-1 and Furin Generate Multiple RGMA Fragments that Regulate Axonal Growth. *Developmental Cell*, 22, pp.391–402.
  - Watabe-Uchida, M. et al., 2006. The Rac Activator DOCK7 Regulates Neuronal Polarity through Local Phosphorylation of Stathmin/Op18. *Neuron*, 51, pp.727–739.
  - Wilson, N.H. & Key, B., 2006. Neogenin interacts with RGMA and netrin-1 to guide axons within the embryonic vertebrate forebrain. *Developmental Biology*, 296(2), pp.485–498.
  - Yamamoto, M., Hassinger, L. & Crandall, J.E., 1990. Ultrastructural localization of stage-specific neurite-associated proteins in the developing rat cerebral and cerebellar cortices. *Journal of neurocytology*, 19, pp.619–627.
  - Yamauchi, J. et al., 2008. ErbB2 directly activates the exchange factor Dock7 to promote Schwann cell migration. *The Journal of cell biology*, 181, pp.351–365.
  - Yamauchi, J. et al., 2011. The atypical Guanine-nucleotide exchange factor, dock7, negatively regulates schwann cell differentiation and myelination. *The Journal of neuroscience: the official journal of the Society for Neuroscience*, 31, pp.12579–12592.
  - Yang, Y.-T., Wang, C.-L. & Van Aelst, L., 2012. DOCK7 interacts with TACC3 to regulate interkinetic nuclear migration and cortical neurogenesis. *Nature Neuroscience*, 15, pp.1201–1210.
  - Zhao, Y. et al., 2011. Automation of large scale transient protein expression in mammalian cells. *Journal of Structural Biology*, 175, pp.209–215.







---

# Chapter 6

## A Role for Bicaudal-D2 in Radial Cerebellar Granule Cell Migration

---

Dick Jaarsma<sup>1,\*</sup>, Robert van den Berg<sup>1,2,\*</sup>, Phebe S. Wulf<sup>1,2,\*</sup>, Susan van Erp<sup>4</sup>, Nanda Keijzer<sup>1</sup>, Max A. Schlager<sup>1</sup>, Esther de Graaff<sup>1,2</sup>, Chris I. De Zeeuw<sup>1,3</sup>, R. Jeroen Pasterkamp<sup>4</sup>, Anna Akhmanova<sup>2,5</sup>, Casper C. Hoogenraad<sup>1,2</sup>

1 Erasmus Medical Center, Department of Neuroscience, 3015 GE Rotterdam, The Netherlands.

2 Cell Biology, Faculty of Science, Utrecht University, 3584 CH Utrecht, The Netherlands.

3 Netherlands Institute for Neuroscience, Royal Dutch Academy of Arts & Sciences, 1105 BA Amsterdam, The Netherlands.

4 Department of Translational Neuroscience, Brain Center Rudolf Magnus, University Medical Center Utrecht, 3584 CG Utrecht, The Netherlands.

5 Department of Cell Biology, Erasmus Medical Center, 3015 GE Rotterdam, The Netherlands.

\* These authors contributed equally

*Nature Communications*, 2014; 5:3411



ARTICLE

Received 1 Dec 2013 | Accepted 7 Feb 2014 | Published 11 Mar 2014

DOI: 10.1038/ncomms4411

# A role for Bicaudal-D2 in radial cerebellar granule cell migration

Dick Jaarsma<sup>1,\*</sup>, Robert van den Berg<sup>1,2,\*</sup>, Phebe S. Wulf<sup>1,2,\*</sup>, Susan van Erp<sup>3</sup>, Nanda Keijzer<sup>1</sup>, Max A. Schlager<sup>1</sup>, Esther de Graaff<sup>1,2</sup>, Chris I. De Zeeuw<sup>1,3</sup>, R. Jeroen Pasterkamp<sup>4</sup>, Anna Akhmanova<sup>2,5</sup> & Casper C. Hoogenraad<sup>1,2</sup>

Bicaudal-D (BICD) belongs to an evolutionary conserved family of dynein adaptor proteins. It was first described in *Drosophila* as an essential factor in fly oogenesis and embryogenesis. Missense mutations in a human BICD homologue, BICD2, have been linked to a dominant mild early onset form of spinal muscular atrophy. Here we further examine the *in vivo* function of BICD2 in *Bicd2* knockout mice. BICD2-deficient mice develop disrupted laminar organization of cerebral cortex and the cerebellum, pointing to impaired radial neuronal migration. Using astrocyte and granule cell specific inactivation of BICD2, we show that the cerebellar migration defect is entirely dependent upon BICD2 expression in Bergmann glia cells. Proteomics analysis reveals that *Bicd2* mutant mice have an altered composition of extracellular matrix proteins produced by glia cells. These findings demonstrate an essential non-cell-autonomous role of BICD2 in neuronal cell migration, which might be connected to cargo trafficking pathways in glia cells.

<sup>1</sup>Erasmus Medical Center, Department of Neuroscience, 3015 GE Rotterdam, The Netherlands. <sup>2</sup>Cell Biology, Faculty of Science, Utrecht University, 3584 CH Utrecht, The Netherlands. <sup>3</sup>Netherlands Institute for Neuroscience, Royal Dutch Academy of Arts & Sciences, 1105 BA Amsterdam, The Netherlands. <sup>4</sup>Department of Translational Neuroscience, Brain Center Rudolf Magnus, University Medical Center Utrecht, 3584 CG Utrecht, The Netherlands. <sup>5</sup>Department of Cell Biology, Erasmus Medical Center, 3015 GE Rotterdam, The Netherlands. \*These authors contributed equally to this work. Correspondence and requests for materials should be addressed to C.C.H. (email: c.hoogenraad@uu.nl).

The Bicaudal-D (*BicD*) gene was initially identified in *Drosophila* based on dominant mutations that induce mirror-image pattern duplications along the antero-posterior axis, thereby giving rise to bicaudal embryos<sup>1</sup>. It was later established that the BICD protein facilitates dynein-mediated transport and is involved in the proper localization of posterior mRNA in *Drosophila* embryos<sup>2,3</sup>. In mammals two homologues of Bicaudal-D are present, named BICD1 and BICD2, which associate with microtubule minus-end-directed motor dynein<sup>4,5</sup> and various cargos, such as the nuclear envelope<sup>6</sup> and Rab6 secretory vesicles<sup>7</sup>. One currently favoured hypothesis is that BICD family members are adaptor proteins involved in microtubule-based transport by docking the dynein motor proteins to appropriate cargos<sup>8–10</sup>. Recently, mutations in BICD2 have been linked to a spectrum of motor neuron disorders, in particular, a dominant mild early onset form of SMA<sup>11–13</sup>, suggesting that BICD2 plays an important role in the nervous system.

To further examine the *in vivo* function of BICD2, we generated *Bicd2* knockout (KO) mice. Here we report that these mice develop defects in laminar organization of the cerebral cortex, hippocampus and cerebellar cortex, indicative of radial neuronal migration defects. Cell-specific inactivation of BICD2 in astrocytes and neuronal precursors revealed that radial cerebellar granule cell migration is non-cell-autonomous and intrinsic to cerebellar Bergmann glia cells. Mass spectrometry analysis revealed that *Bicd2* mutant mice have strongly reduced levels of the extracellular matrix protein Tenascin C. Our data demonstrate that Bergmann glia cells provide critical cues for granule neuron polarization and migration, and that BICD2 is a critical part of the Bergmann glia signalling mechanism responsible for granule cell migration. This study reveals an unexpected action of BICD2 in glia cell-guided granule cell migration that is of key importance for cerebellar development and function.

## Results

**BICD2 is required for cerebral cortex development.** To generate an inducible *Bicd2* KO allele, we introduced two resistance markers by sequential rounds of homologous recombination. In the first round, a neomycin cassette surrounded by loxP sequences was inserted into intron 1. In the second round, a puromycin selection marker, surrounded by loxP sequences and followed by a  $\beta$ -galactosidase (*lacZ*) reporter gene fused to a nuclear localization signal, was inserted downstream of the mouse *Bicd2* gene (Supplementary Fig. 1). Embryonic stem (ES) cells with this floxed *Bicd2* allele (termed *Bicd2<sup>f</sup>*), were transfected with a plasmid expressing Cre recombinase yielding a KO *Bicd2* (*Bicd2<sup>-/-</sup>*) allele, that generates a transcript consisting of exon 1 of *Bicd2* and the *lacZ* reporter gene (Supplementary Fig. 1). *Bicd2<sup>f</sup>* ES cell clones were used to generate mice carrying the inducible and KO *Bicd2* alleles (Supplementary Fig. 1A).

Matings between heterozygous *Bicd2<sup>+/-</sup>* mice yielded *Bicd2<sup>-/-</sup>* mice at near-Mendelian frequencies, but *Bicd2<sup>-/-</sup>* mice displayed increased mortality during early post-natal life resulting in a sub-Mendelian frequency of *Bicd2<sup>-/-</sup>* mice (13% of 208 mice) at P10. Late embryonic and newborn *Bicd2<sup>-/-</sup>* mice were indistinguishable in gross appearance and weight from heterozygous and wild-type littermates (Fig. 1a), but after birth the *Bicd2<sup>-/-</sup>* mice developed an enlarged dome-shaped skull, indicative of hydrocephalus (Fig. 1b). By P14 *Bicd2<sup>-/-</sup>* mice started to show reduced weight compared with their littermates (Fig. 1c), and by P30 all *Bicd2<sup>-/-</sup>* mice died. Behaviourally, *Bicd2<sup>-/-</sup>* mice at P20 displayed motor abnormalities: the mice walked with an abnormal wide-based gait of both fore- and hindpaws, and frequently made missteps when placed on a grid

(Supplementary Movie 1). Furthermore, at 3 weeks of age, the mice were unable to walk on a balance beam and showed clasping rather than extension of the hindlimbs when lifted by their tail.

Examination of *Bicd2<sup>-/-</sup>* mice at P15–P25 revealed no gross alterations in internal organs, except for a smaller size, and confirmed that *Bicd2<sup>-/-</sup>* mice developed severe hydrocephalus, which was characterized by progressive expansion of lateral ventricles (ventriculomegaly), loss of white matter and ependymal cells surrounding the ventricles, severe thinning of the cortex and atrophy of other telencephalic areas, including striatum, hippocampus and septum (Fig. 1d; Supplementary Fig. 2A–D). Apart from cerebellar cortex (see below), other brain regions and spinal cord appeared normal (Supplementary Fig. 2F). Analysis of the aqueduct at P5 suggested a smaller diameter indicative of aqueductal stenosis (Supplementary Fig. 2E).

In addition to the *Bicd2<sup>-/-</sup>* mice which completely lack the gene in all tissues, we generated mice that were deficient in BICD2 in the entire nervous system but showed normal BICD2 expression in most internal organs by crossing floxed *Bicd2<sup>f</sup>* mice with Nestin-Cre mice<sup>14</sup>. Nestin-Cre *Bicd2<sup>f</sup>* mice reproduced the severe progressive hydrocephalus, neurological features and short lifespan of *Bicd2<sup>-/-</sup>* mice (Table 1). Crossing of *Bicd2<sup>f</sup>* mice with GFAP-Cre mice, which exhibit sustained Cre-recombinase expression in astrocytes and transient Cre activity in some neuronal precursor cells<sup>15</sup>, resulted in less severe or no hydrocephalus (Table 1). GFAP-Cre *Bicd2<sup>f</sup>* mice without hydrocephalus revealed a second major nervous system abnormality of BICD2-deficient mice, that is, a disordered laminar organization of the cerebral cortex (Fig. 1e) and hippocampus (Supplementary Fig. 3). Consistent with impaired radial migration, Foxp2, a marker predominantly found in deep corticofugal layer V and VI neurons, was present in superficial layers in GFAP-Cre *Bicd2<sup>f</sup>* mice (Fig. 1f). Corticofugal axonal trajectories (labelled with anti-neurofilament M antibody) arose in superficial instead of deep cortical layers. Importantly the same cortical and hippocampal phenotype was also observed in EMX1-Cre *Bicd2<sup>f</sup>* mice that are selectively deficient for BICD2 in radial glia, glutamatergic neurons and astrocytes in the cortex and hippocampus<sup>16</sup> (Table 1; Fig. 1g). Together, the data from GFAP-Cre and EMX1-Cre *Bicd2<sup>f</sup>* mice indicate that BICD2 is essential for the proper development of the cerebral cortex, and suggest that BICD2 plays a role in radial migration of excitatory neurons. These data are consistent with the neurogenesis and early neuronal migration defects observed after BICD2 knockdown in cortical brain slices by *in utero* electroporation<sup>17</sup>.

**BICD2 is required for cerebellar granule cell migration.** In the cerebral cortex, radial glia progenitor cells give rise to neurons and glia cells and act as a scaffold for radial migration, making it difficult to differentiate between potential glia- and neuron-specific defects and to decipher to which extent disorganized laminar organization follows from neurogenesis abnormalities or impaired migration<sup>18</sup>. In the cerebellar cortex, however, granule cells originate in the external granule cell layer (EGL) and migrate inward to the internal granule cell layer (IGL) along radial processes of Bergmann glia. Granule and glial cells originate from different precursors<sup>19,20</sup>, which makes it easier to establish the origin of migration deficits. *Bicd2<sup>-/-</sup>* mice showed a disproportionately small cerebellum with grossly intact subdivision in vermis and hemispheres and foliation (Fig. 2a; Supplementary Fig. 2), but an altered laminar organization, indicative of the absence of radial granule cell migration. Instead of laminar subdivision into molecular, Purkinje cell and granular layer, in *Bicd2<sup>-/-</sup>* cerebellar cortex the cell bodies of Purkinje cells

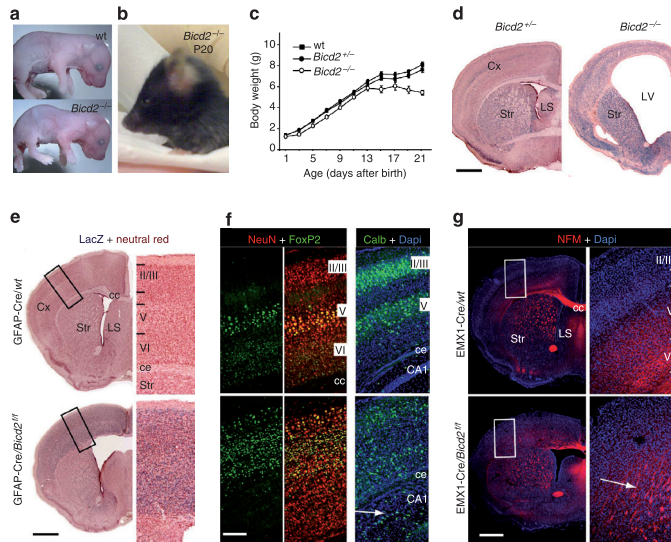


**Figure 1 | Hydrocephalus and disrupted laminar organization of the cortex in BICD2-deficient mice.** (a,b) Photographs of BICD2 KO (*Bicd2*<sup>-/-</sup>) mice showing a normal gross appearance at embryonic day 19 (a), and a dome-shaped head indicative of hydrocephalus at post-natal day 20 (b). (c) X-Y plot of body weight (mean ± s.e., n > 4 per group) showing near-normal weight of *Bicd2*<sup>-/-</sup> mice up to post-natal day 13, and weight loss during subsequent days. (d) Coronal brain sections of P20 mice stained for LacZ and neutral red reveal enlarged lateral ventricles (LV), thinning of the cortex (Cx) and atrophy of several telencephalic areas including striatum (Str) and lateral septum (LS) in homozygote *Bicd2*<sup>-/-</sup> and no change in heterozygote *Bicd2*<sup>+/-</sup> mice. Note the moderate and high level of LacZ staining throughout the forebrain of *Bicd2*<sup>+/-</sup> and *Bicd2*<sup>-/-</sup> mice, respectively, indicative of widespread BICD2 expression. (e) Coronal LacZ/neutral red-stained sections of the cortex of floxed *Bicd2*<sup>fl/fl</sup> crossed with a *GFAP-Cre* line; the high magnification of the primary somatosensory cortex illustrates disrupted cortical laminar organization. Also note the thin corpus callosum (cc) and capsula externa (ce) in *GFAP-Cre/Bicd2*<sup>fl/fl</sup> mice. (f) Immunofluorescence of NeuN and FoxP2 or Calbindin showing altered laminar distribution of FoxP2 and calbindin in *GFAP-Cre/Bicd2*<sup>fl/fl</sup> cortex. FoxP2 that in control mice is present in lamina V and VI pyramidal neurons, in *GFAP-Cre/Bicd2*<sup>fl/fl</sup> cortex is distributed in superficial lamina. Note the absence of a laminar organization of NeuN+ cells *GFAP-Cre/Bicd2*<sup>fl/fl</sup> cortex. Also note disorganized pyramidal cell layer in the CA1 of *GFAP-Cre/Bicd2*<sup>fl/fl</sup> hippocampus (arrow). (g) Immunofluorescence of neurofilament-M (NFM) showing abnormally oriented axonal bundles coursing from the superficial lamina towards the capsula interna in neocortex of *EMX1-Cre/Bicd2*<sup>fl/fl</sup> mice (arrow). Scale bars: 5 mm (a,b), 1 mm (d,e,g), 200 μm (e,f,g).

**Table 1 | Principal features of ubiquitous and region-specific BICD2-deficient mice used in this study.**

Mutant mouse	BICD2-deficiency	Lifespan (weeks)	Hydrocephalus	Disrupted laminar organization		
				Cortex	Hippocampus	Cerebellar cortex
<i>Bicd2</i> <sup>+/-</sup>	Whole body	> 52	-	-	-	-
<i>Bicd2</i> <sup>-/-</sup>	Whole body	3-4	+	+	+	+
<i>Bicd2</i> <sup>fl/fl</sup>						
<i>Nestin-Cre</i>	Entire nervous system	3-4	+	+	+	+
<i>GFAP-Cre</i>	Astrocytes, some populations of neuron	3-4 to >8*	+ or -	+	+	+
<i>EMX1-Cre</i>	Excitatory neurons in cortex, hippocampus	> 8†	-	+	+	-
<i>Math1-Cre</i>	Premigratory granule cells	> 8†	-	-	-	-

\*Death at 3-4 weeks in case of hydrocephalus.  
†Animals were killed at 8 weeks.

(Calbindin +, NeuN -) were positioned near the white matter, while other neurons (NeuN +) were spread over a single superficial layer (Fig. 2b,c). This layer contained both molecular layer interneurons (NeuN +, Parvalbumin +, Calbindin -), as well as a high density of granule cells, identified by immunostaining for the α6 GABA<sub>A</sub> receptor subunit that is

only expressed by adult, post-migratory granule cells (Fig. 2d-g). Cerebellar Golgi cells (mGluR2 +), which are localized in the granule cell layer of wild-type mouse cerebellar cortex, were concentrated between the white matter and the Purkinje cell layer, and did not occur in *Bicd2*<sup>-/-</sup> molecular/granule cell layer (Supplementary Fig. 4). Staining for the glutamate synaptic

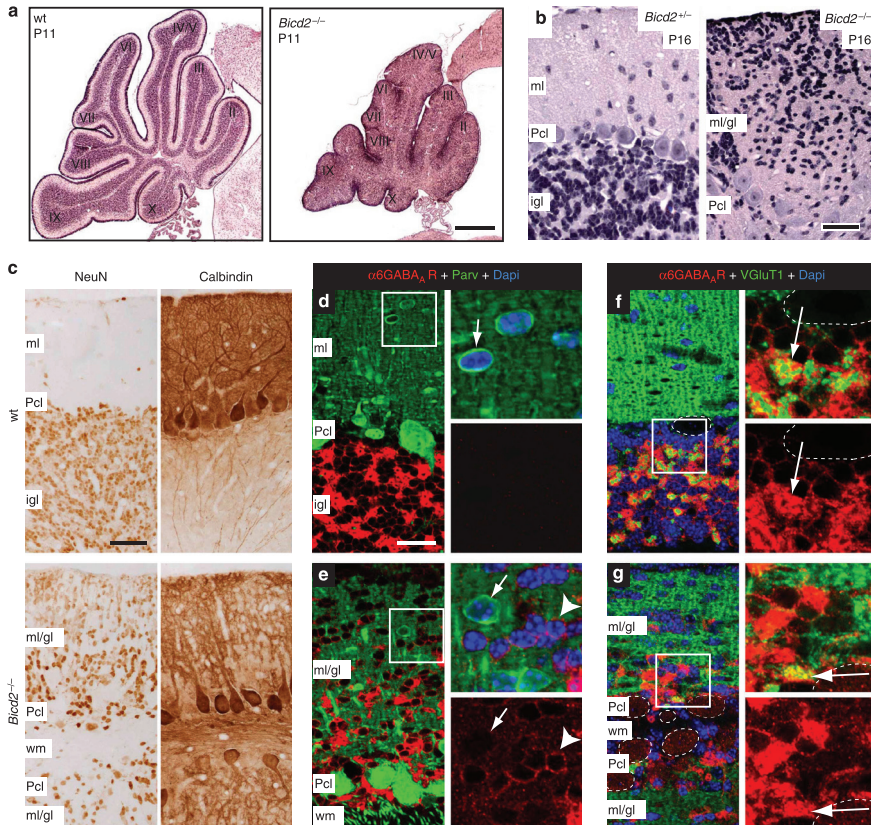


**Figure 2 | Granule cells populate the molecular layer in *Bicd2*<sup>-/-</sup> cerebellar cortex.** (a,b) Sagittal sections of P11 and P16 cerebellum stained with H&E. The low magnification in **a** illustrates the intact folial organization of the vermis of *Bicd2*<sup>-/-</sup> cerebellar cortex. The high magnification in **b** shows the absence of the internal granule cell layer (igl) and a high density of cells in the molecular layer (ml) in *Bicd2*<sup>-/-</sup> cerebellum. (c) Sagittal sections of P16 cerebellum immunostained with anti-NeuN and anti-calbindin. Note that in *Bicd2*<sup>-/-</sup> cerebellar cortex the Purkinje cell layer (Pcl, calbindin<sup>+</sup> cells) is localized adjacent to the white matter (wm), and that Purkinje cell dendritic arbors extend up to the pial surface. (d-g) Double-labelling confocal immunofluorescence of  $\alpha 6$  GABA<sub>A</sub> receptor subunit ( $\alpha 6$ GABA<sub>A</sub>R) with parvalbumine (Parv) and VGLUT1, respectively, in transverse sections of P20 cerebellum. Note the presence of many  $\alpha 6$ GABA<sub>A</sub>R<sup>+</sup> cells (arrow head in **e**), a moderate amount of Parv<sup>+</sup> cells (arrow in **e**), and abundant VGLUT1 labelling (**g**) in the ml/gl layer of *Bicd2*<sup>-/-</sup> cerebellar cortex. The arrow in **f** points to a glomerulus containing both  $\alpha 6$ GABA<sub>A</sub>R<sup>+</sup> granule cell dendritic processes and a VGLUT1<sup>+</sup> mossy fibre ending. Occasionally, double-labelled glomeruli-like structures occur near the Pcl of *Bicd2*<sup>-/-</sup> cerebellar cortex (arrow in **g**). Optical sections in **d-g**, 1  $\mu$ m. Scale bars: 200  $\mu$ m (**a**), 25  $\mu$ m (**b,d**), 50  $\mu$ m (**c**).

vesicle transporter VGLUT1, which is present in parallel fibre and mossy fibre endings in the cerebellar molecular and granular layers, respectively, revealed prominent punctate staining in the *Bicd2*<sup>-/-</sup> molecular/granular layer, indicative of the presence of parallel fibre endings (Fig. 2f,g). VGLUT1-immunostaining near the Purkinje cell layer also revealed sporadic larger irregular structures resembling mossy fibre endings, which accordingly co-distributed with  $\alpha 6$  GABA<sub>A</sub> receptor immunoreactivity, indicative of granule cell dendritic processes in the glomeruli (Fig. 2g). Immunostaining for VGLUT2, which is present in an additional and partially overlapping population of mossy fibre

endings as well as in climbing fibre endings, confirmed the presence of a low number of mossy fibre endings and indicated impaired climbing fibre innervation of Purkinje cells in *Bicd2*<sup>-/-</sup> cerebellar cortex (Supplementary Fig. 4C,D). Immunostaining for zebrin II suggests preserved parasagittal compartmentalization of Purkinje cells (Supplementary Fig. 4E,F).

Analysis of early post-natal brain indicated that *Bicd2*<sup>-/-</sup> cerebellar cortex appeared normal at post-natal day 2, before the onset of radial migration. As in control, the subsequent days was characterized by proliferation of granule cells and the gradual expansion of the area between the Purkinje cell layer and the pial



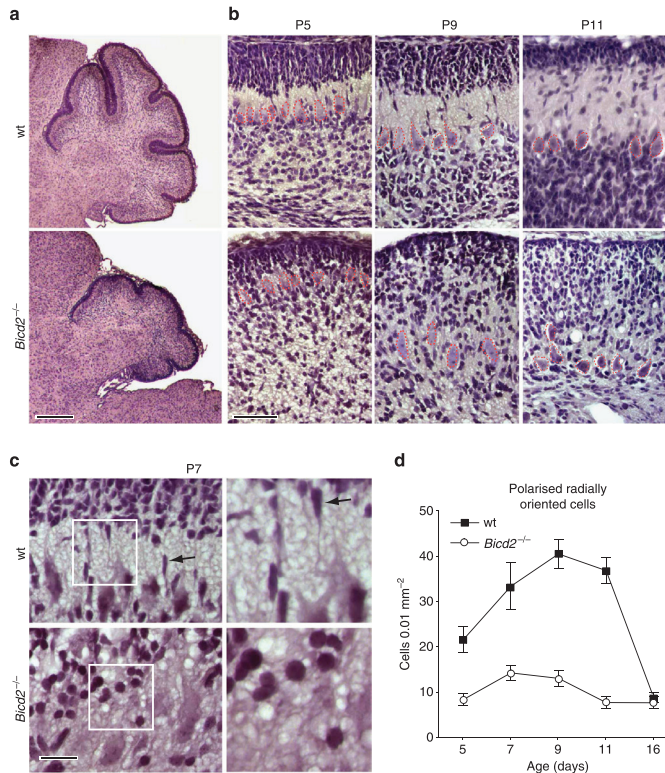


**Figure 3 | No radial granule cell migration in *Bicd2*<sup>-/-</sup> cerebellar cortex.** (a–c) Sagittal paraffin sections of P5 (a,b), P7 (c), P9 and P11 section stained with H&E showing development of *Bicd2*<sup>-/-</sup> cerebellar cortex during the period of radial granule cell migration. Note the multiple flattened radially oriented cells in the nascent molecular layer of wild-type (arrows in b and c) but not in *Bicd2*<sup>-/-</sup> cerebellar cortex. (d) Plot of density of flattened radially oriented cells (mean  $\pm$  s.e.,  $N=10$ ) in the molecular layer (wt mice) or the mixed molecular/granular layer (*Bicd2*<sup>-/-</sup>) extending from the Purkinje cell layer up to 20  $\mu$ m below the pial surface. Scale Bars: 200  $\mu$ m (a), 50  $\mu$ m (b), 20  $\mu$ m (c).

surface. However, instead of migrating and forming the interior granule cell layer, granule cells accumulated throughout the molecular layer (Fig. 3a,b). Consistent with impaired inward radial migration, no granule cells with a polarized radially oriented elongated shape characteristic for migration<sup>21</sup> were present in the molecular layer of *Bicd2*<sup>-/-</sup> P5–P15 cerebellar cortex (Fig. 3c,d). Thus, the absence of profiles of radially migrating cells, the accumulation of granule cells in the molecular layer and the absence of an IGL show that inward radial granule cell migration is severely disrupted in *Bicd2*<sup>-/-</sup> mice (Supplementary Movie 2).

**BICD2 is expressed in Bergman glia but not in granule cells.** Analysis of BICD2 expression by western blotting showed the presence of BICD2 protein in multiple tissues including the brain. It also confirmed the absence of BICD2 in tissue homogenates from *Bicd2*<sup>-/-</sup> mice and reduced expression in heterozygous *Bicd2*<sup>+/-</sup> mice (Fig. 4a, Supplementary Fig. 5). BICD2 is

expressed at relatively high levels in embryonic and early post-natal brain, while its expression decreases after P10, resulting in relatively low levels in adulthood (Fig. 4b, Supplementary Fig. 5). The absence of BICD2 in the KO mice did not lead to a significant change in the expression level of its close homologue BICD1 (Fig. 4c), indicating that there is no up- or downregulation of BICD1 in the absence of BICD2. Moreover, absence of BICD2 in the cerebellum and cortex did not change the expression levels of BICD2 binding partners, such as Rab6 and cytoplasmic dynein (DIC74) and its regulatory proteins dyactin (p150Glued) and Lis1 (Fig. 4c, Supplementary Fig. 5).

Immunohistology shows that BICD2 is diffusely distributed throughout the nervous system. Relatively high staining intensities occurred in non-neuronal cells (NeuN<sup>-</sup>) and some populations of neurons (NeuN<sup>+</sup>), including motor neurons in cranial nerve motor nuclei and large neurons throughout the reticular formation (Supplementary Fig. 6A–E). The specificity of the staining for BICD2 was confirmed by the absence of staining in sections from *Bicd2*<sup>-/-</sup> mice. In post-natal and adult

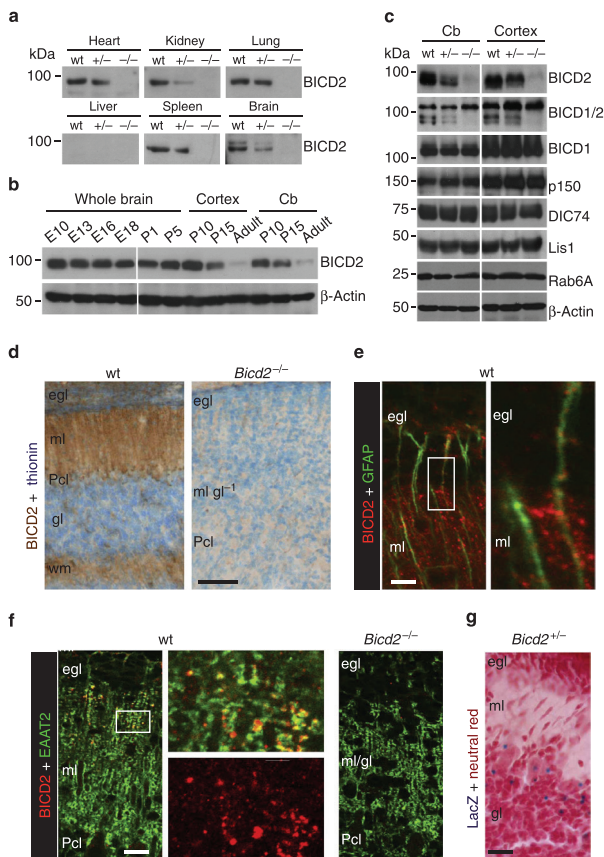


**Figure 4 | Preferential BICD2 expression in Bergman glia in cerebellar cortex.** (a) Western blot with BICD2 antibody (#2294) showing reduced and no expression of BICD2 in tissue homogenates of P20 heterozygote *Bicd2*<sup>+/-</sup> (+/-) and homozygote *Bicd2*<sup>-/-</sup> (-/-) mice, respectively. (b) Western blot showing relatively high BICD2 expression in developing nervous system. (c) Comparative western blot analysis showing unaltered BICD1 (antibody #2295 for BICD1, and upper band in strip stained with antibody #2293 for BICD1/2), dynein components and interacting proteins (dynein p150, dynein intermediate chain 74, Lis1) and Rab6 expression in *Bicd2*<sup>-/-</sup> cortex and cerebellum. Full-size western blots can be found in Supplementary Fig. 5. (d) Immunohistochemistry with anti-BICD2 antibody showing the absence of staining in P10 *Bicd2*<sup>-/-</sup> cerebellar cortex and prominent staining in the molecular layer (ml) and the white matter (wm) of wild-type cerebellar cortex. (e,f) Double-labelling confocal immunofluorescence (optical sections 1 μm) showing co-distribution of BICD2 with GFAP and the excitatory amino-acid transporter EAAT2 in the ml and the egl. Note in right panel in (f) that EAAT2 labelling appears the same as in wild-type in *Bicd2*<sup>-/-</sup> cerebellar cortex. (g) LacZ staining in sagittal cerebellar section of P10 heterozygote *Bicd2*<sup>+/-</sup> mice is predominantly present in the Purkinje cell layer. Scale Bars: 50 μm (d), 20 μm (f,g), 10 μm (e).

cerebellar cortex, BICD2 immunoreactivity occurred in all layers, with the highest staining intensity in the molecular layer and the white matter (Fig. 4d). In the molecular layer, BICD2 immunoreactivity co-localized with GFAP and the excitatory amino-acid transporter EAAT2 (GLT1, SLC1A2) indicating that it is associated with Bergmann glial cells (Fig. 4e,f). No staining above background was observed in Purkinje cells and pre- and post-migratory granule cells in the EGL and IGL, respectively. The preferential labelling of BICD2 in Bergmann glia is in agreement with *in situ* hybridization data from the Allen Mouse

Brain Atlas<sup>22</sup>, and with the preferential distribution of LacZ staining in Bergmann glial cells in cerebellar cortex of heterozygous *Bicd2*<sup>+/-</sup> mice (Fig. 4g). Furthermore, also in neuron-astrocyte cerebellar co-cultures BICD2 staining was present in GFAP-positive astroglial cells but not in MAP2-positive cells (Supplementary Fig. 6f). Taken together, our data indicate that BICD2 is not expressed in premigratory or migrating granule cells, but rather in Bergmann glial cells, which are essential for successful radial migration of granule neurons in the cerebellum.



**BICD2 has a non-cell-autonomous function in migration.** The predominant expression of BICD2 in Bergman glia cells raises the possibility that defects in radial granule cell migration in *Bicd2*<sup>-/-</sup> mice result from the loss of BICD2 function in Bergmann glia. Accordingly, crossing of *Bicd2*<sup>fl/fl</sup> mice with

GFAP-Cre mice, which show sustained Cre-recombinase expression in astrocytes including Bergmann glia, results in the same granule cell migration defects that are observed in global *Bicd2*<sup>-/-</sup> mice (Fig. 5a). However, in view of Cre activity in some neuronal precursor cells including cerebellar granule cells<sup>15</sup>, the data from GFAP-Cre/*Bicd2*<sup>fl/fl</sup> mice do not exclude a role of BICD2 in migrating granule cells. We therefore crossed *Bicd2*<sup>fl/fl</sup> mice with *Math1*-CreERT2 mice, which express tamoxifen-inducible Cre-recombinase in granule precursor cells<sup>23</sup>, and injected pregnant mothers with tamoxifen. *Math1*-CreERT2/*Bicd2*<sup>fl/fl</sup> offspring showed a normal cerebellar cortex, and systematic analysis of sections stained for the post-migratory granule cell marker  $\alpha 6$  GABA<sub>A</sub> receptor showed that all granule cells were in the IGL at P20 (Fig. 5b). This indicated that elimination of BICD2 in premigratory cells does not affect radial granule cell migration. To further exclude that BICD2 has a cell intrinsic role in migrating granule cells, we performed shRNA-mediated knockdown of BICD2 in premigratory granule cells using *ex vivo* electroporation of P10 rat cerebella. Consistent with the data from *Math1*-CreERT2/*Bicd2*<sup>fl/fl</sup> mice, radial granule cell migration was unaltered in BICD2 shRNA treated granule cells (Fig. 5c). These data indicate that cerebellar granule cell migration defects in *Bicd2*<sup>-/-</sup> mice are non-cell-autonomous and intrinsic to astrocytes.

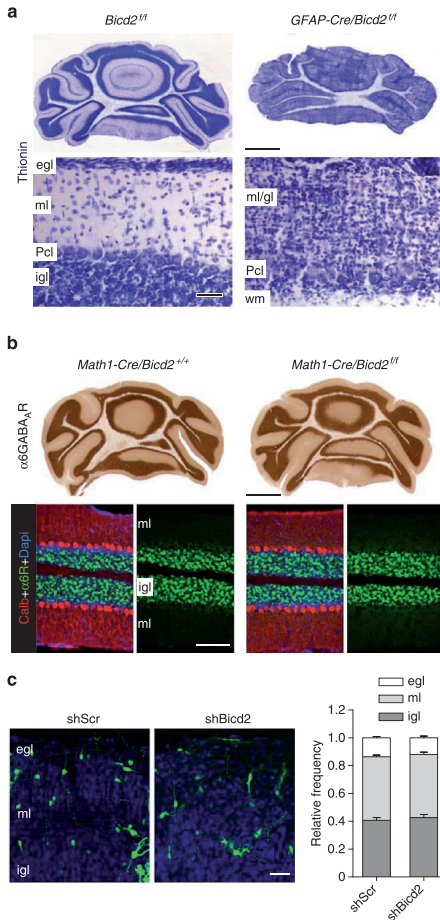


**Figure 5 | BICD2 depletion in premigratory cerebellar granule cell does not influence radial migration.** (a) Coronal thionin-stained sections showing that GFAP-Cre/*Bicd2*<sup>fl/fl</sup> do not develop an IGL. (b) Unaltered distribution of  $\alpha 6$ GABA<sub>A</sub>R-labelled granule cells in P25 *Math1*-CreERT2/*Bicd2*<sup>fl/fl</sup> cerebellar cortex. (c) P10 rat cerebella were *ex vivo* electroporated with *Bicd2* or scrambled control shRNAs and GFP expression vector. The fraction of GFP+ granule cells was quantified for each layer per picture (three separate experiments were performed, total number of pictures analysed for shScr = 40, shBicd2 = 33). The average distribution of GFP+ granule cells is shown in the graph (error bars are s.e.m.,  $n = 3$ ). Scale bars: 1 mm (top a, b), 100  $\mu$ m (b), 50  $\mu$ m (a, c).

**BICD2 does not influence Bergmann glial cell morphology.** All the results indicate that the radial granule cell migration deficit in *Bicd2*<sup>-/-</sup> mice results from a loss of function of BICD2 in Bergmann glia, which has a scaffolding function in radial granule cell migration. It is thus conceivable that the disruption of Bergmann fibre scaffold causes the *Bicd2*<sup>-/-</sup> cerebellar phenotype. GFAP immunohistochemistry showed that *Bicd2*<sup>-/-</sup> mice show abundant radial glial fibre labelling (Fig. 6a,b). *Bicd2*<sup>-/-</sup> radial glia showed an ordered radial organization of in the EGL with orthogonal orientation relative (Fig. 6a-c). In view of a small proportion of GFAP-positive fibres with abnormal non-radial orientation (Fig. 6b), we further analysed Bergmann glial cells in *Bicd2*<sup>-/-</sup> mice crossed with GFAP-GFP transgenic mice that express GFP in a subset of Bergmann glial cells. Consistent with a grossly normal organization of Bergmann glia, the far majority of GFP-labelled Bergmann glia cells had the cell body near the Purkinje cells and radial processes extending up to the pial surface as in wild-type mice (Fig. 6d-g). These results indicate that morphology and structure of Bergmann glial cells are largely unaffected in *Bicd2*<sup>-/-</sup> mice.

**BICD2<sup>-/-</sup> mice have altered extracellular matrix composition.** Having shown that migration defects in *Bicd2*<sup>-/-</sup> mice are intrinsic to the Bergmann glial cells, we wanted to gain a better understanding of how BICD2 regulates cerebellar granule cell migration. We first focussed on the subcellular distribution of known BICD2 binding partners, such as Rab6, dynein/dynactin and RanBP2. Immunofluorescence with antibodies against these proteins revealed no major changes in *Bicd2*<sup>-/-</sup> Bergmann glia (Fig. 6e,g). Moreover, no change in centrosome position or Golgi apparatus morphology was observed in these cells.

Next, we searched for molecular changes in *Bicd2*<sup>-/-</sup> mice using mass spectrometry. Proteomics analysis was performed with biological duplicates on cerebellar extracts from control and homozygote *Bicd2*<sup>-/-</sup> mice at P15. Mass spectrometry analysis of whole lanes revealed several up- and downregulated proteins, and we decided to focus on the factors that were previously found to influence neuronal migration, including signalling factors, extracellular matrix and adhesion molecules<sup>24-28</sup>. Some of these proteins were only mildly affected in the *Bicd2*<sup>-/-</sup> cerebellum,

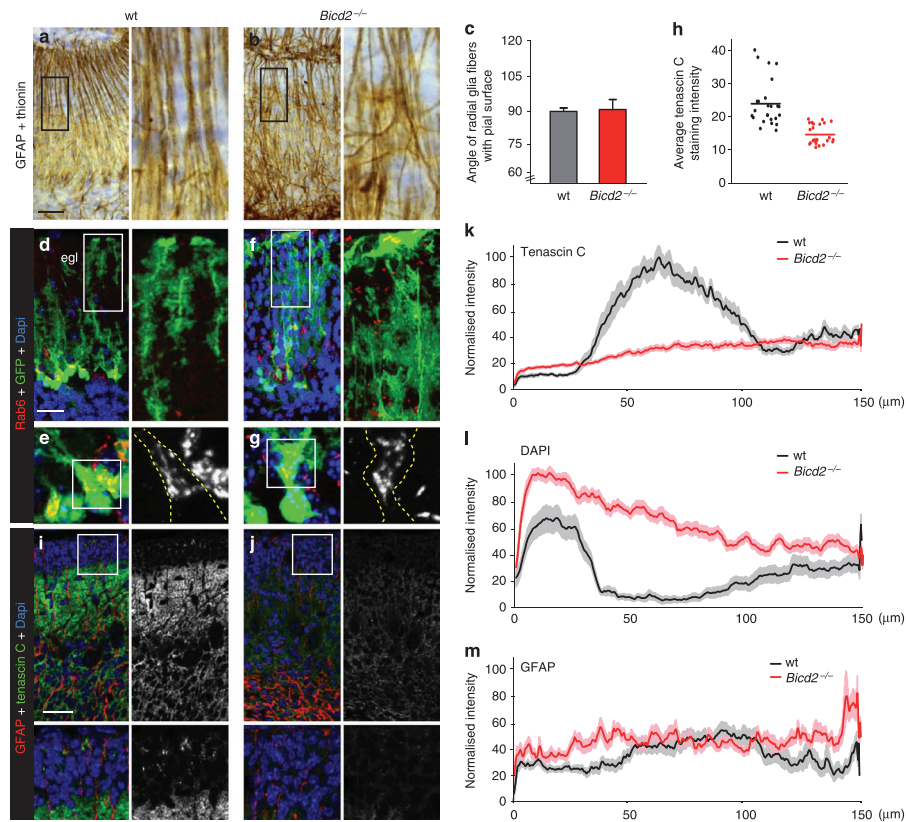


**Figure 6** | Altered extracellular matrix composition in BICD2-deficient cerebellar cortex. (a,b) GFAP immunoperoxidase histochemistry in P10 coronal sections showing ordered radially oriented Bergmann glia processes in wild-type (wt) and more disorganized processes *Bicd2*<sup>-/-</sup> cerebellum. (c) Quantification of the angle of the Bergmann glia cell radial processes with the pial surface (mean ± s.e., N = 250) from wt and *Bicd2*<sup>-/-</sup> mice. (d-g) Maximal projection of confocal stack (11 sections, total thickness of optical section, 5 μm) of Rab6 immunofluorescence in coronal P20 cerebellar sections from wt and *Bicd2*<sup>-/-</sup> mice that also are transgenic for a GFAP-EGFP construct resulting in the expression of EGFP in subsets of astrocytes, including Bergmann glia cells. Note EGFP-positive Bergman glia cells that extend radial processes to the pial surface cerebellum in both wt (d) and *Bicd2*<sup>-/-</sup> (f) cerebellum. Also note that Rab6 immunoreactivity which is mainly distributed in the trans-Golgi apparatus shows the same distribution in wt and *Bicd2*<sup>-/-</sup> Bergman glia cell body (e.g.). (h-j) Double-labelling confocal immunofluorescence (optical sections 1.5 μm) of tenascin and GFAP immunoreactivity showing reduced labelling in *Bicd2*<sup>-/-</sup> cerebellum. (k-m) Fluorescent intensity of the indicated marker in the molecular layer (wt mice) or the mixed molecular/granular layer (*Bicd2*<sup>-/-</sup> mice) from the pial surface up to the Purkinje cell layer. Scale bars: 25 μm (a,d,i).

while others like N-cadherin and integrin β1 showed a strongly reduced expression (Table 2 and Supplementary Data 1). Only two proteins were absent from the *Bicd2*<sup>-/-</sup> cerebellum in two separate experiments, doublecortin (DCX) and Tenascin C. Since microtubule-associated protein DCX is restricted to migrating neurons and absent from Bergmann glia cells<sup>29,30</sup>, we further analysed the extracellular matrix protein Tenascin C. Tenascin C is produced by Bergmann glia cells<sup>31</sup>, has been implicated in neuron-glia cell recognition<sup>32,33</sup> and is known to be important for granule cell migration in the cerebellum<sup>34–37</sup>. We determined the

Tenascin C distribution by immunofluorescence experiments using antibody staining and confirmed that the levels of Tenascin C in the *Bicd2*<sup>-/-</sup> cerebellum were low (Fig. 6h–j). Thus while Tenascin C was abundantly present in the molecular layer of P7–P15 wild-type cerebellum, the levels of Tenascin C were low throughout the cerebellar cortex in *Bicd2*<sup>-/-</sup> mice at this age (Fig. 6i–m). Together these data show that *Bicd2*<sup>-/-</sup> mice have an altered extracellular matrix composition in the molecular layer, which could be responsible for the defects in granule cell migration.

**Table 2 | Proteomics analysis from biological duplicates of cerebellar extracts from control and homozygote *Bicd2*<sup>-/-</sup> mice at P15.**

Identified protein	Protein acc./id	Mascot score				Ratio WT/KO
		WT-06	WT-08	KO-00	KO-02	
Cdc42	IPI00016786	205	261	267	200	1.13
Rac1	IPI00010271	457	452	464	461	0.98
RalA	IPI00217519	247	172	290	227	0.81
Rap1A	IPI00019345	319	452	409	407	0.94
DCX	IPI00216744	107	163	ND	ND	ND
DCLK	IPI00004560	489	492	312	410	1.36
N-cadherin	IPI00290085	249	213	336	246	0.80
Integrin, beta1	IPI00217561	57	103	223	106	0.49
contactin-1	IPI00029751	973	1,107	987	1,131	0.98
contactin-2	IPI00024966	271	289	185	71	2.18
Tenascin C	IPI00220216	209	104	ND	ND	ND

Only the factors identified in the mass spectrometry analysis that were previously found to influence neuronal migration are indicated. The full mass spectrometry list can be found in Supplementary Data 1.

## Discussion

In this study, we have shown that the conserved dynein adaptor protein BICD2 is essential for proper development of the brain, where it plays an important role in the establishment of the laminar organization of the cerebral and cerebellar cortices. In particular, by comparing different mouse lines missing BICD2 in specific cell populations, we demonstrated that BICD2 has a non-cell-autonomous function in driving inward radial migration of cerebellar granule cells. In addition, by using a proteomic approach we provide evidence that the extracellular matrix protein Tenascin C produced by the Bergmann glia cells may account for the non-cell-autonomous role of BICD2 in migration.

Multiple factors have been identified that control granule cell migration in a cell-autonomous manner<sup>24–28</sup>, such as proteins that control centrosome positioning and nucleokinesis<sup>38–41</sup> and neuronal adhesion molecules that mediate granule cell-Bergmann glia interaction<sup>42–44</sup>. Moreover, several abnormalities in Bergmann glia cell structure and function have been shown to cause granule cell migration alterations<sup>19,20</sup>. For instance, mutant mice that disrupt the radial scaffold structure of Bergmann glia fibres develop migration deficits<sup>45–47</sup>. Also mutant mice with Bergmann glia fibres with abnormal end feet at the pial surface show impaired migration and develop clusters of ectopic granule cells<sup>48,49</sup>.

An important feature of the *Bicd2*<sup>-/-</sup> mice is the complete absence of an IGL, indicating a severe disruption of granule cell migration (Supplementary Movie 2). This phenotype is more severe than the migration deficits found in any other granule cell migration deficient mouse model. In addition, the laminar distribution of other cerebellar cortical neurons including Purkinje cells and molecular layer interneurons appears intact, indicating that the migration deficit is specific for granule cells. Furthermore, only subtle abnormalities in the overall Bergmann glia cell organization are observed, suggesting that the granule cell migration deficit in *Bicd2*<sup>-/-</sup> mice cannot be explained by structural changes in Bergmann glia morphology. Nevertheless, our data strongly indicate that the granule cell migration deficits result from a loss of function of BICD2 in Bergmann glia, as BICD2 is expressed in Bergmann glia cells, but not in premigratory or migrating granule cells. In addition, selective deletion of BICD2 in premigratory granule cells does not influence radial migration, while the depletion of BICD2 in astrocytes including Bergmann glia cells leads to the same granule cell migration defects as observed in global *Bicd2*<sup>-/-</sup> mice. The data indicate that BICD2 has a non-cell-autonomous role in granule cell migration in the cerebellar cortex.

How can BICD2 exert non-cell-autonomous effects? We envision two scenarios that are not mutually exclusive. First BICD2 could regulate dynein-mediated trafficking in Bergmann glia cells. BICD2 is a regulator of dynein function and plays a role in dynein-mediated cellular processes, such as microtubule minus-end-directed trafficking<sup>3</sup>. BICD2 binds to the dynein motor complex<sup>4</sup>, promotes a stable interaction between dynein and its accessory factor dynactin<sup>50</sup> and induces microtubule-dependent minus-end-directed transport<sup>5</sup>. Similar to the *Drosophila* BICD mutant embryos<sup>2</sup>, Bergmann glia cells lacking BICD2 could have defects in dynein-mediated transport pathways. However, we did not observe cellular phenotypes related to globally impaired dynein/dynactin function in Bergmann glia cells, such as Golgi fragmentation and other signs of impaired retrograde trafficking. Other dynein regulators, such as lissencephaly 1 (Lis-1) and nuclear distribution protein E (NDE1) have previously been found to control neuronal migration<sup>38,41</sup>.

Second, it is possible that BICD2 is involved in a specific cargo trafficking pathway in Bergmann glia cells. For instance, BICD2 also interacts with the small GTPase Rab6, which controls the targeting and fusion of secretory vesicles to the plasma membrane<sup>8–10</sup>. However, very little is known about the trafficking and secretion mechanisms in Bergmann glia cells. On the basis of the involvement of BICD2 in secretory transport in other systems, we speculate that the trafficking or secretion of neuron–glial cell recognition factors might be altered in *Bicd2*<sup>-/-</sup> mice. Indeed, the extracellular matrix protein Tenascin C produced by Bergmann glia cells is found at relative low levels in *Bicd2*<sup>-/-</sup> mice. Tenascin C is known to mediate the attachment of neurons to astrocyte surfaces in *in vitro* cell binding assays and stimulates granule cell migration in the cerebellum<sup>31,34–37</sup>. It is interesting to note that the early neuronal migration and differentiation marker DCX is not detected in *Bicd2*<sup>-/-</sup> cerebellum extracts, suggesting a potential link between extracellular matrix components and granule cell migration<sup>51</sup>. Our findings demonstrate an essential non-cell-autonomous role of BICD2 in neuronal cell migration, which might be connected to cargo trafficking pathways in Bergmann glia cells.

BICD2-deficient mice also displayed a disordered laminar organization of the cerebral cortex and hippocampus, which is compatible with a deficit in radial outward migration of newly born neurons to the cortical plate. These data imply that BICD2 may also have a similar non-cell-autonomous function in cortical radial glia cells. However, in the cortex, radial glial cells also act as neuronal progenitor cells, making it difficult to differentiate



between potential glia and neuron-specific defects. At least part of the laminar abnormalities can be explained by a recently identified role of BICD2 in cell-cycle-dependent nuclear oscillation in radial glial progenitors<sup>17</sup>. BICD2 recruits dynein to the nucleopore complex in G2 to mediate apical nuclear migration and BICD2 knockdown causes cell cycle arrest and neurogenesis deficits<sup>5,17</sup>. The extent to which different potential functions of BICD2 contribute to cortical and hippocampal migration deficits remains to be determined.

Recently, mutations in BICD2 have been linked to a dominant mild early onset form of SMA<sup>11–13</sup>. The motor symptoms show congenital or early post-natal onset, are non-progressive and are associated with chronic muscle denervation and reinnervation, suggesting problems with maintaining the axon or the neuromuscular synapse. Spinal cord and motor neurons appeared normal in the *Bicd2*<sup>-/-</sup> mice, and we did not observe any motor neuron abnormalities or signs of impaired retrograde transport defects. The differences in phenotypes between *Bicd2*<sup>-/-</sup> mice and the SMA patients with mutations in *BICD2* gene indicate that the motor neuron defects cannot be explained by the loss of BICD2 function. Indeed, a transgenic mouse expressing the N-terminal part of BICD2, which has a strong dynein-recruiting activity and chronically impaired dynein-dynactin function, develops several cellular phenotypes in motor neurons including Golgi fragmentation and neurofilament accumulation in the proximal axon<sup>52</sup>. These phenotypes are compatible with the pathology developed by patients. The missense *BICD2* mutations found in SMA patients could thus exert a gain of function effect, consistent with the dominant character of the disease. Future studies are needed to further unravel the multiple essential roles of BICD2 in nervous system development.

## Methods

**Animals.** All animal experiments were performed in compliance with the guidelines for the welfare of experimental animals issued by the Federal Government of The Netherlands. All animal experiments were approved by the Animal Ethical Review Committee (DEC) of the Erasmus Medical Center and Utrecht University. The BICD2 targeted and KO alleles are crossed into the C57BL/6 inbred strain. For determination of the growth curve groups, we analysed BICD2 mice (both male and female mice) of different genotypes every 2 days from birth to 21 days of age at fixed time points during the day. In addition to the homemade BICD2-deficient mice, we used in this study transgenic mice expressing Nestin-Cre<sup>14</sup> (Jackson Laboratory), EMX1-Cre<sup>16</sup> (Jackson Laboratory), Math1-CreERT2 (ref. 23) (Jackson Laboratory), GFAP-Cre<sup>15</sup> (Jackson Laboratory) and GFAP-GFP transgenic mice (kindly provided by Frank Kirchhoff). Information about the mouse lines can be found in the Jackson Laboratory mouse database (<http://jaxmice.jax.org>).

**Generation of BICD2-deficient mice.** Targeting techniques and the procedures for selection of ES cells and generation of KO mice have been described<sup>53</sup>. We introduced the resistance markers in ES cells by two sequential rounds of homologous recombination (first round, neomycin cassette, 4.2% (9 out of 213) of picked clones targeted; second round, puromycin cassette, 0.3% (1 out of 350) of the picked clones targeted). To test if Cre-mediated excision occurs within the BICD2 locus, we electroporated ES cells with a construct containing the Cre recombinase gene, driven by a thymidine kinase promoter, in a vector backbone with a P<sub>gk</sub> hygromycin-resistance gene. After selection with hygromycin B, we detected the deletion of the BICD2 region between the outermost loxP sites by PCR analysis using primer a/d. The positive ES cell clone that was able to excise the BICD2 locus and contains a correct karyotype, was injected into blastocysts. The chimeras that gave germline transmission were mated into the C57BL/6 background to generate inbred *Bicd2*<sup>fl</sup> (targeted) mice. Heterozygous BICD2 KO (*Bicd2*<sup>-/-</sup>) mice were obtained by crossing F1 heterozygous *Bicd2*<sup>fl</sup> mice with CAG-Cre transgenic mice that express Cre recombinase in the germ-cell lineage (kindly provided by Frank Grosschedl). We determined the genotypes of the heterozygous and homozygous *Bicd2*<sup>fl</sup> and *Bicd2*<sup>-/-</sup> mice by PCR analysis using the primer sets indicated in Supplementary Fig. 1A. PCR primers used are primer a (5'-GTGTAGCAATTCAGGAACATCCATGC-3'), primer-b (5'-AATGGAGAATCTCATCTGTGGCAGG-3'), primer-c (5'-CGCGGGATCAGAGCAGCCGATG-3') and primer-d (5'-TGTCAGCAATCCATCTCTACGCTC-3'). Western blot analysis using homemade anti-rabbit BICD2 antibodies<sup>4</sup> confirmed the lack of BICD2 protein in brain lysates of P20 *Bicd2*<sup>-/-</sup> mice.

To obtain nervous-system-specific KO of BICD2, *Bicd2*<sup>fl</sup> mice were crossed with transgenic mice expressing Cre recombinase under control of the Nestin

promotor<sup>14</sup> (Jackson Laboratory). To examine the role of BICD2 in excitatory neurons in the cortex/hippocampus and preneurogenic granule cells in the cerebellum, *Bicd2*<sup>fl</sup> mice were crossed with EMX1-Cre<sup>16</sup> (Jackson Laboratory) and Math1-CreERT2 transgenic mice<sup>23</sup> (Jackson Laboratory), respectively. To obtain sustained expression of Cre-recombinase in astrocytes, including Bergmann glia cells, *Bicd2*<sup>fl</sup> mice were crossed with GFAP-Cre transgenic mice<sup>15</sup> (Jackson Laboratory). Wild-type and *Bicd2* KO mice were also crossed with GFAP-GFP transgenic mice, to visualize the morphology of GFP-labelled Bergmann glia cells<sup>54</sup> (kindly provided by Frank Kirchhoff). The primer sets for PCR genotyping of the various transgenic mouse lines used in this study are described in the Jackson Laboratory mouse database (<http://jaxmice.jax.org>).

**Histological procedures.** Mice were anesthetized with pentobarbital and perfused transcardially with 4% paraformaldehyde, and brains were either embedded in paraffin and sectioned at 4–6  $\mu$ m, or incubated with increasing concentrations of sucrose (15% and 30%) and rapidly frozen and sectioned at 40  $\mu$ m (freezing microtome) and collected in PBS. Sections were stained with haematoxylin/eosin (paraffin sections), thionin (frozen sections), processed for LacZ staining or processed for immunohistochemistry. For LacZ staining sections were washed with PBS and incubated overnight at 37 °C in PBS buffer containing 1 mg ml<sup>-1</sup> X-gal, 5 mM K<sub>2</sub>Fe(CN)<sub>6</sub>, 5 mM K<sub>3</sub>Fe(CN)<sub>6</sub>, 2 mM MgCl<sub>2</sub>, 0.01% SDS and 0.02% NP-40, washed, mounted on glass slides, and counter stained with Neutral Red. For double and triple-labelling immunofluorescence, we used a two-step procedure with FITC-, cyanine 3 (Cy3)-, Cy5-, Alexa Fluor488-, Alexa Fluor468- and Alexa Fluor633-conjugated secondary antibodies (Jackson ImmunoResearch, West Grove, PA; Invitrogen) diluted at 1:400 (see also Supplementary Methods). For immunohistochemistry, we used an avidin-biotin-immunoperoxidase complex method (ABC; Vector Laboratories) with diaminobenzidine (0.05% as the chromogen, and biotinylated secondary antibodies (Jackson ImmunoResearch, see Supplementary Methods for details).

Primary antibodies used in this study are as follows (see also Supplementary Methods for details): rabbit anti-BICD2 (Ab 2293 and 2294)<sup>4</sup>; mouse anti-calbindin (Sigma, clone CB-955, 1:10,000); rabbit anti-calbindin (Swant, 1:10,000); guinea pig anti-EAAT2 (Millipore, 1:5,000); goat anti-FoxP2 (AbCam, 1:1,000); rabbit anti- $\alpha$ 6GABA<sub>A</sub> receptor (Sigma, 1:1,000); rabbit anti-GFAP (DAKO, 1:5,000); mouse anti-GFAP (Sigma, clone G-A-5, 1:10,000); mouse anti-mGluR2 (AbCam 1:1,000); mouse anti-NeuN (Millipore MAB377, 1:2,000); mouse anti-neurofilament-M (Sigma, 1:10,000); mouse anti-parvalbumin (Sigma, 1:10,000); mouse anti-Rab6 (ref. 7), rabbit anti-Tenascin-C (GenTex, 1:400), guinea pig anti-VGluT1 (Millipore, 1:2,000), guinea pig anti-VGluT2 (Millipore, 1:1,000) and mouse-anti-MAP2 (Sigma, 1:2,000). Sections stained for immunofluorescence were analysed with Zeiss (Oberkochen, Germany) LSM 510 or LSM700 confocal laser scanning microscopes using 40 $\times$ /1.3 and 63 $\times$ /1.4 oil-immersion objectives. Immunoperoxidase-stained sections were analysed and photographed using a Leica DM-RB microscope and a Leica DC300 digital camera.

**Electroporation-mediated transfection of egl cells.** Rat pups were decapitated at P10, the brain was isolated and placed in ice-cold Leibovitz 15 (L15; Invitrogen) medium. The cerebellum was dissected and meninges removed. The most superficial layer (EGL) of the cerebellum was injected at multiple locations to infuse the cerebellar surface with DNA solution (PBS with 0.02% Fast Green, 400 ng  $\mu$ l<sup>-1</sup> pSuper vector, 200 ng  $\mu$ l<sup>-1</sup> eGFP vector). The cerebellum was placed between Genepaddles (5 $\times$ 7 mm) of a BTX ECM 830 Electroporator and 5 pulses of 87 V for 50 ms with 1.0 s intervals were applied. After electroporation, sagittal slices of 350  $\mu$ m were cut using a Tissue Chopper (McIlwain). Slices were cultured on inserts (Millipore, 0.4 mm) incubated in culture medium (50% Earls Basal Medium, 25% HBSS, 25% Normal Horse Serum, 5 mM L-glutamine and Penicillin/Streptomycin) for 4 days at 35 °C with 5% CO<sub>2</sub>. Slices were fixed at DIV4 in 4% paraformaldehyde in PBS overnight at 4 °C. Then slices were blocked for 6 h in blocking buffer (5% Normal Goat Serum, 1% BSA, 1% glycine and 0.4% Triton-X100 in PBS) and incubated with primary rabbit anti-GFP antibody (Abcam; 1:2,000) in blocking buffer overnight at 4 °C. Following three washes in PBS, slices were incubated in secondary goat anti-rabbit antibody (Invitrogen; Alexa 488, 1:750) in blocking buffer overnight at 4 °C. To visualize tissue structure, nuclei were stained with 4',6'-diamidino-2-phenylindole. GFP-positive cells were imaged using an Olympus Fluoview FV1000MPE confocal microscope (20 $\times$  objective). The number of GFP-positive granule cells in each cerebellar layer was quantified with ImageJ (EGL, molecular/migratory layer and IGL). The fraction of GFP-positive granule cells was calculated for each layer per picture. Three separate experiments were performed (total number of pictures analysed for shScrambled = 40, shBicd2 = 33).

**Preparation of tissue extracts and mass spectrometry analysis.** For tissue western blots, total brain, cortex, cerebellum, kidney, lung, spleen, liver and heart were dissected from P20 wild-type, *Bicd2*<sup>+/-</sup> and *Bicd2*<sup>-/-</sup> mice and placed in ice-cold PBS, pH7.4. For developmental western blots, wild-type E10.5 (whole embryo), E13.5, E16, E18, P1, P5 (head only), P10, P15 and adult (cortex and cerebellum) mice were placed in ice-cold PBS, pH 7.4. Samples were homogenized in homogenization buffer (150 mM NaCl, 50 mM Tris, 0.1% v/v SDS, 0.5% v/v NP-40, pH8, 1 $\times$  complete protease inhibitors; Roche), briefly sonicated, 10 min

centrifuged at 900 rcf, resuspended in SDS sample buffer and boiled for 5 min. Protein concentrations were measured using a BCA protein assay kit (Pierce) and 20 µg of protein was loaded in each lane for a subsequent western blot analysis using standard protocols.

For mass spectrometry analysis, the cerebellum was dissected from P15 wild-type and homozygote *Bicd2*<sup>-/-</sup> mice, homogenized, centrifuged and proteins were separated on a 4–12% NuPAGE Bis-Tris gel and stained with the Colloidal Blue staining kit (Invitrogen). Gel lanes were cut into 2-mm slices using an automatic gel slicer and subjected to in-gel reduction with dithiothreitol, alkylation with iodoacetamide and digestion with trypsin as described previously<sup>8</sup>. The Mascot score cutoff value for a positive protein hit was set to 100. Individual peptide tandem mass spectrometry spectra with Mascot scores below 100 were checked manually and either interpreted as valid identifications or discarded. Proteins present in the negative controls (pull-down assays with bio-GFP alone) were regarded as background. For the proteome analysis of the wild-type and homozygote *Bicd2*<sup>-/-</sup>, we focussed on proteins that were previously found to influence neuronal migration, including signalling factors, extracellular matrix and adhesion molecules<sup>24–26</sup>. We searched four mass spectrometry data sets (two from wild-type and two from *Bicd2*<sup>-/-</sup> animals) for the corresponding Mascot score to determine probability of a positive hit and calculated the ratio of wild-type versus KO (Supplementary Data 1).

## References

- Wharton, R. P. & Struhl, G. Structure of the *Drosophila* BicaudalD protein and its role in localizing the posterior determinant nanos. *Cell* **59**, 881–892 (1989).
- Bullock, S. L. & Ish-Horowitz, D. Conserved signals and machinery for RNA transport in *Drosophila* oogenesis and embryogenesis. *Nature* **414**, 611–616 (2001).
- Clausen, M. & Suter, B. BicD-dependent localization processes: from *Drosophila* development to human cell biology. *Annu. Rev. Cell. Biol.* **187**, 539–553 (2005).
- Hoogenraad, C. C. *et al.* Mammalian Golgi-associated Bicaudal-D2 functions in the dynein-dynactin pathway by interacting with these complexes. *EMBO J.* **20**, 4041–4054 (2001).
- Hoogenraad, C. C. *et al.* Bicaudal D induces selective dynein-mediated microtubule minus end-directed transport. *EMBO J.* **22**, 6004–6015 (2003).
- Splinter, D. *et al.* Bicaudal D2, dynein, and kinesin-1 associate with nuclear pore complexes and regulate centrosome and nuclear positioning during mitotic entry. *PLoS Biol.* **8**, e1000350 (2010).
- Matanis, T. *et al.* Bicaudal-D regulates COPI-independent Golgi-ER transport by recruiting the dynein-dynactin motor complex. *Nat. Cell Biol.* **4**, 986–992 (2002).
- Grigoriev, I. *et al.* Rab6 regulates transport and targeting of exocytotic carriers. *Dev. Cell.* **13**, 305–314 (2007).
- Coutelis, J. B. & Ephrussi, A. Rab6 mediates membrane organization and determinant localization during *Drosophila* oogenesis. *Development* **134**, 1419–1430 (2007).
- Januschke, J. *et al.* Rab6 and the secretory pathway affect oocyte polarity in *Drosophila*. *Development* **134**, 3419–3425 (2007).
- Neveling, K. *et al.* Mutations in BICD2, which encodes a Golgin and important motor adaptor, cause congenital autosomal-dominant spinal muscular atrophy. *Am. J. Hum. Genet.* **92**, 946–954 (2013).
- Oates, E. C. *et al.* Mutations in BICD2 cause dominant congenital spinal muscular atrophy and hereditary spastic paraplegia. *Am. J. Hum. Genet.* **92**, 965–973 (2013).
- Peeters, K. *et al.* Molecular defects in the motor adaptor BICD2 cause proximal spinal muscular atrophy with autosomal-dominant inheritance. *Am. J. Hum. Genet.* **92**, 955–964 (2013).
- Dubois, N. C., Hofmann, D., Kaloulis, K., Bishop, J. M. & Trumpp, A. Nestin-Cre transgenic mouse line Nes-Cre1 mediates highly efficient Cre/loxP mediated recombination in the nervous system, kidney, and somite-derived tissues. *Genesis* **44**, 355–360 (2006).
- Zhou, L. *et al.* hGFAP-cre transgenic mice for manipulation of glial and neuronal function in vivo. *Genesis* **31**, 85–94 (2001).
- Gorski, J. A. *et al.* Cortical excitatory neurons and glia, but not GABAergic neurons, are produced in the Emx1-expressing lineage. *J. Neurosci.* **22**, 6309–6314 (2002).
- Hu, D. J. *et al.* Dynein recruitment to nuclear pores activates apical nuclear migration and mitotic entry in brain progenitor cells. *Cell* **154**, 1300–1313 (2013).
- Kriegstein, A. & Alvarez-Buylla, A. The glial nature of embryonic and adult neural stem cells. *Annu. Rev. Neurosci.* **32**, 149–184 (2009).
- Buffo, A. & Rossi, F. Origin, lineage and function of cerebellar glia. *Prog. Neurobiol.* **109**, 42–63 (2013).
- Xu, H. *et al.* Bergmann glia function in granule cell migration during cerebellum development. *Mol. Neurobiol.* **47**, 833–844 (2013).
- Komuro, H. & Rakic, P. Dynamics of granule cell migration: a confocal microscopic study in acute cerebellar slice preparations. *J. Neurosci.* **15**, 1110–1120 (1995).
- Lein, E. S. *et al.* Genome-wide atlas of gene expression in the adult mouse brain. *Nature* **445**, 168–176 (2007).
- Machold, R. & Fishell, G. Math1 is expressed in temporally discrete pools of cerebellar rhombic-lip neural progenitors. *Neuron* **48**, 17–24 (2005).
- Solecki, D. J. Sticky situations: recent advances in control of cell adhesion during neuronal migration. *Curr. Opin. Neurobiol.* **22**, 791–798 (2012).
- Hatten, M. E. Central nervous system neuronal migration. *Annu. Rev. Neurosci.* **22**, 511–539 (1999).
- Chizhikov, V. & Millen, K. J. Development and malformations of the cerebellum in mice. *Mol. Genet. Metab.* **80**, 54–65 (2003).
- Govek, E. E., Hatten, M. E. & Van Aelst, L. The role of Rho GTPase proteins in CNS neuronal migration. *Dev. Neurobiol.* **71**, 528–553 (2011).
- Chedotal, A. Should I stay or should I go? Becoming a granule cell. *Trends Neurosci.* **33**, 163–172 (2010).
- Bai, J. *et al.* RNAi reveals doublecortin is required for radial migration in rat neocortex. *Nat. Neurosci.* **6**, 1277–1283 (2003).
- Huynh, M. A. *et al.* An isoform-specific SnoN1-FOXO1 repressor complex controls neuronal morphogenesis and positioning in the mammalian brain. *Neuron* **69**, 930–944 (2011).
- Bartsch, S. *et al.* Expression of tenascin in the developing and adult cerebellar cortex. *J. Neurosci.* **12**, 736–749 (1992).
- Chiquet-Ehrismann, R. & Tucker, R. P. Tenascins and the importance of adhesion modulation. *Cold Spring Harb. Perspect. Biol.* **3**, a004960 (2011).
- Jones, P. L. & Jones, F. S. Tenascin-C in development and disease: gene regulation and cell function. *Matrix. Biol.* **19**, 581–596 (2000).
- Kruse, J., Keilhauer, G., Faissner, A., Timpl, R. & Schachner, M. The J1 glycoprotein—a novel nervous system cell adhesion molecule of the L2/HNK-1 family. *Nature* **316**, 146–148 (1985).
- Grumet, M., Hoffman, S., Crossin, K. L. & Edelman, G. M. Cytotactin, an extracellular matrix protein of neural and non-neural tissues that mediates glia-neuron interaction. *Proc. Natl Acad. Sci. USA* **82**, 8075–8079 (1985).
- Chuong, C. M., Crossin, K. L. & Edelman, G. M. Sequential expression and differential function of multiple adhesion molecules during the formation of cerebellar cortical layers. *J. Cell Biol.* **104**, 331–342 (1987).
- Husmann, K., Faissner, A. & Schachner, M. Tenascin promotes cerebellar granule cell migration and neurite outgrowth by different domains in the fibronectin type III repeats. *J. Cell Biol.* **116**, 1475–1486 (1992).
- Tanaka, T. *et al.* Lis1 and doublecortin function with dynein to mediate coupling of the nucleus to the centrosome in neuronal migration. *J. Cell Biol.* **165**, 709–721 (2004).
- Ohshima, T. *et al.* Migration defects of *cdk5*(<sup>-/-</sup>) neurons in the developing cerebellum is cell autonomous. *J. Neurosci.* **19**, 6017–6026 (1999).
- Yamasaki, T. *et al.* Pax6 regulates granule cell polarization during parallel fiber formation in the developing cerebellum. *Development* **128**, 3133–3144 (2001).
- Hippenmeyer, S. *et al.* Genetic mosaic dissection of Lis1 and Ndel1 in neuronal migration. *Neuron* **68**, 695–709 (2010).
- Renaud, J. *et al.* Plexin-A2 and its ligand, Sema6A, control nucleus-centrosome coupling in migrating granule cells. *Nat. Neurosci.* **11**, 440–449 (2008).
- Rio, C., Rieff, H. L., Qi, P., Khurana, T. S. & Corfas, G. Neuregulin and erbB receptors play a critical role in neuronal migration. *Neuron* **19**, 39–50 (1997).
- Adams, N. C., Tomoda, T., Cooper, M., Dietz, G. & Hatten, M. E. Mice that lack astrocytes have slowed neuronal migration. *Development* **129**, 965–972 (2002).
- Yue, Q. *et al.* PTEN deletion in Bergmann glia leads to premature differentiation and affects laminar organization. *Development* **132**, 3281–3291 (2005).
- Wang, X., Imura, T., Sofroniew, M. V. & Fushiki, S. Loss of adenomatous polyposis coli in Bergmann glia disrupts their unique architecture and leads to cell nonautonomous neurodegeneration of cerebellar Purkinje neurons. *Glia* **59**, 857–868 (2011).
- Lin, Y. *et al.* Neuron-derived FGF9 is essential for scaffold formation of Bergmann radial fibers and migration of granule neurons in the cerebellum. *Dev. Biol.* **329**, 44–54 (2009).
- Belvindrah, R. *et al.* Integrin-linked kinase regulates Bergmann glial differentiation during cerebellar development. *Mol. Cell Neurosci.* **33**, 109–125 (2006).
- Ma, S., Kwon, H. J. & Huang, Z. Ric-8a, a guanine nucleotide exchange factor for heterotrimeric G proteins, regulates bergmann glia-basement membrane adhesion during cerebellar foliation. *J. Neurosci.* **32**, 14979–14993 (2012).
- Splinter, D. *et al.* BICD2, dynactin, and LIS1 cooperate in regulating dynein recruitment to cellular structures. *Mol. Cell Biol.* **23**, 4226–4241 (2012).
- Dityatev, A., Seidenbecher, C. I. & Schachner, M. Compartmentalization from the outside: the extracellular matrix and functional microdomains in the brain. *Trends Neurosci.* **33**, 503–512 (2010).
- Teuling, E. *et al.* A novel mouse model with impaired dynein/dynactin function develops amyotrophic lateral sclerosis (ALS)-like features in motor neurons and improves lifespan in SOD1-ALS mice. *Hum. Mol. Genet.* **17**, 2849–2862 (2008).

53. Hoogenraad, C. C. *et al.* Targeted mutation of *Cyln2* in the Williams syndrome critical region links CLIP-115 haploinsufficiency to neurodevelopmental abnormalities in mice. *Nat. Genet.* **32**, 116–127 (2002).
54. Nolte, C. *et al.* GFAP promoter-controlled EGFP-expressing transgenic mice: a tool to visualize astrocytes and astrogliosis in living brain tissue. *Glia* **33**, 72–86 (2001).

#### Acknowledgements

We thank Dr Frank Kirchhoff for providing the GFAP-GFP transgenic mice, Dr Frank Grosveld for providing the CAG-Cre transgenic mice, Dr Jeroen Demmers for help with mass spectrometry analyses and Elize Haasdijk for excellent technical assistance. This work is supported by the Netherlands Organization for Scientific Research (NWO-ALW-VICI, AA, CCH), the Netherlands Organization for Health Research and Development (ZonMW-TOP, CIDZ, AA, CCH; ZonMW-VIDI, RJP), the European Science Foundation (EURYI, CCH), EMBO Young Investigators Program (YIP, CCH) and Het Prinses Beatrix Spierfonds grants (DI, CCH and CIDZ).

#### Author contributions

D.J., E.d.G., R.J.P., A.A. and C.C.H. conceived and designed the experiments; D.J., R.v.d.B., P.S.W., S.v.E., N.K. and M.A.S. performed the experiments. D.J., R.v.d.B., P.S.W., S.v.E. and N.K. analysed the data. C.I.D.Z. contributed reagents/materials/analysis tools. D.J. and C.C.H. coordinated the study and wrote the paper.

#### Additional information

**Supplementary Information** accompanies this paper at <http://www.nature.com/naturecommunications>

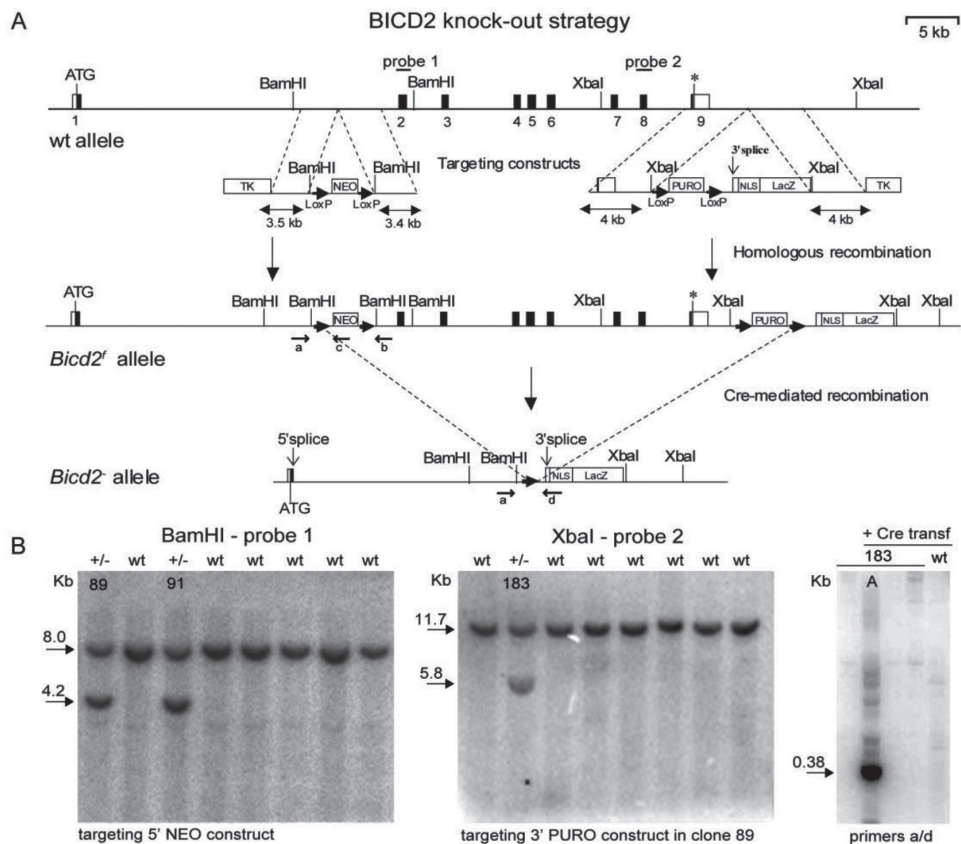
**Competing financial interests:** The authors declare no competing financial interests.

**Reprints and permission** information is available online at <http://npg.nature.com/reprintsandpermissions/>

**How to cite this article:** Jaarsma, D. *et al.* A role for Bicaudal-D2 in radial cerebellar granule cell migration. *Nat. Commun.* **5**:3411 doi: 10.1038/ncomms4411 (2014).

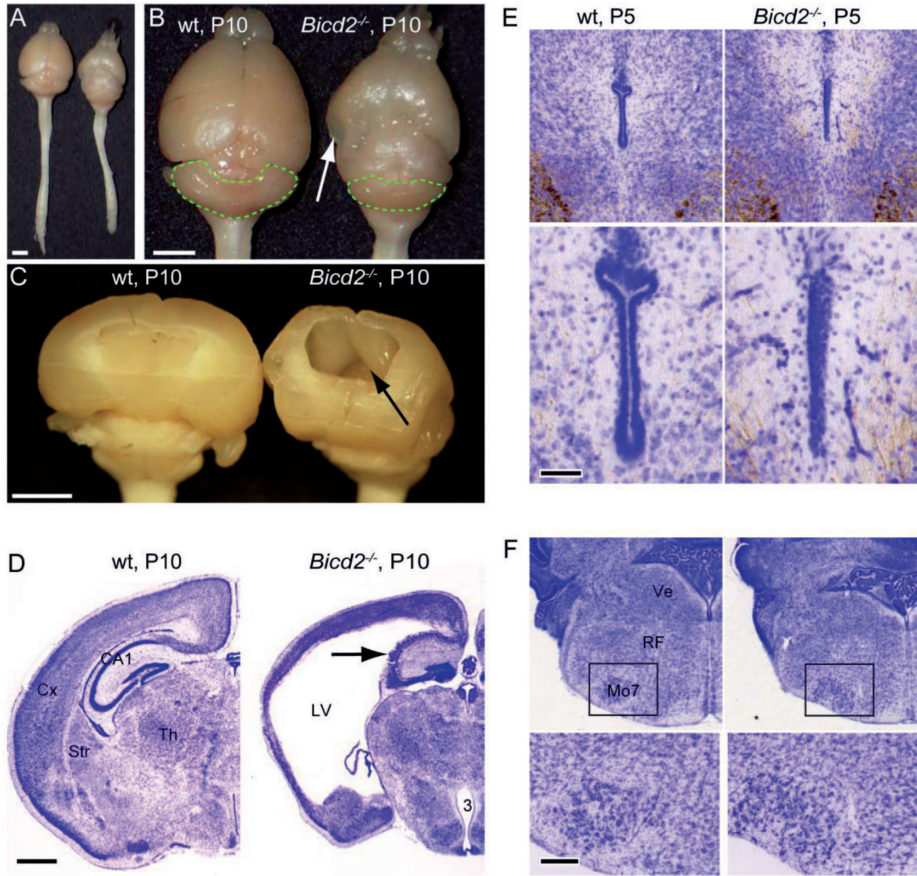


# Supplemental Information



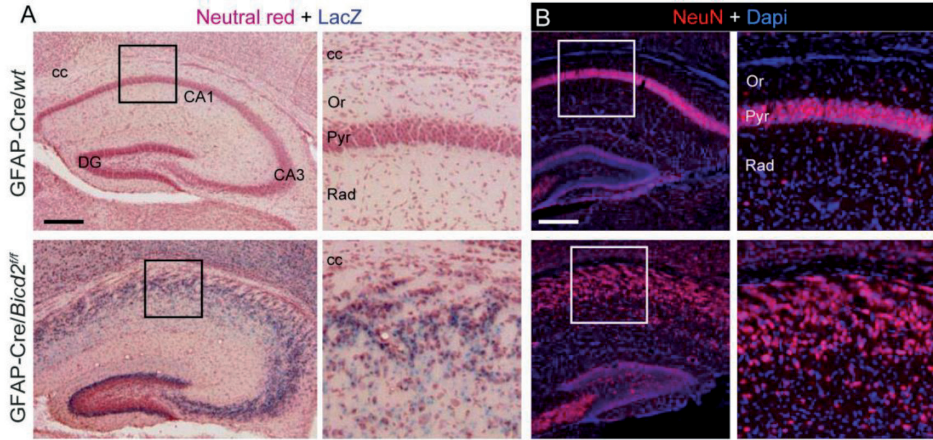
**Supplementary Figure 1. Generation of inducible BICD2 knock-out mice.**

**A)** The mouse *BICD2* locus and gene targeting constructs. To generate an inducible *Bicd2* knockout allele, we introduced a neomycin-resistance gene surrounded by loxP sequences into intron 1, and a puromycin selection marker, surrounded by loxP sequences and followed by  $\beta$ -galactosidase (*lacZ*) reporter gene fused to a nuclear localization signal (NLS), downstream of the mouse *Bicd2* gene. The top line represents *Bicd2*, with exons indicated by solid boxes (white boxes, 5' and 3' UTRs; black boxes, coding regions). Exon 1 contains the start codon (ATG) and exon 9 contains the stop codon (asterisk). The positions of Southern-blot probes 1 and 2 (horizontal lines) and PCR primers a, b, c and d (arrows) are indicated. Selected restriction enzyme sites are shown (BamHI and XbaI). The targeting constructs are shown below *Bicd2*. Homology with the *Bicd2* gene is indicated, as are the lengths of the homologous regions. The loxP sites are represented by arrows. NEO, neomycin-resistance cassette; PURO, puromycin-resistance cassette; TK, thymidine kinase gene; HA-NLS-lacZ, HA- and NLS-tagged lacZ cassette, containing an engineered splice acceptor site (3' splice) and polyadenylation signal (not indicated). The doubly targeted *BICD2* allele, *Bicd2<sup>f</sup>* (targeted), is shown below the targeting constructs. Cre-mediated recombination at the outermost loxP sites of the *Bicd2<sup>f</sup>* allele removes most of the *Bicd2* sequences and generates the *Bicd2<sup>-</sup>* allele, which is represented by the bottom line. The splice acceptor site at the 5' end of the reporter *lacZ* cassette can be spliced onto *Bicd2* exon 2 sequences, generating a hybrid *Bicd2-lacZ* transcript. **B)** Southern-blot analysis of gene targeting and Cre-mediated recombination events. Left, Southern blot of DNA derived from wildtype (wt) and 5' NEO-targeted ES cells and digested with BamHI. The blot was hybridized with (external) probe 1, which detects fragments of 8 kb (wildtype allele) and 4.2 kb (NEO-targeted allele). One NEO-targeted clone with the correct karyotype was electroporated with the PURO targeting construct. Middle, blot with XbaI-digested DNA from a doubly targeted line (*Bicd2<sup>f</sup>*) probed with external probe 2, which detects fragments of 11.7 kb (NEO allele) and 5.8 kb (NEO/PURO allele). This *Bicd2<sup>f</sup>* ES cell line was electroporated with a Cre-recombinase construct to knock-out the *Bicd2* locus (*Bicd2<sup>-</sup>*). Cre-mediated recombination was identified (right) using PCR analysis using primers a/d.



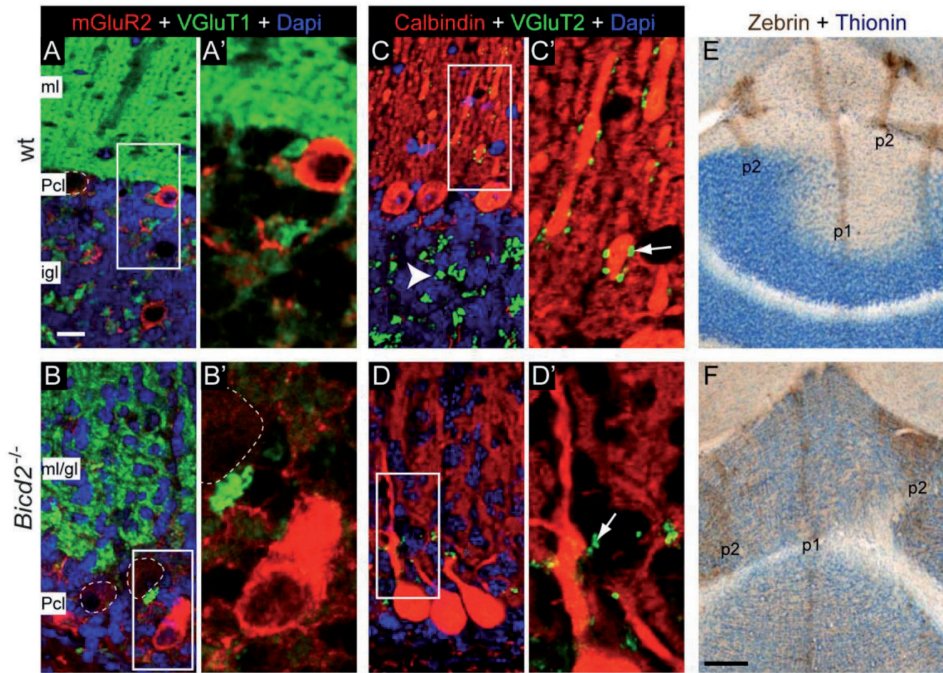
**Supplementary Figure 2. Hydrocephalus and disrupted laminar organization of the cortex in BICD2-deficient mice**

**A-D)** Macroscopic images (**A-C**) and coronal thionin-stained section of P10 nervous system showing enormous expansion of caudal lateral ventricles (LV, arrow in **C**) and thinning of the cortex (arrows in **A B**) in *Bicd2*<sup>-/-</sup> brain. Also note disorganized pyramidal layer in the hippocampus (arrow in **D**) and smaller cerebellum (green contour) in *Bicd2*<sup>-/-</sup> brain. **E)** Coronal sections at the level of the mesencephalon showing the aqueduct. Sections are processed for neurofilament-M immunohistochemistry and counterstained with thionin. Note the absence of a clear lumen in *Bicd2*<sup>-/-</sup> aqueduct indicative of aqueductal stenosis. **F)** Coronal thionin-stained sections at the level of the rostral myelencephalon. The facial motor nucleus (Mo7) has a normal appearance in *Bicd2*<sup>-/-</sup> mice; RF, reticular formation; Ve, vestibular nuclei. Scale bars: 2 mm (**A-C**), 1 mm (**D**), 200  $\mu$ m (**E,F**).



**Supplementary Figure 3. Hippocampal abnormalities in BICD2-deficient mice**

Coronal brain sections of P20 mice stained for LacZ and neutral red (**A**) or processed for NeuN immunofluorescence and Dapi counterstaining (**B**), showing disorganized pyramidal layer in CA1 and ubiquitous LacZ expression in hippocampus of GFAP-Cre *Bicd2<sup>fl/fl</sup>* mice. Scale bars: 200  $\mu$ m.

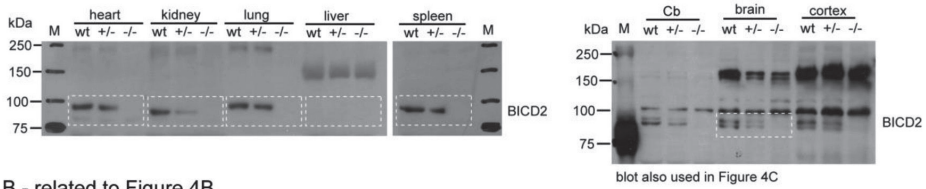


**Supplementary Figure 4. Unaltered laminar distribution of Golgi cells and mossy fibers in BICD2-deficient mice**

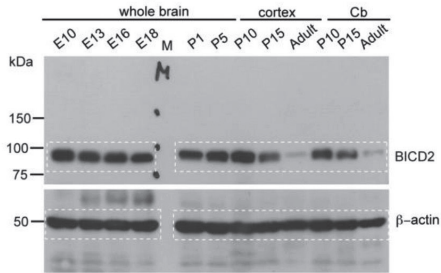
**A, B**) Maximal projections of confocal stacks (optical section, 5 μm) of anti-metabotropic mGluR2 receptor and anti-VGlut1 immunofluorescence in transverse sections of P20 cerebellum showing that cerebellar Golgi cells (mGluR2+, arrow in) are distributed in or below the Purkinje cells (mGluR2-, outlined by dashed lines) in *Bicd2*<sup>-/-</sup> cerebellum. **C, D**) Maximal projections (optical section, 5 μm) of VGlut2 and calbindin immunofluorescence showing VGlut2-labeled climbing fibers (arrow in **C'**) and mossy fibers (arrow head in **C**) in wild-type cerebellum, and a few synaptic terminal-like structures on proximal Purkinje cell dendrites (Calb+) in *Bicd2*<sup>-/-</sup> cerebellum. **F**) Anti-zebrin immunohistochemistry and thionin counterstaining in transverse sections of the anterior vermis (lobule III, IV) showing parasagittal zones with zebrin-positive (p1, p2) and zebrin-negative Purkinje cells. *Bicd2*<sup>-/-</sup> cerebellum retains the zonal organization of Purkinje cells. Scale bars: 25 μm (**A**), 50 μm (**B**).



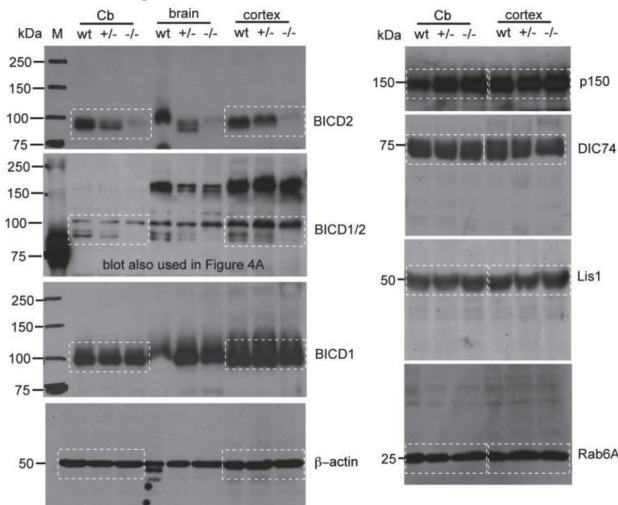
A - related to Figure 4A



B - related to Figure 4B



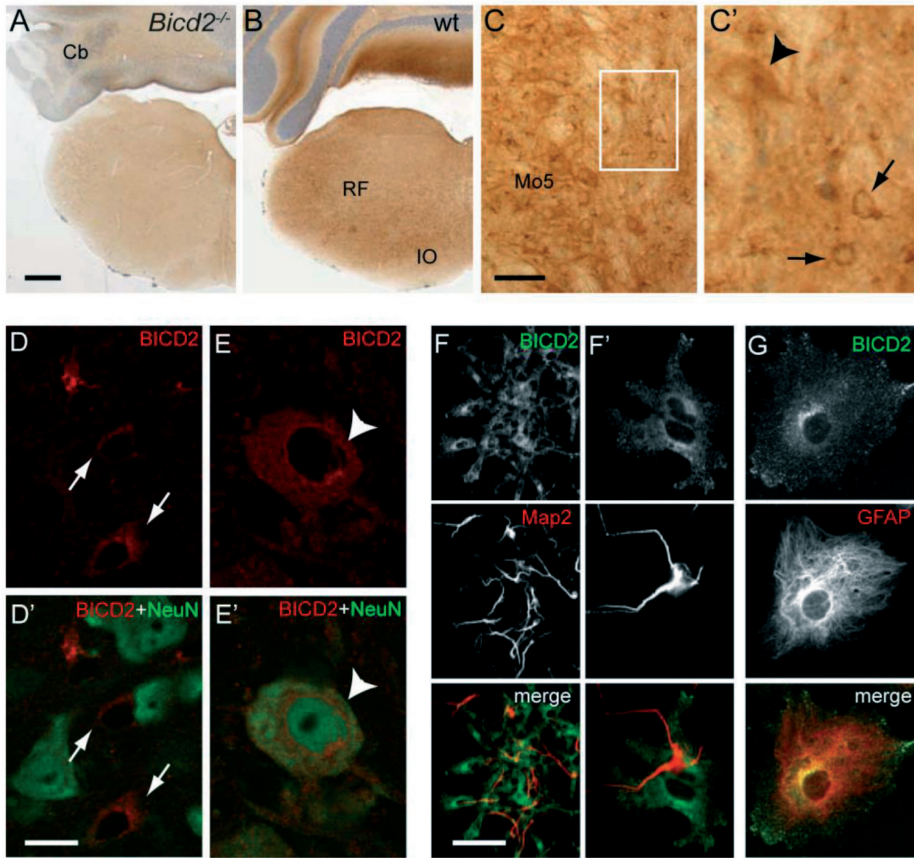
C- related to Figure 4C



**Supplementary Figure 5. Full size Western blots related to Figure 4A-C**

**A)** Western blot with BICD2 antibody (#2294) showing reduced and no expression of BICD2 in tissue homogenates of P20 heterozygote *Bicd2*<sup>+/-</sup> (+/-) and homozygote *Bicd2*<sup>-/-</sup> (-/-) mice, respectively. **B)** Western blot showing relatively high BICD2 expression in developing nervous system. **C)** Comparative Western blot analysis using BICD1 (antibody #2295 for BICD1 and antibody #2293 for BICD1/2), dynein components and interacting proteins (dynein p150, dynein intermediate chain 74, Lis1) and Rab6 expression in *Bicd2*<sup>-/-</sup> cortex and cerebellum. M = marker. Selected parts of the Western blots (indicated in white boxes) can be found in Figure 4.





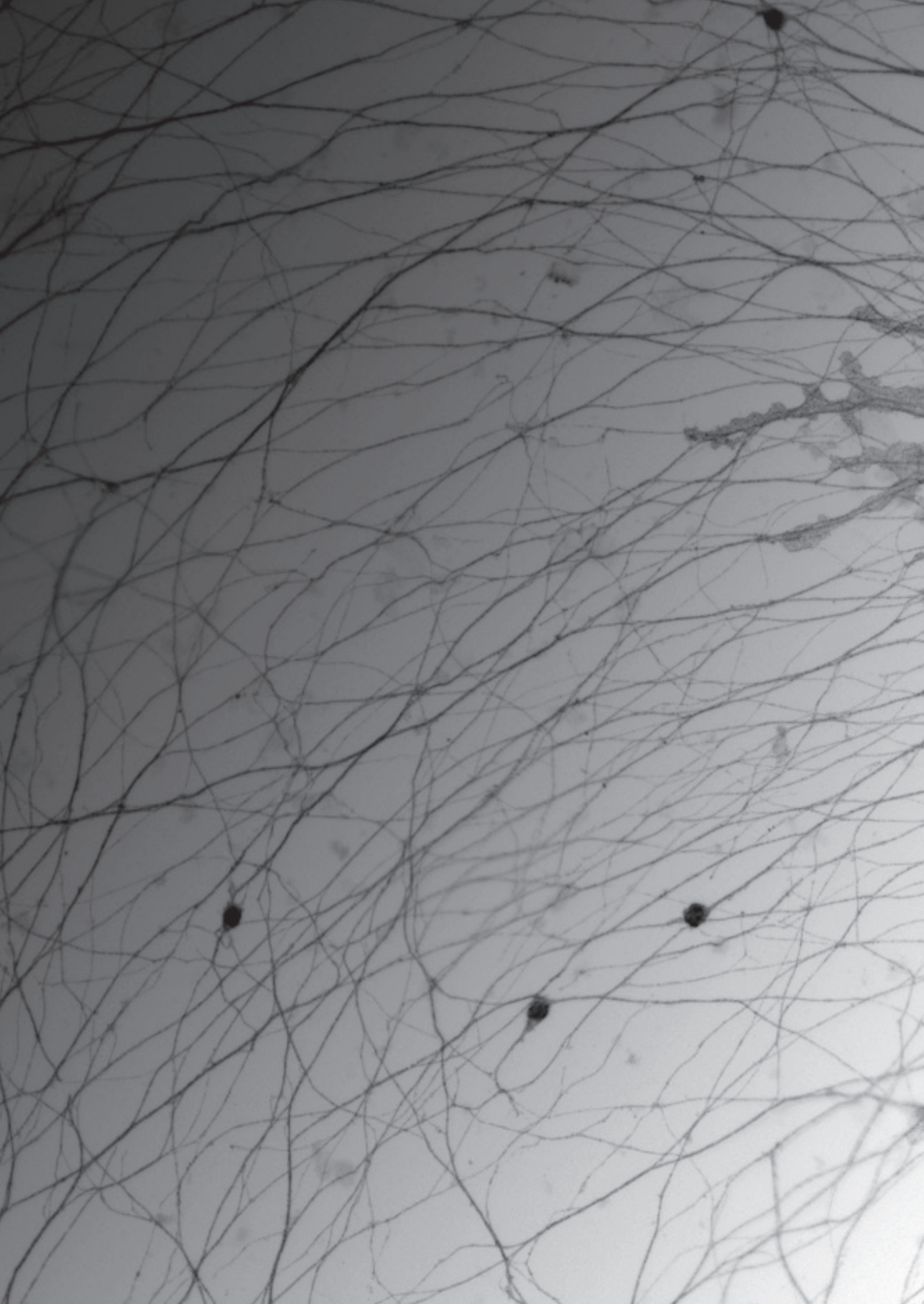
**Supplementary Figure 6. BICD2-immunoreactivity in glia and large neurons**

**A, B**) Immunohistochemistry with anti-BICD2 antibody in coronal sections of the caudal brain stem of P20 mice showing the absence of staining in *Bicd2*<sup>-/-</sup> mice and ubiquitous staining in wild-type brain stem and cerebellum. RF, reticular formation; IO, inferior olive. **C**) Anti-BICD2 staining in the trigeminal motor nucleus (Mo5) and adjacent reticular formation, showing increased staining levels in motor neurons (arrow head) and glial cells (arrows). **D, E**) Double-labeling confocal immunofluorescence (optical sections 1 μm) of BICD2 and NeuN showing the lower BICD2 staining intensities in neurons (NeuN+ in **D**) as compared to surrounding glia (NeuN- in **D**). Some neurons such as large neurons in the reticular formation (arrow head in **E**), however showed higher BICD2 staining levels. **F, G**) Double-labeling of BICD2 with MAP2 (**F**) or GFAP (**G**), respectively in primary neuron-astrocyte cerebellar co-cultures, indicates the absence of BICD2 in Map2+ cells and a fine punctate distribution of BICD2 in GFAP+ cells. Scale bars: 500 μm (**A**), 200 μm (**C**), 20 μm (**D-F**).

## Supplementary methods

### Antibodies used in this study

Antibody	company	name/number	concentration
rabbit anti-BICD2	homemade (REF 4)	#2294	1:500
mouse anti-calbindin	Sigma	clone CB-955	1:100000
rabbit anti-calbindin	Swant	CB-38a	1:100000
guinea pig anti EAAT2	Millipore	AB1738	1:5000
goat anti-FoxP2	Abcam	Ab1307	1:1000
rabbit anti- $\alpha$ 6GABAA receptor	Sigma	G 5544	1:1000
rabbit anti-GFAP	DAKO	Z0334	1:5000
mouse anti-GFAP	Sigma	clone G-A-5	1:10000
mouse anti-mGluR2	Abcam	AB 15672	1:1000
mouse anti-NeuN	Millipore	MAB377	1:1000
mouse anti-neurofilament-M	Sigma	clone RM044	1:10000
mouse anti-parvalbumin	Swant	Mab 235	1:10000
mouse anti-Rab6	homemade (REF 7)	mRab6	1:400
rabbit anti-Tenascin-C	Gene Tex	GTX62552	1:400
guinea pig anti-VGluT1	Millipore	AB5905	1:2000
guinea pig anti-VGluT2	Millipore	AB2251	1:2000
mouse-anti-MAP2	Sigma	clone HM-2	1:2000
Cy5-donkey anti-guinea pig IgG	Jackson Immunoresearch	706-175-148	1:400
Alexa Fluor488-donkey anti-goat IgG	Jackson Immunoresearch	705-545-147	1:400
Cy3-donkey anti-goat IgG	Jackson Immunoresearch	705-165-147	1:400
Cy3-donkey anti-mouse IgG	Jackson Immunoresearch	715-165-151	1:400
FITC-donkey anti-mouse IgG	Jackson Immunoresearch	715-095-151	1:400
Alexa Fluor488donkey anti-mouse IgG	Jackson Immunoresearch	715-545-150	1:400
FITC-donkey anti-rabbit IgG	Jackson Immunoresearch	711-095-152	1:400
Alexa Fluor488donkey anti-rabbit IgG	Jackson Immunoresearch	711-545-152	1:400
Cy3 donkey anti-rabbit IgG	Jackson Immunoresearch	711-165-152	1:400
Cy5 donkey anti-rabbit IgG	Jackson Immunoresearch	711-175-152	1:400





---

# Chapter 7

## Genome-wide microRNA profiling of human temporal lobe epilepsy identifies modulators of the immune response

---

Anne A. Kan<sup>1,\*</sup>, Susan van Erp<sup>1,\*</sup>, Alwin A.H.A. Derijck<sup>1</sup>, Marina de Wit<sup>1</sup>, Ellen V.S. Hessel<sup>1</sup>, Eoghan O'Duibhir<sup>1</sup>, Wilco de Jager<sup>2</sup>, Peter C. van Rijen<sup>3</sup>, Peter H. Gosselaar<sup>3</sup>, Pierre N.E. de Graan<sup>1</sup>, R. Jeroen Pasterkamp<sup>1</sup>.

1 Department of Neuroscience and Pharmacology, University Medical Center Utrecht, Universiteitsweg 100, 3584 CG, Utrecht, The Netherlands

2 Department of Pediatric Immunology, University Medical Center Utrecht, Universiteitsweg 100, 3584 CG, Utrecht, The Netherlands

3 Department of Neurology and Neurosurgery, University Medical Center Utrecht, Universiteitsweg 100, 3584 CG, Utrecht, The Netherlands

\* These authors contributed equally

*Cellular and Molecular Life Sciences*, 2012; 69(18):3127-45

## Genome-wide microRNA profiling of human temporal lobe epilepsy identifies modulators of the immune response

Anne A. Kan · Susan van Erp · Alwin A. H. A. Derijck · Marina de Wit · Ellen V. S. Hessel · Eoghan O'Duibhir · Wilco de Jager · Peter C. Van Rijen · Peter H. Gosselaar · Pierre N. E. de Graan · R. Jeroen Pasterkamp

Received: 1 February 2012/Revised: 22 March 2012/Accepted: 2 April 2012  
© The Author(s) 2012. This article is published with open access at Springerlink.com

**Abstract** Mesial temporal lobe epilepsy (mTLE) is a chronic neurological disorder characterized by recurrent seizures. The pathogenic mechanisms underlying mTLE may involve defects in the post-transcriptional regulation of gene expression. MicroRNAs (miRNAs) are non-coding RNAs that control the expression of genes at the post-transcriptional level. Here, we performed a genome-wide miRNA profiling study to examine whether miRNA-mediated mechanisms are affected in human mTLE. miRNA profiles of the hippocampus of autopsy control patients and two mTLE patient groups were compared. This revealed segregated miRNA signatures for the three different patient groups and 165 miRNAs with up- or down-regulated

expression in mTLE. miRNA in situ hybridization detected cell type-specific changes in miRNA expression and an abnormal nuclear localization of select miRNAs in neurons and glial cells of mTLE patients. Of several cellular processes implicated in mTLE, the immune response was most prominently targeted by deregulated miRNAs. Enhanced expression of inflammatory mediators was paralleled by a reduction in miRNAs that were found to target the 3'-untranslated regions of these genes in reporter assays. miR-221 and miR-222 were shown to regulate endogenous ICAM1 expression and were selectively co-expressed with ICAM1 in astrocytes in mTLE patients. Our findings suggest that miRNA changes in mTLE affect the expression of immunomodulatory proteins thereby further facilitating the immune response. This mechanism may have broad implications given the central role of astrocytes and the immune system in human neurological disease. Overall, this work extends the current concepts of human mTLE pathogenesis to the level of miRNA-mediated gene regulation.

A. A. Kan and S. van Erp contributed equally to this work.

**Electronic supplementary material** The online version of this article (doi:10.1007/s00018-012-0992-7) contains supplementary material, which is available to authorized users.

A. A. Kan · S. van Erp · A. A. H. A. Derijck · M. de Wit · E. V. S. Hessel · E. O'Duibhir · P. N. E. de Graan · R. J. Pasterkamp (✉)  
Department of Neuroscience and Pharmacology, University Medical Center Utrecht, Universiteitsweg 100, 3584 CG, Utrecht, The Netherlands  
e-mail: r.j.pasterkamp@umcutrecht.nl

P. N. E. de Graan  
e-mail: p.n.degraan@umcutrecht.nl

W. de Jager  
Department of Pediatric Immunology,  
University Medical Center Utrecht, Universiteitsweg 100,  
3584 CG, Utrecht, The Netherlands

P. C. Van Rijen · P. H. Gosselaar  
Department of Neurology and Neurosurgery,  
University Medical Center Utrecht, Universiteitsweg 100,  
3584 CG, Utrecht, The Netherlands

**Keywords** Mesial temporal lobe epilepsy · Nuclear localization · Immune regulation · Immune system · MicroRNA · RNA profiling · Temporal lobe epilepsy

### Introduction

Temporal lobe epilepsy (TLE) is a neurological condition characterized by recurrent seizures that originate from the temporal lobe. TLE accounts for one-third of all patients with epilepsy [1] and can be divided into several subgroups including mesial TLE (mTLE). mTLE is associated with characteristic pathological features and about 30 % of

mTLE patients are pharmaco-resistant [2]. The pathological mechanisms underlying mTLE are poorly understood. Recent studies show that patterns of gene expression are significantly altered in experimental and human mTLE [3–7]. Thus, the regulatory mechanisms that normally control gene expression may be affected. For example, it was recently shown that transcriptional repressors play a key role in acquired HCN1 channelopathy [8]. Insight into how regulation of gene expression is altered may provide important new insights into mTLE pathogenesis and could yield novel therapeutic targets.

During the past several years, microRNAs (miRNAs) have emerged as important post-transcriptional regulators of gene expression, providing a completely new level of control of gene expression. miRNAs are short (20–23 nucleotides), non-coding RNAs that recognize partially complementary target sequences in select mRNAs and predominantly inhibit protein expression by either destabilizing their mRNA targets or by inhibiting protein translation [9–13]. miRNA-mediated mechanisms have been shown to contribute to the regulation of brain development and homeostasis [11, 14] and can be affected in neural diseases such as multiple sclerosis [15–17].

Recent animal studies support the hypothesis that miRNAs may contribute to the pathogenesis of epilepsy [18–21]. To systematically assess the role of miRNAs in human mTLE, we conducted the first genome-wide miRNA expression profiling study of human mTLE patients. The observed microRNA signatures led us to (1) unveil a marked aberrant expression and nuclear localization for miRNAs in mTLE patients, and (2) identify components of the immune response as targets of the most strongly regulated miRNAs in mTLE.

## Materials and methods

### Patient selection and tissue collection

Hippocampal tissue samples of pharmaco-resistant mTLE patients were obtained after surgery at the University Medical Centre Utrecht. Patients were selected for surgery according to the criteria of the Dutch Epilepsy Surgery Program [22]. The excision was based on clinical evaluations, interictal and ictal EEG studies, MRI and intraoperative electrocorticography. Informed consent was obtained from all patients for all procedures approved by the Institutional Review Board. Immediately after en bloc resection of the hippocampus, the tissue was cooled in physiological saline (4 °C) and cut on a precooled plate into three slices perpendicular to its longitudinal axis. The two outer parts were used for pathological analysis. In the operating room, the middle section was divided into a part

that was immediately frozen on powdered dry ice and a part that was immersion-fixed in 4 % paraformaldehyde in 0.1 M phosphate buffer for 24 h at 4 °C. Following fixation, tissue was embedded in paraffin and stored at 4 °C. Frozen samples were stored at –80 °C. Frozen and paraffin-embedded control hippocampal tissue samples were obtained from postmortem cases without hippocampal aberrations from the Netherlands Brain Bank (www.brainbank.nl). All control material was collected from donors with written informed consent for brain autopsy and the use of the material and clinical information for research purposes. Prior to dissection, brain pH was measured interventricularly using an 18-GA 3.50-in. spinal needle. Detailed histological examination of the hippocampal material from all patients used in this study showed that all samples were devoid of tumor tissue. All patient samples used in this study had RIN values >6 (range 6.4–8.4; mean 7.2) [23–25] confirming that all RNA samples were of excellent quality. Table 1 provides a summary of the clinical data of all patients included in the study. Hippocampal specimens were divided into three groups: a non-epileptic autopsy control group (control,  $n = 10$ ), a group of mTLE patients without signs of hippocampal sclerosis (mTLE–HS,  $n = 10$ ) and an mTLE group with hippocampal sclerosis (mTLE + HS,  $n = 10$ ). The severity of HS was determined by an experienced neuropathologist using the Wyler classification method [26] defining W0 as hippocampal tissue without HS and W4 as tissue with the most severe type of HS. Wyler classification was independently verified on paraffin-embedded tissue.

### RNA isolation and quality control

Nissl stained cryo-sections were generated to ensure that all anatomical regions were equally represented in each sample. For the purpose of RNA isolation, 25- $\mu$ m-thick cryo-sections were cut until approximately 20 mg of tissue was collected. This material was stored at –80 °C until all samples were collected. Then, all samples were thawed and processed in parallel in QIAzol lysis reagent to prevent RNA degradation. Total RNA was extracted using the miRNeasy kit (Qiagen) according to the manufacturer's protocol. RNA quality (RIN value; Table 1) was assessed using a RNA 6000 Nano chip on the 2100 Bioanalyzer (Agilent) and RNA quantity was determined using Nanodrop (Thermo Scientific).

### microRNA array

1,000 ng total RNA per patient sample and reference (pool of all samples) was labeled with Hy3<sup>TM</sup> and Hy5<sup>TM</sup> fluorescent labels, respectively, using the miRCURY<sup>TM</sup> LNA



**Table 1** Clinical data of mTLE and autopsy control patients

Patient group	Age (years)	Gender	Age of onset (years)	COD/pathology	PMD (h)	Brain pH	RIN values	AED's	Engel score
1) Control	50	F	–	Metastasized broncocarcinoma	4	6.98	6.9	–	–
2) Control	58	M	–	Unknown. ALS patient	7	6.46	6.4	–	–
3) Control	62	M	–	Unknown, non-demented control	7	6.36	6.4	–	–
4) Control	73	F	–	Subdural hematoma	6.5	n.d.	8.4	–	–
5) Control	71	M	–	Pancreas carcinoma	9	6.64	7.5	–	–
6) Control	64	F	–	Respiratory failure	4.5	6.45	8	–	–
7) Control	70	M	–	Sepsis with broncopneumonia	20.5	6.68	6.5	–	–
8) Control	94	F	–	CVA	4	6.68	6.8	–	–
9) Control	48	M	–	DMT I-induced organ failure	5.5	6.88	7.8	–	–
10) Control	74	M	–	Pulmonary carcinoma	8	6.87	7.9	–	–
Median	67	M6, F4	–	–	6.75	6.68	7.2	–	–
11) TLE–HS	45	M	18	W0, FCD type1 to 2A in cortex	–	–	8.1	LTG, PHT	I A
12) TLE–HS	46	F	16	W0, MCD type 1 in cortex	–	–	8.2	CBZ, VPA	I A
13) TLE–HS	46	M	33	W0, epilepsy after head trauma	–	–	7.1	CBZ, VPA, TPR	I A
14) TLE–HS	42	F	20	W0, DNT WHO grade I	–	–	8.3	CBZ, LTG, LEV	I A
15) TLE–HS	34	F	24	W0, cortical cavernoma	–	–	7.4	CBZ	I A
16) TLE–HS	40	F	17	W0, MCD type 1 in cortex	–	–	8	LEV, LTG, CBZ	I A
17) TLE–HS	43	F	10	W0, therapy-resistant epilepsy	–	–	8.1	PHT, LTG	I A
18) TLE–HS	47	M	16	W0, therapy-resistant epilepsy	–	–	8.6	CBZ, VPA, LTG, LEV	II A
19) TLE–HS	28	M	12	W0, therapy-resistant epilepsy	–	–	7.4	CBZ, TPR.	I A
20) TLE–HS	54	M	35	W0, ganglioglioma WHO grade I	–	–	8.2	OXC, LTG, CLO	I A
Median	44	M5, F5	17.5	–	–	–	8.1	–	–
21) TLE + HS	49	F	12	MTS W4	–	–	8	OXC, CLO	I A
22) TLE + HS	44	F	13	MTS W2	–	–	7.9	CBZ, OXC, CLO	I A
23) TLE + HS	41	M	1	MTS W4	–	–	8.1	CBZ	I A
24) TLE + HS	52	F	20	MTS W4	–	–	8.1	CBZ, CLO, DZP	I A
25) TLE + HS	50	M	2.5	MTS W4	–	–	8.6	CBZ, GBP	II A
26) TLE + HS	36	F	14	MTS W4	–	–	7.6	OXC, LZP	n.d.
27) TLE + HS	42	M	0.7	MTS W4	–	–	8.1	LEV, LTG	II A
28) TLE + HS	36	M	10	MTS W4	–	–	8.2	OXC, PGB	I A
29) TLE + HS	41	M	0.6	MTS W4	–	–	9.2	PHT, CLO, CBZ, LTG	I A
30) TLE + HS	42	F	8	MTS W4	–	–	9.1	LEV, LTG, PBT	I A
Median	42	M5, F5	9	–	–	–	8.1	–	–

*COD* cause of death, *PMD* postmortem delay, *RIN* RNA integrity number, *AED* anti-epileptic drug, *n.a.* not applicable, *CVA* cerebrovascular accident, *ALS* amyotrophic lateral sclerosis, *DMT I* diabetes mellitus type I, *W0–W4* Wyler score, *FCD* focal cortical dysplasia, *WHO grade* world health organization grading scale of malignancy, *LTG* lamotrigine, *PHT* phenytoin, *CBZ* carbamazepine, *VPA* valproinic acid, *TPR* topiramate, *LEV* levetiracetam, *OXC* oxcarbazepine, *CLO* clobazam, *DZP* diazepam, *GBP* gabapentin, *LZP* lorazepam, *PGB* pregabalin, *PBT* phenobarbital

Array power labeling kit (Exiqon) following procedures described by the manufacturer. Hy3<sup>TM</sup>-labeled samples and a Hy5<sup>TM</sup>-labeled reference RNA sample were mixed pairwise and hybridized to the miRCURY<sup>TM</sup> LNA Array version 5th Generation (Exiqon), which contains capture probes targeting all human (hsa) miRNAs registered in miRBASE version 15.0 at the Sanger Institute. The hybridization was performed according to the miRCURY<sup>TM</sup> LNA array manual using a Tecan HS4800 hybridization station (Tecan). After hybridization,

microarray slides were scanned and stored in an ozone free environment (ozone level below 2.0 ppb) in order to prevent bleaching of the fluorescent dyes. The miRCURY<sup>TM</sup> LNA array microarray slides were scanned using the Agilent G2565BA Microarray Scanner System (Agilent) and image analysis was carried out using ImaGene 8.0 software (BioDiscovery). The quantified signals were background corrected (Normexp with offset value 10) [27] and normalized using the global Lowess (LOcally WEighted Scatterplot Smoothing) regression algorithm.

The 130 miRNAs that passed the filtering criteria on variation across samples were submitted to a principal component analysis ( $SD > 0.50$ ) to identify general similarities and differences. Additionally, a univariate general linear model analysis was applied with age and gender as covariates using the top 30 changed miRNAs. This analysis did not result in loss of Bonferroni corrected significance for any of the groups (see Online Resource 2c) and nor did it result in significant  $p$  values for either age or gender ( $p > 0.05$ ). As pH and PMD are potential confounders only in autopsy control patients, we performed additional Pearson's correlations tests on the top 30 changed miRNAs against pH and PMD in this group. No significant correlations were detected for pH and PMD.

#### Quantitative PCR

Based on the array profiling data, miR-29a and miR-423-3p were identified as normalization miRNAs using Norm-Finder [28] showing minimal variation across all samples ( $SD = 0.17$ ). Total RNA from all control or nine mTLE + HS (Wyller 4, excluding patient #22) patients was pooled and used for first strand cDNA synthesis using a universal cDNA synthesis kit (Exiqon). Duplicate cDNAs were generated for each RNA pool. Quantitative PCR reactions were run on a 7900HT Real-Time PCR System (Applied Biosystems) using microRNA LNA<sup>TM</sup> PCR primer sets and SYBR Green master mix (Exiqon). All samples were run in duplicate and the base for exponential amplification was verified to be two by standard curve analysis for all primer sets.  $C_t$  values were determined using SDS software (Applied Biosystems) with manual baseline and threshold settings. Normalization and expression analysis based on the  $DC_t$  method was performed using Qbase version 1.3.5.

#### In situ hybridization

Non-radioactive in situ hybridization was performed on slides that contained three sections, one of each patient group. Per group, six of the ten patients used for the microarray study were analyzed. In situ hybridization and subsequent immunohistochemistry were performed on 7- $\mu$ m-thick paraffin sections as described previously [29]. Briefly, sections were deparaffinated, acetylated (10 min at RT) and treated with proteinase K (5  $\mu$ g/ml 5 min at RT). Prehybridization was performed for 1 h at RT. Hybridization was performed with 10–20 nM double-DIG (3' and 5')-labeled locked nucleic acid (LNA) probe for human miR-124, miR-20a, miR-92b, miR-193a-3p, miR-138, miR-221, miR-222, miR-635, miR-637, or miR-665 (Exiqon) for 2 h at 55 °C. The slides were washed in  $0.2 \times$  SSC for 1 h at 60 °C and blocked for 1 h with 10 % fetal calf

serum (FCS) in B1 (0.1 M Tris pH 7.5/0.15 M NaCl). Subsequently, slides were incubated with anti-digoxigenin-AP Fab fragments (1:2,500, Roche Diagnostics) in 10 % FCS in B1 overnight at 4 °C. The slides were reacted with 5-bromo-4-chloro-3-indolyl phosphate (BCIP) and nitro-blue tetrazolium (NBT) substrates (NBT/BCIP stock solution, Roche Diagnostics) in B3 (0.1 M Tris pH 9.5/0.1 M NaCl/50 mM  $MgCl_2$ ) for 6–20 h at RT. Staining was terminated by washing the slides in PBS. Slides were mounted in 90 % glycerol in PBS or further processed for immunohistochemistry. Sections stained in parallel with scrambled LNA-DIG probe, a commonly used control for miRNA-ISH [30], were devoid of staining.

#### Immunofluorescent double labeling

For double labeling, in situ hybridization was followed by immunohistochemistry. Briefly, slides were blocked for 1 h at RT in 1 % FCS in PBS/0.2 % TritonX100 before primary antibody was applied overnight at 4 °C. Anti-glial fibrillary acidic protein (GFAP) antibodies (1:6,000, Dako Cytomation, Glostrup, Denmark) were used to localize the astrocytic marker GFAP. Donkey-anti-rabbit Alexa 488 (Invitrogen, Molecular Probes, Oregon, USA) was used as secondary antibody. Sections incubated without primary antibody were devoid of signal. Finally, all slides were reacted with 4',6'-diamidino-2-phenylindole (DAPI) to fluorescently stain the nucleus. Images were taken using Axioscop 1 and Axiovert 2 microscopes (Carl Zeiss). Some images were pseudocolored using Photoshop CS2 (Adobe).

#### Target analysis of deregulated miRNAs

To identify mRNAs that are targeted by miRNAs deregulated in mTLE, a set of genes involved in glutamatergic and GABAergic transmission, immune response and  $K^+$ /water homeostasis was selected and the validated and predicted miRNA interactions of these genes were extracted from miRecords. The predictions were generated based on a minimal overlap of four prediction algorithms. The overlap between each miRNA interaction list and the 15 most up- and 15 most down-regulated miRNAs was determined by Venn analysis using a Web-based tool (<http://www.pangloss.com/seidel/Protocols/venn.cgi>).

#### Bead-based ELISA

Bead-based ELISA was performed to determine CCL3, CCL22, and ICAM1 protein levels [31, 32]. In brief, 20 mg of hippocampal tissue from the same ten patients in each of the three patient groups used for miRNA profiling was homogenized in lysis buffer (Lysis M, Roche), sonicated, centrifuged at  $4,500 \times g$ , filtered through a 0.22- $\mu$ m column

and frozen at 0.5 µl/µl. Bead-bound and capture antibodies for CCL3 (capture: mouse monoclonal, detection: goat polyclonal), CCL22 (capture: mouse monoclonal, detection: chicken polyclonal) and ICAM1 (capture: mouse monoclonal, detection: sheep polyclonal) were used in a 50-µl homogenate. All antibodies were purchased from R&D systems (Abington, United Kingdom).

#### Luciferase reporter assays

The psiCHECK<sup>TM</sup>-2 vector (Promega) was used as a reporter for testing the ability of individual miRNAs to inhibit protein expression. This vector contains the coding sequences of both firefly and Renilla luciferases. While the firefly luciferase gene is constitutively transcribed and used for normalization, the Renilla gene contains a multiple cloning site (MCS) in its 3' untranslated region (UTR) enabling the introduction of miRNA-binding sites. miRNA-binding sites predicted by at least three different algorithms in miRecords were cloned into the psiCHECK<sup>TM</sup>-2 vector. Oligonucleotides representing different predicted miRNA-binding sites (Table 2) were phosphorylated, annealed and cloned into the NotI and XhoI sites of the MCS. For reporter assays, HEK293 cells were seeded in 24-well plates ( $8 \times 10^4$  cells/well) and transfected with 250 ng reporter construct and 25 pmol miRIDIAN miRNA or non-targeting control mimic (cel-miR-67; both from Dharmacon) per well using Lipofectamine 2000 (Invitrogen). Cells were harvested 24 h after transfection for analysis of luciferase activity using the Dual-Luciferase Assay System (Promega) and a Wallac Victor Luminometer. Relative luciferase activities were obtained by normalizing Renilla luciferase activity to that of firefly luciferase.

#### Western-blot analysis

HeLa cells were transfected with 125 pmol miRIDIAN miRNA or non-targeting control mimic per well of a six-well plate using Lipofectamine 2000 (Invitrogen). At 48 h after transfection, cells were washed in ice-cold  $1 \times$  PBS and lysed in 150 µl of lysis buffer (20 mM Tris pH 8, 150 mM KCl, 1 % Triton) supplemented with protease inhibitors (Complete; Roche) per well. Cell lysates were separated on a gradient NuPAGE (7–12 %) polyacrylamide gel (Invitrogen) and transferred to nitrocellulose blots. Blots were blocked overnight in 5 % non-fat milk powder in TBS-Tween. Next, the blots were incubated with primary antibodies in TBS-Tween for 1 h at RT [(mouse anti- $\alpha$ -tubulin (T-5168, 1:5,000, Sigma-Aldrich) and mouse anti-ICAM1 (sc-8439, 1:1,000, Santa Cruz)]. Following secondary antibody incubation, antibody binding was visualized using a chemiluminescence reagent kit (SuperSignal West Dura; Thermo Scientific) and quantified using ImageJ software. For each lane, the intensity of the  $\alpha$ -tubulin band was used to normalize the ICAM1 signal. All relative ICAM1 intensities were compared to that of control transfected cells.

## Results

#### Genome-wide microRNA expression profiling in human mTLE

We determined genome-wide miRNA expression profiles in hippocampal tissue from mTLE patients without (mTLE–HS) or with hippocampal sclerosis (mTLE + HS), and in

**Table 2** Target Oligonucleotides for microRNA-binding sites

	Forward	Reverse
<b>ICAM1</b>		
miR-635	tcgagGAGTGCCAGGGAATATGCCCAAGCTAgc	ggccgcTAGCTTGGGCATATTCCTGGGCACTCc
miR-637_1	tcgagCATTGGCCAACCTGCCTTTCCCAAGAGgc	ggccgcCTTCTGGGAAAGGCAGGTTGGCCAATGc
miR-637_2	tcgagGGTCTCTGGCCTCACGGAGCTCCAGTCTTgc	ggccgcAGGACTGGGAGCTCCGTGAGGCCAGAGACCCc
miR-221&222	tcgagGAAGTGGCCCTCCATAGACATGTGTAGCATCAAAACgc	ggccgcGTTTGTATGTACTACATGTCTATGGAGGGCCACTTCc
<b>CCL22</b>		
miR-625	tcgagTGGGATTTGGGGTTTTCTCCCCAgc	ggccgcTGGGGGAGAAAACCCCAATCCCAc
miR-620	tcgagAACTCTGCAATCCCTGATCTCCATCCgc	ggccgcGGATGGAGATCAGGGAATGCAGAGAGTTc
miR-665	tcgagAGGCTGGTCTCAAACCTCTGGGCTCAAGCGATCCCTCGGCTCgc	ggccgcGAGCCAGGAGGATCGTTGAGCCAGGAGTTTGTAGACCAGCCTc
miR-635	tcgagCAAGGCAATTGCTCGCCCAAGCAGgc	ggccgcCTGCTTGGGCGAGCAATGCCTTGc
<b>CCL3</b>		
miR-622	tcgagTGGCACCAAGCCACCAGACTGACAgc	ggccgcTGTCAGTCTGGTGGCTTTGGTGCCAc

Table shows primers used to clone predicted miRNA-binding sites into the psiCheck-2 vector. Sequences are derived from the 3'UTR of *Ccl3*, *Ccl22* and *Icam1* in addition to NotI and XhoI restriction sites (indicated in *lower case*). The strongest miRNA-binding sites predicted by at least three different algorithms were tested

autopsy control patients (Table 1), an experimental design which has been used previously [33–36]. The miRNA expression data were subjected to unbiased clustering by samples and miRNAs, and 130 miRNAs passed the filtering criteria on variation across samples (Online Resource 2a). A principle component analysis (PCA) of these miRNAs showed that miRNA expression patterns of individuals within each patient group were similar, but that profiles between groups differed. One mTLE + HS patient (Table 1; number 22) appeared to cluster with the mTLE–HS (W0) group. Indeed, neuropathological reassessment of this patient revealed only mild hippocampal sclerosis (W2 diagnosis).

Analysis of changes in the expression of individual miRNAs identified 165 miRNAs with  $p$  values lower than  $3.92 \times 10^{-05}$  (Bonferroni corrected). Fifty-one of these miRNAs showed a fold change of  $>2.0$  (Table 3) and were used in a two-way hierarchical clustering (Fig. 1b). This analysis revealed different patterns of expression (Fig. 2a). One set of miRNAs showed increased expression in the mTLE + HS group as compared to control and mTLE–HS (e.g., miR-193a-3p, miR-92b). Another set contained miRNAs with decreased expression in the TLE + HS group only (e.g., miR-184, miR-138). Interestingly, miR-221 and miR-222, which are derived from a common polycistronic precursor, were also down-regulated in mTLE + HS patients (fold change = 1.9). As expected, linear regression analysis revealed strong co-regulation of these two clustered miRNAs in our data ( $R^2 = 0.976$ ), supporting the validity of the microarray. A third group contained miRNAs with decreased expression in both mTLE groups (e.g., miR-637, miR-665, miR-642). Analysis of miRNAs displaying significant but less prominent fold changes revealed additional patterns of expression changes, e.g., up- or down-regulated expression in mTLE–HS patients as compared to control and mTLE + HS (e.g., miR-890). Furthermore, the expression of a large set of miRNAs was similar in all three patient groups (e.g., miR-191 and miR-130b) (Fig. 2a).

To confirm the expression changes in the microarray data, 11 miRNAs were assayed by qPCR. Candidates showed significant differences between autopsy control and mTLE + HS patients and a fold change of  $>2$  (miR-221/222 were selected because of their genomic organization and hippocampal enrichment). QPCR reactions (excluding patient #22 from the mTLE + HS group) for the selected miRNAs yielded expression changes to those obtained by microarray analysis (Fig. 2b).

#### Differential miRNA expression in human mTLE

The specific distribution of several regulated miRNAs (identified in the microarray) in the control human

**Table 3** Strongly regulated microRNAs in mTLE

miRNA	mTLE–HS vs. control ( $\Delta$ LMR)	mTLE + HS vs. control ( $\Delta$ LMR)
let-7f	0.33	1.05
miR-9	0.52	1.06
miR-16	0.47	1.1
miR-17	0.44	1.07
miR-20a	0.45	1.51
miR-26b	0.21	1.18
miR-27a	0.34	1.34
miR-32	0.51	1.88
miR-32*	–0.7	–1.17
miR-92b	0.06	1.1
miR-99a	0.34	1.03
miR-106a	0.43	1.02
miR-126*	0.45	1.45
miR-129-3p	0.79	1.35
miR-135a	0.2	1.4
miR-138	0.22	–0.85
miR-141*	–1.05	–1.22
miR-146b-3p	–0.88	–1.16
miR-184	0.14	–1.24
miR-185*	–0.97	–1.49
miR-190	0.65	1.62
miR-193a-3p	0.3	1.53
miR-195	0.21	1.08
miR-203	0.81	1.06
miR-214	–1.08	–0.96
miR-220c	–1.16	–1.49
miR-301a	0.29	1.13
miR-340*	0.43	1.09
miR-362-3p	0.44	1.23
miR-374a	0.44	1.66
miR-374b	0.3	1.01
miR-490-3p	–0.81	–1.16
miR-597	0.94	1.14
miR-625	0.46	1.02
miR-635	–0.93	–1.22
miR-637	–1.83	–2.53
miR-642	–1.03	–1.54
miR-660	0.28	1.09
miR-665	–1.87	–2.38
miR-920	–0.73	–1
miR-934	–1.05	–1.27
miRPlus-F1021	–0.98	–1.31
miRPlus-E1026	–1.62	–1.96
miRPlus-E1185	–0.61	–1.05
miRPlus-E1212	–0.68	–1.08
miRPlus-E1232	–0.69	–1.09

**Table 3** continued

miRNA	mTLE-HS vs. control (ΔLMR)	mTLE + HS vs. control (ΔLMR)
miR-1255a	-1.04	-1.37
miR-1297	0.4	1.73
miR-1304	-1.13	-1.43
miR-1469	-1.32	-2.05
miR-1973	-0.2	-1.09

Those miRNAs are listed, which were at least two-fold and significantly regulated ( $p < 3.92 \times 10^{-05}$ ) in mTLE-HS and/or mTLE + HS in comparison to control ΔLMR difference in means of the  $\log^2$  median ratios

hippocampus (Online Resource 1) prompted us to examine which cells contribute to the mTLE-associated changes in miRNA levels. Using miRNA-ISH, we compared the hippocampal localization of several strongly regulated miRNAs between all patient groups. Changes in hippocampal miRNA expression in autopsy controls, mTLE-HS and mTLE + HS patients are documented in Fig. 3 for two representative miRNAs [miR-138 (down-regulation) and miR-92b (up-regulation)]. The first change observed was a reduction in miRNA expression in the CA1, CA3, and CA4 subfields (observed for miR-124, miR-92b, miR-138) (Fig. 3a, b) in mTLE + HS patients. Moreover, in mTLE + HS patients expression of the selected miRNAs in the DG was diffuse as a result of granule cell dispersion (Fig. 3b).

Another prominent expression change was an increase in miRNA expression in small-sized cells in gliotic regions of the mTLE + HS hippocampus (CA1 and CA4; observed for miR-92b, miR-637, miR-665) (Fig. 3). To characterize these cells, miRNA-ISH was combined with immunohistochemistry for GFAP, an astrocyte marker. As expected, many of the small-sized cells expressing miR-92b, miR-637, or miR-665 in the CA1 and CA4 regions of mTLE + HS, and also mTLE-HS, patients were GFAP-positive (Fig. 4). In addition, small-sized GFAP-negative cells, possibly representing microglia, expressed the miRNAs.

**Abnormal nuclear distribution of miRNAs in neurons and astrocytes in mTLE**

Most miRNAs localize and function in the cytoplasm. Analysis of miRNA expression patterns in autopsy controls confirmed localization of miR-92b, miR-637, and miR-665 in the cytoplasm of neurons (Fig. 5a, b). In striking contrast, in mTLE patients their expression was prominent in the nucleus (shown by the co-localization with nuclear DAPI signals) in addition to cytoplasmic labeling. Nuclear

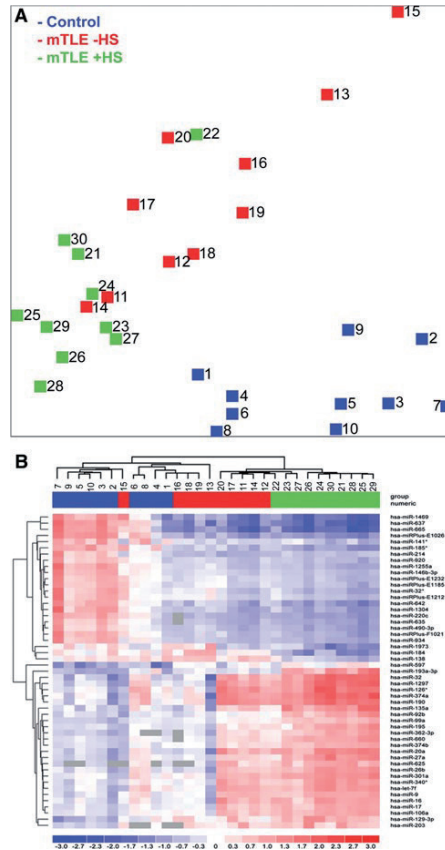


**Fig. 1** miRNA expression profiling in human mTLE. miRNA expression profiles were determined in hippocampal tissue of autopsy control (blue) and mTLE patients without (-HS; red) and with (+HS; green) hippocampal sclerosis using LNA-based microarray technology. **a** Principle component analysis (PCA) of the microarray data. Clustering of the samples using 130 miRNAs with the highest degree of variance (Table S1A: Sheet Exp. matrix (unsupervised), labeled in green). The PCA shows that individuals within a patient group cluster together, whereas the three groups segregate. **b** A heat map of 51 statistically significant miRNAs with a fold change of >2.0 depicted as a two-way hierarchical cluster (Table S1B: Sheet Exp. matrix (TTEST), labeled in green). Blue denotes down-regulated expression and red up-regulated expression compared to the mean. Gray boxes indicate probes without signal. Numbers 1–30 in **a** and **b** depict individual patients (Table 1)

signals for miR-92b, miR-637, and miR-665 were also observed in GFAP-positive astrocytes in mTLE patients (Fig. 4a–c). The atypical nuclear staining was observed in



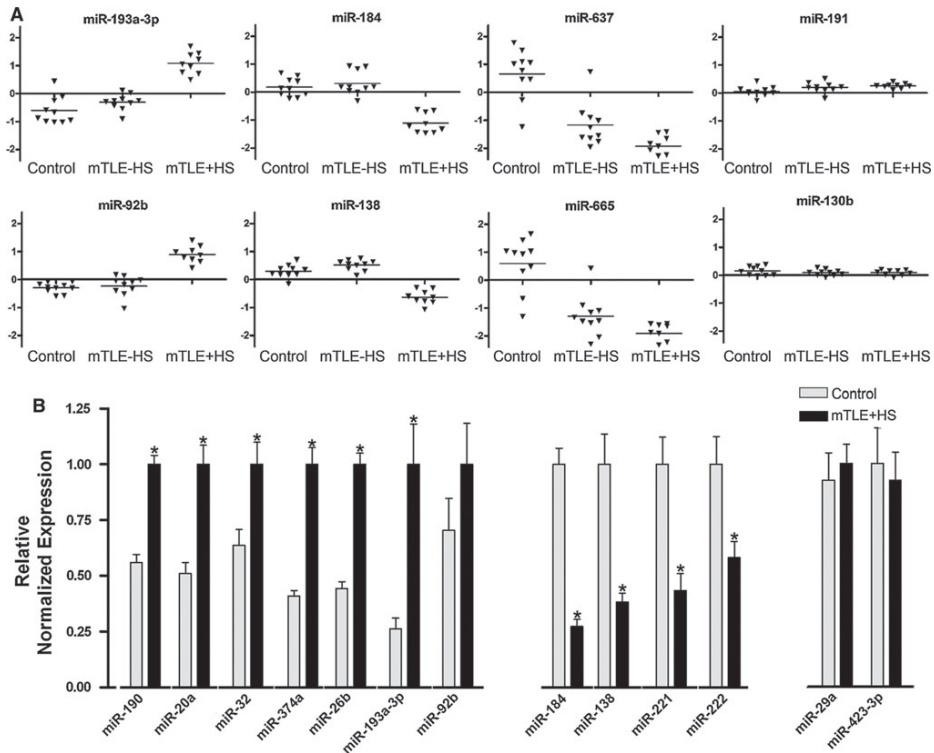


**Fig. 2** Differential expression of miRNAs in human mTLE. **a** Scatter plots of  $\log^2$  Hy3/Hy5 ratios of representative miRNAs showing different expression profiles. Triangles represent individual patients. Gray horizontal bars indicate group means. miRNAs-193a-3p and 92b are up-regulated in mTLE + HS, and miR-184 and miR-138 are down-regulated in mTLE + HS. miR-637 and miR-665 are down-regulated in both mTLE patient groups. Several miRNAs

including miR-191 and miR-130b do not show differential regulation between the three patient groups. **b** Validation of the microarray data by quantitative PCR (qPCR) on 11 candidate miRNAs in pooled patient samples (autopsy control and mTLE + HS). Graphs represent relative normalized expression with SEM. miR-29a and miR-423-3p served as normalization miRNAs. Significant change  $*p < 0.05$

all mTLE patients, but in none of the autopsy controls. In contrast, the signal for miR-138 and for several other miRNAs (not shown) was confined to the cytoplasm in mTLE patients (Fig. 5a, b).

The immune response as a target of miRNAs in mTLE

A single miRNA can regulate multiple different mRNAs and a single mRNA can be regulated by several miRNAs. Therefore, the mTLE-associated changes in miRNA expression and subcellular distribution observed in this study may have profound effects on biological functions. To study the biological significance of the most robust

miRNA expression, we focused on genes and processes with firmly established roles in mTLE, i.e., glutamatergic/GABAergic transmission, the immune response, and glial  $K^+$  and water homeostasis (Table 4) [5, 37, 38]. The predicted miRNA interactions of the selected genes were extracted from miRecords (Online Resource 3) and compared to the 30 most regulated miRNAs (15 up- and 15 down-regulated; Online Resource 2). Many of the selected genes contained predicted binding sites for miRNAs regulated in mTLE. For several genes, more than 10 % of the total set of miRNAs predicted to target the gene were deregulated in mTLE. The most prominently targeted mRNAs were found in the immune response group. For

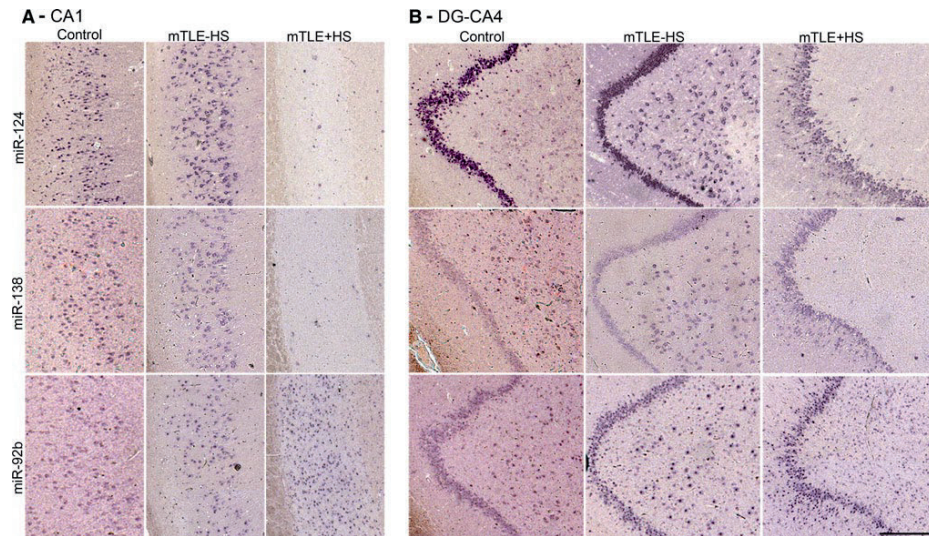


**Fig. 3** Changes in miRNA distribution in human mTLE. The spatial distribution of selected miRNAs across the three patient groups was determined by miRNA-ISH on consecutive hippocampal paraffin sections. Expression patterns (**a** CA1 subfield; **b** DG and CA4) are shown for three miRNAs in one subject per patient group (autopsy control, mTLE-HS and mTLE + HS). miR-138 and miR-92b were selected as examples of distinct expression pattern changes (up- and

down-regulation). miR-124 served as a neuronal marker and technical control. Expression of miR-124 and miR-138 in neurons is almost completely lost in the CA1 and CA4 regions in mTLE + HS patients. In contrast, miR-92b expression is increased in small-sized cells in both CA1 and CA4 in mTLE + HS. Also note the granule cell dispersion that is characteristic of mTLE + HS in **b**. 1–4, cornu ammonis (CA) subfields 1–4; DG, dentate gyrus. Scale bar 200  $\mu$ m

example, 50, 31, and 14 % of miRNAs predicted to target CCL3, ICAM1 and CCL22, respectively, were deregulated in mTLE (Table 4). This is intriguing as immune cells and their inflammatory mediators play an important role in the pathophysiology of seizures and epilepsy [38].

If miRNAs are important for modulating the immune response in mTLE, changes in miRNA expression are expected to induce reciprocal changes in the expression of immune proteins. Indeed, multiplex immunoassays (in the same patient samples used for miRNA profiling) revealed an up-regulation of CCL3 and CCL22 in both mTLE groups and a specific up-regulation of ICAM1 in mTLE + HS patients (Fig. 6a–c). Having identified (1) increased expression for CCL3, CCL22, and ICAM1, and (2) several down-regulated miRNAs that may target these cues in the same tissue (Table 4), we tested these miRNAs for their targeting of the 3'UTR of CCL3, CCL22, and ICAM1. One or more strong binding sites were examined for each miRNA in luciferase assays (Table 2), excluding miRNAs with inconsistent or low array signals (Fig. 6d–f). miR-622 did not target the 3'UTR of CCL3 (Fig. 6g). In contrast, miR-597, miR-620, miR-625, miR-665 targeted

CCL2. ICAM1 was a target for miR-221, miR222, and miR-635 (Fig. 6h, i).

The potential regulation of ICAM1 by miRNAs is intriguing as ICAM1 protein, but not mRNA, levels are changed in human mTLE, hinting at changes at the post-transcriptional level (Fig. 6c) [3, 39]. Therefore, we tested the effect of miRNAs on endogenous ICAM1 expression. Transfection of miR-221 and miR-222 mimics into HeLa cells strongly suppressed endogenous ICAM1 expression (Fig. 6j). A smaller but non-significant effect was observed for miR-635 and miR637.

Increased expression of ICAM1 is associated with different cell types in neural disorders including epilepsy [39–42]. Immunohistochemistry for ICAM1 in our mTLE patient material revealed enhanced ICAM1 expression in blood vessels and GFAP-positive astrocytes in the mTLE + HS hippocampus (Fig. 6k). This is reminiscent of recent observations in an experimental model of mTLE [42]. Microarray and qPCR experiments show that expression of miR-221 and miR-222 is down-regulated in mTLE + HS (Figs. 2b; 7a, b). In line with these data, we found that in mTLE + HS miR-221 and miR-222

**Fig. 4** Expression of microRNAs in GFAP-positive astrocytes in mTLE. To characterize the small-sized cells expressing miR-92b, miR-637 and miR-665 in the hippocampus of mTLE patients, miRNA-ISH was combined with immunohistochemistry for glial fibrillary acidic protein (GFAP) on hippocampal sections of mTLE-HS and mTLE + HS patients. The miRNA-ISH signal is pseudocolored in *green*, nuclear DAPI staining in *blue* and GFAP labeling in *red*. The lower part of each panel shows images of individual astrocytes at a higher magnification. In mTLE, but not control (not shown), patients miR-92b (a, b), miR-637 (c, d) and miR-665 (e, f) expression is predominantly localized to the nucleus of GFAP-positive astrocytes. Scale bar 40  $\mu$ m

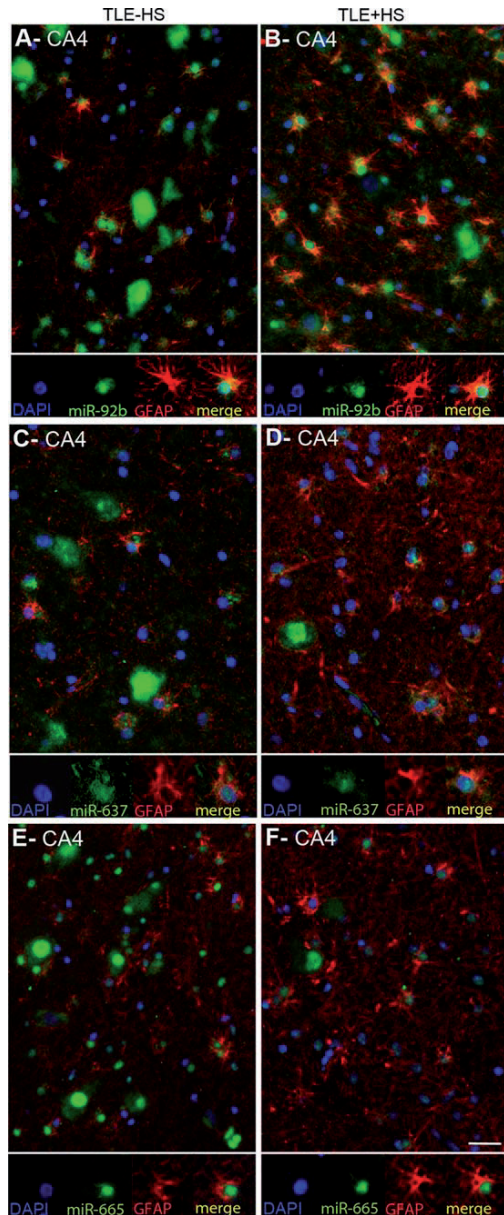


**Table 4** Deregulated miRNA target components of key pathways in mTLE

Protein name	Gene name	No predicted miRNAs	mTLE-regulated miRNAs	
			No	Name
<b>Glutamate transmission</b>				
GLUA1	<i>GRIA1</i>	7	0	
GLUA2	<i>GRIA2</i>	48	1	miR-203,
GLUA3	<i>GRIA3</i>	47	3	miR-32, miR-92b, miR-203
GLUA4	<i>GRIA4</i>	65	3	miR-26b, miR-27a, miR-625
NR1	<i>GRIN1</i>	31	3	miR-16, miR-195, miR-214
NR2A	<i>GRIN2A</i>	22	1	miR-597
NR2B	<i>GRIN2B</i>	16	2	miR-625, miR-642
NR2C	<i>GRIN2C</i>	1	0	
NR2D	<i>GRIN2D</i>	1	0	
mGLUR1	<i>GRM1</i>	46	4	miR-139-5p, miR-490-3p, miR-497, miR-642
mGLUR5	<i>GRM5</i>	21	0	
VGLUT1	<i>SLC17A7</i>	25	5	miR-17, miR-20a, miR-138, miR-620, miR-622
EAAT1	<i>SLC1A3</i>	31	2	miR-490-3p, miR-625
EAAT2	<i>SLC1A2</i>	167	17	miR-16, miR-17, miR-20a, miR-27a, miR-139-5p, miR-195, miR-203, miR-214, miR-221, miR-497, miR-620, miR-625, miR-635, miR-642, miR-660, miR-665, miR-934
EAAT3	<i>SLC1A1</i>	36	5	miR-9, miR-26b, miR-374a, miR-374b, miR-620
GS	<i>GLUL</i>	36	1	miR-625
PAG	<i>GLS</i>	37	1	miR-660
<b>GABA transmission</b>				
GABA <sub>A</sub> R $\alpha$ 1	<i>GABRA1</i>	48	7	miR-16, miR-129-3p, miR-139-5p, miR-195, miR-203, miR-221, miR-222
GABA <sub>A</sub> R $\alpha$ 2	<i>GABRA2</i>	5	0	
GABA <sub>A</sub> R $\alpha$ 3	<i>GABRA3</i>	0	0	
GABA <sub>A</sub> R $\alpha$ 4	<i>GABRA4</i>	121	6	miR-26b, miR-203, miR-374b, miR-620, miR-642, miR-660
GABA <sub>A</sub> R $\alpha$ 5	<i>GABRA5</i>	9	1	miR-203
GABA <sub>A</sub> R $\alpha$ 6	<i>GABRA6</i>	2	0	
GABA <sub>A</sub> R $\beta$ 1	<i>GABRB1</i>	6	0	
GABA <sub>A</sub> R $\beta$ 2	<i>GABRB2</i>	94	4	miR-9, miR-190, miR-203, miR-637
GABA <sub>A</sub> R $\beta$ 3	<i>GABRB3</i>	89	5	miR-27a, miR-203, miR-597, miR-622, miR-642
GABA <sub>A</sub> R $\gamma$ 1	<i>GABRG1</i>	80	6	miR-17, miR-26b, miR-135a, miR-221, miR-222, miR-597
GABA <sub>A</sub> R $\gamma$ 2	<i>GABRG2</i>	32	2	miR-203, miR-221
GABA <sub>A</sub> R $\gamma$ 3	<i>GABRG3</i>	2	0	
GABA <sub>B</sub> R 1	<i>GABBR1</i>	1	1	miR-620
GABA <sub>B</sub> R 2	<i>GABBR2</i>	53	7	let-7f, miR-9, miR-17, miR-20a, miR-106a, miR-139-5p, miR-203
<b>Immune response</b>				
IL-1 $\alpha$	<i>IL1A</i>	24	1	miR-146b-3p
IL-1 $\beta$	<i>IL1B</i>	3	0	
IL-1Ra	<i>IL1RN</i>	28	0	
IL-5	<i>IL5</i>	7	1	miR-642
IL-6	<i>IL6</i>	15	1	let-7f
IL-7	<i>IL7</i>	16	1	miR-203
IL-10	<i>IL10</i>	26	3	let-7f, miR-27a, miR-597
IFN- $\alpha$	<i>IFNA1</i>	1	0	
TNF- $\alpha$	<i>TNF</i>	4	0	
CCL2	<i>CCL2</i>	8	0	
CCL3	<i>CCL3</i>	2	1	miR-622

**Table 4** continued

Protein name	Gene name	No predicted miRNAs	mTLE-regulated miRNAs	
			No	Name
CCL4	<i>CCLA</i>	3	0	
CCL5	<i>CCL5</i>	8	0	
CCL22	<i>CCL22</i>	36	5	miR-597, miR-620, miR-625, miR-635, miR-665
VEGF	<i>VEGFA</i>	73	5	<i>miR-16</i> , <i>miR-17</i> , <i>miR20a</i> , <i>miR106a</i> , miR-637,
ICAM1	<i>ICAM1</i>	16	5	miR-203, <i>miR-221</i> , <i>miR-222</i> , miR-635, miR-637,
K <sup>+</sup> buffering				
AQP4	<i>AQP4</i>	93	4	miR-203, miR-597, miR-622, miR-635
KIR4.1	<i>KCNJ10</i>	52	6	miR-17, miR-20a, miR-106a, miR-298, miR-635, miR-637

miRNA target predictions were performed for groups of genes and pathways implicated in mTLE. The number of miRNAs predicted to interact with the mRNAs of the indicated genes is listed followed by the number and names of mTLE-deregulated miRNAs within this predicted mRNA-miRNA set. *Italic* miRNAs have validated interactions with the listed target transcript

*AQP4* aquaporin 4; *CCL* chemokine (C-C motif) ligand; *EAAT1-3* excitatory amino acid transporter 1-3; *GABA<sub>A</sub>R α1-γ3* GABA-A receptor subunits α1-γ3; *GABA<sub>B</sub>R 1-2* GABA-B receptor subunits 1-2; *GLU1-4* glutamate receptor, ionotropic AMPA subunit 1-4; *G5* glutamine synthetase; *ICAM1* intercellular adhesion molecule 1; *IFN-α* Interferon-α; *IL* Interleukin; *Kir4.1* glial inwardly rectifying potassium channel Kir4.1; *mGluR* metabotropic glutamate receptor; *NRI-2b* NMDA subunit 1-2b; *PAG* phosphate activated glutaminase; *TNF-α* tumor necrosis factor; *VEGF* vascular endothelial growth factor; *vGLUT1* vesicular glutamate receptor 1

expression was reduced in astrocytes in the CA1, CA3 and CA4 regions compared to control and mTLE+HS patients (Online Resource 1; Fig. 7b, c, e, f). No specific signals were detected in blood vessels. In all, these experiments show a reciprocal regulation of miR-221/222 and ICAM1 in astrocytes in mTLE + HS.

## Discussion

Discrepancies between mTLE-associated changes at the mRNA and protein level provide support to the idea that post-transcriptional regulation is affected in mTLE. For example, ICAM1 protein levels are up-regulated in the sclerotic mTLE hippocampus, but this change is not detected at the mRNA level (Fig. 6) [3, 39]. In the present study, analysis of miRNA signatures in mTLE patients revealed different levels of miRNA deregulation (changes in expression and subcellular distribution) and led us to identify astrocytes and the immune response as a target of deregulated miRNAs in mTLE. These findings extend the current concepts of mTLE pathogenesis to the level of miRNA-mediated post-transcriptional gene regulation. Because of the central role of astrocytes and the immune response, our results may have implications for other neurological and neurodegenerative disorders.

microRNAs target components of the immune response in mTLE

We used a selection of genes/cellular processes associated with mTLE to begin to address the significance of our

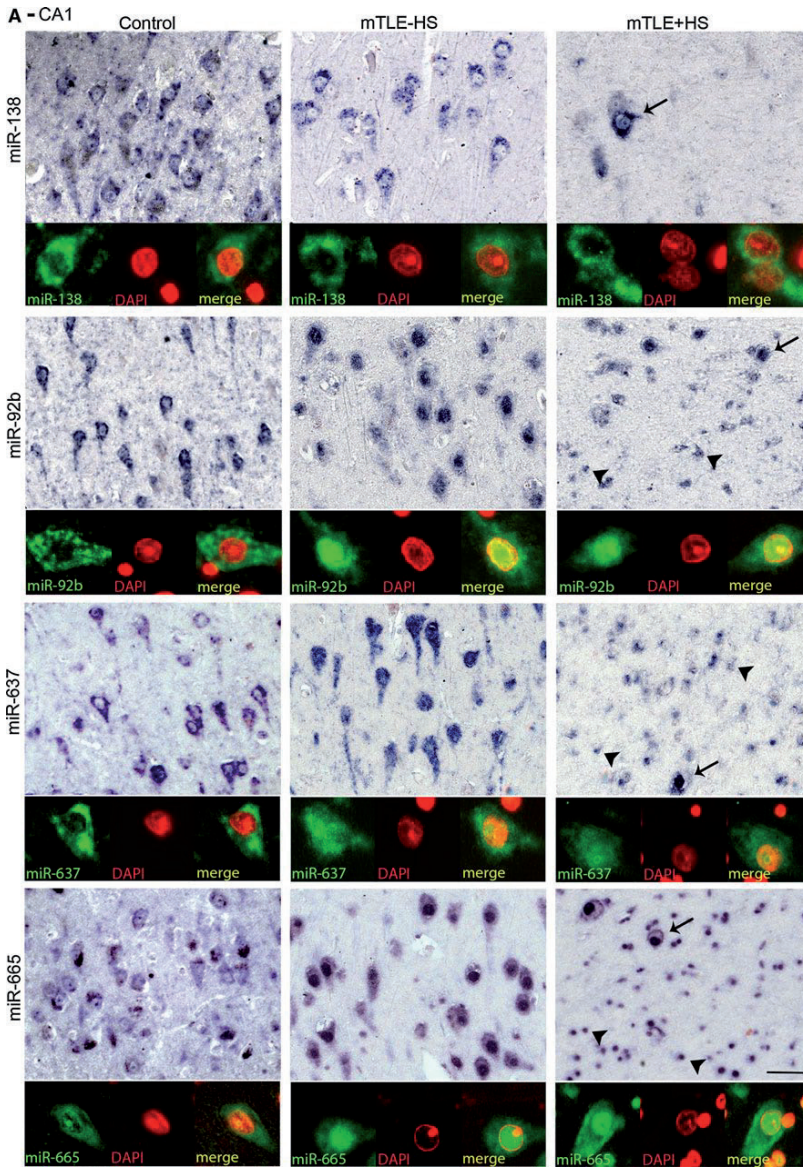
**Fig. 5** mTLE-associated nuclear mislocalization of miRNAs. Analysis of the miRNA-ISH data (as shown in Fig. 4 and 5) reveals a nuclear mislocalization for miR-92b, miR637, and miR665 in mTLE, but not for miR-138. In both CA1 (a) and CA4 (b), neuronal miRNA-138 expression is cytosolic in all three patient groups, a pattern observed for most miRNAs. In contrast, miR-92b, miR-637 and miR-665 are also found in the nucleus in mTLE+HS and mTLE + HS but not control patients. Double labeling with DAPI confirms this mTLE-associated nuclear localization, which is observed both in neurons (arrows) and small-sized cells (arrowheads). Scale bar 40 μm

observations (Table 4). Among the selected candidates, inflammatory mediators were most prominently targeted by deregulated miRNAs. This is in line with the idea that inflammation may play a central role in epilepsy [38].

In vitro experiments revealed that miR-221 and miR-222 target the 3'UTR of ICAM1 (CD54). ICAM1 mediates interactions with other (immune) cells to influence processes such as inflammation [43]. In line with previous studies, we observed an increase in ICAM1 expression in blood vessels and GFAP + astrocytes in the mTLE + HS hippocampus [40, 42, 44]. Astrocytes contribute significantly to the pathogenic process of epilepsy [45]. Although the function of astrocyte-associated ICAM1 remains poorly understood, it has been proposed to mediate leukocyte accumulation, microglia recruitment, and cytokine production (e.g., IL-1β, IL-6) [40, 44, 46, 47].

In our study, miR-221 and miR-222 were expressed in astrocytes, but not in blood vessels, and their expression was reduced in mTLE + HS material. Interestingly, ICAM1 has been validated as a target for miR-221 or miR-222 in cholangiocytes, epithelial and cancer cells. In these cells, physiological stimuli induce different biological effects that depend on the miRNA-mediated regulation of





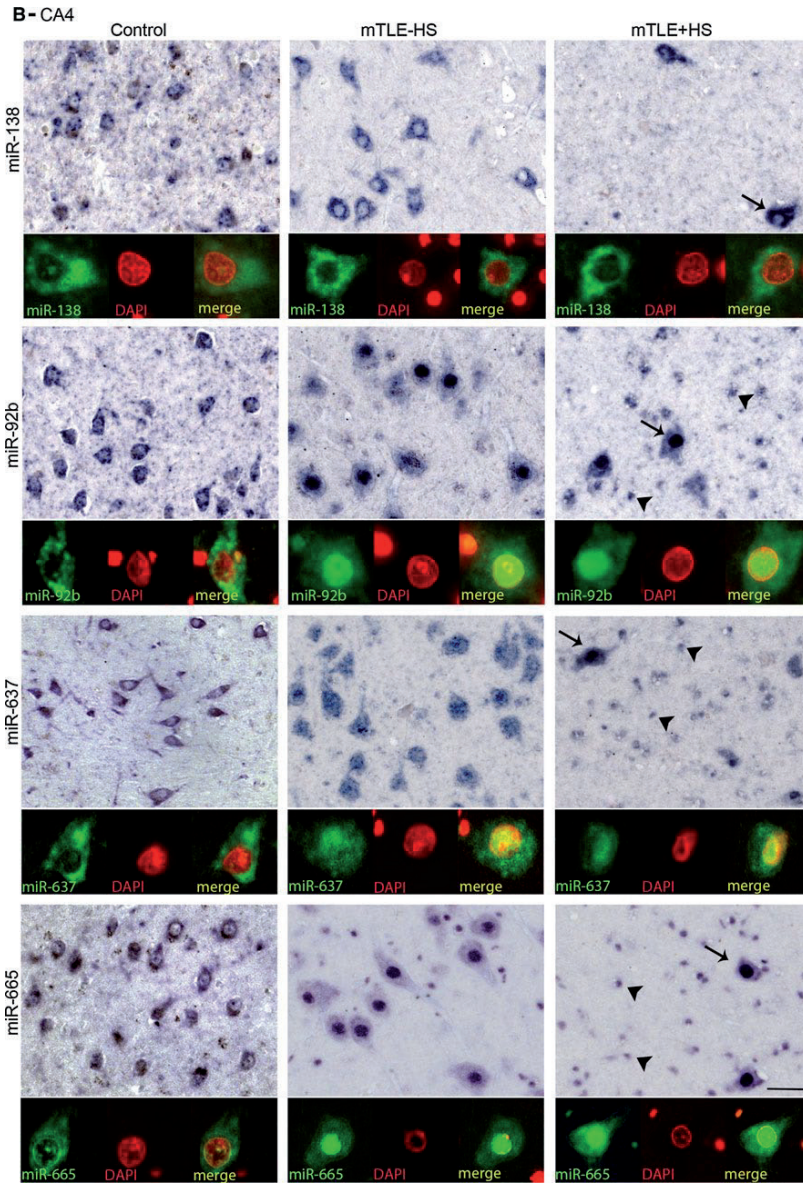
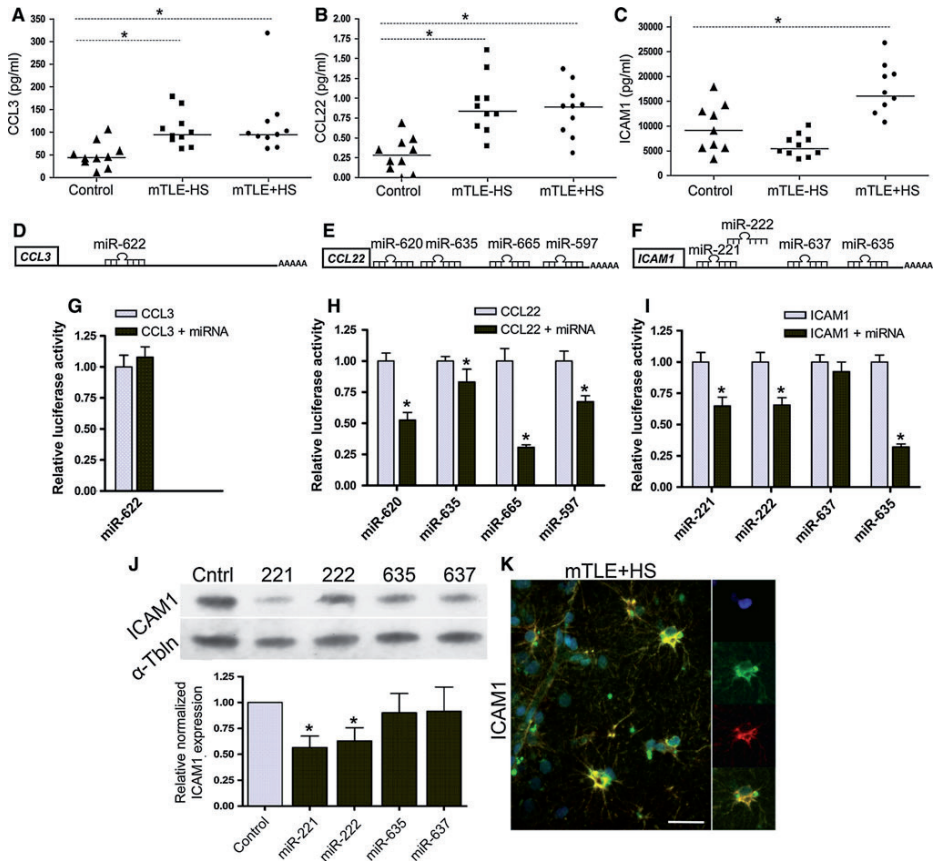


Fig. 5 continued



**Fig. 6** microRNAs deregulated in mTLE target the immune response. Quantitative ELISA measurements on the samples used for miRNA profiling (Table 1;  $n = 10$  per group) show an increase in hippocampal expression of CCL3 (a) and CCL22 (b) in mTLE patient groups, and increased expression of ICAM1 (c) in mTLE + HS patients. Symbols represent individual patients, horizontal lines group means. 3'UTRs of CCL3 (d), CCL22 (e) and ICAM1 (f) with the relative location of the strongest predicted binding sites for the miRNAs that were most robustly regulated in mTLE. Luciferase activity in HEK293 cells transfected with the psiCheck-2 vector containing the binding sites indicated in d-f and corresponding miRNA mimic (black bar) or non-targeting control mimic (light blue bar). Levels of Renilla luciferase reporter activity were normalized to the levels of constitutively expressed firefly luciferase. The relative normalized means as compared to control  $\pm$  SD ( $n = 3$  independent

experiments) are shown. Significant differences between the control miRNA and the miRNAs predicted to target CCL3, CCL22, and ICAM1 are indicated ( $p < 0.05$ ). **j** Lysates from HeLa cells transfected with miRNA mimics for miR-221, 222, 635, or 637 or non-targeting control were subjected to Western blotting for ICAM1. Upper panel shows a representative blot incubated with antibodies against ICAM1 and  $\alpha$ -tubulin ( $\alpha$ -Tbn). Lower panel shows microdensitometry from four independent experiments. Normalized means  $\pm$  SEM are shown. **k** Double immunofluorescent labeling on hippocampal tissue of a mTLE + HS patient reveals co-labeling of ICAM1 protein (green) with the astrocyte marker glial fibrillary acidic protein (GFAP) (red). Small panels on the right show images of an individual astrocyte at a higher magnification. Significant change  $*p < 0.05$ . Scale bar 40  $\mu$ m

ICAM1 expression [48–50]. Thus, miRNAs not merely fine-tune ICAM1 expression, but can robustly regulate ICAM1 expression to trigger biologically meaningful

effects. Based on our findings and the current knowledge of astrocyte-associated ICAM1, we propose that the down-regulation of miR-221 and miR-222 in mTLE + HS is



linked to a local up-regulation of ICAM1 in astrocytes. Interestingly, recent work has shown that miR-222 can regulate ICAM1 in glioma cells [49]. Enhanced ICAM1 expression may then contribute to the release of other inflammatory mediators and the recruitment of immune cells, thereby augmenting and/or sustaining the immune response (Fig. 7g).

Previous work indicates that the expression of ICAM1 is regulated post-transcriptionally in mTLE. Our results provide support to this idea by revealing a down-regulation of miRNAs that target ICAM1. The factors that trigger this decrease, and thereby potentially enhance ICAM1 levels, are unknown. ICAM1 protein expression can be regulated by a variety of signals [43]. Intriguingly, some of these signals, such as IFN- $\gamma$ , have been shown to regulate ICAM1 at the post-transcriptional level [46].

Post-transcriptional regulation by miRNAs affects about a third of all protein-coding genes. Given the abundant and robust changes in miRNA expression reported in our study, one has to assume that in addition to CCL22 and ICAM1 the expression of many other proteins is regulated by miRNAs in mTLE. Indeed, our analysis of a limited number of genes and cellular processes (Table 4) revealed several interesting candidates for such regulation. Further studies are needed to establish the implications of these predicted interactions.

#### Nuclear mislocalization of miRNAs in human mTLE

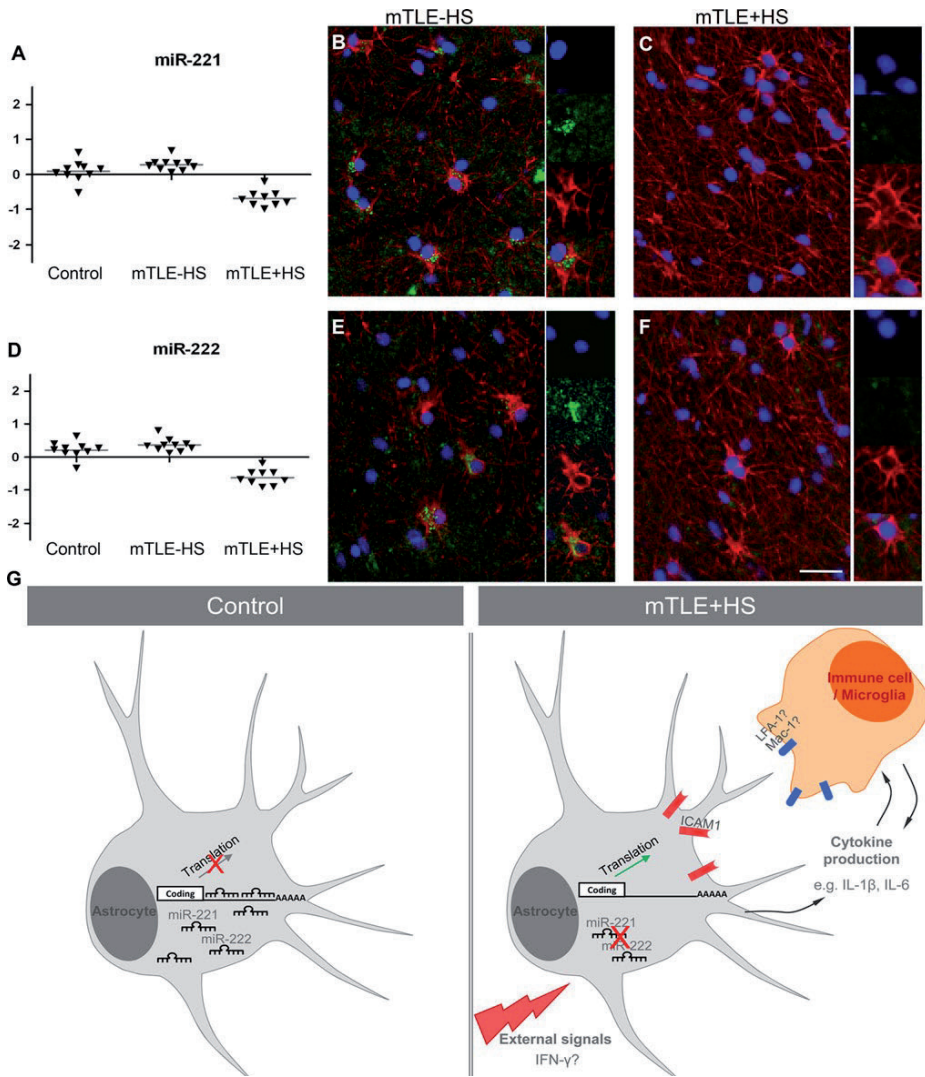
miRNAs are generally considered to be cytoplasm-localized regulatory RNAs. However, in our study a specific subset of miRNAs (miR-92b, miR-637, and miR-665) also displayed high levels of expression in the nucleus of neurons and glial cells in mTLE tissue but not controls. To the best of our knowledge, our study is the first to unveil a disease-associated nuclear mislocalization of miRNAs. Preliminary studies show a similar nuclear mislocalization of miR-92b in the pilocarpine-induced status epilepticus rat model of TLE (our own unpublished observations). It is therefore tempting to speculate that the nuclear mislocalization of miRNAs may be part of mTLE pathogenesis. It is unclear why these miRNAs aberrantly localize in the nucleus. One possibility is that they relocalize to the nucleus from the cytoplasm. Relocalization of miRNAs from the cytoplasm to the nucleus has been reported previously. For example, miR-29b contains a specific hexanucleotide sequence that directs its nuclear localization [51]. Furthermore, an active karyopherin-based shuttling system for cytoplasmic-nuclear transport of miRNAs has been reported. Final processing of miRNAs normally occurs in the cytoplasm and the LNA miRNA-ISH probes used in this study are thought to selectively detect fully processed, mature miRNAs, providing further

**Fig. 7** Decreased astrocyte-associated expression of miR-221 and miR-222 in mTLE + HS. **a, d** Scatter plots of  $\log^2$  Hy3/Hy5 ratios for miR-221 and miR-222. **Triangles** represent individual patients and **gray horizontal bars** group means. **b, c, e, f** miRNA-ISH combined with immunofluorescent labeling for glial fibrillary acidic protein (GFAP). The miRNA-ISH signal is pseudocolored in **green**, nuclear DAPI staining in **blue** and GFAP labeling in **red**. The **right part** of each panel shows images of individual astrocytes at a higher magnification. miR-221 and miR-222 are detected in GFAP-positive astrocytes in controls (not shown) and mTLE-HS patients (**b, e**). In contrast, expression of miR-221 and miR-222 is absent or weak in astrocytes of the mTLE + HS hippocampus (**c, f**). **g** Hypothetical model of miRNA-regulated expression of ICAM1 in astrocytes in mTLE. In mTLE + HS, expression of miR-221 and miR-222 is down-regulated in astrocytes in the hippocampus as compared to control. These miRNAs target the 3'UTR of ICAM1 and reduce ICAM1 expression. Therefore, reduced miR-221 and miR-222 expression in mTLE + HS may induce enhanced astrocyte-associated expression of ICAM1. In line with this model, ICAM1 protein expression is increased in astrocytes in mTLE + HS patients. Astrocyte-associated ICAM1 has been associated with the recruitment, accumulation, and activation of leukocytes and microglia. These cells express ICAM1-binding partners such as LFA-1 and Mac-1 and ICAM1-LFA-1/Mac-1 interactions can trigger the production of inflammatory mediators by astrocytes and immune cells. These effects may contribute to the enhanced and sustained immune response observed in the mTLE + HS hippocampus. The signals that trigger changes in astrocyte-associated miRNA expression are unknown but may include factors such as IFN- $\gamma$ , which can regulate ICAM1 expression at the post-transcriptional level. **Scale bar** 40  $\mu$ m

support for a cytoplasm-to-nucleus shuttling model in mTLE. What could be the functional consequences of the nuclear mislocalization of miRNAs? Due to their nuclear localization miR-92b, miR-637, and miR-665 may fail to regulate their normal cytoplasmic target transcripts. In addition, they may acquire new functions in the nucleus such as transcriptional regulation. Both scenarios will have profound effects on protein expression. Future studies will need to focus on revealing the full set of miRNAs mislocalized in the nucleus in mTLE and on the causes and consequences of this abnormal distribution.

#### Differential microRNA expression in mTLE: cause and/or consequence?

Several different patterns of miRNA expression changes were detected in mTLE patients. It is possible that some of these changes are seizure- and/or drug-induced or a consequence of the gliosis or neuron loss that characterize mTLE [52, 53]. Further detailed cellular analysis per miRNA will be required to investigate which changes are solely related to neuron loss and/or gliosis. Nevertheless, such differences in miRNA expression may still be relevant for the disease process, e.g., in the recurrence of seizures or the regulation of gliosis. It is also important to note that statistical analyses did not reveal any effect of confounding factors such as postmortem delay or age. Other types of



miRNA expression changes, e.g., a specific down-regulation of astroglial miR-221 and miR-222 expression in mTLE + HS (Fig. 6) or mTLE–HS specific alterations, do not correlate directly with gross morphological changes, seizures or medication, the latter two of which are common

to both mTLE patient groups (Table 1). These changes indicate that while some alterations in miRNA expression may be shared by both mTLE groups, others are unique to mTLE–HS or mTLE + HS. This is also supported by the clearly segregated miRNA signatures of the different



patient groups in the PCA plot (Fig. 1a). Since the human material used in this study represents an end-stage of the epileptogenic process, an important future goal is to determine whether the changes in miRNA expression or distribution represent a cause or a consequence of the disease process. A causal role for miRNAs in epilepsy is suggested by recent animal studies reporting changes in miRNA levels already during the process of epileptogenesis [18–21]. In the future, manipulation of the here identified deregulated miRNAs in animal models of TLE will help to address the functional, and potentially pathogenic, role of changes in the expression and subcellular distribution of these small RNAs.

**Acknowledgments** We wish to thank the patients who donated their tissue for our studies. We thank Kees Braun, David Vilanova and Eugene Berezikov for helpful comments on the manuscript. We thank Chris Jewell for help with the statistical analyses and the Netherlands Brain Bank for providing tissue samples. This work was supported by the Netherlands Organization for Health Research and Development (ZonMW-VIDI and ZonMW-TOP), the Human Frontier Science Program (HFSP-CDA) and the European Union [mdDANeurodev, FP7/2007-2011, n° 222999] (to R.J.P.) and by the National Epilepsy Fund of the Netherlands [NEF, Grant n° 06-09] and the Epilepsies of Childhood Foundation (EPOCH) (to P.N.E. de G.).

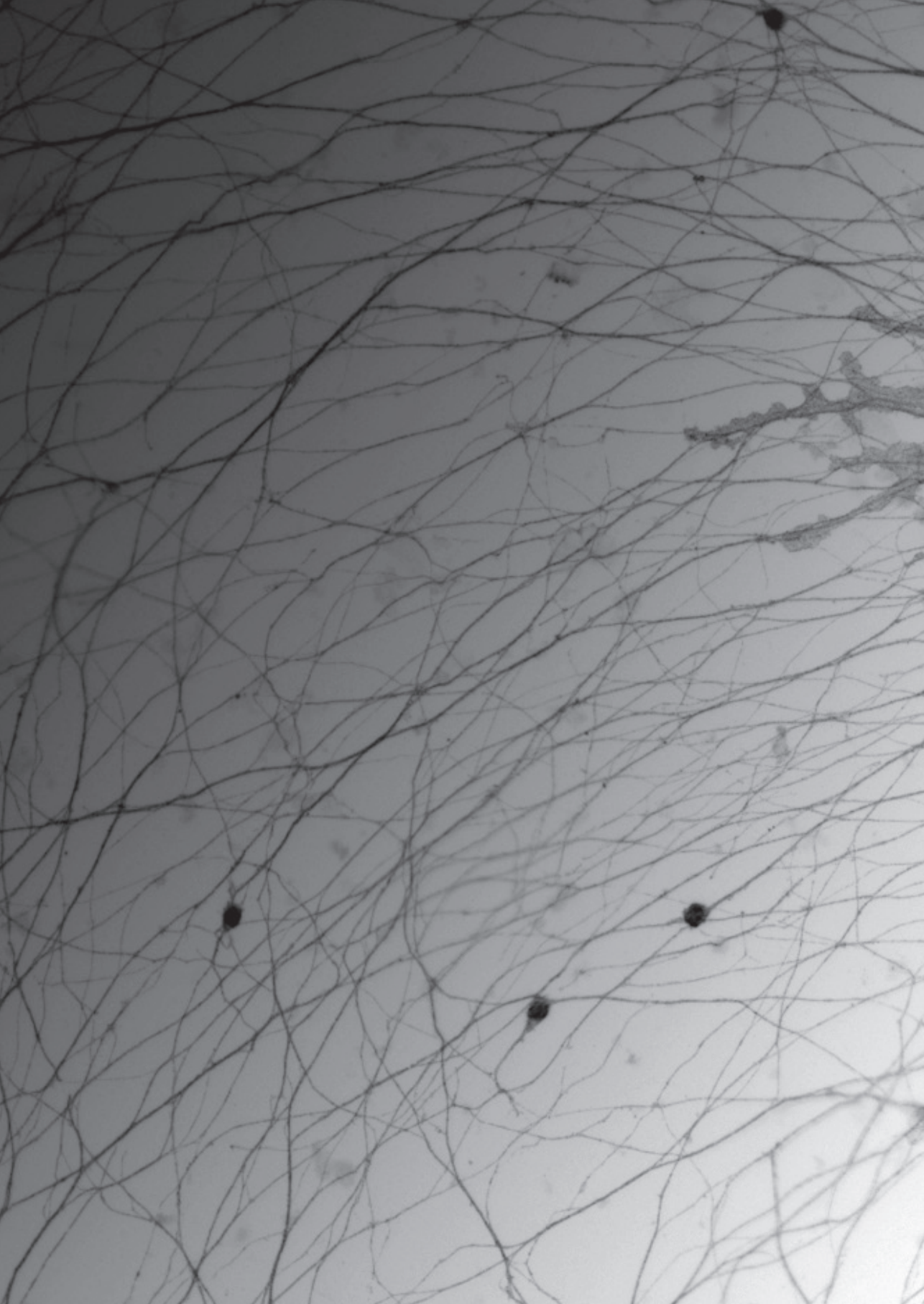
**Open Access** This article is distributed under the terms of the Creative Commons Attribution License which permits any use, distribution, and reproduction in any medium, provided the original author(s) and the source are credited.

## References

- Engel J Jr (2001) A proposed diagnostic scheme for people with epileptic seizures and with epilepsy: report of the ILAE task force on classification and terminology. *Epilepsia* 42(6):796–803
- Wieser HG (2004) ILAE Commission Report. Mesial temporal lobe epilepsy with hippocampal sclerosis. *Epilepsia* 45(6):695–714
- van Gassen KL, de Wit M, Koerkamp MJ, Rensen MG, van Rijen PC, Holstege FC, Lindhout D, de Graan PN (2008) Possible role of the innate immunity in temporal lobe epilepsy. *Epilepsia* 49(6):1055–1065
- Lukasiuk K, Dabrowski M, Adach A, Pitkanen A (2006) Epileptogenesis-related genes revisited. *Prog Brain Res* 158:223–241
- Rakhade SN, Jensen FE (2009) Epileptogenesis in the immature brain: emerging mechanisms. *Nat Rev Neuro* 5(7):380–391
- Pitkanen A, Lukasiuk K (2009) Molecular and cellular basis of epileptogenesis in symptomatic epilepsy. *Epilepsy Behav* 14(Suppl 1):16–25
- Gorter JA, van Vliet EA, Aronica E, Breit T, Rauwerda H, Lopes da Silva FH, Wadman WJ (2006) Potential new anti-epileptogenic targets indicated by microarray analysis in a rat model for temporal lobe epilepsy. *J Neurosci* 26(43):11083–11110
- McClelland S, Flynn C, Dube C, Richichi C, Zha Q, Ghestem A, Esclapez M, Bernard C, Baram TZ (2011) Neuron-restrictive silencer factor-mediated hyperpolarization-activated cyclic nucleotide gated channelopathy in experimental temporal lobe epilepsy. *Ann Neurol* 70(3):454–464
- Ambros V (2004) The functions of animal microRNAs. *Nature* 431(7006):350–355
- Bartel DP (2004) MicroRNAs: genomics, biogenesis, mechanism, and function. *Cell* 116(2):281–297
- Kosik KS (2006) The neuronal microRNA system. *Nat Rev Neurosci* 7(12):911–920
- Eulalio A, Huntzinger E, Izaurralde E (2008) Getting to the root of miRNA-mediated gene silencing. *Cell* 132(1):9–14
- Filipowicz W, Bhattacharyya SN, Sonenberg N (2008) Mechanisms of post-transcriptional regulation by microRNAs: are the answers in sight? *Nat Rev Genet* 9(2):102–114
- Schratt G (2009) MicroRNAs at the synapse. *Nat Rev Neurosci* 10(12):842–849
- Junker A, Krumbholz M, Eisele S, Mohan H, Augstein F, Bittner R, Lassmann H, Wekerle H, Hohlfeld R, Meinl E (2009) MicroRNA profiling of multiple sclerosis lesions identifies modulators of the regulatory protein CD47. *Brain* 132(Pt 12):3342–3352
- Saugstad JA (2010) MicroRNAs as effectors of brain function with roles in ischemia and injury, neuroprotection, and neurodegeneration. *J Cereb Blood Flow Metab* 30(9):1564–1576
- Williams AH, Valdez G, Moresi V, Qi X, McAnally J, Elliott JL, Bassel-Duby R, Sanes JR, Olson EN (2009) MicroRNA-206 delays ALS progression and promotes regeneration of neuromuscular synapses in mice. *Science* 326(5959):1549–1554
- Aronica E, Fluiter K, Iyer A, Zurolo E, Vreijling J, van Vliet EA, Baayen JC, Gorter JA (2010) Expression pattern of miR-146a, an inflammation-associated microRNA, in experimental and human temporal lobe epilepsy. *Eur J Neurosci* 31(6):1100–1107
- Liu DZ, Tian Y, Ander BP, Xu H, Stamova BS, Zhan X, Turner RJ, Jickling G, Sharp FR (2010) Brain and blood microRNA expression profiling of ischemic stroke, intracerebral hemorrhage, and kainate seizures. *J Cereb Blood Flow Metab* 30(1):92–101
- Nudelman AS, DiRocco DP, Lambert TJ, Garelick MG, Le J, Nathanson NM, Storm DR (2010) Neuronal activity rapidly induces transcription of the CREB-regulated microRNA-132, in vivo. *Hippocampus* 20(4):492–498
- Hu K, Zhang C, Long L, Long X, Feng L, Li Y, Xiao B (2011) Expression profile of microRNAs in rat hippocampus following lithium-pilocarpine-induced status epilepticus. *Neurosci Lett* 488(3):252–257
- Debets RM, van Veelen CW, van Huffelen AV, van Emde BW (1991) Presurgical evaluation of patients with intractable partial epilepsy: the Dutch epilepsy surgery program. *Acta Neurol Belg* 91(3):125–140
- Ibberson D, Benes V, Muckenthaler MU, Castoldi M (2009) RNA degradation compromises the reliability of microRNA expression profiling. *BMC Biotechnol* 9:102
- Becker C, Hammerle-Fickinger A, Riedmaier I, Pfaffl MW (2010) mRNA and microRNA quality control for RT-qPCR analysis. *Methods* 50(4):237–243
- Durrenberger PF, Fernando S, Kashefi SN, Ferrer I, Hauw JJ, Seilhean D, Smith C, Walker R, Al Sarraj S, Troakes C, Palkovits M, Kasztner M, Huitinga I, Arzberger T, Dexter DT, Kretzschmar H, Reynolds R (2010) Effects of antemortem and postmortem variables on human brain mRNA quality: a BrainNet Europe study. *J Neuropathol Exp Neurol* 69(1):70–81
- Wyler AR, Dohan FC, Schweitzer JB, Berry AD (1992) A grading system for mesial temporal pathology (hippocampal sclerosis) from anterior temporal lobectomy. *J Epilepsy* 5(4):220–225
- Ritchie ME, Silver J, Oshlack A, Holmes M, Diyagama D, Holloway A, Smyth GK (2007) A comparison of background correction methods for two-colour microarrays. *Bioinformatics* 23(20):2700–2707
- Andersen CL, Jensen JL, Orntoft TF (2004) Normalization of real-time quantitative reverse transcription-PCR data: a model-based variance estimation approach to identify genes suited for normalization, applied to bladder and colon cancer data sets. *Cancer Res* 64(15):5245–5250

29. Obernosterer G, Martinez J, Alenius M (2007) Locked nucleic acid-based in situ detection of microRNAs in mouse tissue sections. *Nat Protoc* 2(6):1508–1514
30. Jorgensen S, Baker A, Moller S, Nielsen BS (2010) Robust one-day in situ hybridization protocol for detection of microRNAs in paraffin samples using LNA probes. *Methods* 52(4):375–381
31. de Jager W, Prakken BJ, Bijlsma JW, Kuis W, Rijkers GT (2005) Improved multiplex immunoassay performance in human plasma and synovial fluid following removal of interfering heterophilic antibodies. *J Immunol Methods* 300(1–2):124–135
32. Hulse RE, Kunkler PE, Fedynyshyn JP, Kraig RP (2004) Optimization of multiplexed bead-based cytokine immunoassays for rat serum and brain tissue. *J Neurosci Methods* 136(1):87–98
33. Proper EA, Hoogland G, Kappen SM, Jansen GH, Rensen MG, Schrama LH, van Veelen CW, van Rijen PC, van Nieuwenhuizen O, Gispén WH, de Graan PN (2002) Distribution of glutamate transporters in the hippocampus of patients with pharmacoresistant temporal lobe epilepsy. *Brain* 125(Pt 1):32–43
34. Notenboom RG, Hampson DR, Jansen GH, van Rijen PC, van Veelen CW, van Nieuwenhuizen O, de Graan PN (2006) Up-regulation of hippocampal metabotropic glutamate receptor 5 in temporal lobe epilepsy patients. *Brain* 129(Pt 1):96–107
35. Rigau V, Morin M, Rousset MC, de Bock F, Lebrun A, Coubes P, Picot MC, Baldy-Moulinier M, Bockaert J, Crespel A, Lerner-Natoli M (2007) Angiogenesis is associated with blood–brain barrier permeability in temporal lobe epilepsy. *Brain* 130(Pt 7):1942–1956
36. Loup F, Picard F, Yonekawa Y, Wieser HG, Fritschy JM (2009) Selective changes in GABAA receptor subtypes in white matter neurons of patients with focal epilepsy. *Brain* 132(Pt 9):2449–2463
37. Seifert G, Schilling K, Steinhauser C (2006) Astrocyte dysfunction in neurological disorders: a molecular perspective. *Nat Rev Neurosci* 7(3):194–206
38. Vezzani A, French J, Bartfai T, Baram TZ (2011) The role of inflammation in epilepsy. *Nat Rev Neurol* 7(1):31–40
39. Nakahara H, Konishi Y, Beach TG, Yamada N, Makino S, Tooyama I (2010) Infiltration of T lymphocytes and expression of icam-1 in the hippocampus of patients with hippocampal sclerosis. *Acta Histochem Cytochem* 43(6):157–162
40. Akiyama H, Kawamata T, Yamada T, Tooyama I, Ishii T, McGeer PL (1993) Expression of intercellular adhesion molecule (ICAM)-1 by a subset of astrocytes in Alzheimer disease and some other degenerative neurological disorders. *Acta Neuropathol* 85(6):628–634
41. Klegeris A, Giasson BI, Zhang H, Maguire J, Pelech S, McGeer PL (2006) Alpha-synuclein and its disease-causing mutants induce ICAM-1 and IL-6 in human astrocytes and astrocytoma cells. *FASEB J* 20(12):2000–2008
42. Zattoni M, Mura ML, Deprez F, Schwendener RA, Engelhardt B, Frei K, Fritschy JM (2011) Brain infiltration of leukocytes contributes to the pathophysiology of temporal lobe epilepsy. *J Neurosci* 31(11):4037–4050
43. Dietrich JB (2002) The adhesion molecule ICAM-1 and its regulation in relation with the blood–brain barrier. *J Neuroimmunol* 128(1–2):58–68
44. Miklossy J, Doudet DD, Schwab C, Yu S, McGeer EG, McGeer PL (2006) Role of ICAM-1 in persisting inflammation in Parkinson disease and MPTP monkeys. *Exp Neurol* 197(2):275–283
45. Seifert G, Carmignoto G, Steinhauser C (2010) Astrocyte dysfunction in epilepsy. *Brain Res Rev* 63(1–2):212–221
46. Lee SJ, Drabik K, Van Wagoner NJ, Lee S, Choi C, Dong Y, Benveniste EN (2000) ICAM-1-induced expression of proinflammatory cytokines in astrocytes: involvement of extracellular signal-regulated kinase and p38 mitogen-activated protein kinase pathways. *J Immunol* 165(8):4658–4666
47. McGeer PL, McGeer EG (2008) Glial reactions in Parkinson's disease. *Mov Disord* 23(4):474–483
48. Gong AY, Hu G, Zhou R, Liu J, Feng Y, Soukup GA, Chen XM (2011) MicroRNA-221 controls expression of intercellular adhesion molecule-1 in epithelial cells in response to *Cryptosporidium parvum* infection. *Int J Parasitol* 41(3–4):397–403
49. Ueda R, Kohanbash G, Sasaki K, Fujita M, Zhu X, Kastnerhuber ER, McDonald HA, Potter DM, Hamilton RL, Lotze MT, Khan SA, Sobol RW, Okada H (2009) Dicer-regulated microRNAs 222 and 339 promote resistance of cancer cells to cytotoxic T-lymphocytes by down-regulation of ICAM-1. *Proc Natl Acad Sci USA* 106(26):10746–10751
50. Hu G, Gong AY, Liu J, Zhou R, Deng C, Chen XM (2010) miR-221 suppresses ICAM-1 translation and regulates interferon-gamma-induced ICAM-1 expression in human cholangiocytes. *Am J Physiol Gastrointest Liver Physiol* 298(4):G542–G550
51. Hwang HW, Wentzel EA, Mendell JT (2007) A hexanucleotide element directs microRNA nuclear import. *Science* 315(5808):97–100
52. Houser CR (1999) Neuronal loss and synaptic reorganization in temporal lobe epilepsy. *Adv Neurol* 79:743–761
53. Proper EA, Oestreicher AB, Jansen GH, Veelen CW, van Rijen PC, Gispén WH, de Graan PN (2000) Immunohistochemical characterization of mossy fibre sprouting in the hippocampus of patients with pharmacoresistant temporal lobe epilepsy. *Brain* 123(Pt 1):19–30







A grayscale microscopic image of a neural network, showing a dense web of thin, branching processes (dendrites and axons) with several larger, darker cell bodies (soma) scattered throughout. A semi-transparent white rectangular box is overlaid in the upper left quadrant, containing the chapter title. A dotted line is positioned above the text within the box.

# Chapter 8

## General Discussion



---

The development of a fully functional brain requires the orchestration of simultaneously coordinated migration, projection and network formation to connect millions of neurons. When neuronal connections are lost or neurons die as a result of neurodegenerative disease or injury, the regenerative capacities of the adult central nervous system (CNS) are limited. In order to develop clinical strategies to improve this regenerative potential, we need to 1) increase our understanding of the guidance cues and cellular processes that regulate neural circuit formation during development, and 2) investigate the pathological changes that occur following adult CNS injury and/or disease. These insights will lead to novel therapeutic targets for future (pre)clinical studies. This thesis contributes to our understanding of; 1) signaling downstream of the axon guidance receptor Neogenin; 2) intrinsic and extrinsic regulation of neuronal migration; and 3) molecular changes associated with human epilepsy. These approaches not only identify novel factors involved in the regulation of neural development, but also characterize the pathology of a neurological disease. The following section discusses the implications of the results described in this thesis and suggests promising directions for future research.

## **1. Molecular pathway: RGM-Neogenin signaling**

### **1.1 The formation of a pH-dependent Neogenin:RGM double dimer promotes signaling efficiency**

Although several components of the Neogenin signaling cascade have been described over the past few years, details regarding the molecular interaction between Neogenin and its ligand RGM were lacking. Neogenin is the only receptor capable of binding RGM and RGMs are amongst the most potent axonal inhibitory proteins (Rajagopalan et al. 2004). In **Chapter 3**, the crystal structure of the Neogenin and RGM-receptor complex was solved. Two RGM molecules form a complex with two Neogenin molecules, creating a staple-like structure that pins the Neogenin dimer together at the cell membrane. RGM has two interacting domains that are involved in Neogenin binding. The first binding site (site-1) is essential for functional interaction, since loss of this site completely abolishes Neogenin binding and signaling. The second binding site (site-2) is required for the formation of the 2:2 ligand:receptor complex. Altering site-2 significantly reduced RGM-induced neuronal outgrowth inhibition, suggesting that the establishment of the 2:2 complex promotes efficient signaling. Additional experiments are required to determine how 2:2 complexes establish this increased efficiency. One possibility is that the relatively rigid complexes form signaling islands in the membrane, resulting in a local concentration of intracellular downstream signaling components and thus increased signaling

efficiency. The site-2 interaction is pH-sensitive, and does not take place in an acidic environment such as the intracellular milieu. This provides another mechanism for the regulation of Neogenin signaling. When Neogenin and RGM are both expressed in the same cell, the pH-sensitive 2:2 interaction will ensure that premature intracellular signaling does not occur. A role for cis-Neogenin binding has been described for RGM in bone morphogenetic protein (BMP) signaling during bone development and iron homeostasis, and recently evidence for cis signaling in neurons has been reported (Zhou et al. 2010; Zhang et al. 2009; Tassew et al. 2013).

Concurrently, pH-dependent ligand binding may also act as a mechanism for signaling termination. Endocytosis is a common mechanism for axon guidance receptors to clear activated ligand-receptor complexes from the membrane (O'Donnell et al. 2009; Winckler & Mellman 2010). The pH in the endosome is typically low compared to the neutral pH at the cell surface and this may contribute to Neogenin signaling extinguishing. Currently, no mechanism for the termination of Neogenin signaling is known and it remains to be investigated whether endocytosis is involved in this process.

## 1.2 Lrig2 mediates ligand-dependent axon guidance receptor shedding

An additional method to terminate membrane receptor signaling following ligand binding is extracellular cleavage (Bai & Pfaff 2011). Neogenin sensitivity to RGMa has been shown to be modified by the metalloprotease ADAM17, but the function and regulation of this cleavage was unclear (Okamura et al. 2011). In **Chapter 4** we identified a role for leucine-rich repeat and immunoglobulin-like protein Lrig2 in the regulation of Neogenin ecto-domain shedding. Lrig2 interaction with Neogenin prevents extracellular cleavage by ADAM17. Upon RGMa binding, the Lrig2-Neogenin interaction is alleviated and ADAM17-induced cleavage takes place. This ligand-dependent ecto-domain shedding provides a valuable mechanism for the growth cone to minimize unintended cleavage in the presence of an active sheddase while retaining immediate responsiveness. The function of RGMa-induced shedding is currently unresolved but an intriguing possibility is that it clears activated ligand-receptor complexes from the membrane to ensure continuous sensitivity and to tightly control the duration of signaling.

One of the most fascinating findings of **Chapter 4** is that Lrig2-regulated ADAM17 cleavage is not limited to Neogenin. So far, we have tested two other ADAM17 target proteins, NCAM1 and Sema4D, and our results imply that 1) Lrig2 also interacts with these proteins, and 2) this interaction is able to prevent ADAM17-induced cleavage. These observations hint at a common mechanism

---

for the regulation of ADAM17 target-specificity by Lrig2. Since there is no known consensus cleavage site sequence for ADAM17 it is unclear how substrate-specificity is established. ADAM17 is expressed in almost every tissue and cell type and it targets a large number of proteins involved in a broad range of cellular processes in development and disease (Scheller et al. 2011). For instance, during inflammation and cancer the cell surface activity of ADAM17 is increased (Gooz 2010). Inhibition of ADAM17 has been reported to be beneficial in preclinical studies, demonstrating its therapeutic potential (Rose-John 2013). However, human clinical trials using chemical inhibitors of ADAM17 report liver toxicity, potentially induced by off-target effects (Moss et al. 2008). Because of the ambiguous nature of ADAM17, target-specific inhibition would greatly reduce these undesired side effects. It would therefore be valuable to further investigate the potential of Lrig2 in regulating cleavage of additional, disease-associated ADAM17 targets. The mechanism of cleavage protection described in **Chapter 4** may direct future research towards finding an alternative method to inhibit ADAM17.

### 1.3 Novel directions for improving axonal regeneration

Whereas Neogenin signaling has been mainly studied in developmental processes, Neogenin expression is maintained in the adult CNS. The impact of this expression becomes apparent when neurons are confronted with external trauma. Numerous studies have confirmed the upregulation of RGMa following for example rat spinal cord injury, optic nerve injury and following human focal cerebral ischemia and traumatic brain injury (Doya et al. 2006; Hata et al. 2006; Schnichels et al. 2011; Schnichels et al. 2012; Schwab et al. 2005). The upregulation of RGMa expression occurs at the site of the lesion and elevated RGMa is detected on several cellular structures such as myelinated fibers, neurons, oligodendrocytes, microglia and macrophages (Schwab et al. 2005). Elevated RGMa expression is thought to inhibit the regeneration of Neogenin-positive axons. Indeed, administration of RGMa blocking antibodies at the lesion site improves the number of regenerating axons and increases motor function after spinal cord injury (Hata et al. 2006). Unfortunately, the clinical potential of blocking antibodies is low because they are relatively large and notoriously difficult to target to the CNS.

The data in **Chapter 3** provide insight into the interaction between Neogenin and RGM which may contribute to future experiments aimed at increasing axonal regeneration. For example, rather than blocking antibodies, much smaller peptides specifically interfering with site-1 or site-2 Neogenin-RGMa binding may be developed. A large number of predicted target-peptides could be tested for their efficiency at reducing sensitivity to RGMa in an *in vitro* screen. Available

experimental tools that are suitable at this scale include 1) protein binding assays using AP-tagged RGMa, and 2) functional assays monitoring neurite outgrowth.

Furthermore, it would be highly interesting to focus future research on the therapeutic potential of interfering with Lrig2 function. In **Chapter 4**, Lrig2 knockdown had a much stronger effect on optic nerve regeneration than knockdown of Neogenin. This implies that Lrig2 may be regulating the ectodomain shedding of additional cell surface molecules in injured neurons and axons. Several inhibitory factors are produced at the injury site, including adhesion molecules and guidance molecules such as semaphorins and ephrins (Tang 2003). ADAM17 targets several of the neuronal receptors for these cues (Janes et al. 2005; Romi et al. 2014). Therefore, instead of targeting individual inhibitory surface molecules, targeting Lrig2 may efficiently decrease the sensitivity of axons to multiple different neuronal regeneration inhibitors. In **Chapter 4**, Lrig2 expression was inhibited by siRNA-mediated knockdown following optic nerve injury. Therapeutic alternatives worth exploring are the local administration of Lrig2 neutralizing antibodies or the infusion of (part of) the Lrig2 extracellular domain. This Lrig2 fragment would need to compete with endogenous Lrig2 for interaction with surface molecules but be unable to prevent cleavage by ADAM17, thus obtaining a dominant negative function. Surface molecules interacting with dominant negative Lrig2 would be accessible for ADAM17, leading to increased shedding and decreased sensitivity to regeneration inhibitors. Additional experiments are required to determine which Lrig2 molecular domains are responsible for the functionally distinct steps of surface molecule interaction and blocking of cleavage.

## 2. Cellular process: cerebellar granule cell migration

### 2.1 Dock7 mediates RGMa-induced Neogenin signaling during CGN migration

Neuronal migration depends on extrinsic and intrinsic factors. Extracellular factors include secreted cues that signal by binding to guidance receptors located in the neuronal cell membrane. The effect of this ligand-receptor binding is the rearrangement of the cytoskeleton to promote movement of the entire cell in a specific direction. The intracellular cues regulating signal transduction from the cell membrane to the cytoskeleton remain largely unknown. In **Chapter 5** we discovered a role for the axon guidance receptor Neogenin in cerebellar granule neuron (CGN) migration. Furthermore, we showed that the cytoplasmic cue dedicator of cytokinesis 7 (Dock7) is an interactor of Neogenin and that it is required for RGMa-induced signaling in migrating CGNs.

---

Knockdown of Dock7 and knockdown of Neogenin have a similar effect on the migration of CGNs, suggesting that Dock7 is a downstream mediator of Neogenin signaling. Dock7 has previously been shown to be involved in the migration of Schwann cells and to regulate interkinetic nuclear migration in cortical progenitor cells (Yamauchi et al. 2008; Yang et al. 2012). Intriguingly, the migration of these two cell types involves different Dock7-mediated molecular pathways. Dock7 activity as guanine exchange factor (GEF) is required for Schwann cell migration. In contrast, in cortical progenitors another structural domain of Dock7 acts to indirectly inhibit microtubule (MT) assembly. Additional experiments are needed to establish which of these Dock7 molecular pathways is involved in Neogenin signaling during CGN migration. The first possibility is that Dock7 GEF activity is induced upon Neogenin signaling. However, Dock7 specifically activates Rac/Cdc42 while RGMa-induced Neogenin signaling reportedly does not lead to Rac activation (Watabe-Uchida et al. 2006; Yamauchi et al. 2008; Hata et al. 2006; Conrad et al. 2007). It seems therefore unlikely that the Dock7 GEF pathway is part of Neogenin signaling. The second Dock7 molecular pathway involved in migration concerns its interaction with transforming acidic coiled-coil-containing protein 3 (TACC3), a MT-depolymerizing protein. Interaction of Dock7 antagonizes TACC3 functioning and loss of Dock7 leads to reduced interkinetic nuclear migration in cortical progenitor cells (Yang et al., 2012). There are currently no reports linking Neogenin signaling to modulation of the MT cytoskeleton. Therefore, it is highly interesting to pursue the hypothesis of Neogenin-induced Dock7-mediated MT manipulation. A starting point may be knockdown of wildtype Dock7 in migrating CGNs followed by the introduction of truncated Dock7 lacking the TACC3-binding site. If truncated Dock7 would rescue the migration phenotype observed following Dock7 knockdown, this indicates that Dock7-mediated TACC3 inhibition is dispensable for Neogenin signaling in migrating CGNs.

Finally, there is a possibility that Dock7 acts upstream of Neogenin through its interaction with MyosinVI (Majewski et al. 2012). This motor-protein is involved in trafficking cargo to and from the plasma membrane (Buss et al. 2002). MyosinVI has furthermore been shown to be involved in the transport of early endosomes (Sweeney & Houdusse 2010; Tumbarello et al. 2013). The regulation of local endocytosis and exocytosis is a key element of neuronal migration and is highly dependent on intracellular transport (Yap & Winckler 2012). Mislocalization of Neogenin as a result of loss of Dock7 could explain the resemblance of phenotypes following Neogenin and Dock7 knockdown. Experiments aimed at measuring surface levels of Neogenin following Dock7 knockdown could test this hypothesis.



## 2.2 Intracellular signaling in glia controls neuronal migration by determining the extracellular landscape

Intracellular transport is crucial to provide basic building blocks throughout the cell and to deliver signals going to and coming from the nucleus. During migration, highly polarized cells such as neurons face increased challenges at the level of intracellular transport since both the extracellular environment and intracellular structure are dramatically changing as the cell migrates. Although neuroscience research often focuses exclusively on neuronal cells, glial cells are omnipresent and essential in the brain. There are several types of glial cells with diverse functions. **Chapter 6** underlines the importance of glial cells for correct neuronal migration.

**Chapter 6** reports that glial cell-specific loss of BicD2 expression severely disrupts CGN migration while neuron-specific knockdown has no effect. BicD2 is a cytoplasmic cargo-protein involved in dynein-associated MT-mediated intracellular transport and secretory vesicle trafficking (Hoogenraad et al. 2001; Hoogenraad et al. 2003). The expression of extracellular matrix protein Tenascin C was found to be reduced in BicD2 knockout mice, suggesting that 1) BicD2 is responsible for the trafficking of Tenascin C and 2) glial extracellular matrix (ECM) proteins are required for CGN migration. Surprisingly little is known about trafficking mechanisms in glial cells and about the role of glia-derived ECM components in neuronal migration. This study stresses the crucial role of glial cells in neuronal development and encourages future research to increase our understanding of the role of glia-established ECM composition.

Interestingly, mutations in BicD2 have recently been associated with spinal muscular atrophy (SMA) (Neveling et al. 2013; Oates et al. 2013; Peeters et al. 2013). BicD2 knockout mice do not show motor neuron defects as observed in SMA, although BicD2 is endogenously expressed in the spinal cord (**Chapter 6** and Peeters et al., 2013). In fact, the SMA-associated mutations may induce a gain-of-function phenotype since SMA-mutated BicD2 has increased affinity for dynein leading to altered anterograde trafficking (Peeters et al. 2013; Oates et al. 2013). It remains to be investigated whether it is mutant BicD2 expression in motor neurons that is responsible for the SMA-phenotype. In light of the strong glia-specific function for BicD2 in neuronal migration, it would be interesting to explore the role of SMA-mutated BicD2 in glial cells. A recent study has shown that impaired glial functioning at least partly contributes to the SMA phenotype caused by loss of survival motor neuron 1 (SMN1) expression (Hunter et al. 2013). Interestingly, wild type neurons co-cultured with SMN1-knockout Schwann cells show reduced myelination and neurite density (Hunter et al. 2013). This indicates that the intrinsic properties of glial cells are important not only during development but also in disease. A similar

---

*in vitro* model may be used to gain insight in the intrinsic glial role of SMA-mutated BicD2 in neuronal functioning.

## **3 Disease: microRNAs in temporal lobe epilepsy**

### **3.1 Cell type-specific changes and altered subcellular localization of miRNAs in TLE**

At the time of publication in 2012, the study performed in **Chapter 7** was the first to report on genome-wide miRNA expression changes in human temporal lobe epilepsy (TLE) patient material. **Chapter 7** shows that the expression profiles of specific miRNAs correlate with disease severity and that several miRNAs are specifically up- or downregulated in TLE patients. Cell type-specific changes in neurons and glial cells were discovered by *in situ* hybridization. A combination of strategies revealed that immune response modulator ICAM1 is one of the miRNA targets affected in TLE. Furthermore, the subcellular localization of specific miRNAs is affected in patients. Whereas these miRNAs in control tissue are detected in the cytoplasm, in patient tissue they reside in the nucleus. Two scenarios may explain this observation in TLE patients; 1) mature miRNAs are transported from the cytoplasm back into the nucleus or 2) export of the related pre-miRNAs from the nucleus to the cytoplasm fails. Since nuclear export of miRNAs is regulated in a common pathway, and nuclear localization is specific for a subset of miRNAs, the latter option seems less likely. In favor of the first scenario, there is increasing evidence for the nuclear import and function of mature miRNAs (Liang et al. 2013). The question remains whether nuclear re-localization of specific miRNAs is a contributing factor to or a result of epileptogenesis. An interesting candidate miRNA for future research is miR-92b because it shows profound nuclear expression specifically in TLE patients and it is conserved in rodents. A first step would be to analyze nuclear presence of miR-92b following seizure-inducing stimulation. If miR-92b nuclear re-location is seizure-dependent, follow-up experiments may be aimed at elucidating its function. Moreover, sequencing of nuclear versus cytoplasmic RNA fractions may allow identification of additional seizure-induced nuclear miRNAs. This is highly interesting since it is currently unknown if miRNA shuttling to the nucleus is dynamically regulated (Liang et al. 2013). Comparing nuclear miRNAs prior to and following seizure induction would provide the first indication of a physiological stimulus involved in this mechanism.

### 3.2 The contribution of animal models to understand miRNAs in epileptogenesis

The patient tissue used in **Chapter 7** represents a late chronic stage of TLE. This resected human material is scarce and the data obtained is therefore of high value. However, based on this data it is impossible to discern whether miRNA expression changes contribute to or are the consequence of epilepsy. Dissecting cause and consequence requires the analysis of gene expression changes during the course of epileptogenesis. Several animal models have been developed for this purpose and numerous studies looking at gene expression changes, including miRNAs, during epileptogenesis have been published (Pitkänen & Lukasiuk 2009; Jimenez-Mateos & Henshall 2013). The reported changes in these studies only partly overlap, as may be expected from the diverse use of animal models, experimental designs and expression profiling platforms. Hence, the identification of the same miRNA by more than one independent study implies a robustness of its role in epilepsy. Additionally, these miRNAs may hold the highest potential for therapeutic application. In the following section a selection of miRNAs with promising clinical relevance will be discussed. Several studies confirm the involvement of the selected miRNAs in epileptogenesis or epilepsy. Moreover, preclinical studies manipulating their expression have been performed.

#### ***miR-34a***

Most research on miR-34a has focused on its role in the regulation of apoptosis in relation to cancer. Overexpression of miR-34a induces apoptosis and silencing miR-34a reduces cell death (Welch et al. 2007; Raver-Shapira et al. 2007; Chang et al. 2007). MiR-34a is upregulated immediately after seizure induction in both mice and rats (Hu et al. 2012; Sano et al. 2012). In rats, blocking miR-34a shortly after status epilepticus reduces the level of seizure-induced neuronal cell death (Hu et al. 2012). However, this effect was not replicated in mouse models (Sano et al. 2012).

MiR-34a expression has thus far not been associated with human epilepsy and no significant expression changes were found in **Chapter 7**. This could be explained by the fact that in rodents miR-34a is regulated immediately after the initial seizure but not in sustained seizures or epilepsy. Targeting miR-34a in humans immediately after brain trauma or initial seizure may prevent neuronal cell death. However, because of the risks involved in silencing a potent tumor suppressor gene, miR-34a seems to be a less attractive target for therapeutic application.

---

### **miR-132**

MiR-132 expression is upregulated by (seizure-induced) neuronal activity and it is involved in modulating dendritic morphology (Vo et al. 2005; Impey et al. 2010; Nudelman et al. 2010). Elevated levels of miR-132 are found in a rat model and in human patient tissue (Guo et al. 2014). In the dataset described in **Chapter 7** expression of miR-132 is moderately increased in patients but this change does not reach statistical significance ( $p = 0.08$ ). Blocking miR-132 reduces seizure-induced neuronal death, but does not affect seizure severity or duration (Jimenez-Mateos et al. 2011). In contrast, pretreatment with miR-132 blocking probes reduces occurrence of spontaneous seizures after status epilepticus in rats (Huang et al. 2014). Unfortunately, treatment preceding initial trauma is less relevant for human patients and no data have been published reporting protective effects of silencing miR-132 after the occurrence of spontaneous seizures.

### **miR-134**

Overexpression of miR-134 leads to reduced spine volume *in vitro* (Schratt et al. 2006) and reduced dendrite length *in vivo* (Christensen et al. 2010). MiR-134 is upregulated in several animal models of epilepsy and in brain tissue from human epilepsy patients (Jimenez-Mateos et al. 2012; Jimenez-Mateos et al. 2014; Peng et al. 2013). In **Chapter 7**, miR-134 detection failed in 16 out of 30 RNA samples irrespective of epilepsy pathology. This may reflect a technical inter-platform difference for this specific miRNA, and it underlines the importance of using independent techniques to validate results.

Blocking miR-134 prior to initial seizure reduces seizure-induced damage and neuronal cell death (Jimenez-Mateos et al. 2012; Jimenez-Mateos et al. 2014). Interestingly, silencing miR-134 after the initial seizure effectively inhibits the occurrence of spontaneous seizures. Moreover, the severity of the remaining seizures is significantly reduced (Jimenez-Mateos et al. 2012). Despite the reported effects of miR-134 on spine density and volume, silencing of miR-134 does not affect basic hippocampus dependent behavior (Jimenez-Mateos et al. 2014). Although additional behavioral testing is required, the clinical potential of miR-134 inhibition is fascinating. Silencing miR-134 in the epileptogenic period following initial injury may provide significant protection from the development of epilepsy.

### **miR-146a**

One of the most prominent findings of **Chapter 7** was the dysregulation of miRNAs targeting immune response-related genes. An example of a miRNA modulator of the immune response is miR-146a (Rusca & Monticelli 2011). This

miRNA is upregulated in a rat model of epilepsy and in human TLE patients as well as in human epilepsy-associated glioneuronal lesions (Aronica et al. 2010; Iyer et al. 2012; Omran et al. 2012). In the samples profiled in **Chapter 7**, miR-146a was slightly but significantly upregulated in patients with hippocampal sclerosis compared to other patients ( $p=0.02$ ) and controls ( $p=0.007$ ). In line with this, upregulation of miR-146a is most prominent during acute stages of TLE and only mildly increased at chronic stages (Omran et al. 2012). MiR-146a is expressed in reactive astrocytes and negatively regulates IL1-induced release of cytokines (Iyer et al. 2012). Based on these findings the upregulation of miR-146a *in vivo* in acute TLE could be an endogenous mechanism to minimize neuronal damage. The potential beneficial effect of increasing miR-146a expression *in vivo* remains to be investigated.

### 3.3 Clinical potential for miRNA expression manipulation

Several animal studies have revealed the potential of altering miRNA expression as a therapeutic strategy during epileptogenesis. Based on **Chapter 7** our knowledge of epilepsy-associated miRNA expression in humans has increased which may contribute to the identification of promising clinical targets. The human data may be used 1) to select novel miRNAs for functional experiments in animal models of epilepsy, and 2) to validate miRNAs previously discovered in animal models for their relevance to human epilepsy. There are several possibilities for manipulating the expression and function of miRNAs *in vivo*, and some encouraging preclinical trials using miRNA function-blocking agents have been described in the previous section. Successful clinical trials using similar reagents but targeting different diseases in human patients have been performed (Bhalala et al. 2013; Janssen et al. 2013). Nevertheless, additional testing of the efficiency and safety of miRNA function-blocking as a treatment for human epilepsy is required.

An additional use for miRNA expression profiles of human patients may be the development of diagnostic tools. In **Chapter 7**, patterns of miRNA expression in the hippocampus were found to correlate to disease pathology. Interestingly, miRNA expression changes in the brain are reflected in blood and plasma (Liu et al. 2010; Gorter et al. 2014). A fascinating prospect for future research would be to investigate if miRNA expression profiles at earlier stages of the disease correlate to specific pathological profiles at later stages. This information may then be used to predict for example disease progression and pharmaco-resistance in patients. If so, miRNA expression profiles obtained from blood samples may be a non-invasive diagnostic tool contributing to formulating individualized treatment plans.



---

## Final words

Strict regulation of a multitude of cell types creates a delicate balance in the brain that is vital for functioning during development and easily disturbed after injury. The overall aim of this thesis was to increase our understanding of developmental processes so that this knowledge may ultimately lead to novel strategies increasing the regenerative potential of the human brain. The first approach undertaken in this thesis was to study the axon guidance receptor Neogenin because it is involved in several developmental processes and also has a function in the adult brain. These results provide new directions for future research aimed at developing therapeutic targets for improving axonal regeneration by investigating how Neogenin interacts with its ligands and how responsiveness to RGMa is regulated. The second approach used in this thesis focuses on the cellular process of neuronal migration, which is dependent on intrinsic and extrinsic factors. A role for Neogenin and its newly identified interactor Dock7 in neuronal migration is described. Dock7 is revealed as an intrinsic neuronal factor required for RGMa-induced signaling. Additionally, we show that expression in glial cells of the intracellular transport protein BicD2 is an essential extrinsic factor for CGN migration. This finding underlines the importance of extrinsic properties for correct neuronal development and encourages future research on glial functioning. In the third and final approach this thesis contributes to our understanding of the molecular pathways involved in TLE, a disease characterized by neuron loss and gliosis. A disturbance of miRNA expression in both neurons and glial cells may contribute to the underlying pathogenesis. Taken together, this thesis 1) increases our knowledge of guidance cues and cellular processes involved in neuronal development, and 2) marks molecular changes that arise as a result of adult CNS injury and/or neuronal death. These insights lay the groundwork for designing preclinical studies aimed at improving the regenerative ability of the adult CNS.

## References

- Aronica, E. et al., 2010. Expression pattern of miR-146a, an inflammation-associated microRNA, in experimental and human temporal lobe epilepsy. *The European journal of neuroscience*, 31, pp.1100–1107.
- Bai, G. & Pfaff, S.L., 2011. Protease Regulation: The Yin and Yang of Neural Development and Disease. *Neuron*, 72, pp.9–21.
- Bhalala, O.G., Srikanth, M. & Kessler, J. a, 2013. The emerging roles of microRNAs in CNS injuries. *Nature reviews. Neurology*, 9, pp.328–39.
- Buss, F., Luzio, J.P. & Kendrick-Jones, J., 2002. Myosin VI, an actin motor for membrane traffic and cell migration. *Traffic (Copenhagen, Denmark)*, 3, pp.851–858.
- Chang, T.C. et al., 2007. Transactivation of miR-34a by p53 Broadly Influences Gene Expression and Promotes Apoptosis. *Molecular Cell*, 26, pp.745–752.
- Christensen, M. et al., 2010. Recombinant Adeno-Associated Virus-Mediated microRNA Delivery into the Postnatal Mouse Brain Reveals a Role for miR-134 in Dendritogenesis in Vivo. *Frontiers in neural circuits*, 3, p.16.
- Conrad, S. et al., 2007. Neogenin-RGMA signaling at the growth cone is bone morphogenetic protein-independent and involves RhoA, ROCK, and PKC. *The Journal of biological chemistry*, 282, pp.16423–16433.
- Doya, H. et al., 2006. Induction of repulsive guidance molecule in neurons following sciatic nerve injury. *Journal of Chemical Neuroanatomy*, 32, pp.74–77.
- Gooz, M., 2010. ADAM-17: the enzyme that does it all. *Critical reviews in biochemistry and molecular biology*, 45, pp.146–169.
- Gorter, J.A. et al., 2014. Hippocampal subregion-specific microRNA expression during epileptogenesis in experimental temporal lobe epilepsy. *Neurobiology of Disease*, 62, pp.508–520.
- Guo, J. et al., 2014. Expression of p-CREB and activity-dependent miR-132 in temporal lobe epilepsy. *International Journal of Clinical and Experimental Medicine*, 5(7), pp.1297–1306.
- Hata, K. et al., 2006. RGMA inhibition promotes axonal growth and recovery after spinal cord injury. *The Journal of cell biology*, 173, pp.47–58.
- Hoogenraad, C.C. et al., 2003. Bicaudal D induces selective dynein-mediated microtubule minus end-directed transport. *EMBO Journal*, 22, pp.6004–6015.
- Hoogenraad, C.C. et al., 2001. Mammalian golgi-associated Bicaudal-D2 functions in the dynein-dynactin pathway by interacting with these complexes. *EMBO Journal*, 20, pp.4041–4054.
- Hu, K. et al., 2012. MicroRNA expression profile of the hippocampus in a rat model of temporal lobe epilepsy and miR-34a-targeted neuroprotection against hippocampal neurone cell apoptosis post-status epilepticus. *BMC Neuroscience*, 13, p.115.
- Huang, Y. et al., 2014. MicroRNA-132 silencing decreases the spontaneous recurrent seizures. *International Journal of Clinical and Experimental Medicine*, 7(7), pp.1639–1649.
- Hunter, G. et al., 2013. SMN-dependent intrinsic defects in Schwann cells in mouse models of spinal muscular atrophy. *Human molecular genetics*, pp.1–16.

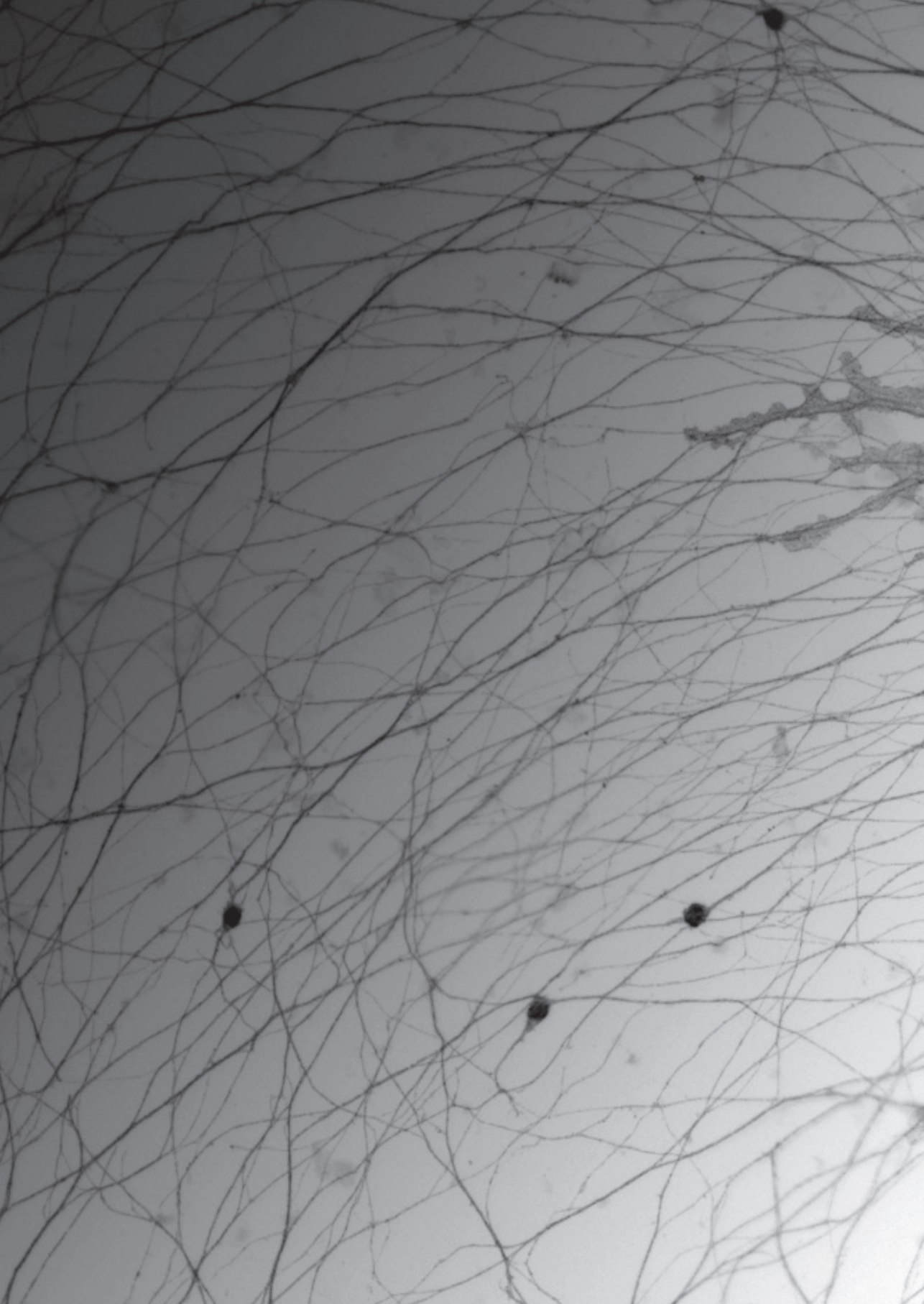
- 
- Impey, S. et al., 2010. An activity-induced microRNA controls dendritic spine formation by regulating Rac1-PAK signaling. *Molecular and Cellular Neuroscience*, 43, pp.146–156.
  - Iyer, A. et al., 2012. MicroRNA-146a: A Key Regulator of Astrocyte-Mediated Inflammatory Response. *PLoS ONE*, 7.
  - Janes, P.W. et al., 2005. Adam meets Eph: An ADAM substrate recognition module acts as a molecular switch for ephrin cleavage in trans. *Cell*, 123, pp.291–304.
  - Janssen, H.L. a et al., 2013. Treatment of HCV infection by targeting microRNA. *The New England journal of medicine*, 368, pp.1685–94.
  - Jimenez-Mateos, E.M. et al., 2014. Antagomirs targeting microRNA-134 increase hippocampal pyramidal neuron spine volume in vivo and protect against pilocarpine-induced status epilepticus. *Brain Structure and Function*.
  - Jimenez-Mateos, E.M. et al., 2011. MiRNA expression profile after status epilepticus and hippocampal neuroprotection by targeting miR-132. *American Journal of Pathology*, 179, pp.2519–2532.
  - Jimenez-Mateos, E.M. et al., 2012. Silencing microRNA-134 produces neuroprotective and prolonged seizure-suppressive effects. *Nature Medicine*, 18, pp.1087–1094.
  - Jimenez-Mateos, E.M. & Henshall, D.C., 2013. Epilepsy and microRNA. *Neuroscience*, 238, pp.218–229.
  - Liang, H. et al., 2013. Nuclear microRNAs and their unconventional role in regulating non-coding RNAs. *Protein and Cell*, 4, pp.325–330.
  - Liu, D.-Z. et al., 2010. Brain and blood microRNA expression profiling of ischemic stroke, intracerebral hemorrhage, and kainate seizures. *Journal of cerebral blood flow and metabolism: official journal of the International Society of Cerebral Blood Flow and Metabolism*, 30, pp.92–101.
  - Majewski, Ł. et al., 2012. Dock7: A GEF for Rho-family GTPases and a novel myosin VI-binding partner in neuronal PC12 cells. *Biochemistry and Cell Biology*, 90, pp.565–574.
  - Moss, M.L., Sklair-Tavron, L. & Nudelman, R., 2008. Drug insight: tumor necrosis factor-converting enzyme as a pharmaceutical target for rheumatoid arthritis. *Nature clinical practice. Rheumatology*, 4, pp.300–309.
  - Neveling, K. et al., 2013. Mutations in BICD2, which encodes a golgin and important motor adaptor, cause congenital autosomal-dominant spinal muscular atrophy. *American Journal of Human Genetics*, 92, pp.946–954.
  - Nudelman, A.S. et al., 2010. Neuronal activity rapidly induces transcription of the CREB-regulated microRNA-132, in vivo. *Hippocampus*, 20, pp.492–498.
  - O'Donnell, M., Chance, R.K. & Bashaw, G.J., 2009. Axon growth and guidance: receptor regulation and signal transduction. *Annual review of neuroscience*, 32, pp.383–412.
  - Oates, E.C. et al., 2013. Mutations in BICD2 cause dominant congenital spinal muscular atrophy and hereditary spastic paraplegia. *American Journal of Human Genetics*, 92, pp.965–973.
  - Okamura, Y., Kohmura, E. & Yamashita, T., 2011. TACE cleaves neogenin to desensitize cortical neurons to the repulsive guidance molecule. *Neuroscience Research*, 71(1), pp.63–70.

- Omran, A. et al., 2012. Interleukin-1 $\beta$  and microRNA-146a in an immature rat model and children with mesial temporal lobe epilepsy. *Epilepsia*, 53, pp.1215–24.
- Peeters, K. et al., 2013. Molecular defects in the motor adaptor BICD2 cause proximal spinal muscular atrophy with autosomal-dominant inheritance. *American Journal of Human Genetics*, 92, pp.955–964.
- Peng, J. et al., 2013. Expression patterns of miR-124, miR-134, miR-132, and miR-21 in an immature rat model and children with mesial temporal lobe epilepsy. *Journal of Molecular Neuroscience*, 50, pp.291–297.
- Pitkänen, A. & Lukasiuk, K., 2009. Molecular and cellular basis of epileptogenesis in symptomatic epilepsy. *Epilepsy and Behavior*, 14, pp.16–25.
- Rajagopalan, S. et al., 2004. Neogenin mediates the action of repulsive guidance molecule. *Nature cell biology*, 6, pp.756–762.
- Raver-Shapira, N. et al., 2007. Transcriptional Activation of miR-34a Contributes to p53-Mediated Apoptosis. *Molecular Cell*, 26, pp.731–743.
- Romi, E. et al., 2014. ADAM metalloproteases promote a developmental switch in responsiveness to the axonal repellent Sema3A. *Nature communications*, 5, p.4058.
- Rose-John, S., 2013. ADAM17, shedding, TACE as therapeutic targets. *Pharmacological Research*, 71, pp.19–22.
- Rusca, N. & Monticelli, S., 2011. MiR-146a in Immunity and Disease. *Molecular biology international*, 2011, p.437301.
- Sano, T. et al., 2012. MicroRNA-34a upregulation during seizure-induced neuronal death. *Cell Death and Disease*, 3, p.e287.
- Scheller, J. et al., 2011. ADAM17: A molecular switch to control inflammation and tissue regeneration. *Trends in Immunology*, 32, pp.380–387.
- Schnichels, S., Heiduschka, P. & Julien, S., 2011. Different spatial and temporal protein expressions of repulsive guidance molecule a and neogenin in the rat optic nerve after optic nerve crush with and without lens injury. *Journal of Neuroscience Research*, 89, pp.490–505.
- Schnichels, S., Heiduschka, P. & Julien, S., 2012. RGMA and neogenin protein expression are influenced by lens injury following optic nerve crush in the rat retina. *Graefes archive for clinical and experimental ophthalmology = Albrecht von Graefes Archiv für klinische und experimentelle Ophthalmologie*, 250(1), pp.39–50.
- Schratt, G.M. et al., 2006. A brain-specific microRNA regulates dendritic spine development. *Nature*, 439, pp.283–289.
- Schwab, J.M. et al., 2005. Spinal cord injury-induced lesional expression of the repulsive guidance molecule (RGM). *European Journal of Neuroscience*, 21, pp.1569–1576.
- Sweeney, H.L. & Houdusse, A., 2010. Myosin VI Rewrites the Rules for Myosin Motors. *Cell*, 141, pp.573–582.
- Tang, B.L., 2003. Inhibitors of neuronal regeneration: Mediators and signaling mechanisms. *Neurochemistry International*, 42, pp.189–203.
- Tassew, N. et al., 2013. Modifying Lipid Rafts Promotes Regeneration and Functional Recovery. *Cell Reports*.
- Tumbarello, D. a, Kendrick-Jones, J. & Buss, F., 2013. Myosin VI and its cargo adaptors - linking endocytosis and autophagy. *Journal of cell science*, 126, pp.2561–70.

- 
- Vo, N. et al., 2005. A cAMP-response element binding protein-induced microRNA regulates neuronal morphogenesis. *Proceedings of the National Academy of Sciences of the United States of America*, 102, pp.16426–16431.
  - Watabe-Uchida, M. et al., 2006. The Rac Activator DOCK7 Regulates Neuronal Polarity through Local Phosphorylation of Stathmin/Op18. *Neuron*, 51, pp.727–739.
  - Welch, C., Chen, Y. & Stallings, R.L., 2007. MicroRNA-34a functions as a potential tumor suppressor by inducing apoptosis in neuroblastoma cells. *Oncogene*, 26, pp.5017–5022.
  - Winckler, B. & Mellman, I., 2010. Trafficking guidance receptors. *Cold Spring Harbor perspectives in biology*, 2.
  - Yamauchi, J. et al., 2008. ErbB2 directly activates the exchange factor Dock7 to promote Schwann cell migration. *The Journal of cell biology*, 181, pp.351–365.
  - Yang, Y.-T., Wang, C.-L. & Van Aelst, L., 2012. DOCK7 interacts with TACC3 to regulate interkinetic nuclear migration and cortical neurogenesis. *Nature Neuroscience*, 15, pp.1201–1210.
  - Yap, C.C. & Winckler, B., 2012. Harnessing the Power of the Endosome to Regulate Neural Development. *Neuron*, 74, pp.440–451.
  - Zhang, A.S. et al., 2009. Hemojuvelin-neogenin interaction is required for bone morphogenic protein-4-induced hepcidin expression. *Journal of Biological Chemistry*, 284, pp.22580–22589.
  - Zhou, Z. et al., 2010. Neogenin Regulation of BMP-Induced Canonical Smad Signaling and Endochondral Bone Formation. *Developmental Cell*, 19, pp.90–102.









---

# **Addendum**

**Nederlandse Samenvatting  
Curriculum Vitae  
List of Publications  
Dankwoord**

---

# Nederlandse samenvatting

## Inleiding

In de hersenen geven zenuwcellen (neuronen) door middel van elektrische stroompjes boodschappen aan elkaar door. Op deze manier komt informatie over bijvoorbeeld de situatie elders in het lichaam binnen in een bepaald hersengebied en wordt deze doorgestuurd naar andere hersengebieden om ervoor te zorgen dat er actie wordt ondernomen. Het netwerk dat verschillende hersengebieden verbindt, wordt tijdens de embryonale ontwikkeling aangelegd.

Terwijl de aanleg van nieuwe zenuwbanen tijdens de ontwikkeling over het algemeen probleemloos verloopt, is het volwassen centrale zenuwstelsel slecht in staat om bestaande zenuwbanen te repareren. De gevolgen van beschadigingen aan de hersenen na bijvoorbeeld een ongeval of bij neurodegeneratieve ziektes zijn desastreus en vrijwel onomkeerbaar. Om beter te begrijpen waarom herstel van het volwassen zenuwstelsel zo moeizaam gaat, is het van belang om te begrijpen hoe de aanleg van dit zenuwstelsel tijdens de ontwikkeling plaatsvindt. Daarnaast is het belangrijk om na te gaan wat er precies gebeurt in het brein op het moment dat er sprake is van een neurodegeneratieve ziekte of andere beschadiging. Dit proefschrift benadert deze aspecten vanuit drie uitgangspunten: 1) op het moleculaire niveau wordt gekeken naar een signaalmolecuul en zijn receptor. Vervolgens wordt 2) op het niveau van de cel neuronale migratie onderzocht, een cellulair proces tijdens ontwikkeling dat afhankelijk is van de juiste intrinsieke en extrinsieke factoren. Ten slotte wordt 3) op het niveau van hersenweefsel onderzocht welke veranderingen kenmerkend zijn voor een aandoening die gepaard gaat met verlies van neuronen (epilepsie). **Hoofdstuk 1** beschrijft deze drie uitgangspunten en bevat achtergrondinformatie.

## Moleculaire Reactieroute: Signaalmoleculen en hun Receptor

Tijdens de ontwikkeling van het brein moeten pasgeboren neuronen hun weg vinden naar hun eindbestemming, waar zij een functioneel onderdeel van het hersennetwerk zullen vormen. Om de juiste weg te kunnen vinden, zijn er verschillende signaalmoleculen aanwezig in het embryonale brein. Alleen de neuronen met receptoren voor deze signaalmoleculen zullen in staat zijn hierop te reageren. Signaalmoleculen kunnen een aantrekkend of afstotend effect hebben op het groeiende neuron. De gevoeligheid van neuronen voor bepaalde signaalmoleculen is ten eerste afhankelijk van de aanwezigheid van de juiste receptor. Deze receptor zit op de buitenkant van de cel waardoor deze zijn omgeving kan waarnemen. Behalve de aanwezigheid van de juiste receptor, bestaan er een aantal mechanismes om de gevoeligheid voor signaalmoleculen



in detail te regelen. Zo kan het bijvoorbeeld voorkomen dat de receptor al aanwezig is, terwijl het voor het ontwikkelingsstadium van de cel nog te vroeg is om deze te activeren. Zodra de juiste situatie zich voordoet, kan de cel dan de aanwezige receptoren 'aan' zetten. Een aantal voorbeelden van mechanismes om deze gevoeligheid te regelen worden gegeven in **Hoofdstuk 2**. In dit hoofdstuk wordt een specifieke groep signaalmoleculen besproken waarvan al relatief veel bekend is; de class 3 Semaphorins. Er zijn echter een groot aantal soorten signaalmoleculen waarvan nog zeer weinig bekend is. Een voorbeeld hiervan zijn de Repulsive Guidance Molecules (RGMs). Er is een RGMa, RGMb en RGMc binnen deze groep, en de eerste twee hebben belangrijke functies in de ontwikkeling van het zenuwstelsel. Daarnaast zijn RGMa en RGMb ook aanwezig in het volwassen zenuwstelsel. RGMs hebben een afstotende werking op de uitlopers van neuronen (axonen). Tijdens de ontwikkeling is deze afstotende werking van belang om de juiste verbindingen te maken en onjuiste te voorkomen. Maar bij een beschadiging aan het volwassen zenuwstelsel kunnen RGMs het reparatieproces tegenwerken doordat zij verhoogd aanwezig zijn. Dit maakt deze signaalmoleculen zeer interessant. Door te onderzoeken hoe de gevoeligheid voor RGMs wordt geregeld tijdens ontwikkeling, kunnen we wellicht manieren bedenken om RGMs uit te schakelen na schade aan het volwassen zenuwstelsel.

De eerste stap die van belang is voor het functioneren van signaalmoleculen zoals RGMs, is de interactie met een receptor. De receptor voor RGM is Neogenin. Deze zit in het celmembraan en dan met name in de uitlopers van het neuron. Het RGM-bindende domein steekt door het membraan aan de buitenkant van de cel en het intracellulaire deel is verantwoordelijk voor het doorgeven van het signaal naar de binnenkant van de cel. Hoewel we weten dat Neogenin de enige receptor voor RGM is, is er nog niet veel bekend over hoe deze twee eiwitten interacteren en hoe dit uiteindelijk zorgt voor afstoting van het axon. In **Hoofdstuk 3** werd daarom gekeken welke specifieke stukken van het eiwit (eiwitdomeinen) belangrijk zijn voor de binding van RGM aan Neogenin. Er blijken twee bindingsplekken te zijn, site-1 en site-2, die er samen voor zorgen dat twee RGM moleculen binden aan twee Neogenin moleculen (een quadruplex). Om te kijken wat de rol van de twee domeinen is, werden er RGM eiwitten gemaakt waarbij specifiek een aminozuur van site-1 of site-2 veranderd werd waardoor de binding niet meer plaats kan vinden. Uit experimenten met deze site-1 en site-2 veranderde eiwitten blijkt dat site-1 essentieel is voor binding van RGM aan Neogenin. Site-2 speelt ook een rol in binding, maar dan met name in de vorming van de quadruplex structuur, aangezien er zonder site-2 nog wel duplexstructuren worden gevormd. Om na te gaan of de verminderde binding functionele gevolgen heeft, werden vervolgens de veranderde eiwitten gebruikt in kweekexperimenten met neuronen. Normaal gesproken heeft RGM een remmende werking op de uitgroei van axonen. Zoals



---

verwacht is dit effect niet aanwezig wanneer de site-1 binding met Neogenin niet meer plaats kan vinden. Opvallender is dat ook bij verlies van site-2 binding de remmende werking van RGM significant minder is. Dit laat zien dat de quadruplexstructuur van groot belang is voor het produceren van een krachtige respons op RGM.

Nu we een beter idee hebben van hoe de interactie tussen RGM en Neogenin eruit ziet, is de volgende stap om te bestuderen hoe de cel zijn signaalsterkte voor RGM kan regelen. In theorie zou dit bijvoorbeeld kunnen door de hoeveelheid Neogenin receptoren toe of af te laten nemen. Hoe meer Neogenin, des te sterker zal de gevoeligheid voor RGM zijn, en omgekeerd. In **Hoofdstuk 4** werd ontdekt dat neuronen een iets ingewikkelder mechanisme gebruiken. Gevoeligheid van neuronen voor RGMa blijkt namelijk niet alleen afhankelijk te zijn van Neogenin maar ook van het eiwit Lrig2 (leucine-rich repeat and immunoglobulin-like protein 2). Dit eiwit steekt, net als Neogenin, door het membraan heen en kan met zijn extracellulaire deel binden aan Neogenin, maar niet aan RGMa. Uit een experiment waar neuronen geen Lrig2 meer kunnen maken blijkt dat deze neuronen ook niet meer reageren op RGMa. Het ligt voor de hand om te controleren of Lrig2 wellicht een effect heeft op de hoeveelheid Neogenin in het membraan. Uit deze experimenten blijkt dat er net zoveel Neogenin aanwezig is in de cel met of zonder Lrig2. Bij nader onderzoek en door middel van een andere methode werd echter gevonden dat er wel een effect is op de hoeveelheid extracellulair Neogenin. In cellen zonder Lrig2 zit er minder Neogenin op de buitenkant van de cel en is de cel dus minder gevoelig voor RGMa. Dit wordt verklaard door de aanwezigheid van een derde celmembraan eiwit; het enzym ADAM17. ADAM17 enzym kan het extracellulaire deel van een zeer groot aantal eiwitten, waaronder Neogenin, afknippen. Voor de cel is dit belangrijk om bijvoorbeeld regelmatig de buitenkant van het celmembraan te verversen en verouderde receptoren te verwijderen zodat er nieuwe voor in de plaats kunnen komen. Lrig2 blokkeert het knippen van Neogenin door ADAM17 en voorkomt daarmee dat Neogenin te vroeg wordt verwijderd. Pas op het moment dat RGMa bindt aan Neogenin, laat Lrig2 los en kan ADAM17 de gebruikte receptor van het celmembraan afknippen.

De ontdekking van dit mechanisme is zeer interessant omdat het extra mogelijkheden biedt voor onderzoek naar de verbetering van het reparatievermogen van het volwassen zenuwstelsel. Zoals eerder genoemd, komen RGMa en Neogenin voor in het volwassen zenuwstelsel en is een gevolg hiervan dat neuronen na beschadiging niet terug groeien; zij worden afgestoten door RGMa. In een experiment om de regeneratie van beschadigde neuronen te verbeteren, werd Neogenin dan wel Lrig2 expressie geblokkeerd na het toedienen van een laesie aan de oogzenuw in muizen. Zoals verwacht leidt verlaging van Neogenin expressie ertoe dat er meer regeneratie optreedt, immers de neuronen zijn minder gevoelig voor RGMa.

Opmerkelijk was dat zowel het aantal regenererende axonen als de afgelegde groei afstand aanzienlijk toeneemt na verlaging van Lrig2 expressie. Dit verschil is groter dan na verlaging van Neogenin. Dit werd verklaard door experimenten die laten zien dat Lrig2 niet alleen Neogenin beschermt tegen vroegtijdig knippen door ADAM17, maar dat dit mechanisme ook gebruikt wordt voor andere receptoren. Samenvattend laat dit hoofdstuk zien dat Lrig2 een zeer interessant doelwit is voor het ontwikkelen van nieuwe klinische methodes gericht op het vergroten van axonale regeneratie.

## Cellulair proces: Neuronale Migratie

Het eerste deel van dit proefschrift was gericht op de structuur en werking van signaalmoleculen en hun receptor op eiwitniveau. In het tweede deel kijken we op het niveau van de cel naar een proces dat essentieel is voor de ontwikkeling van het zenuwstelsel; neuronal migratie. Bij dit cellulaire proces spelen signaalmoleculen een belangrijke rol. Ze dienen als het ware als verkeersborden die de weg wijzen aan het migrerende neuron. Echter, er zijn tal van andere factoren die invloed hebben op het vinden van de juiste route. Van groot belang is ten eerste de interne situatie van de cel; zijn de juiste cellulaire onderdelen aanwezig om te kunnen reageren op signaalmoleculen en om voort te kunnen bewegen? Deze factoren zijn cel-eigen oftewel intrinsiek voor de cel. Ten tweede heeft de omgeving van de cel een grote invloed op neuronale migratie. Het extracellulaire milieu is niet een open ruimte met daarin een aantal signaalmoleculen, maar is volgepakt met verschillende celtypes en eiwitten, waarvan signaalmoleculen slechts een deel uitmaken. Al deze extrinsieke factoren vormen samen een balans met de intrinsieke factoren die uiteindelijk essentieel is voor de correcte aanleg van zenuwbanen en verbindingen.

Voor dit deel van het proefschrift wordt de migratie van cerebellaire granuulcellen (CGC) gebruikt als een modelsysteem. De kleine hersenen (cerebellum) ontwikkelen zich namelijk op een zeer stereotype manier en de migratie van de CGCs is voorspelbaar en relatief eenvoudig te manipuleren. In **Hoofdstuk 5** wordt onderzocht wat de rol van Neogenin is tijdens de migratie van CGCs. Uit een serie experimenten blijkt dat Dock7, een eiwit dat bindt aan het intracellulaire deel van Neogenin, essentieel is voor RGMA signaaltransductie. Van Dock7 is al bekend dat het betrokken is bij cellulaire migratie, maar nog niet of dat ook geldt voor migratie gestuurd door RGMA en Neogenin. In de experimenten in dit hoofdstuk werd eerst gekeken waar de drie eiwitten tot expressie komen. Dock7 en Neogenin blijken aanwezig te zijn in CGCs die bezig zijn met een bepaalde stap in hun migratie traject. RGMA is ook aanwezig op specifieke plekken van dit traject, maar wordt niet door CGCs maar door andere celtypes gemaakt. Vervolgens werd de expressie van Neogenin of Dock7 in migrerende CGCs geblokkeerd. Hieruit blijkt dat zowel

---

Neogenin als Dock7 een rol spelen in CGC migratie; neuronen die één van deze twee eiwitten missen, migreren minder ver binnen dezelfde tijd in vergelijking met controle neuronen. Dit effect lijkt te maken te hebben met gevoeligheid voor RGMa. In een ander experiment werd namelijk gevonden dat bij neuronen die op dezelfde manier selectief minder Dock7 hebben, er geen effect op migratie door RGMa meer is. De resultaten in dit proefschrift laten voor het eerst zien dat Dock7 belangrijk is voor neuronale migratie en dat deze intrinsieke regulatie via Neogenin verloopt. Vervolgonderzoek zal zich richten op het uitvinden hoe het mechanisme van Neogenin regulatie door Dock7 precies in elkaar steekt.

In **Hoofdstuk 6** ligt de nadruk op een niet-neuronaal celtype dat uitermate belangrijk is voor de ontwikkeling en het functioneren van neuronen: de glia cel. Glia cellen zijn alomverteenwoordigd in het brein en hebben uiteenlopende functies. Een van deze functies is het geven van steun tijdens neuronale migratie. Deze steun is in het geval van migrerende CGCs vrij letterlijk; de neuronen gebruiken uitlopers van glia cellen om zich aan vast te houden, terwijl ze naar hun eindbestemming migreren. Interessant genoeg blijkt de aanwezigheid van een intracellulair eiwit in glia cellen essentieel te zijn voor de migratie van CGCs. Dit eiwit, BicD2, is betrokken bij intracellulair transport van vracht (bijvoorbeeld andere eiwitten) over het cytoskelet. Een transgene muis die het BicD2 gen mist (knockout), heeft ernstige defecten aan de neuronale migratie, onder andere van de CGCs. Omdat BicD2 in veel verschillende celtypes voorkomt, is de volgende stap om erachter te komen welk celtype gevoelig is voor het ontbreken van dit gen. Voor de hand liggend zou zijn dat neuronen zelf het gen nodig hebben, aangezien het defect zichtbaar is in neuronen. Maar het tegendeel blijkt waar te zijn; wanneer BicD2 selectief uit neuronen wordt verwijderd, is er geen migratie defect. Echter, wanneer BicD2 selectief uit glia cellen wordt verwijderd, is het migratie defect even groot als bij de volledige knockout. Deze bevindingen benadrukken hoe belangrijk glia cellen zijn voor de aanleg van een functioneel brein.

## **Ziekte: Epilepsie**

De eerste twee delen van dit proefschrift zijn gericht op het begrijpen van respectievelijk moleculen en cellulaire processen betrokken bij de embryonale ontwikkeling. In het derde en laatste deel wordt gekeken naar moleculen en cellulaire processen die verstoord zijn bij een neurologische aandoening waarbij neuronen afsterven; epilepsie. In het epileptogene brein zijn een aantal moleculaire en cellulaire processen verstoord waardoor aanvallen ontstaan. Deze aanvallen kunnen weer verdere verstoringen in het brein veroorzaken waardoor een vicieuze cirkel ontstaat. Een van de meest opvallende verschijnselen in het brein van epilepsiepatiënten is het verlies van neuronen. Nadat neuronen doodgaan komen er veelal glia cellen voor in de plaats. Een deel van deze cellen zijn reactief;

ze produceren stoffen die een immuunreactie opwekken. De aanwezigheid van een immuunreactie is een ander kenmerk van het epileptische brein en draagt waarschijnlijk bij aan de verhoogde gevoeligheid voor volgende aanvallen.

Hoewel we veel weten over de cellulaire processen die betrokken zijn bij epilepsie, weten we nog erg weinig over de moleculaire oorzaken die hieraan ten grondslag liggen. In **Hoofdstuk 7** wordt daarom gekeken naar de rol van microRNAs, een groep moleculen die betrokken zijn bij de regulatie van een groot aantal genen en die daarom kunnen functioneren als hoofdschakelaars bij deze cellulaire processen. Een speciale techniek waarbij naar alle microRNAs tegelijk kan worden gekeken, wordt gebruikt om de hersenen van patiënten te vergelijken met normale hersenen. Er blijken grote verschillen te zijn tussen deze twee groepen in de hoeveelheid van bepaalde microRNAs. Voor patiënten onderling komen de microRNA expressieprofielen juist veel overeen. Dit is een aanwijzing dat er een gezamenlijk moleculair mechanisme betrokken is bij het ontstaan van epilepsie. Van een aantal microRNAs wordt uitgezocht in welke celtypes ze tot expressie komen. Sommigen blijken specifiek in neuronen voor te komen, terwijl anderen meer in glia cellen aanwezig zijn. Een paar van deze glia-specifieke microRNAs blijken een rol te hebben in het onderdrukken van genen die de immuunreactie vormen. Deze microRNAs zijn verminderd aanwezig in patiënten, wat bij kan dragen aan de karakteristieke verhoogde immuunreactie.

## Afsluiting

Dit proefschrift draagt bij aan ons begrip van een aantal moleculaire en cellulaire ontwikkelingsprocessen die de potentie hebben om toegepast te worden in de zoektocht naar nieuwe therapieën voor hersenziekten. Daarnaast hebben we een aantal moleculaire processen geïdentificeerd die kenmerkend zijn voor patiënten met epilepsie. In **Hoofdstuk 8** worden de implicaties van de resultaten uit dit proefschrift voor toekomstig onderzoek in meer detail besproken. Door het ontrafelen van moleculaire en cellulaire processen die een rol spelen tijdens de embryonale ontwikkeling kunnen we erg veel leren over de werking van het zenuwstelsel. Het is fascinerend hoe een complexe mix van celtypes in een embryo kan uitgroeien tot een functioneel brein dat bovendien bij vrijwel iedereen op dezelfde manier is aangelegd. Behalve fascinerend, is het ook waardevol om deze processen te bestuderen. Er zijn een groot aantal aandoeningen waarbij beschadigingen aan het zenuwstelsel rampzalige en blijvende gevolgen hebben, zoals bijvoorbeeld bij de ziekte van Alzheimer en Parkinson. Het is op dit moment onmogelijk om het eenmaal beschadigde zenuwstelsel weer volledig te repareren. De sleutel tot het verbeteren van dit regeneratieve vermogen is wellicht te vinden in het zich nog ontwikkelende brein. De bevindingen uit dit proefschrift vormen een basis voor verder onderzoek in deze richting.

---

## Curriculum Vitae

Susan van Erp was born on November 13<sup>th</sup> 1984 in Veghel, the Netherlands. After graduating in 2002 from the secondary school Sint Bonifatius College in Utrecht, she studied Biology at Utrecht University. In 2005 she obtained her Bachelor of Science degree and then continued her education by following the Master program Experimental and Clinical Neuroscience at Utrecht University, beginning in 2006. Two scientific research projects were performed as part of this Master degree. The first project took place under the supervision of Frank Jacobs in the laboratory of Prof. Marten Smidt at the Rudolf Magnus Institute of Neuroscience, University Medical Center Utrecht. The aim of this project was identifying Pitx3 interacting proteins. The second research project was carried out under supervision of Matthew Mason in the laboratory of Prof. Joost Verhaagen at the Netherlands Institute for Neuroscience, Amsterdam Medical Center. This project involved microarray profiling of a conditional knockout mouse model for facial nerve regeneration. After obtaining her Master of Science degree (*cum laude*) in 2008, she pursued a PhD in the laboratory of Prof. Jeroen Pasterkamp at the Brain Centre Rudolf Magnus, University Medical Center Utrecht in 2009. During this time she worked on a number of projects studying the regulation and expression of several signalling molecules involved in brain development and disease. The results of these research projects are described in this thesis. Susan will continue her research career as a postdoctoral scientist in the laboratory of Prof. Charles ffrench-Constant at the Scottish Centre for Regenerative Medicine, Edinburgh University, United Kingdom.



## List of publications

**S. van Erp\***, D.M.A. van den Heuvel\*, Y. Fujita, A.J.C.G.M. Hellemons, M. Kuijpers, J. Demmers, H. Hedman, C.C. Hoogenraad, T. Yamashita, and R.J. Pasterkamp. Lrig2 Negatively Regulates Ectodomain Shedding of Axon Guidance Receptors by ADAM Proteases at the Neuronal Growth Cone. *Submitted*

D. Jaarsma\*, R. van den Berg\*, P.S. Wulf\*, **S. van Erp**, N. Keijzer, M.A. Schlager, E. de Graaff, C.I. De Zeeuw, R.J. Pasterkamp, A. Akhmanova, C.C. Hoogenraad. A role for Bicaudal-D2 in radial cerebellar granule cell migration. *Nature Communications*, 2014; 5:3411

M.A. van Gestel, **S. van Erp**, L.E. Sanders, M.A.D. Brans, M.C.M. Luijendijk, M. Merkestein, R.J. Pasterkamp, R.A.H. Adan. shRNA-induced saturation of the microRNA pathway in the rat brain. *Gene therapy*, 2014; 21(2):205-11

C.H. Bell, E. Healey\*, **S. van Erp\***, B. Bishop, C. Tang, R.J.C. Gilbert, A. Radu Aricescu, R.J. Pasterkamp, C. Siebold. Structure of the Repulsive Guidance Molecule (RGM)-Neogenin Signaling Hub. *Science*, 2013; 341(6141):77-80

A.A. Kan\*, **S. van Erp\***, A.A.H.A. Derijck, M. de Wit, E.V.S. Hessel, E. O'Duibhir, W. de Jager, P.C. van Rijen, P.H. Gosselaar, P.N.E. de Graan, R.J. Pasterkamp. Genome-wide microRNA profiling of human temporal lobe epilepsy identifies modulators of the immune response. *Cellular and Molecular Life Sciences*, 2012; 69(18):3127-45

A.A.H.A. Derijck, **S. van Erp** and R.J. Pasterkamp. Semaphorin signaling: molecular switches at the midline. *Trends in Cell Biology*, 2010; 20(9):568-76

F.M. Jacobs, **S. van Erp**, A.J. van der Linden, L. von Oerthel, J.P. Burbach, M.P. Smidt. Pitx3 potentiates Nurr1 in dopamine neuron terminal differentiation through release of SMRT-mediated repression. *Development*, 2009; 136(4):531-40

(\* these authors contributed equally)

---

## Dankwoord

De mensen die direct aan het onderzoek in dit proefschrift hebben meegewerkt staan natuurlijk al vernoemd als coauteurs bij elk hoofdstuk. Toch zijn er nog een aantal mensen die betrokken waren bij de tot stand koming van dit boekje maar die niet bij de auteurs horen. En sommige coauteurs zijn zoveel meer dan alleen dat. Dan zijn er nog de mensen die niet perse met dit boekje te maken hebben gehad maar die wel te maken hadden met mij en daardoor ook van grote invloed zijn geweest. Hier wil ik de gelegenheid nemen om al deze mensen te bedanken.

Ten eerste mijn promotor Jeroen Pasterkamp. Ik heb zo ontzettend veel van je geleerd. Je gedrevenheid en doorzettingsvermogen werken enorm motiverend bij het doen van vaak frustrerend langzame of verraderlijk veranderlijke experimenten. Ik heb groot respect, en bewondering, voor jouw manier van onderzoek doen. Heel erg bedankt voor al je hulp, tijd en toewijding.

Peter Burbach, mijn tweede promotor, bedankt voor je input in mijn onderzoek. Met name je kalme en tactische houding tijdens de laatste stressvolle weken heb ik erg gewaardeerd.

The members of my reading committee: Prof. Hans Bos, Prof. Joost Verhaagen, Prof. Anna Akhmanova, Prof. Chris de Zeeuw and Prof. David Henshall, I would like to thank you for reviewing my thesis.

The Pasterlab. Since I joined the group in 2009, its composition has gradually changed almost entirely. Still it has always felt like one group to me; a number of people who share their enthusiasm for science and who support each other when needed and celebrate together when possible. It has been great to be part of that group, so thanks to each (former) member!

Dianne, ik heb jouw passie voor Neogenin overgenomen. Bedankt voor je eindeloze geduld als ik weer eens om eeuwen oude western blots of antilichamen kwam vragen. Ik ben supertrots op onze gezamenlijke (bijna) paper en dat jij mij bij wil staan als paranimf!

Mijn tweede paranimf Eljo. Ik sta elke keer weer versteld bij het horen van jouw dagindeling. Ondanks je toch al drukke schema lijkt je altijd weer tijd te vinden om nog wat extra te doen of om hulp te bieden zodra iemand daar om vraagt. En dan laat je het ook nog lijken alsof het allemaal heel vanzelfsprekend en makkelijk is. Gewoon doen en doorgaan. Weet je wel hoe bijzonder dat is? Heel veel succes

.....

met de laatste maanden van je PhD en welke keuze je ook maakt voor daarna, ik weet zeker dat je er wat geweldigs van gaat maken!

Lieve Anita, je bent een van die co-auteurs die eigenlijk veel meer is. Je bent de afgelopen jaren een enorme steun geweest bij het uitvoeren van experimenten en het meten van eindeloos veel growthcones. Maar net zo veel steun ben je dankzij je betrokkenheid en interesse ook wat betreft niet-werk gerelateerde zaken. Ik wens jou, Niek, en Peter ontzettend veel geluk toe en natuurlijk heel veel succes met je opleiding en daarna!

Bart. Films, muziek, eten, klimmen, reizen, je bizarre sportieve uitspattingen; naast het toch al onuitputtelijke onderwerp dat elk aspect van onderzoek omvat denk ik niet dat ik ooit uitgepraat zal zijn met je... De laatste loodjes zijn fucking zwaar, maar het grote Bart en Hannah in Portland avontuur gaat ongetwijfeld awesome worden. Heel erg veel succes met alles en als je ooit in de buurt bent, kom zeker langs! O en namens Tuna heel erg bedankt voor jullie goede zorgen...

Ewout, voor mij is jouw nuchtere, relativiserende kijk op de wetenschap vaak erg welkom en gewaardeerd geweest. Je bent me een jaar geleden voorgedaan naar Edinburgh en ik moet zeggen, je enthousiasme werkt behoorlijk aanstekelijk. Heel erg bedankt voor je tips&tricks en ik hoop dat we elkaar vaak tegen komen!

Ewoud, we hebben jarenlang naast elkaar in het lab gewerkt, al was het vanwege de onmiskenbare puinhoop lastig te zien waar de ene bench begon en de ander ophield. Bedankt voor het geduldig beantwoorden van al mijn vragen en voor het meelachen om Coen en Sander. Heel veel succes in New York met al je grants!

Vamshi, it was cool to watch from a short distance how the miRNA project developed after you took over, and I really enjoyed discussing new, exciting or unexpected, results with you. All the best to you, Sada, and the new baby!

Leo, je staat altijd klaar om te helpen, met de meest uiteenlopende zaken. Bedankt voor alles dat je doet; hoe hopeloos we zijn zonder jou is pijnlijk duidelijk op het moment dat je er een tijdje niet bent. Ik zal je humor, verhalen en algemene aanwezigheid in het lab erg gaan missen...

Het RMI. De sfeer op het lab, lekker pipetteren met de radio aan en met net wie je tegenkomt spannende nieuwe experimenten, vreemde resultaten of gewoon het afgelopen weekend bespreken. De labdag, paas/kerst/sinterklaaslunch, en zo nu en dan een lichtelijk uit(de hand)gelopen afdelingsborrel... De goede

---

herinneringen die ik aan de afgelopen jaren op het RMI heb, zijn bijna volledig met dank aan jullie; de analisten van 4e en 5e verdieping, de oude en nieuwe AIO's en postdocs, en andere koffiekamer bezoekers! Zonder namen te gaan noemen en misschien mensen te vergeten; ik hoop dat je weet dat ik het over jou heb als je dit leest...

Kamergenoten. Margriet, de zelfverklaard meest belangrijke persoon bij de tot stand koming van dit boek. Wat was het leuk om naast je te zitten 'werken' op de computer en wat was het ongelooflijk rustig als je weer eens met zwangerschapsverlof was. Je bent m'n grote voorbeeld wat betreft combineren van werk-kinderen en ik hoop dat we ipv tijdens de lunch via whatsapp blijven bijpraten... Frank M, jouw rust en humor zijn een geweldige combinatie, heel erg bedankt voor je behulpzaamheid bij allerlei vragen en problemen. Francesca, I miss hearing you say 'Ahhh so sweet!!' and 'Frizzled3' as I miss discussing work and every other aspect of life with you on a daily basis. I wish you so much luck and happiness and hope you will enjoy Helsinki and your postdoc! Sara, thank you for bringing more Italian influences to our rather boring Dutch culture with your genuine enthusiasm and excitement. You've made me realize more than once that also small things are worth being amazed by.

The master student internships I supervised, thank you for your contribution to Chapter 5. Renate, inmiddels ben je alweer een hele tijd zelf AIO. Ik hoop dat je je fascinatie voor wetenschap en enthousiasme om mooie plaatjes en goed gelukte experimenten behoudt! Stephen, science can be frustrating but with your persistence and intelligence I know that if you want to you will do great.

Mijn eigen eerste lab-ervaring was in de groep van Marten als student van Frank. Het is vaak zo dat hoe je iets eenmaal geleerd hebt, ook is zoals je het zal blijven doen. Ik hoop ontzettend dat dit ook geldt voor onderzoek doen, want ik denk niet dat ik hierin een beter voorbeeld had kunnen hebben. Frank, heel erg bedankt voor alles en veel succes met je eigen groep!

Dit boek zoals het nu in fysieke uitvoering in je handen ligt, is te danken aan Proefschrift-AIO. Guus, heel erg bedankt voor je ontzettend snelle en flexibele manier van werken!

Dan de mensen die verder van de inhoud van dit boek af staan, maar dicht bij mij zelf. Marieke, de afgelopen jaren was ik veel te vaak te laat op of te druk voor afspraken. Nu is het eindelijk af, en kan ik je alsnog niet zo vaak zien als ik zou willen, alleen nu om logistieke redenen. Ik hoop dat je weet hoe belangrijk je

.....

al 25 jaar voor me bent. Ilse, het was zo fijn om jou in de buurt te hebben om spontaan samen te eten, drinken, praten, of watdanook. En het is vreselijk dat je nu opeens heel ver weg bent. Kom alsjeblieft heel vaak langs! Bouke, heel erg bedankt voor je second opinion bij het maken van de Nederlandse samenvatting, hij is een stuk verbeterd na je aanpassingen. Alco en Tjeerd, de ene dag zaten we nog in ons zelden schoon noch opgeruimd sloopappartement een biertje te drinken als huisgenoten, en nu zijn we opeens allemaal binnen iets meer dan een jaar verantwoordelijke ouders geworden. Gelukkig zijn we niet gestopt met dat biertje drinken zo nu en dan, en ik hoop dat dit ook nog heel lang zo zal blijven...

Pim en Marianne, Loes en Gershon, Bram en Shaquira; het gaat zelden over werk als we elkaar zien, behalve dan misschien om die mix van fascinatie en afgrijzen op jullie gezichten te krijgen bij het horen van de experimenten die ik zoal deed. Het is altijd vanzelfsprekend gezellig en relaxed en daarom ontzettend fijn om bij jullie te zijn. Ik hoop dan ook dat jullie nog heel vaak komen logeren.

Ruud en Saskia, pap en mam, ik ben onbeschrijfelijk dankbaar voor jullie onvoorwaardelijke steun en hulp. Zelfs bij keuzes die jullie nou niet direct zelf hadden genomen, staan jullie zonder uitzondering en als vanzelfsprekend altijd voor me klaar. Dit waardeer ik zo, en jullie zijn vreselijk belangrijk voor me. Dit boek is in elk opzicht dankzij jullie.

Eoghan, you know exactly how to motivate me to continue when I am stuck and you will discuss and come up with solutions for any possible problem or obstacle. At the same time you know much better than me that there are things that are far more important than any experiment and you can somehow manage to convince me. Thank you for insisting to go on holidays. I feel happiest when you are by my side and I am looking forward to the next forty years!



*“Eventually, all components will be catalogued, connections between them will be described, and the consequences of removing each component or their combinations will be documented. This will be the time when the question, previously obscured by the excitement of productive research, would have to be asked: Can the information that we accumulated help us to repair the radio?”*

Yuri Lazebnik, Cancer Cell, 2002